

**A quantitative approach to the evolution of the central Walvis Basin
offshore NW-Namibia:
structure, mass balancing, and hydrocarbon potential**

Dissertation zur Erlangung des
naturwissenschaftlichen Doktorgrades
der Bayerischen Julius-Maximilians-Universität Würzburg

vorgelegt von

Matthias Kukulus

aus Donauwörth

Würzburg, 2004

Eingereicht am: 28. Januar 2004

1. Gutachter: Prof. Dr. Volker Lorenz

2. Gutachter: Prof. Dr. Andreas Henk

der Dissertation

1. Prüfer: Prof. Dr. Volker Lorenz

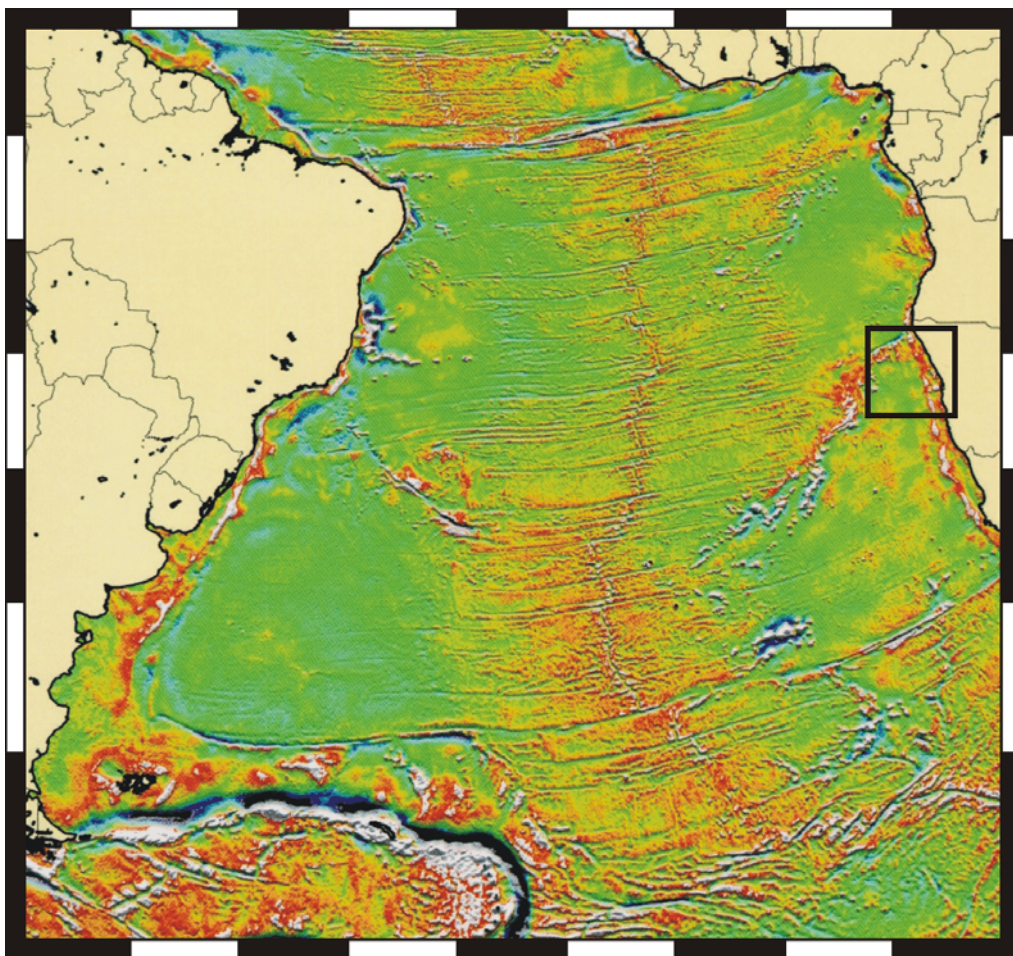
2. Prüfer: Prof. Dr. Franz Theodor Fürsich

der mündlichen Prüfung

Tag der mündlichen Prüfung: 3. Dezember 2004

Doktorurkunde ausgehändigt am:

**A quantitative approach to the evolution of the central Walvis Basin
offshore NW-Namibia:
structure, mass balancing, and hydrocarbon potential**



Die Natur ist unerbittlich und unveränderlich, und es ist ihr gleichgültig, ob die verborgenen Gründe und Arten ihres Handelns dem Menschen verständlich sind oder nicht.

Galileo Galilei

Acknowledgements

This work was initiated and supervised by Andreas Henk whose steady support and readiness for discussions is gratefully acknowledged. I am thankful to Volker Lorenz who raised my enthusiasm for geological field work in Namibia.

My friend and colleague Ralf Junker is thanked for a very fruitful cooperation and good times in the field; this work could not have been realised without his support.

Many thanks go to Roger Swart and Alex Warne from *NAMCOR* for any cooperation and for the provision of essential data and samples.

I thank Karin Klauss, Isolde Schmidt, Marie-Luise Bühler, and Hiltrud Müller-Sigmund for their helpful support in sample preparation.

Andreas Danilewsky is gratefully acknowledged for his generous help and the introduction into SEM analysis. Manfred Martin is thanked for the opportunity to perform XRF analysis. I thank Andreas Beha for his supportive work with *PetroMod2D*.

I particularly acknowledge Matthias Raab for instructive discussions of the denudation history. Fritz Schlunegger and Giovanni Bertotti are thanked for the discussion of the general model concept. I thank Rodney Grapes for discussing the geochemical results. The encouragement of Robert Gatliff is appreciated who provided the opportunity to present first results at the Petroleum Group Meeting of the Geological Society of London.

I would like to thank my friends and colleagues Gustl, Roman, Carmen, Majo, Heike, Ansgar, Sabine, Claudia S., Claudia P., Elmar, Rudy, and Aron for any help and for accompanying me through all this.

Special thanks are owed to Suse and my parents for any support and assistance during my apprenticeship and, not at least, for their patience.

This work was funded by the German Research Foundation (DFG) through the Postgraduate Research Program/ "Graduiertenkolleg – Geowissenschaftliche Gemeinschaftsforschung in Afrika" at the University of Würzburg/ Germany which is gratefully acknowledged.

Table of contents

	page
Abstract	1
Zusammenfassung	2
1 Introduction to the study area	4
2 Geologic setting onshore	7
2. 1 Late Proterozoic Basement.....	10
2. 2 Permo-Carboniferous MS.....	17
2. 3 Triassic-Jurassic MS.....	18
2. 4 Cretaceous MS.....	19
2. 5 Post-breakup magmatism and sedimentation.....	22
2. 6 Geology of the Albin Ridge – the last outpost of South Atlantic rifting.....	24
2. 6. 1 Local stratigraphic framework.....	27
2. 6. 2 Tectonic implications.....	32
3 Geodynamic evolution of the Namibian margin	37
3. 1 The basin forming mechanisms.....	37
3. 2 Rifting and breakup chronology.....	38
3. 3 Deep structure of the margin.....	42
3. 4 Gravity structure of the margin.....	46
3. 5 Offshore basins and their seismic features.....	49
3. 6 Detailed seismic and stratigraphic characterisation of the postrift strata.....	56
3. 6. 1 Q to N/ All (W1 to W4-1).....	58
3. 6. 2 N/ All to K (W4-2 to W5-4).....	58
3. 6. 3 K to LII (W5-5 to W5-6).....	59
3. 6. 4 LII to L/ D (W6-1 to W6-3).....	59
3. 6. 5 L/ D to seafloor (W6-4 to W7).....	61
3. 7 Subsidence history of the central Walvis Basin.....	62
3. 7. 1 Database and basic principles of backstripping.....	62
3. 7. 2 Results of the subsidence analysis.....	69
4 Morphotectonic evolution of the margin – a mass and process balance	73
4. 1 Calculation of the material eroded onshore.....	75
4. 1. 1 Implications from topography and stratigraphic remnants.....	78
4. 1. 2 Quantitative denudation history inferred from AFT analysis.....	81
4. 2 Calculation of the material deposited offshore.....	90
4. 3 Petrography of Maastrichtian deep sea turbidite sands and implications for provenance.....	97
4. 3. 1 Microscopical analysis.....	97
4. 3. 2 SEM analysis.....	102

4. 4 Geochemical signature of the basin fill and representative onshore samples – implications for provenance.....	108
4. 5 Mass balance.....	113
5 Basin modelling.....	117
5. 1 Sequence stratigraphic framework.....	117
5. 1. 1 Geometrical inventory of seismic stratigraphy.....	117
5. 1. 2 Tectonic mechanisms and sea level concepts.....	118
5. 1. 3 Stratigraphic response to sea level changes.....	119
5. 2 Model basics and setup.....	122
5. 2. 1 The diffusion equation.....	122
5. 2. 2 Program modules.....	124
5. 2. 3 Constant model parameters.....	124
5. 2. 4 Variable model parameters.....	126
5. 3 Model results.....	130
5. 3. 1 Parameter study (1): sinusoidal runs.....	130
5. 3. 2 Parameter study (2): AFT shift runs.....	135
5. 3. 3 Parameter study (3): manual runs.....	138
5. 3. 4 The best fit model.....	142
5. 4 Discussion of the model results.....	144
6 Hydrocarbon potential of the central Walvis Basin.....	146
6. 1 Introduction.....	146
6. 2 Potential source rocks.....	147
6. 2. 1 Prerift strata.....	147
6. 2. 2 Synrift strata.....	148
6. 2. 3 Postrift strata.....	148
6. 2. 3. 1 Barremian/ Aptian.....	148
6. 2. 3. 2 Late Cenomanian/ Early Turonian.....	149
6. 3 Migration of hydrocarbons.....	160
6. 4 Potential reservoir rocks.....	163
6. 4. 1 Barremian to mid Albian carbonates.....	163
6. 4. 2 Upper Campanian to Maastrichtian sandstones.....	164
6. 4. 2. 1 Petrographic composition.....	164
6. 4. 2. 2 Characterisation of pore space and reservoir quality.....	164
6. 4. 3 Base Tertiary mounded features.....	165
6. 5 Schematic play concepts.....	166
6. 6 Discussion of the hydrocarbon potential.....	167
7 Conclusions and discussion.....	169
8 References.....	176
9 Appendix	

Abstract

Rifting and breakup of West Gondwana in the Late Jurassic/ Early Cretaceous initiated the formation of the South Atlantic and its conjugated pair of passive continental margins. The Walvis Basin offshore NW-Namibia is an Early Cretaceous to recent depositional centre with a typically wedge-shaped postrift sedimentary succession covering an area of 105000km². A 2D model transect across the central Walvis Basin and adjacent onshore areas is used as a case study to investigate quantitatively the denudational history of the evolving passive margin and the related contemporaneous depositional postrift evolution offshore. The database for both the onshore and offshore part of the model traverse is well constrained by own field work, published data as well as by seismic and well data supported by samples. The ultimate goal of this project is to present an integrated approach towards a quantitative link between surface processes and internal processes in terms of a mass and process balance.

The Namibian passive margin is characterised by long-lived denudational uplift resulting in the development of a gently inclined coastal plain separated from the elevated hinterland by the Great Escarpment. In the onshore part of the study area, the exposed stratigraphic record comprises Late Proterozoic to Cambrian metasedimentary rocks and intrusive complexes of the Damara Group that are unconformably overlain by shallow marine to lacustrine sediments of the Karoo Supergroup. With a significant hiatus, these are overlain by rift-related continental debris flow, fluvial, and aeolian deposits that interfinger with the base of the Early Cretaceous Etendeka Group volcanic sequence. The Albin Ridge is a unique NNW-SSE-striking morphological feature preserved in NW-Namibia with sedimentological and tectonic implications that can be directly related to South Atlantic rifting.

Rifting and oceanic onset in the evolving South Atlantic propagated from S to N, leading to seafloor spreading in the Walvis Basin with the magnetic anomaly M4, at the latest. Margin evolution is influenced by intense magmatism associated with the Tristan da Cunha mantle plume thus forming a textbook example of a volcanic passive margin. Rift-related features as well as mid to lower crustal levels are strongly overprinted by basaltic magmatism. This observation is supported by v_p -modelling at a lithospheric scale, by the recognition of seaward dipping reflector wedges, by subsidence analysis as well as by reduced basal heat flow inferred from maturity modelling of the basin fill. A wide basaltic continent-ocean-transition zone also corresponds to the observed gravity signature of the margin.

Stratigraphic remnants combined with implications from apatite fission track analysis are used to reconstruct the thickness of erosion and the denudational history of the onshore part of the model traverse quantitatively. A maximum thickness of 5km of erosion in the coastal plain can be deduced which is suggested to be the most probable estimation as well. An amount of 44000km³ of clastic detritus has been supplied to the adjacent basin segment during passive margin evolution. The depositional history of the offshore postrift sequence is reconstructed from the depthconverted seismic section ECL 89-41. The interpretation of seismic marker horizons calibrated with high resolution biostratigraphic well data reveals an amount of 58000km³ of sediment deposited in the offshore part of the model transect since breakup. Reconstructing the postrift denudational and depositional history, respectively, depicts a broad qualitative correspondence, yet the mass balance calculations indicate a volumetric misfit of 25%. This observation is supported by petrographic and geochemical provenance studies as well as by stratigraphic basin modelling which reveal a misfit of even 50%. It is suggested that only half of the sediment, at the most, encountered offshore can be attributed to nearby volcanic sources; a substantial proportion of the detritus has been transported into the model traverse by coast-parallel currents that may have already been established during early margin evolution. Provenance considerations indicate that the Etendeka volcanic plateau has already been eroded below its base until the Maastrichtian; this is supported by a major denudation peak in the Late Cretaceous.

Basement subsidence, basal heat flow, global sea level changes, and sediment supply rates inferred from the denudational history are incorporated into a stratigraphic basin model. The final basin model is not only capable of supporting the volumetric misfit in the order of 50% that is already indicated by provenance analysis but also of reproducing the geometry and stratigraphic architecture observed offshore. Stratigraphic modelling therefore provides physical explanations of main sequence

boundaries and the lithological composition of the basin fill. This integrated model approach also implies strong predictive power for undrilled parts or less well documented passive margins.

A thermal maturity model is based on the final stratigraphic model in order to assess the hydrocarbon potential of the central Walvis Basin. TOC and Rock-Eval pyrolysis data indicate good source rock potential for Late Cenomanian to Early Turonian carbonaceous claystones encountered in well 2012/13-1. Maturity modelling suggests marginally mature conditions for this interval at the well site but significantly improved conditions closer to the coast. Possible play concepts assessing a variety of source rock – trap relationships are discussed. The central Walvis Basin reveals all major elements of a valid hydrocarbon system yet they are untested to date.

Zusammenfassung

Die Entstehung des Südatlantiks und seiner konjugierten passiven Kontinentalränder begann im späten Jura und der frühen Kreide mit dem Rifting und Auseinanderbrechen Westgondwanas. Das Walvis Becken vor der Küste NW-Namibias ist seitdem Sedimentationsraum und nimmt eine Fläche von 105000km² ein. Die Sedimente dieses passiven Kontinentalrands weisen den für Postrift Ablagerungen typischen keilförmigen Querschnitt auf. Eine 2D Traverse über das zentrale Walvis Becken und die angrenzenden Küstenbereiche dient als Fallbeispiel, um die Abtragungsgeschichte des sich entwickelnden Kontinentalrands quantitativ mit der zeitgleichen Schelfsedimentation zu verknüpfen. Sowohl für den Schelfbereich als auch für den kontinentalen Bereich der Modelltraverse besteht eine solide Datenbasis, die sich aus Ergebnissen eigener Geländearbeit, publizierten Daten und aus seismischen Schnitten und Bohrungsdaten zusammensetzt, die zudem durch Bohrlochproben ergänzt werden. Ziel vorliegender Arbeit ist es, einen integrativen Ansatz für eine quantitative Verknüpfung von Oberflächenprozessen mit krustalen Prozessen im Sinne einer Massen- und Prozessbilanz zu liefern.

Der passive Kontinentalrand Namibias zeichnet sich durch eine langlebige Hebungsgeschichte aus, die schließlich zur Entwicklung einer flach einfallenden Küstenabdachung führte, welche vom hoch gelegenen kontinentalen Hinterland durch die Grosse Randstufe getrennt wird. Der kontinentale Bereich des Arbeitsgebiets umfasst jungproterozoische bis kambrische metasedimentäre Gesteine und Intrusivkomplexe der Damara Gruppe, die diskordant von flachmarinen und lakustrinen Ablagerungen der Karoo-Supergruppe überlagert werden. Mit einer deutlichen Schichtlücke werden diese wiederum von Schuttstromablagerungen sowie fluvialen und äolischen Sedimenten überlagert, die das jungkretazische Rift-Ereignis dokumentieren. Diese verzahnen sich im Topbereich mit basalen vulkanischen Einheiten der Etendeka Gruppe. Der NNW-SSE streichende Albin Rücken in NW-Namibia stellt das einzig erhaltene Beispiel für Rift-Morphologie dar und lässt sedimentologische wie tektonische Schlussfolgerungen über die Öffnung des Südatlantiks zu.

Die Ozeanisierung des sich entwickelnden Südatlantiks schritt von S nach N fort, um spätestens mit der Ozeanbodenanomalie M4 zur Bildung ozeanischer Kruste im Bereich des Walvis Beckens zu führen. In Zusammenhang mit der Aktivität des Tristan da Cunha Hot Spots entwickelte sich ein stark magmatisch geprägter passiver Kontinentalrand, der als klassisches Beispiel für den vulkanischen Typ gelten kann. Riftstrukturen wie auch mittel- bis unterkrustale Bereiche sind durch basaltischen Magmatismus stark überprägt. Wellenlaufzeiten-Modelle im Lithosphärenmaßstab, ozeanwärts einfallende seismische Reflektoren (SDR), Ergebnisse der Subsidenzanalyse sowie ein reduzierter basaler Wärmefluss, der aus Maturitäts-Modellierungen abgeleitet werden kann, stützen diese Beobachtung. Der breite, basaltisch geprägte Übergangsbereich zwischen kontinentaler und ozeanischer Kruste wird auch durch Schwerefeldmessungen angezeigt.

Mit Hilfe von Erosionsrelikten kann in Kombination mit Apatit-Spaltspur Analysen die Mächtigkeit der Erosion wie auch ihr zeitlicher Verlauf seit der passiven Kontinentalrandentwicklung für den

kontinentalen Bereich des Modellschnitts annähernd quantitativ rekonstruiert werden. Eine maximale Überdeckung von bis zu 5km im Bereich der Küstenabdachung wurde ermittelt. Diese stellt gleichzeitig auch die plausibelste Abschätzung dar. Ein Abtragungsvolumen von 44000km^3 wurde somit als klastischer Detritus für das angrenzende Beckensegment im Verlauf der Postrift Entwicklung bereitgestellt. Die Rekonstruktion der Ablagerungsgeschichte auf Basis der tiefenkonvertierten seismischen Linie ECL 89-41 ergibt jedoch ein Volumen von 58000km^3 für die marine Postrift Sequenz im Modellschnitt; die zeitliche Entwicklung kann dabei mit Hilfe seismischer Leithorizonte, an biostratigraphischen Bohrungsdaten kalibriert, nachvollzogen werden. Der zeitliche Verlauf sowohl von Abtragung als auch Sedimentation weist eine grosse qualitative Übereinstimmung auf, allerdings ergibt die reine Bilanzierung der Massen eine Diskrepanz von 25%. Liefergebietsanalysen auf Basis von petrographischen und geochemischen Daten sowie quantitative Beckenmodellierungen stützen diese Beobachtung und deuten sogar auf eine Volumen-Diskrepanz von 50% hin. Nur etwa die Hälfte der Kontinentalrandsedimente kann vermutlich den vulkanischen Liefergebieten im unmittelbaren Modellschnitt zugeordnet werden; ein beträchtlicher Anteil von nicht-vulkanischem Detritus muss durch küstenparallele Strömungen, die bereits in der Frühphase der Kontinentalrandentwicklung Bestand hatten, in die 2D Modelltraverse transportiert worden sein. Überlegungen zur Liefergebietsentwicklung legen nahe, dass die Vulkanite des Etendeka Plateaus zumindest lokal bereits während des Maastrichts vollständig erodiert wurden. Extrem hohe Denudationsraten in der Oberkreide untermauern diese These.

Beckensubsidenz, basaler Wärmefluss, globale Meeresspiegelschwankungen sowie die aus der Abtragungsgeschichte abgeleiteten Sedimentzufuhrdaten gehen in ein quantitatives stratigraphisches Beckenmodell ein. Ein optimales Beckenmodell kann erstellt werden, welches in der Lage ist, sowohl die bereits aus Liefergebietsanalysen ermittelte Volumendiskrepanz von 50% zu bekräftigen, als auch die Geometrie und Stratigraphie der Beckenfüllung nachzubilden. Somit kann eine prozessorientierte Erklärung für bedeutende Sequenzgrenzen und die lithologische Zusammensetzung der Kontinentalrandsedimente geliefert werden. Dieser integrative Ansatz besitzt zudem ein großes prognostisches Potential, etwa für nicht erbohrte Bereiche der Beckenfüllung oder weniger vollständig dokumentierte Schelfbereiche.

Auf Basis einer stratigraphischen Modellierung wird ein thermisches Modell zur Bewertung des Kohlenwasserstoffpotentials im zentralen Walvis Becken erstellt. Messungen des organischen Kohlenstoffanteils sowie Rock-Eval Pyrolysedaten weisen auf ein gutes Muttergesteinspotential karbonatischer Ton- und Siltsteine des späten Cenoman und frühen Turon im Bereich der Bohrung 2012/13-1 hin. Modellierungen zeigen für dieses Intervall Maturitätsbedingungen an der Untergrenze des Erdölbildungsfensters an, die zur Küste hin zunehmend günstiger für die Generierung von Kohlenwasserstoffen werden. Das zentrale Walvis Becken weist alle wesentlichen Merkmale funktionsfähiger Kohlenwasserstoff-Systeme auf, die bisher jedoch noch nicht eingehend geprüft wurden; eine Reihe möglicher Mutter-/ Speichergesteins-Beziehungen wird diskutiert.

1 Introduction

This study of passive margin evolution focusses on a 2D model transect across the NW-Namibian continental margin at a latitude of 20-21°S (fig. 1-1). The central Walvis Basin and adjacent onshore areas are used as a case study to quantitatively link erosion onshore with contemporaneous sedimentation offshore during passive margin formation (fig. 1-2).

Margin evolution in Namibia is genetically linked with the opening of the South Atlantic that was initiated in the Late Jurassic and Early Cretaceous. Particularly the early evolution of the margin is strongly influenced by rift-related magmatism for which the volcanics of the huge Etendeka flood basalt province as well as prominent intrusive complexes like Brandberg, Messum Crater, and the Erongo Mountains (fig. 1-1) bear impressive witness.

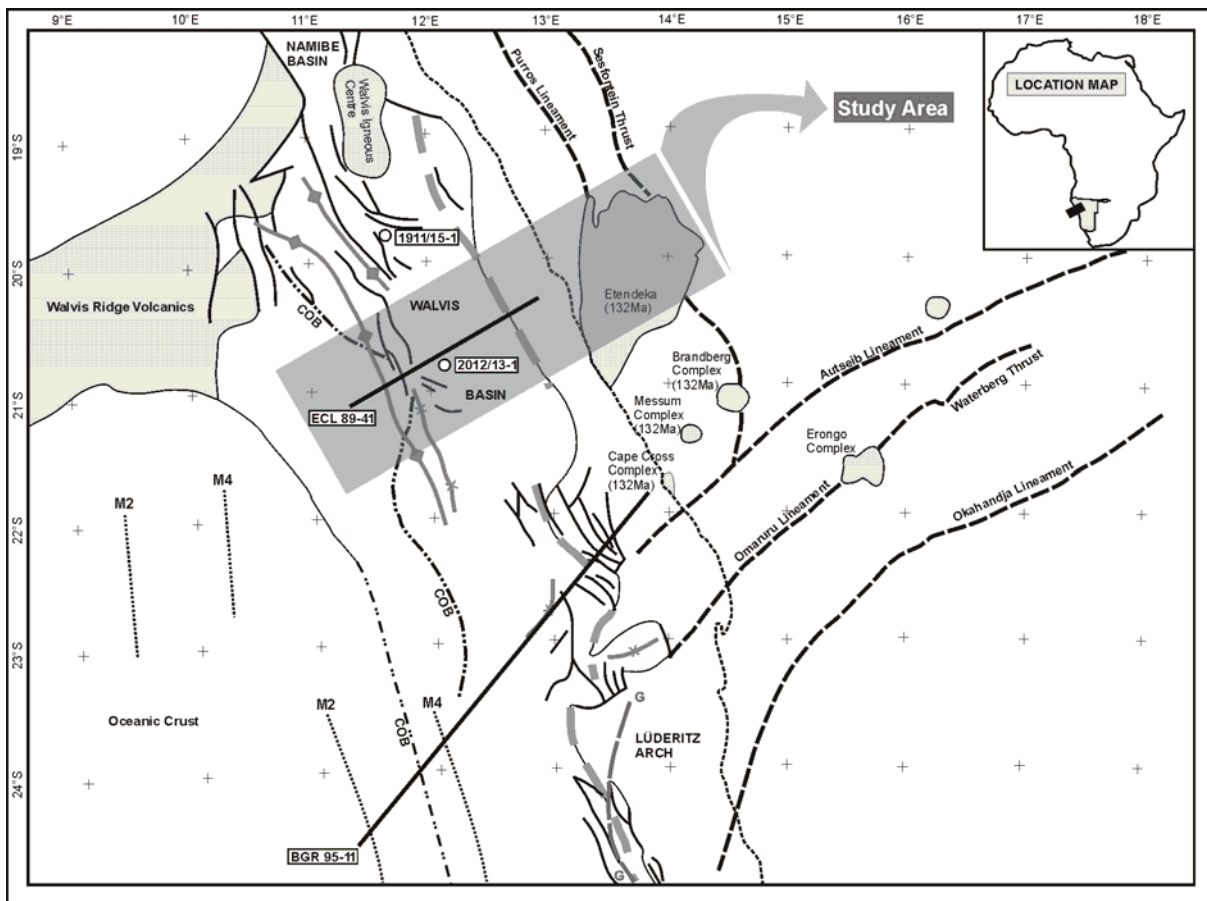


Fig. 1-1. Major structural and geological elements of NW-Namibia relevant for the postrift evolution of the margin. The onshore part of the model traverse covers large areas of the Lower Cretaceous Etendeka volcanic plateau; the offshore part is well documented by the seismic section ECL 89-41 and well 2012/13-1. Major Late Proterozoic basement structures (e.g. Waterberg-Omaruru Lineament) became reactivated as the loci of preferred intrusion of Early Cretaceous igneous complexes as well as of preferred denudation especially during the early passive margin evolution. Map based on <http://www.namcor.com.na/pdfs/GEOMAP.pdf>.

The Namibian margin has undergone long-lived uplift and erosion that resulted in the present day morphology of a deeply eroded coastal plain separated from the elevated hinterland by the Great Escarpment. Exposed geology in the study area (chapter 2) comprises Late Proterozoic to Cambrian metasedimentary rocks and intrusive complexes of the Damara Group that are unconformably overlain by Permian to Triassic deposits of the Karoo Supergroup. Early Cretaceous sedimentation is represented by debris flow and fluvial deposits of the Albin Ridge Member which is a unique example of rift-related clastic deposition (chapter 2.6). Tholeiitic basalts, basaltic andesites, and silica-rich quartz latites extruded within a very short period of time between 133Ma and 131Ma (Renne et al., 1996) to form the huge Etendeka plateau which is the most prominent geological feature in the onshore part of the study area (fig. 1-1).

Based on extensive published data and own field work, implications from stratigraphic remnants combined with the denudation history obtained from published apatite fission track data can be utilised to extract a quantitative history of uplift and erosion for the onshore part of the study area (chapter 4.1). This information can be transferred into sediment supply rates to the adjacent basin segment and thus serve as improved input parameter for stratigraphic basin modelling (chapter 5).

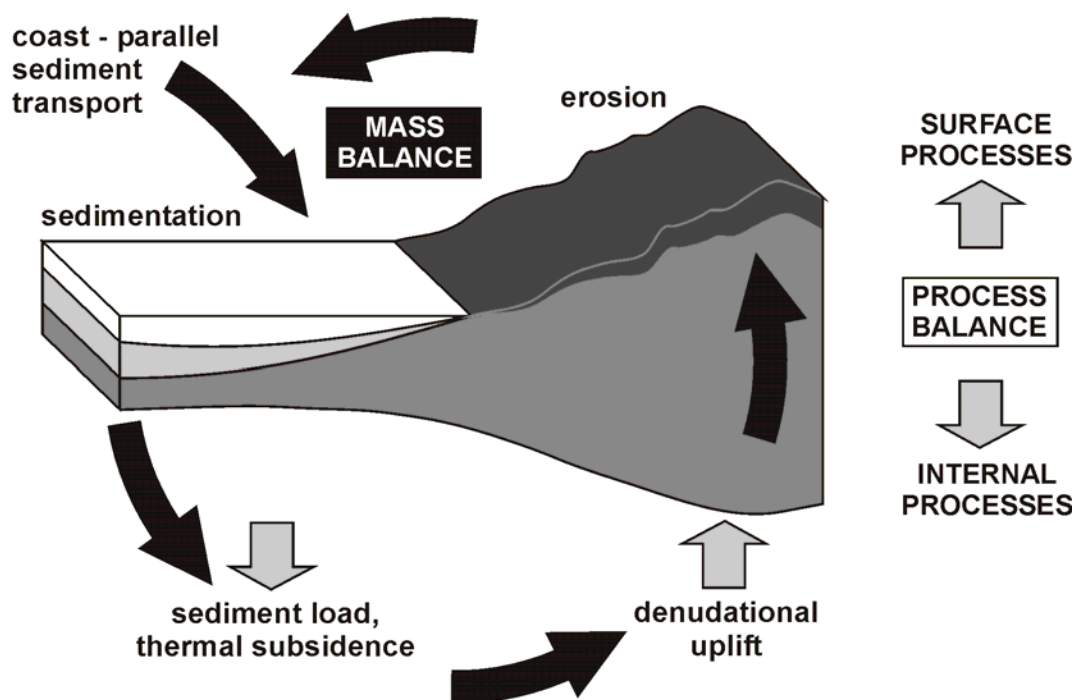


Fig. 1-2. Schematic illustration of the general model concept of a mass and process balance. The main objective of the study is to quantitatively link uplift and erosion onshore with contemporaneous subsidence and sedimentation offshore within a well documented transect across the NW-Namibian passive continental margin. The integrated approach enables quantitative insights into the feedback mechanisms between surface processes and lithospheric processes during passive margin evolution.

The Walvis Basin offshore NW-Namibia is a Cretaceous to recent depositional centre that covers an area of 105000km². It exhibits a wedge-shaped geometry typical of passive margin postrift sediments. The seismic section ECL 89-41 through the central part of the Walvis Basin can be calibrated with data and samples from well 2012/13-1 (fig. 1-1) which provides sufficient information to quantitatively constrain the postrift evolution offshore (chapter 3.6 & 4.2). Additional information can be projected into the model traverse from well 1911/15-1 and the seismic section BGR 95-11 (fig. 1-1) in order to more fully assess the geodynamic evolution of the NW-Namibian margin (chapter 3).

Mass balance calculations (chapter 4.5) are refined by provenance studies based on microscopical, SEM, and geochemical analysis (chapter 4.3 & 4.4). Modelling deposition and stratigraphic architecture in the central Walvis Basin (chapter 5) utilises subsidence rates derived from backstripped well data (chapter 3.7), estimations of global sea level changes, and sediment supply rates inferred from calculations of volumes eroded onshore (chapter 4.1). Basin modelling provides not only additional independent control for the mass balance calculations, but also gives insight into the complex feedback mechanisms between surface processes and lithospheric processes during passive margin evolution (fig. 1-2).

This integrated and multidisciplinary approach to passive margin evolution within a well defined 2D model transect implies a strong predictive potential and proves to allow even quantitative conclusions on differential transport in the third dimension. Furthermore, the stratigraphic basin model can be used as improved input for a thermal maturity model assessing the hydrocarbon potential of the central Walvis Basin (chapter 6) which is currently of heavy economic interest for Namibia.

2 Geologic setting onshore

Rifting and breakup of Westgondwana in the Late Jurassic and Early Cretaceous resulted in the formation of the South Atlantic Ocean. The present Namibian passive continental margin has undergone long-lived uplift and erosion and is characterised by the development of a major escarpment that generates two distinct drainage regimes.

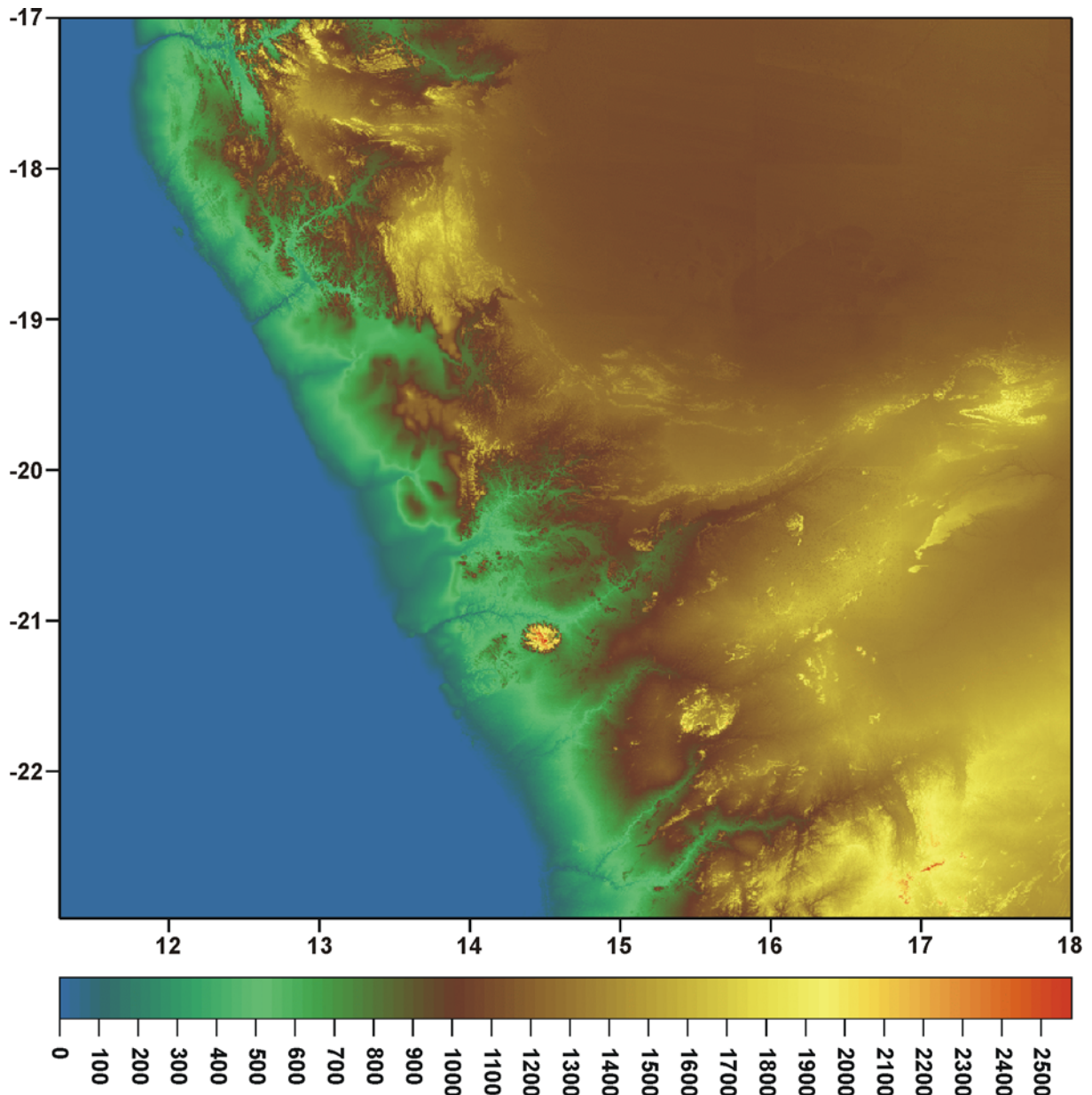
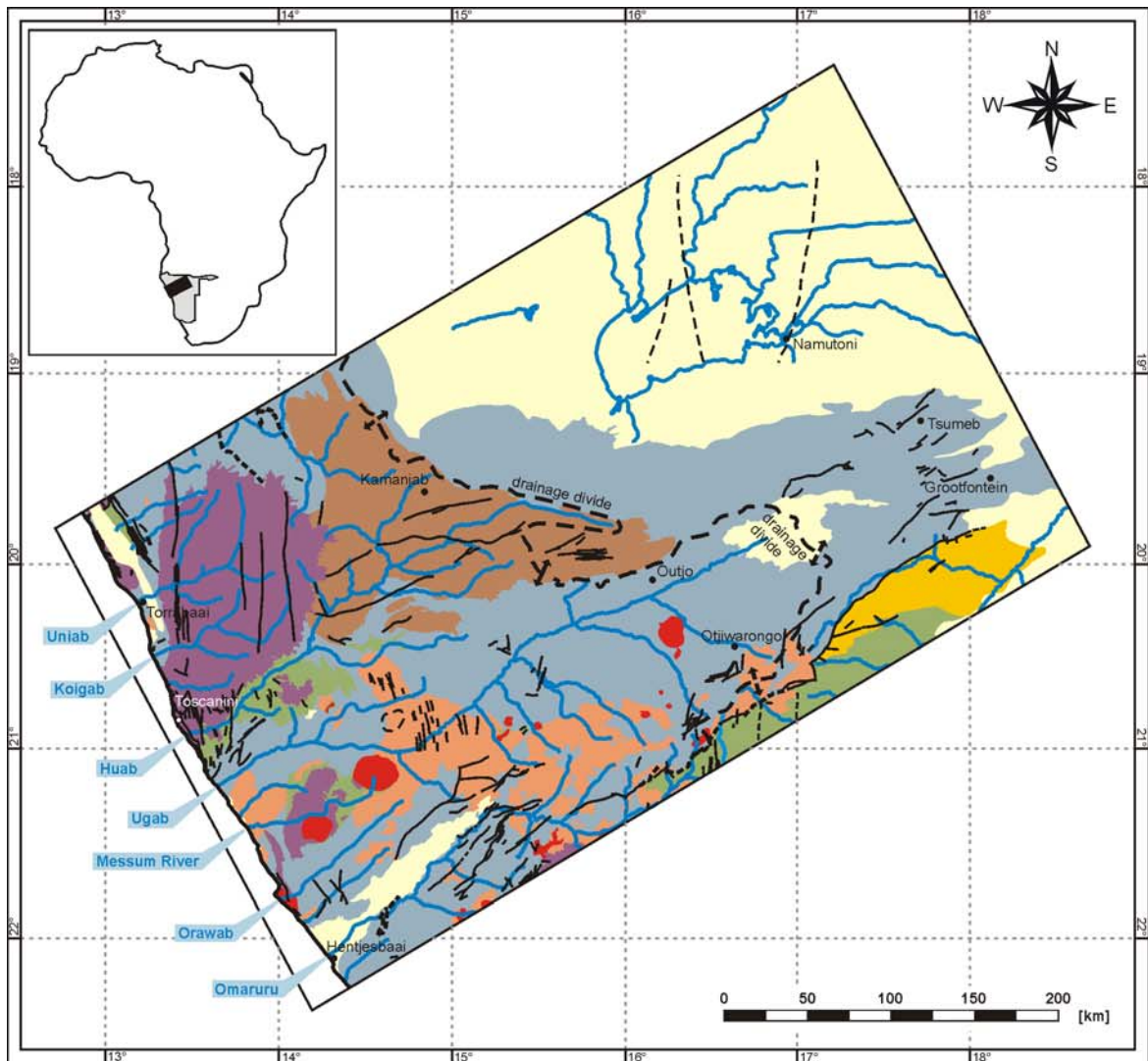


Fig. 2-1. Digital elevation model of NW-Namibia generated with *SURFER*. A gently inclined coastal plain (green colours) is separated from the continental interior (brown to yellow colours) by a distinct morphological feature, the Great Escarpment. Data obtained from the USGS global digital elevation model GTOPO30 with a horizontal grid spacing of 30 arc seconds (<http://edcdaac.usgs.gov/gtopo30/gtopo30.html>).

Significant denudation in the order of kilometres occurred in the exterior catchment whereas the Namibian continental interior is denuded to a much lower degree (see chapter 4.1). Isostatic response to contrasting rates of denudation and, additionally, the effects of climate and lithology contributed to the Mesozoic and Cenozoic landscape evolution of Namibia (Gallagher & Brown, 1997; Gilchrist & Summerfield, 1990): a narrow, gently inclined coastal plain is separated from an interior plateau by the Great Escarpment. The current drainage divide of NW-Namibia is closely related to the geomorphologic feature of the Great Escarpment which is best illustrated by a digital elevation image of the area (fig. 2-1).

In contrast to the offshore sediments that provide continuous information on the continental margin evolution (chapter 3.6) only a very incomplete record of the extensional history is preserved onshore. However, the extensional history of the Namibian passive continental margin started as early as 160Ma prior to the final breakup in the Permo-Carboniferous. Stollhofen (1999) differentiates the Namibian onshore geology into three major sedimentary megasequences (MS): (a) a Permo-Carboniferous megasequence, (b) a Triassic-Jurassic megasequence and (c) a Cretaceous megasequence by means of major erosional unconformities; each is related to a basin-forming extensional period. Wanke (2000) examined the tectonic implications of the Karoo-Etendeka unconformities of NW-Namibia in great detail.

The depositional environments record a progressive climatic change from Permo-Carboniferous glacial to Lower Cretaceous semi-arid conditions. Extreme aridification dates from the Late Miocene due to nearshore upwelling and the establishment of the Benguela system (Siesser, 1980).



KEY TO OUTCROP GEOLOGY

PRE-DAMARA BASEMENT TERRANE
(Congo Craton)

Kamanjab Inlier: Granite, Granodiorite, Paragneiss, Metasedimentary Rock, Various Formations

DAMARA SEQUENCE - Vendian to Cambrian
(Kaoko & Damara orogenic belt)

Mokolian & Namibian: Granite, Granodiorite, Gneiss, Metasediments, Metavolcanics, Conglomerate, Arkose, Shale, Tuff

Cambrian: Granite, Granodiorite, Monzonite, Syenite, Gneiss, Serpentinite, Alaskite, Gabbro, Norite

KAROO-SEQUENCE

Carboniferous to Jurassic: Tillite, Boulder Shale, Limestone, Mudstone, Shale, Siltstone, Sandstone, Conglomerate

Jurassic: Etjo Aeolian Sandstone (Waterberg)

ETENDEKA/ EARLY CRETACEOUS

Etendeka: High-Silica-Basalt, Latite, Quartz-Latite, Minor Aeolian Sandstone

Post-Karoo Igneous Complexes: Granite, Syenite, Diorite, Gabbro, Rhyolite, Carbonatite, plugs of various ages

CRETACEOUS TO RECENT

Kalahari Beds and Recent Cover: Alluvium, Sand, Gravel, Calcrete, Namib Desert Sand Sea, Coastal Salt-Pan

- Fault
- Fault concealed or not accurately located
- Thrust
- Ephemeral River

Fig. 2-2. Geological map of a segment of northern Namibia. Modified from the “South West Africa/ Namibia geological map 1:1000000” of Miller & Schalk (1980).

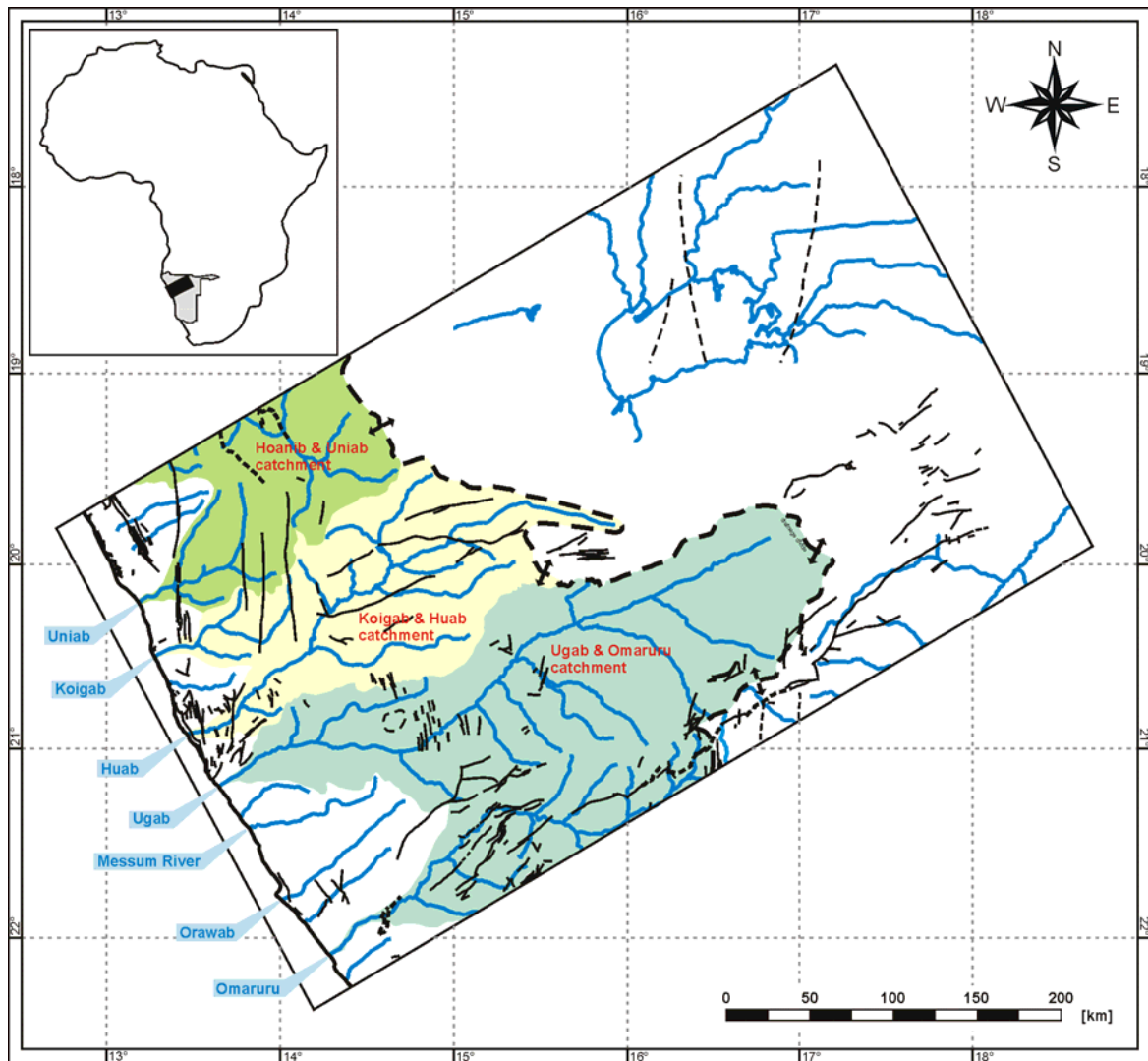


Fig. 2-3. Catchment areas of the Hoanib, Uniab, Koigab, Huab, Ugab, and Omaruru ephemeral rivers, respectively. Map based on the “Atlas of Namibia” database provided by the Ministry of Environment and Tourism/ Namibia (<http://www.dea.met.gov.na/data/data.htm>).

2. 1 Late Proterozoic Basement

Large areas of the Namibian geology exposed onshore are associated with the Late Proterozoic Pan-African orogenic cycle (Geological map of Namibia 1:1000000; Miller & Schalk, 1989; Porada, 1989). The SW-NE-striking continental branch of the Damara Orogen resulted from the collision of the Kongo-craton with the Kalahari-craton between 600Ma and 535Ma (Lawrence, 1989). Low-grade metamorphic siltstones and sandstones of the Damara Group represent the flysch-sediments of this orogeny.

Southern America collided with the newly formed African continent around 500Ma to form the coastal branch of the Damara Orogen with a NNW-SSE-trend (Stanistreet et al. 1991). The latter is preserved in the form of the Kaoko Belt and Gariiep Belt in the coastal areas of northern and southern Namibia, respectively (fig. 2-4).

These Proterozoic zones of crustal weakness and heterogeneity exerted a fundamental control on the Paleozoic to Mesozoic extensional history and final breakup of the Gondwana super-continent. Figure 2-4 illustrates Proterozoic cratonic and orogenic areas closely associated with Phanerozoic rift basins. Proterozoic faults and thrusts became the loci of major and multi-phased reactivation (e.g. Waterberg-Omaruru Lineament; see fig. 1-1).

Moreover, modelling with apatite fission-track data suggests that both branches of the Damara Orogen have been preferentially and deeply eroded during the Mesozoic and Cenozoic (Raab, 2001); their outcrop areas coincide roughly with the coastal plain and major SW-NE-striking lineaments in central Namibia (fig. 1-1 & 2-4). Plate I gives an overview of the outcrop geology of deeply eroded basement areas as well as of the morphology of the Great Escarpment.

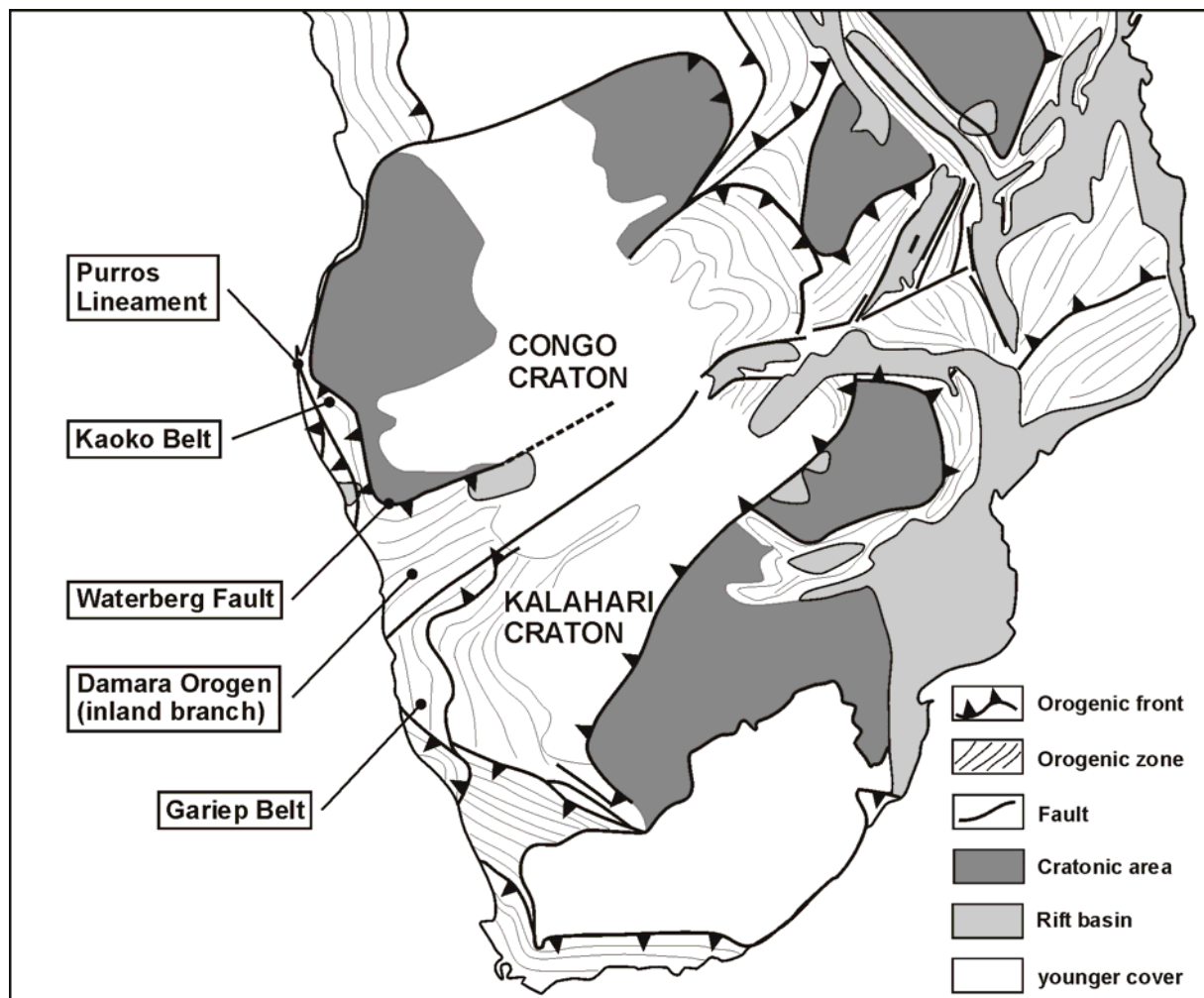


Fig. 2-4. Proterozoic cratonic and orogenic zones of southern Africa. Distribution of Phanerozoic rift basins is closely associated with the orogenic belts. Proterozoic zones of crustal weakness exerted fundamental control on the Paleozoic and Mesozoic extensional history of Gondwana. Modified from Daly et al. (1989).

Legend Plates I – IV

Plate I

I-1. Damara metasedimentary rocks of the “Zerrissene Group” west of the Brandberg; car for scale; location: c. 21°04` S, 14°16` E.

I-2. Folded, coarse-grained, low-grade metamorphic sandstone of the Damara Sequence west of the Goboboseb Mountains; Ralf (185cm) for scale; location: 21°17,151` S, 14°02,446` E.

I-3. Spitzkoppe Early Cretaceous igneous complex NW of Usakos, emplaced in deeply eroded Damara basement; boulders in the foreground are c. 2m high; location: 21°49,979` S, 15°09,779` E.

I-4. The Great Escarpment at Spreetshoogte Pass north of Solitaire; view to the NW over the coastal plain; location: c. 23,8°S, 16,1°E.

Plate II

II-1. Dark-grey to black silty shales of the Verbrandeberg Formation at the type-locality “Verbrandeberg” WSW of Khorixas; hammer (30cm) for scale; location: 20°37,368` S, 14°25,137` E.

II-2. Coarse-grained trough-crossbedded fluvial sandstone of the Tsarabis Formation; hammer (30cm) for scale; location: 20°37,368` S, 14°25,137` E.

II-3. Channel-shaped, crossbedded carbonaceous siltstone within grey shales of the Huab Formation in the Goboboseb Mountains NW of Messum Crater; scale = 10cm; location: 21°14,559` S, 14°04,149` E.

II-4. Stromatolithic bioherm of the shallow marine Huab Formation in the Goboboseb Mountains NW of Messum Crater; hammer (30cm) for scale; location: 21°14,906` S, 14°03,836` E.

Plate III

III-1. Medium-grained, low-angle hummocky-crossbedded sandstone of the Huab Formation in the Goboboseb Mountains NW of Messum Crater; hammer (30cm) for scale; location: 21°14,906` S, 14°03,836` E.

III-2. Diagenetic “cone-in-cone” structures in carbonates of the Huab Formation in the Goboboseb Mountains NW of Messum Crater; coin (2cm) for scale; location: 21°16,070` S, 14°04,492` E.

III-3. Horizontally bedded red to grey siltstones of the lacustrine Gai As Formation; interbedded fine-grained sandstones (hammer) show low-angle crossbedding; hammer (30cm) for scale; location: isolated “inselberg” SW of Messum Crater, 21°34,133` S, 14°07,702` E.

III-4. Red siliceous concretion within purple shales at the top of the Gai As Formation; hammer (30cm) for scale; location: Albin Ridge, east of Mile 108/ Skeleton Coast, 21°25,844` S, 13°53,839` E.

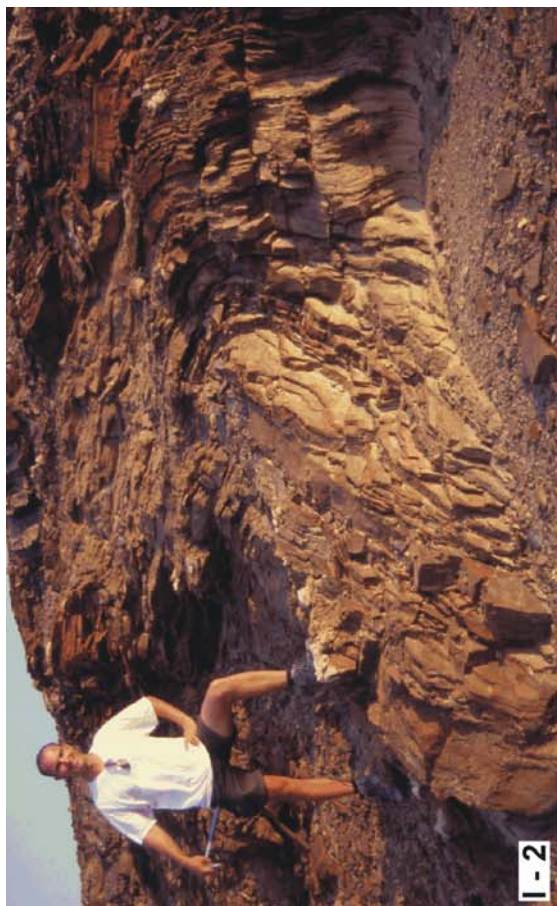
Plate IV

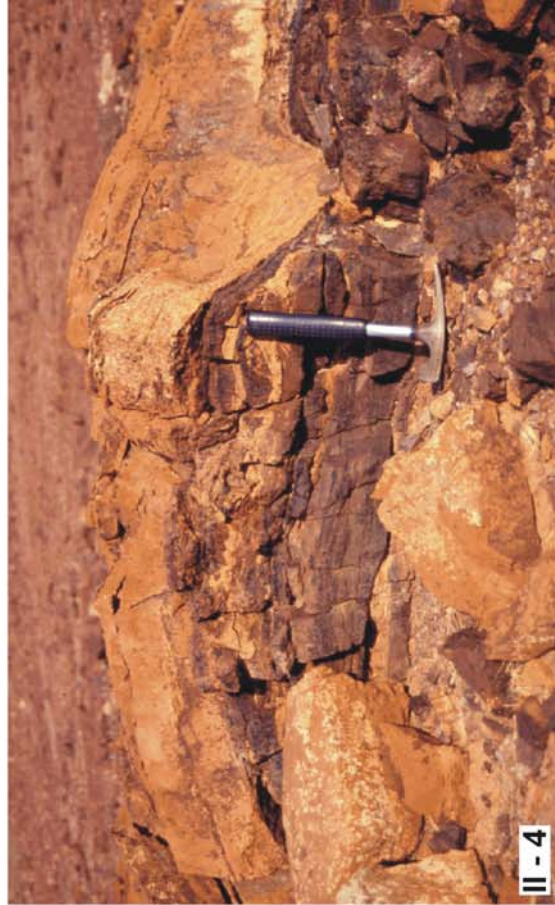
IV-1. Grain-supported conglomerate of the fluvial to alluvial Albin Ridge Member; clasts are predominantly Damara metasedimentary rocks and subordinate weathered, amygdoidal basaltic rocks; imbrication (165/ 35) indicates northnortheasterly oriented transport; scale = 10cm; location: Albin Ridge, east of Mile 108/ Skeleton Coast, 21°25,844` S, 13°53,839` E.

IV-2. Alluvial to fluvial conglomerates and coarse-grained sandstones of the Krone Member; Ralf (185cm) for scale; location: type-locality “Farm Krone”/ Huab valley, 20°29,128` S, 14°01,607` E.

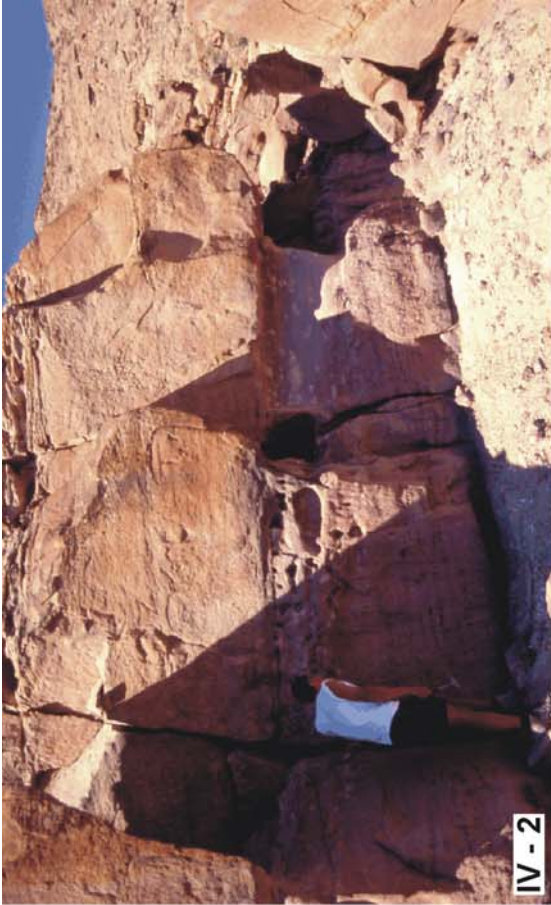
IV-3. Large-dimensional tabular crossbedding of aeolian sandstones of the Twyfelfontein Formation; hammer (30cm) for scale; location: type locality “Twyfelfontein” WSW of Khorixas, 20°37,368` S, 14°25,137` E.

IV-4. “Tafelkop” mountain west of the Brandberg; type locality of the “Tafelop Basalts” that constitute the base of the Awahab Formation within the Etendeka Group in the Huab area; hardly weathering Quartz-Latites tend to build plateaus and the top of the mountain; more easily weathering basalts build the low-angle flanks; car for scale; location: 21°04,297` S, 14°15,883` E.







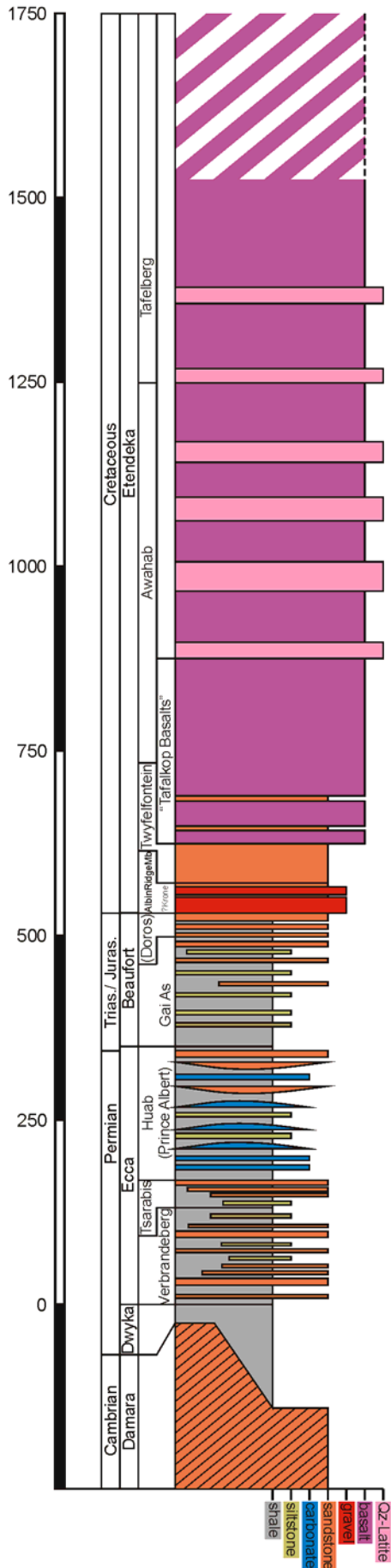


2. 2 Permo-Carboniferous MS

The pre-breakup evolution of southern Gondwana was dominated by the development of the Paleozoic-Mesozoic Karoo and Paraná Basins, respectively. They formed as extensive foreland basins in front of the northward advancing Cape Fold Belt which is associated with the southern Gondwana active margin (Samfrau subduction zone) during the Early Permian (Tankard et al., 1982). Thick sedimentary sequences of the Karoo Supergroup accumulated in the southern part of the foreland basin and thin rapidly northward. The occurrence of Karoo basins in Namibia is restricted to smaller basins preferentially in the SE and NW of the country. In NW-Namibia the spatial pattern of deposition was strongly controlled by synsedimentary fault activity. Maximum thicknesses vary between 250m and 700m (Horsthemke et al., 1990).

According to Stollhofen (1999), the foreland evolution was overprinted by first contemporaneous extensional events that are interpreted as intracontinental rift systems. A NW-SE to NNW-SSE oriented rift shoulder has already been established and canalised the southward directed ice transport to the west of an early rift shoulder during the deposition of the glacial Dwyka Formation. In northern Namibia U-shaped valleys containing remnants of glacial deposits are exhumed indicating that the present land surface locally represents the Permo-Carboniferous landscape (Martin, 1953; Visser, 1995). Their orientation orthogonal to the rift suggests that glaciers transported debris westward into the rift basin depression. Succeeding delta complexes of the Permian Ecca Group advanced in a SSE-direction whereas marine transgressions prograded to the NNW; the latter comprises the Mesosaurus-bearing Whitehill Formation in southern Namibia. Plate II and plate III (1, 2) give an impression of the outcrop geology of the Ecca Group which comprises the Verbrandeberg Formation, the Tsarabis Formation, and the Huab (Prince Albert) Formation in the study area.

Fine-grained peaty overbank deposits of a meandering river system are typical of the Verbrandeberg Formation. The fluvio-deltaic Tsarabis Formation represents a general coarsening upward cycle and characteristically shows trough-crossbedding; wood remnants are common. Grey carbonaceous claystones of the Huab (Prince Albert) Formation are widespread in the study area. They are typically interbedded with stromatolitic bioherm-structures and hummocky-crossbedded sandstones. Cone-in-cone structures are a characteristic feature of the Huab (Prince Albert) Formation (plate III-2). Their formation is due to fibrous calcite crystals growing under stress in the sediment. The growth of the cones, which are circular on the top side of a layer, takes place while the sediment is still in a plastic state (Boggs, 2001) and is therefore a diagenetic feature.



Apart from minor marine transgressions during the Late Cretaceous and Cenozoic, which affected only the shelf and a narrow coastal strip, Namibia has remained a terrestrial environment since the Triassic (Dingle et al., 1983).

In figure 2-5 a simplified standard-section of the lithology and stratigraphy in the NW-Namibian study area with maximum preserved thicknesses is presented; it is compiled from own fieldwork and from a synthesis of the reviews given by Stollhofen (1999), Horsthemke et al. (1990), and Milner et al. (1994).

2. 3 Triassic-Jurassic MS

Continental environments with fluvio-lacustrine and aeolian sediments prevailed throughout this sequence including the Beaufort Group and the Stromberg Group. In Namibia this succession is very condensed and locally reduced to fault-bounded traps due to pronounced thermal uplift of the early rift shoulder.

The Waterberg area in central Namibia is bounded to the north by the Waterberg-Omaruru-Lineament (fig. 1-1 & 2-4) which represents a reactivated Late Proterozoic suture parallel to the continental branch of the Damara Orogen. It provides excellent examples of the fluvio-lacustrine Omingonde Formation and the aeolian Etjo Formation. Aeolianites of the Etjo Formation are absent in NW-Namibia (Stollhofen, 1999).

Fig. 2-5. Simplified standard-section of the lithology and stratigraphy in the study area with maximum preserved thicknesses. Compiled from own fieldwork and from Stollhofen (1999), Horsthemke et al. (1990), and Milner et al. (1994).

Lower Jurassic predominantly tholeiitic flood basalts of the Kalkrand Formation are restricted to southern Namibia; they terminate the Triassic-Jurassic megasequence. With Toarcian ages around 186-183Ma (Duncan et al., 1997), they correlate with the southeastern South African basalts of the Drakensberg Group.

Aeolian sediments intercalating with the base of Mesozoic flood basalts have generally been assigned to the Etjo Formation, even though far from the type locality "Mount Etjo" in the central Namibian Waterberg area (fig. 2-2; Miller & Schalk, 1980). Since there are two flood basalt provinces established in Namibia (Lower Jurassic Kalkrand lavas in southern Namibia; Lower Cretaceous Etendeka lavas in NW-Namibia; chapter 2.4) Stollhofen (1999) proposes a more differentiated stratigraphic classification of Mesozoic aeolian sediments. On the basis of detailed facies interpretation and correlation with the South African Clarens Formation as well as vertebrate biostratigraphy, a Lower Jurassic age can be attributed to the Etjo Formation. Besides the Waterberg area (fig. 2-2), the top of the Gamsberg, which marks the northern termination of the well established Great Escarpment of southern Namibia (plate I-4), represents a prominent equivalent to this stratigraphic level.

In the Huab and Albin Ridge areas of NW-Namibia, aeolian sediments of varying thickness show a complex intercalation with the base of the Etendeka Group lavas (Jerram et al. 1999) that extruded within a short period (133-131Ma) in the Lower Cretaceous (Renne et al., 1996; chapter 2.4). Horsthemke et al. (1990) and Swart (1992/93) stated a minimum age for these deposits of Early Cretaceous (c. 135Ma) and associated them with the Etjo Formation. Stanistreet & Stollhofen (1999), however, recommended to classify these Lower Cretaceous aeolian sediments after the type locality in the Huab area as "Twyfelfontein Formation" (fig. 2-5). This discrimination becomes important with regard to the interpretation of the Kudu gas-reservoirs offshore southern Namibia.

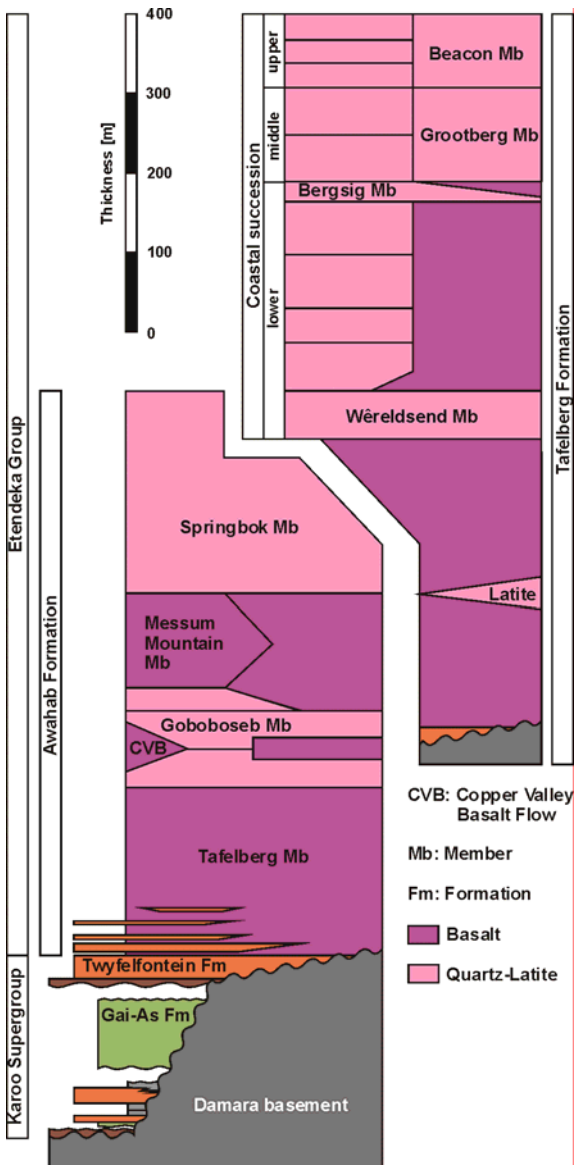
In the study area, the Triassic-Jurassic MS is restricted to the Gai As Formation. However, this classification is based on lithostratigraphy; U/ Pb-dating with zircons revealed a Permian age of $265 \pm 2,5$ Ma for the uppermost Gai As Formation in the Huab area (Stollhofen, 1999). It comprises red lacustrine siltstones and shales including increasingly more turbidite deposits towards the top; pedogenic features and concretions are common (plate III-3,4).

2. 4 Cretaceous MS

Early Cretaceous Paraná-Etendeka volcanics in Brazil and NW-Namibia represent one of the world's largest flood basalt provinces. The Etendeka Group comprises the vast majority of the Cretaceous MS in the study area. The extruded volume for the Etendeka and Paraná flood basalts has been estimated to be $0,07 \times 10^6 \text{km}^3$ and

$1,2 \times 10^6 \text{ km}^3$, respectively (Milner et al., 1992). In Brazil, the Paraná volcanics cover an area of about $1,2 \times 10^6 \text{ km}^2$, with a maximum preserved thickness of 1700m; Etendeka remnants in Namibia cover about $8 \times 10^4 \text{ km}^2$, with a maximum preserved thickness of about 900m (Erlank et al., 1984).

More than 90% of the Paraná province consist of tholeiites. More silica-rich rhyolites/quartz latites tend to occur only in the SE of the region, and occur as the uppermost components of the sequence (Hawkesworth et al., 1992). Etendeka volcanics reveal a more pronounced bimodal geochemical signature. Tholeiitic basalts and basaltic andesites constitute c. 50% of the exposed volcanic sequence; the remainder are silica-rich quartz latites that are interpreted as rheoignimbrites (Milner et al. 1992; Hawkesworth et al., 1992). Figure 2-6 provides an overview of the lithostratigraphic subdivision of the Etendeka Group. Age determination ($^{40}\text{Ar}/^{39}\text{Ar}$) on Etendeka volcanic rocks (Renne et al., 1996) indicates a very restricted phase of extrusive magmatism of only about 1Ma duration between $131,7 \pm 0,7 \text{ Ma}$ and $132,3 \pm 0,7 \text{ Ma}$;



intrusive activity is suggested to have lasted at least 2-3Ma longer than recorded by volcanics.

High asthenospheric melt potential during the late rift stages and breakup which is documented in intense flood basalt volcanism is ascribed to the Tristan da Cunha mantle plume impinging on already thinned lithosphere or lithosphere under extension. The bathymetric features of the Rio Grande Rise and Walvis Ridge, respectively, result from the passage of spreading oceanic lithosphere over the plume (see fig. 3-3). There is considerable debate on the relative role of the mantle plume and the overlying lithosphere as magmatic source regions. (e.g. Hawkesworth et al., 1992). Gladchenko et al. (1997) suggest that the Tristan da Cunha plume may not be responsible for the entire "South Atlantic Igneous Province".

Fig. 2-6. Lithostratigraphic subdivision and nomenclature of the Etendeka Group in the southern Etendeka province. Modified from Milner et al. (1994).

Rifting and breakup in the south started earlier (c. 150Ma; Nürnberg & Müller, 1991) than in the north and may be due to locally increased lithospheric melt potential not related to the Tristan plume. Additionally, the plume location at the time of breakup is unclear. O'Connor & Duncan (1990) and Turner et al. (1994) suggested an eastward migration of the plume from the NW-Paraná Basin. Figure 3-3 represents a compilation of South Atlantic spreading stages and the spatial relationship to the Tristan da Cunha hot spot (see chapter 3.2).

Location and relative timing of volcanism may have been controlled by the mode of rifting and pre-existing zones of lithospheric weakness (Harry & Sawyer, 1992). Generally, in an active mode of rifting, doming and volcanism is followed by rifting, whereas in a passive mode of rifting, volcanism follows rifting. The discrimination between active and passive is not always clear as weak or already thinned lithosphere may "attract" a plume. Huisman et al. (2001) proposed a twostage extension model, where a change from plate-mode passive extension to diapiric-mode active extension might provide an alternative to the classical end-member models of rifting.

Spatially related to the SW-NE-trending Damara inland branch indicated by the Autseib lineament and the Waterberg-Omaruru lineament, respectively (fig. 1-1 & 2-4), is a group of some 20 Early Cretaceous granitic intrusions and subvolcanic ring complexes named "Damaraland Igneous Complexes" (fig. 2-2; Trumbull et al., in press); ages range from 135Ma to 124Ma (Milner et al., 1995) and are related to breakup and oceanic onset. A great variety of rock types can be distinguished: granitic associations, differentiated basic complexes, carbonatitic centres, and composite complexes reflecting the interaction between mantle-derived magmas of plume or lithospheric origin and the Damara basement rocks. Most basalts of the Etendeka province show isotopic and trace element ratios different from ocean island basalts related to the Tristan da Cunha hot spot which is a matter of current debate. Tristan plume signature, however, appears to be typical for the Damaraland Igneous Complexes. Milner et al. (1995) identified plume signature in gabbros of the Okenyenya; Trumbull et al. (in press) did so in gabbros and syenites from the Messum Complex. Nd-isotopic ratios from the Brandberg anorogenic granite intrusion indicate a mantle source magma with up to 20% contamination by Damara crust (Schmitt et al., 2000).

Following breakup, long-lived uplift of the former rift flanks created pronounced relief and base level change resulted in significant denudation of the newly formed continental margin. Cox (1989) suggested that this uplift is associated with plume-related magmatic underplating in the Late Jurassic and Early Cretaceous. Flexure and isostatic rebound as a consequence of denudational unloading (Gilchrist &

Summerfield, 1990; fig. 4-1) may be an additional effect that contributed to the morphology of the present Namibian passive continental margin. The Brandberg intrusion in NW-Namibia provides indirect constraints on post-intrusive denudation. With a peak elevation of c. 2600m and the surrounding landsurface being at an elevation of 600m, on average, at least 2000m of regional post-magmatic denudation can be suggested (Brown et al., 2000; chapter 4.1).

Immediately prior to the deposition of the Etendeka Group volcanics, continental aeolian deposits of the Twyfelfontein Formation have covered huge areas of NW-Namibia. They are characterised by well-sorted dune sands and large-dimensional planar crossbedding (plate IV-3). The dunes are complexly interfingering with the basal units of the Etendeka volcanics as examined by Jerram et al. (1999).

Prior to the Twyfelfontein aeolianites, in turn, coarse-grained conglomerates and debris-flow deposits have been accumulated; an isolated, up to 40m thick occurrence is preserved in the Albin Ridge area on the coastal plain (plate IV-1) which therefore might resemble a unique example of synrift-sedimentation onshore (chapter 2.6). Locally, traces of resedimented aeolian deposits appear to be preserved towards the top of the Albin Ridge Member; the unit shows a conformable, thermally altered contact with the basal volcanics of the Etendeka Group which is in close correspondence with the Twyfelfontein-Etendeka contact in the Huab area.

Farther inland, in the Huab area, fluvial sandstones and conglomerates of the up to 8m thick Krone Member directly underly the dune sands of the Twyfelfontein Formation. By analogy, they are suggested to represent a correlative of the Albin Ridge Member (plate IV-2; fig. 2-5; e.g. Wanke, 2000).

2. 5 Post-breakup magmatism and sedimentation

Slightly after breakup (125Ma; Erlank et al., 1984; Renne et al., 1996) mafic dykes intruded in the Horingbaai area in NW-Namibia. Although they are locally associated with the Etendeka plateau, they often show intrusive contacts with the base of the Etendeka flood basalts and differ in their geochemical composition (Duncan & Armstrong, 1990). The Horingbaai dolerites have often been interpreted as feeder dykes for the Etendeka basalts but according to Stollhofen (1999) they more likely appear to be associated with the oceanic onset of the adjacent rift segment.

Numerous carbonatite dykes and kimberlite pipes have been emplaced in the Gibeon area of southern Namibia around 67Ma (pers. comm. V. Lorenz; Smith, 1986; Gilchrist et al., 1994); very few dykes also intruded in NW-Namibia (see Geological map of Namibia 1:1000000, Miller & Schalk, 1980). This Late Cretaceous phase of magmatism is not only in close temporal relationship with a denudation peak that can be observed all along the Namibian passive continental margin (Gallagher & Brown,

1999; Raab, 2001); there is also evidence for major plate tectonic reorientation and increased number of fracture zones within the South Atlantic and the western Indian Ocean basins. This change occurred in the Late Cretaceous between magnetic anomalies C34 (83Ma) and C31 (67Ma) and was associated with a significant decrease and the onset of asymmetry of spreading rates in the South Atlantic (Cande et al., 1988; Nürnberg & Müller, 1991; Brown et al., 2000).

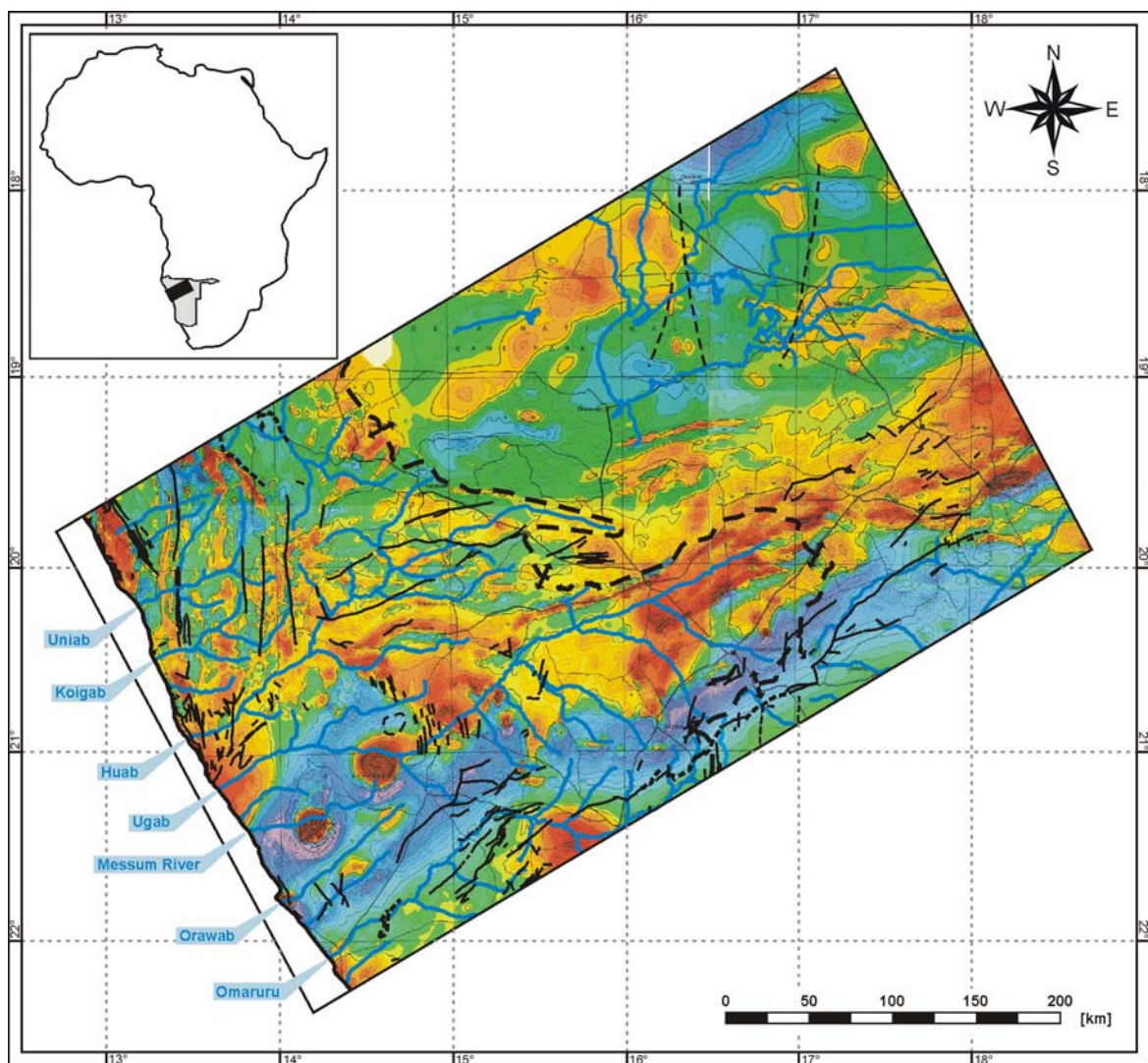


Fig. 2-7. Airborne magnetic anomaly map of a segment of northern Namibia. Derived from the "Airborne Magnetic Anomaly Map of Namibia 1:1000000" published by the Geological Survey of Namibia; documentation by Eberle et al. (1995, 2002).

Post-Etendeka stratigraphic evolution in Namibia is dominated by the deposition of the intra-cratonic Kalahari Basin sediments. The base of the generally less than 200m thick sediments that cover huge areas in central southern Africa is thought to be Late Cretaceous/ Early Tertiary in age (Thomas & Shaw, 1990). The elastic plate model of the SW-African margin presented in figure 4-1 predicts an intra-cratonic

flexural basin which is in good agreement with the southern African Kalahari Basin in terms of wavelength and amplitude (i.e. sediment thickness).

Cenozoic sedimentation in Namibia is largely confined to the Namib Sand Sea in a c. 150km wide zone covering the coastal plain between the coastline and the Great Escarpment in southern Namibia. The oldest unit (Tsondab Sandstone Formation) unconformably overlies deeply eroded basement and has a probable maximum age of Early Paleocene (Ward, 1988). Extremely arid climatic conditions that led to the formation of the Namib Sand Sea probably have prevailed since the Miocene, when the Benguela Current offshore Namibia has been established (Siesser, 1980).

The airborne magnetic dataset of Namibia reflects in great detail the geological features outlined above, especially those associated with the Proterozoic mobile belts. Several airborne magnetic surveys that were conducted over the last decades have been compiled by Eberle et al. (1995, 2002) in order to illuminate crustal evolution and regional distribution of mineralisation. Extended moderate amplitude anomalies resulting from deep-seated sources are associated with the peripheral areas of the Proterozoic Kalahari- and Kongo-cratons, respectively. A striking subcontinental magnetic low runs parallel to the northern termination of the Damara mobile belt (blue in fig. 2-7). The Etendeka plateau basalts and the anorogenic intrusive complexes of Brandberg and Messum are, in turn, related to distinct magnetic highs (yellow and brown colours). The section presented in figure 2-7 is derived from the "Airborne Magnetic Anomaly Map of Namibia 1:1000000" published by the Geological Survey of Namibia.

2. 6 Geology of the Albin Ridge – the last outpost of South Atlantic rifting

The Albin Ridge is a unique coast-parallel morphological feature related to South Atlantic rifting preserved onshore NW-Namibia (plate V-4). The NNW-SSE striking mountain ridge has a length of about 30km, a width of circa 5km and is located about 150km north of Swakopmund; it reaches an elevation of up to 270m above the surrounding coastal plain with an elevation of 25 to 80m. The northern tip of the Albin Ridge (21°25,388`S, 13°53,558`E) is located 6km from the coastline, its southern termination is located about 10km inland. Since the Albin Ridge is tilted 15-25° to the ENE, its seaward face – a result of retrogressive erosion – is excellently exposed (plate V-4). The Albin Ridge provides access to one of the rare onshore examples of Early Cretaceous sedimentation that is directly related to South Atlantic rifting.

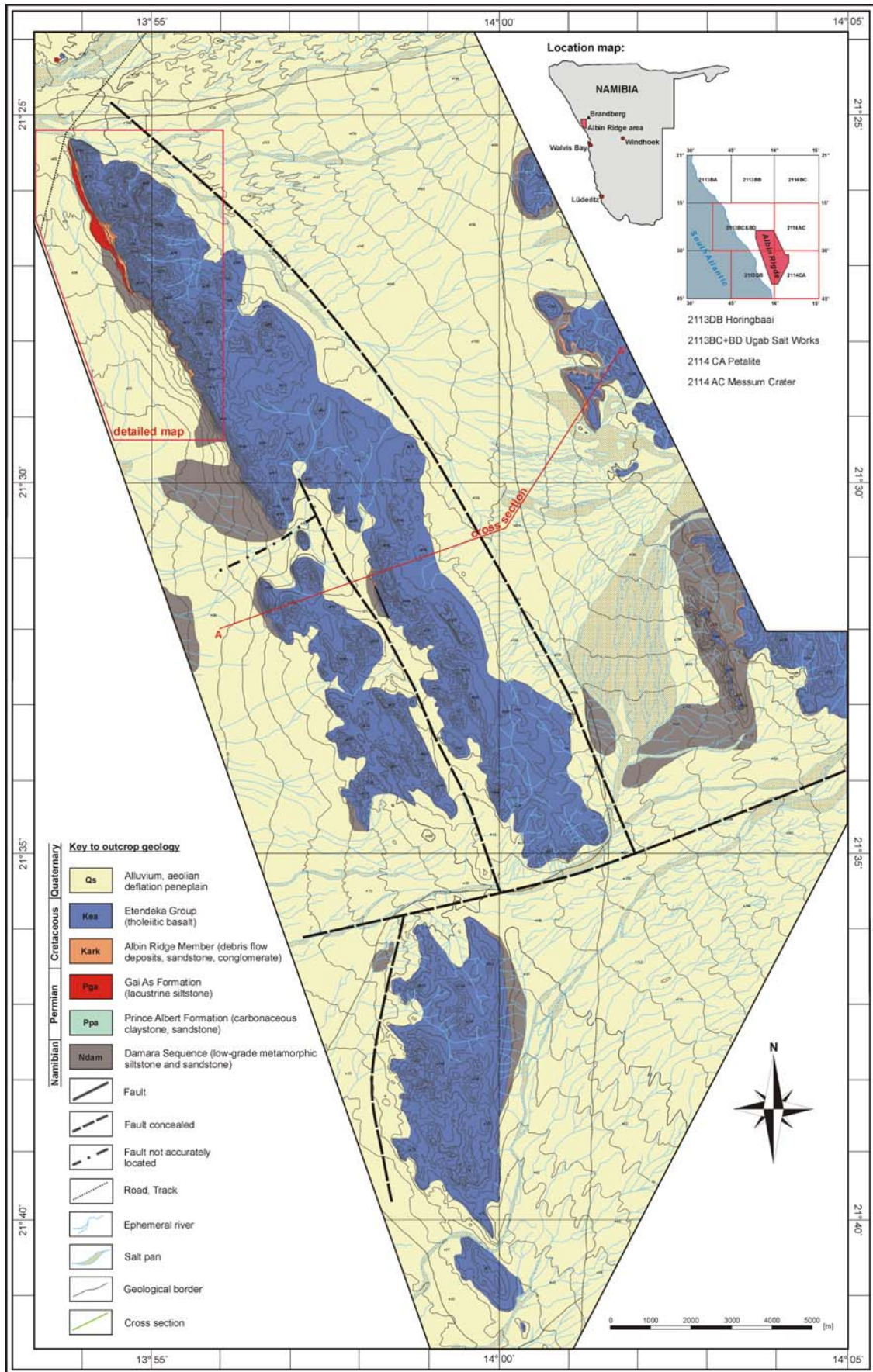


Fig. 2-8. Geological map of the Albin Ridge, southern Skeleton Coast/ NW-Namibia (mapped by R. Junker & M. Kukulius, 2000).

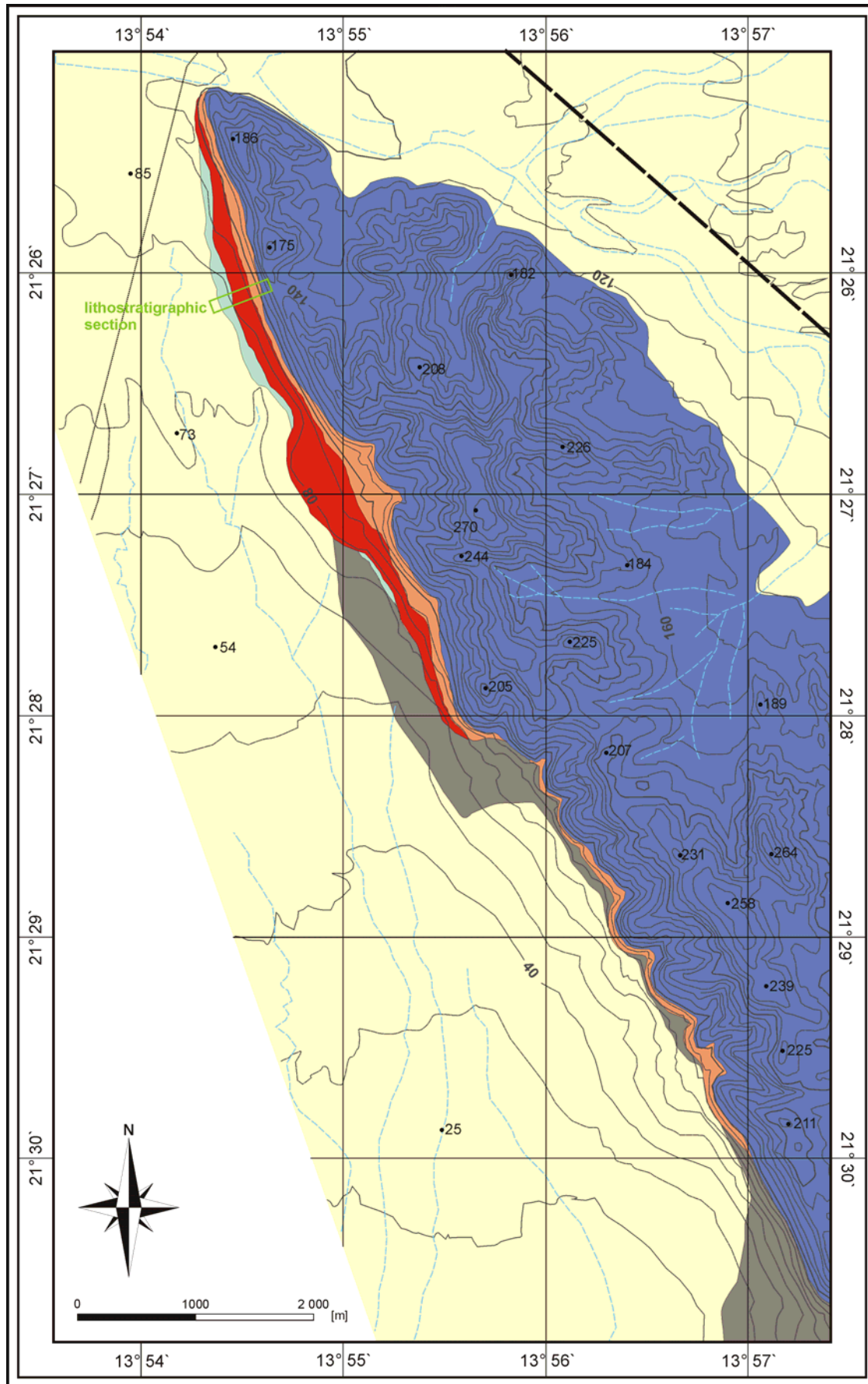
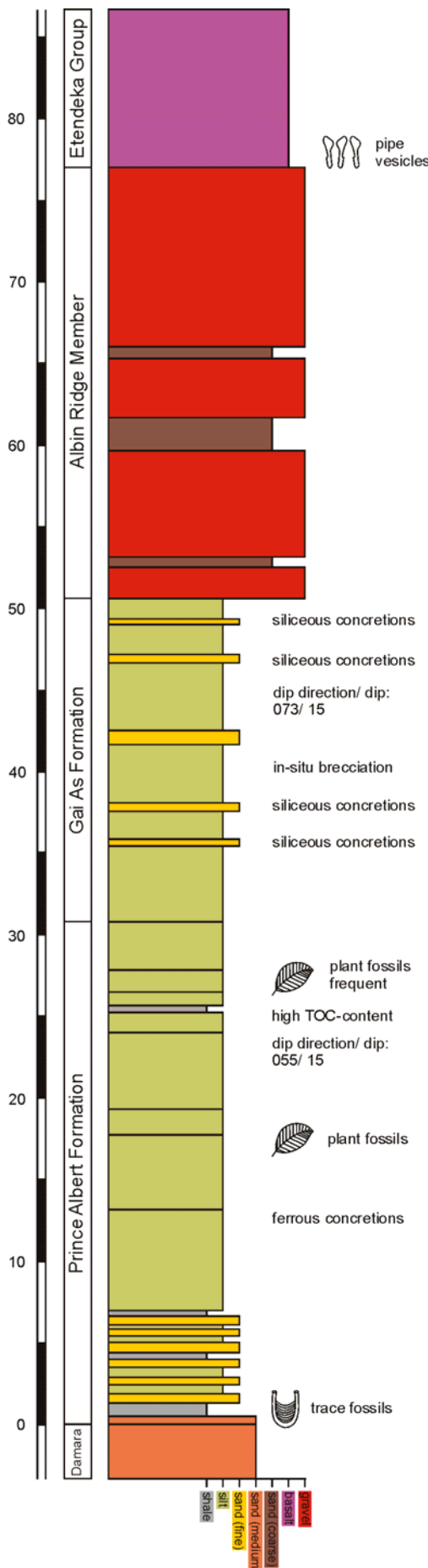


Fig. 2-9. Detailed geological map of the Albin Ridge, southern Skeleton Coast/ NW-Namibia (see fig. 2-8 for location).



During a field campaign in October/ November 2000, the Albin Ridge as well as the adjacent westernmost areas of the Messum Crater intrusive complex have been mapped in detail within the framework of a diploma mapping project of the University of Würzburg/ Germany (fig. 2-8; Junker et al., 2001).

2. 6. 1 Local stratigraphic framework

Since the regional lithostratigraphy of the NW-Namibian study area has already been outlined above (fig. 2-5), local modifications in the Albin Ridge area are briefly discussed in the following chapter. A representative stratigraphic section from the northernmost part of the Albin Ridge comprising the Karoo and Lower Cretaceous sedimentary succession is illustrated in figure 2-10; its exact location is indicated by a green box in the detailed geological map presented in figure 2-9.

The oldest sequences exposed on the western flank of the Albin Ridge morphological feature are low-grade metamorphic siltstones and fine- to medium-grained sandstones of the Late Proterozoic ("Namibian") to Cambrian Damara Group. These isoclinally folded metasediments (plate I-2) are rich in mica. Damara rocks underly the entire coastal plain but they are badly exposed due to coverage by a hammada-type Quaternary deflation peneplain (fig. 2-8). The top of the Damara sequence depicts a significant angular unconformity and erosional incision indicates a Lower Paleozoic land surface.

Fig. 2-10. Schematic lithostratigraphic section of the Karoo and Lower Cretaceous clastic succession of the Albin Ridge (see fig. 2-9 for location).

Damara rocks are unconformably overlain by light grey to bluish grey carbonaceous, partly ferrous siltstones of the Permian Prince Albert Formation. The deltaic to shallow marine Prince Albert Formation is widespread in southern Namibia; it is suggested to be equivalent to the Verbrandeberg Formation (fluvial), Tsarabis Formation (deltaic), and Huab Formation (shallow/ marginally marine) of NW-Namibia (fig. 2-5; Stollhofen, 1999).

The Prince Albert Formation reaches up to 30m thickness at the Albin Ridge. Its facial development is very similar to the Upper Ecca Group of southern Namibia for which fossils interpreted as plant remnants are typical (fig. 2-11b). In the western Goboboseb Mountains circa 20km to the NW of the Albin Ridge, a stratigraphic equivalent typical of the NW-Namibian Huab Formation is developed (chapter 2.2). The Albin Ridge, therefore, appears to roughly mark this facies change. However, the very base of both the Prince Albert Formation at the Albin Ridge and the Huab Formation in the western Goboboseb Mountains can unambiguously be correlated by means of an about 1m thick chert-layer with characteristic trace fossils.



Fig. 2-11. Selected samples from the clastic sequence of the Albin Ridge. (a) Red cherts of the base of the Prince Albert Formation (Dwyka?) showing characteristic small infaunal trace fossils (Pascichnia); location: 21°26,075`S, 13°53,941`E. (b) Light grey carbonaceous siltstones of the Prince Albert Formation showing ferrous plant or plant-like fossils typical of the Ecca Group; location: 21°26,075`S, 13°53,941`E. (c) Black siltstones of the upper Prince Albert Formation with probably enhanced TOC content; location: 21°25,609`S, 13°53,806`E. (d) Brown conglomerate of the Albin Ridge Member followed by a thin layer of overbank claystones; the latter are topped again by fluvial coarse clastics with basal erosion; clasts are predominantly metasedimentary sandstones of the Damara sequence and subordinate hydrothermal quartzes; location: 21°28,493`S, 13°55,514`E; diameter of coin = 1,5cm.

They occur in the form of small, 1-2mm wide, straight, circular, and radial grooves on the top side of a layer (fig. 2-11a). Although very small and simple, these trace fossils are relatively diverse. Up to five species of infaunal traces derived from creeping and feeding of organisms, or a combination of both (*Pascichnia*), can be interpreted. A marine paleoenvironment, however, cannot be deduced from these traces with certainty (pers. comm. M. Schlirf). An affiliation of this interval to the Lower Permian glaciogenic Dwyka Formation should also be considered.

The Prince Albert Formation in general has a homogeneous appearance. Locally, thermal alteration due to intruding sills and dykes as well as the formation of ferricrete due to weathering occurs. Sporadically, horizons of accumulated plant or plant-like fossil remnants (fig. 2-11b) are intercalated. Towards the top of this sequence, a 2m thick layer of black siltstones with a probably enhanced TOC-content (fig. 2-11c) can be observed. Facial similarities with the Whitehill Formation of the Upper Ecca Group of southern Namibia might be suggested. Equivalent stratigraphic positions offshore NW-Namibia would have attained significant burial depths and thus high maturity levels for potential oil or gas generation as outlined in chapter 6.5.

A significant hiatus characterises the transition from the Prince Albert Formation to the Upper Permian Gai As Formation (Stollhofen, 1999). The latter comprises red, evenly bedded lacustrine shales and siltstones. Condensed sections as well as pedogenic features, in-situ brecciation, and siliceous concretions are common in the Gai As sequence indicating sediment starvation. Although fossil vertebrate and fish remnants as well as benthonic bivalve fauna (*Terraia altissima*) have been documented in the Gai As Formation in the Huab area (Stollhofen, 1999), no fossil relicts have been encountered at the Albin Ridge. Fluvial deposits towards the top of the Gai As Formation which are leading over to the Doros Formation of the Huab area and which indicate a general shallowing of the paleoenvironment, are not preserved in the Albin Ridge area, either. The Gai As Formation reaches up to 43m of thickness at the northern tip of the Albin Ridge morphological feature.

An unconformity comprising almost 130Ma of non-deposition or erosion can be identified between the lacustrine Gai As Formation and the alluvial to fluvial deposits of the Albin Ridge Member, although erosional incision or angular unconformities cannot be observed. The Early Cretaceous Albin Ridge Member is a local facial feature that reaches up to 30m of thickness. The succession predominantly consists of coarse-grained alluvial debris-flow deposits (plate IV-1). A grain-supported texture of subrounded metasedimentary rocks of the Damara sequence that make up 80-90% of the detritus indicates relatively short transportation distances. Hydrothermal quartzes which can be attributed to quartz-veins embedded in the Damara sequence contribute up to 15% of the detritus. In the lower third of the section, however, up to 30cm large subrounded boulders of vesicular basalt occur as accessory components (plate V-1). Although highly altered, they indicate a close association and

petrographic similarity (Swart, 1992/93) with rift-related volcanism and thus suggest the Albin Ridge Member to be a unique example of synrift-sedimentation onshore.

In the upper third of the Albin Member succession, light grey to pink or green, medium-grained granitic pebbles become significant accessory components. They are generally rounded and up to 8cm large. Late Proterozoic granites of the Damara sequence (Durissa Bay Granite, Bockock's Bay Granite, Torrabay Granite, Mile 110 Granite; see "Geological map of Namibia 1:1000000"; Miller & Schalk, 1989) or the Early Cretaceous Brandberg and Cape Cross intrusive complexes might serve as potential sources. Unfortunately, no unequivocal relationship could be established.

Towards the top of the section, locally coarse-grained trough-bedded fluvial sandstones with occasionally preserved overbank fines can be observed. These might be related to braided river systems draining the foothills of a paleo-rift shoulder. It has been suggested that these sands represent reworked aeolian deposits which could be associated with the Twyfelfontein Formation of the Huab area (pers. comm. H. Stollhofen); this would indicate the Albin Ridge Member to be a correlative of the Krone Member as it has been outlined above.

In the southwestern Goboboseb Mountains and along the western termination of the Messum intrusive complex (fig. 2-8 & 2-12) the Albin Ridge Member is developed with significantly reduced thicknesses of 0,2-2m.

The morphological feature of the Albin Ridge is predominantly due to a c. 200m thick sequence of basaltic lava flows which overly the clastic sequence below. Erlank et al. (1984) and Marsh et al. (2001) recognised that the Albin basalts are a petrographic variant of the Tafelberg type (fig. 2-6) with a tendency to be compositionally more primitive; additionally, their SiO₂-content (45,9-53,2%) is distinctly lower than that of the Tafelberg lavas (50,3-56,3%). The low-Ti, plagioclase-phyric tholeiitic Albin basalts occur at the base of the Etendeka volcanic sequence that has been extruded within a short period between 131,7±0,7Ma and 132,3±0,7Ma (Renne et al., 1996).

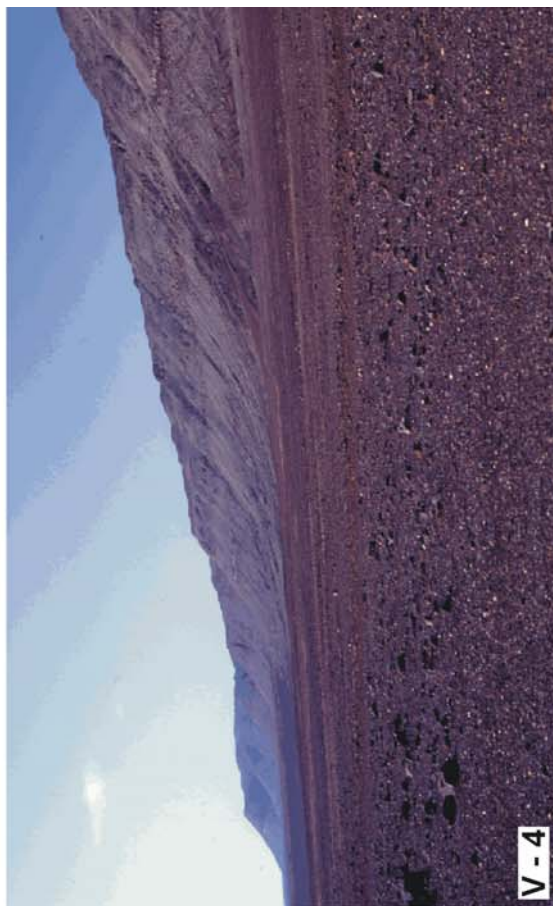
Legend Plate V

V-1. Grain supported debris flow deposit of the Albin Ridge Member; vesicular basaltic clasts (white contour) that can be attributed to synrift-magmatism contribute up to 5% of the detritus; basalt occurs preferentially in the lower third of section; hammer for scale; location: 21°26,945`S, 13°54,589`E.

V-2. Albin Ridge Member-Etendeka Group boundary (indicated by white line); base of the basaltic lava flow is characterised by pipe vesicles; scale = 10cm; location: 21°28,846`S, 13°55,715`E.

V-3. Isolated dune sands of the Twyfelfontein Formation intercalated with basal units of the Etendeka Group in the Huab area; hammer for scale; location: Farm Krone, 20°29,128`S, 14°01,607`E.

V-4. Topographic impression of the Albin Ridge – an isolated tilted block related to South Atlantic rifting protruding out of the coastal plain in the southern Skeleton Coast area; topographic height c. 150-200m; view to the north; location: 21°29,179`S, 13°55,435`E.



Single lava flows that become up to a few metres thick can be distinguished in the field; their particular bases are normally indicated by vesicular zones. Calcite-filled basal pipe vesicles are illustrated in plate V-2. The Messum Crater subvolcanic complex is known to be the eruptive centre of the Awahab Formation quartz latites (Goboboseb & Springbok quartz latites; fig. 2-6; Milner & Ewart, 1989; Marsh et al., 2001); it appears to be justified to consider Messum as eruptive site for the Albin basalts as well.

The Prince Albert Formation, the Gai As Formation, and the Albin Ridge Member, respectively, are only preserved in the northernmost part of the Albin Ridge morpho-tectonic feature; they successively pinch out towards the SSE as it is indicated by the detailed map in figure 2-9. The majority of the Albin Ridge basalts rests directly on a paleo-land surface of metasedimentary Damara rocks thus displaying a prominent angular unconformity.

2. 6. 2 Tectonic implications

Tectonic processes observed at the Albin Ridge can entirely be attributed to the opening of the South Atlantic in the Early Cretaceous. The Albin Ridge is located at the transition from the rift basin depression and thus the area of the future zone of oceanic onset to the west and, on the other hand, the rift shoulder that gives rise to the evolution of the Great Escarpment to the east (Stollhofen, 1999).

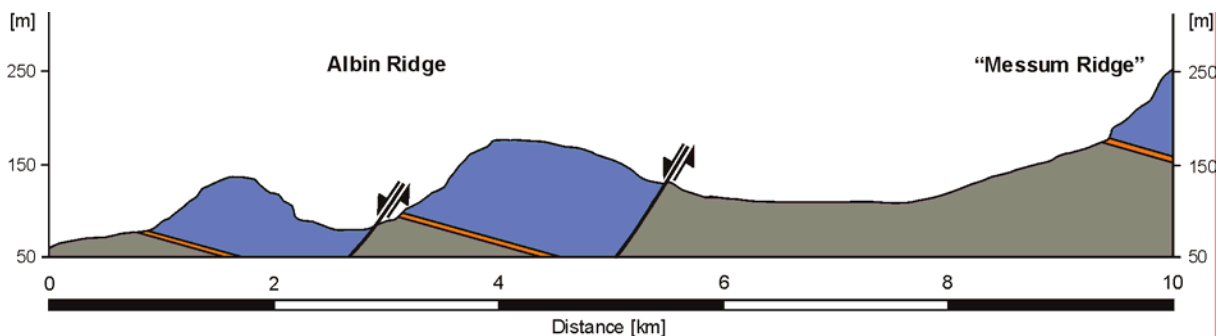


Fig. 2-12. SW-NE-oriented cross section through the Albin Ridge and “Messum Ridge” tilted blocks (see fig. 2-8 for location).

Three major NNW-SSE striking normal faults and one WSW-ENE striking strike-slip fault exert fundamental control on the tectonic inventory of the Albin Ridge (fig. 2-8). The Albin Ridge in general represents a typical rift-related block antithetically tilted to the ENE along probably listric normal faults. The Karoo and Cretaceous deposits of the northern Albin Ridge reveal a bedding of 053/25 on average. Figure 2-12 illustrates a cross-section through the central part of Albin Ridge – Messum Ridge tilted block system where the displacement is partitioned into a set of two normal

faults. The western termination of the Messum intrusive complex exhibits a bedding between 085/05 and 025/25 which is very similar to that of the Albin Ridge; this feature has therefore been termed “Messum Ridge” in the field. The well exposed base of the Etendeka volcanics enables the total displacement documented by the normal faults to be estimated; a vertical offset of 3800m has been calculated which appears to be well within the dimensions expected for a major rift-graben.

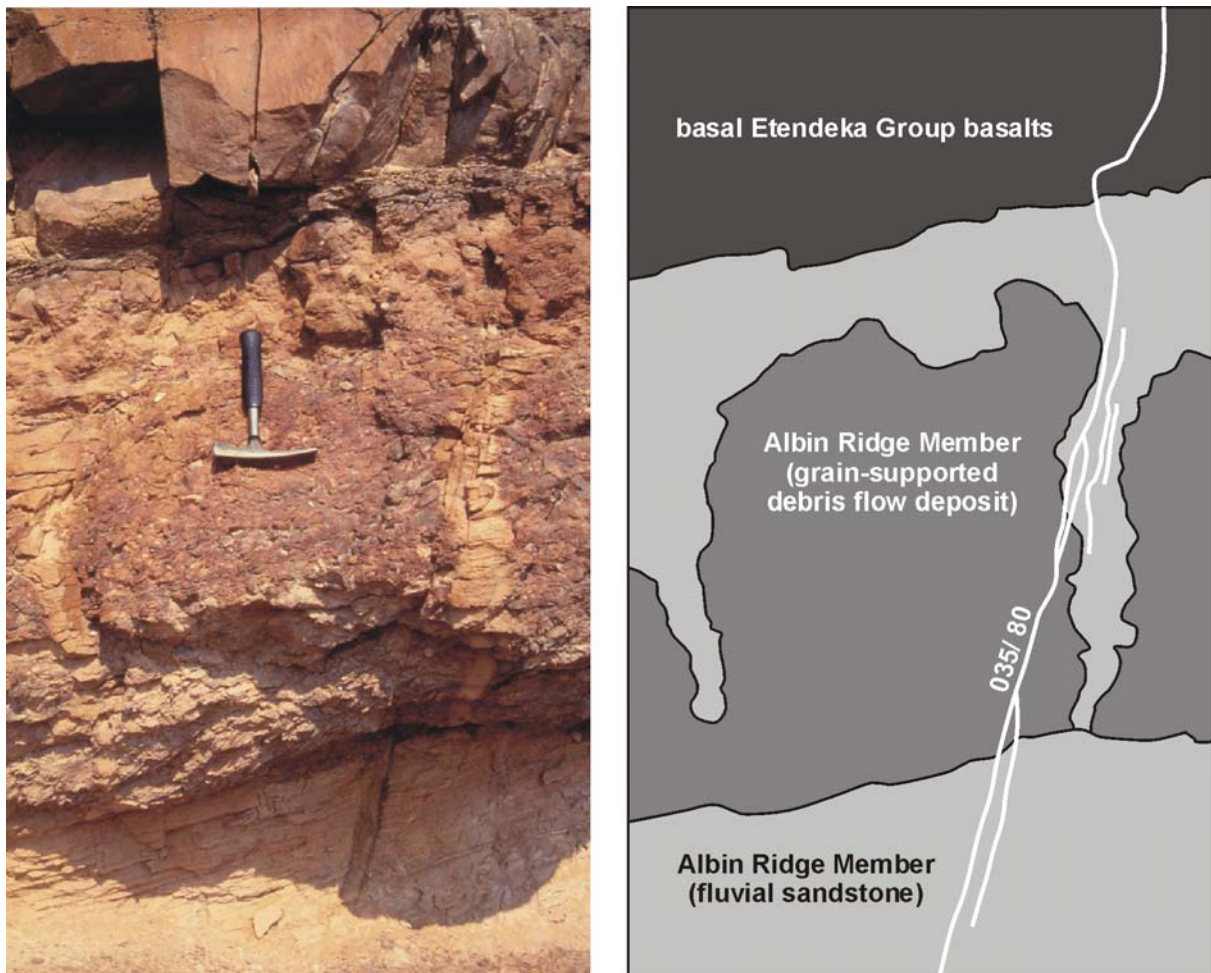


Fig. 2-13. Steep sediment-filled fissures at the Albin Ridge Member-Etendeka Group boundary indicate syndimentary extensional faulting during South Atlantic rifting. It is suggested that the Albin Ridge Member is a rare example of synrift deposition preserved in Namibia; hammer for scale; location: 21°26,737`S, 13°54,454`E.

The southern part of the Albin Ridge shows a slight dextral displacement along a major crosscutting fault. Topography as well as the southwestern termination of the miscoloured satellite image (fig. 2-8 & 2-15) support the trend of this fault. Furthermore, the polarity of dip of the associated normal fault appears to change. A typical tilt-block signature remains preserved. However, the halfgraben-bounding fault is located at the western termination of the block and the lower boundary of the Etendeka volcanics is exposed in the eastern part. The WSW-ENE-striking structure is therefore interpreted as a prominent regional transfer fault; it might be associated

with the southern termination of the Messum subvolcanic complex as well as with the Autseib Lineament which runs parallel further south (fig. 1-1 & 2-15). The Autseib and Omaruru transfer-transform systems, however, are suggested to displace magnetic anomalies offshore (M2, M4) in a sinistral manner (Rabinowitz & La Brecque, 1979; Austin & Uchupi, 1982; Gerrard & Smith, 1982).

It can be assumed that major tectonic activity took place after the deposition of the basal Etendeka volcanics (132-131Ma) because they are tilted and offset together with the underlying Karoo and Early Cretaceous sediments on which they rest concordantly. The end of major post-depositional tectonic activity is suggested to be equivalent with the age of final oceanic onset in the northern Walvis Basin 129-128Ma or 126Ma, at the latest (see chapter 3.2).

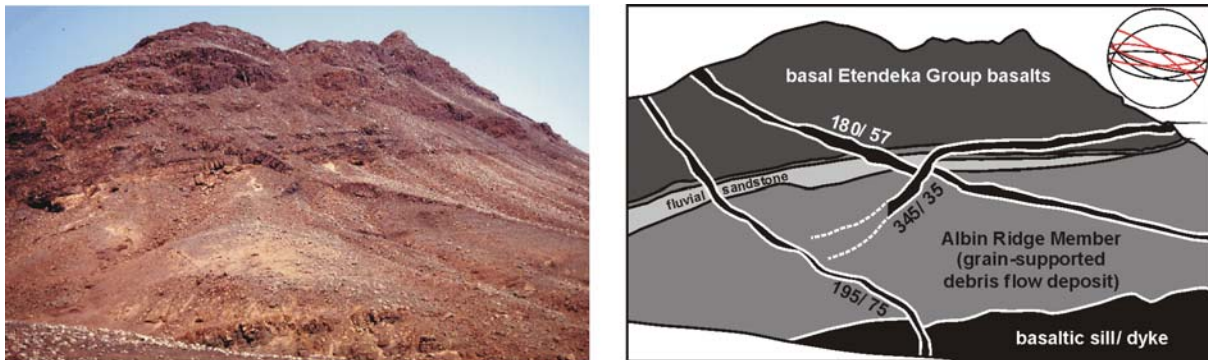


Fig. 2-14. Sill-dyke-systems and intrusion tectonics at the Albin Ridge Member-Etendeka Group boundary. It is suggested that the dykes did not act as feeder-dykes for the overlying basalts; they show intrusive contacts and are more likely related to the Horingbaai dyke-swarm which is slightly younger than the Etendeka Group basalts (125Ma; Erlank et al., 1984; Renne et al., 1996). Stereographic net diagram indicates spatial orientation of some dykes (black) and sediment-filled fissures (red). Height of section c. 100m.

Figure 2-13, however, indicates that extensional faulting already occurred contemporaneously with the deposition of the Albin Ridge Member. In the upper part of the section several steep fault-related fissures within grain-supported debris flow deposits can be observed which are filled with fluvial sands from the top down; this process affords sediment not yet consolidated by diagenesis. The sediment-filled fissures display a WNW-ESE pattern which is roughly parallel to one array of the Horingbaai dolerite dykes described -oriented by Erlank et al. (1984; fig. 2-15). The Horingbaai dykes, however, have been dated as 130-125Ma in age which is slightly younger than Etendeka volcanism. Additionally, they reveal a MORB-compatible geochemical signature. Stollhofen (1999) therefore suggests the dolerites to be associated with the oceanic onset in the adjacent offshore segment.

Basaltic sill-dyke systems are frequently observed in the Albin Ridge area as well (fig. 2-14). They display complex age-relationships and offsets in the order of 0,5-2m. Due to their preferential weathering, a macroscopic comparison with the Etendeka basalts is rather difficult. All of the observed contacts are intrusive (fig. 2-14); they are therefore interpreted in analogy to the Horingbaai dyke swarm as younger sill-dyke systems that have not acted as feeder-dykes for the overlying Albin basalts. Equivalent to the sediment-filled fissures, the dykes reveal a preferential WNW-ESE-orientation.

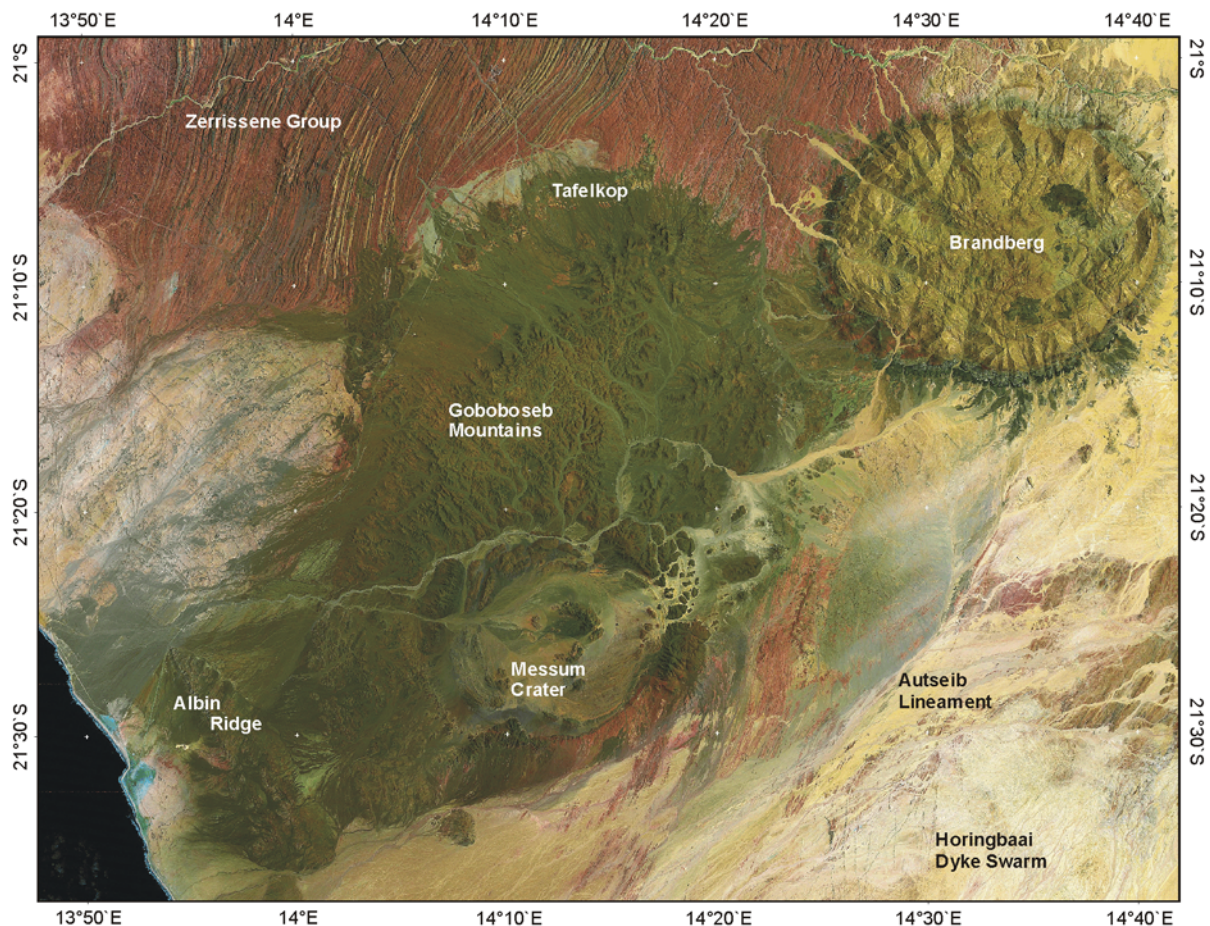


Fig. 2-15. Miscoloured satellite image of a section of NW-Namibia comprising the area between the Albin Ridge in the SW and the Brandberg intrusive complex to the NE; created with *ENVI*. Some of the locations referred to in the text are labelled.

The Albin Ridge morpho-tectonic feature is closely related to Early Cretaceous continental rifting in NW-Namibia. Primarily, the coarse debris flow deposits indicate short transportation distances and a high-energy relief; basaltic detritus provides excellent temporal constraints for its deposition (Swart, 1992/93). The observed fault pattern is analogous to that Etheridge et al. (1989) proposed for typical upper plate margins (see fig. 3-1), albeit an order of magnitude smaller. Stollhofen (1999) correlated the Albin Ridge tilted block system with the Purros Lineament of NW-

Namibia and interpreted the Albin Ridge to mark the proper Early Cretaceous rift shoulder.

Based on the field studies presented above, it is suggested that the Albin Ridge as a local feature is an outstanding example for South Atlantic rifting preserved in Namibia, both in terms of tectonic processes as well as in terms of the associated deposition. The recognition of tilted-block characteristics for the western termination of the Messum Crater (fig. 2-12), however, suggests that additional prominent normal faults may have been active farther inland during rifting. The Albin Ridge has evidently accommodated a significant amount of extensional normal faulting but the term "rift shoulder" should probably be applied to a wider region.

3 Geodynamic evolution of the Namibian margin

3.1 The basin forming mechanisms

The South Atlantic has long been regarded as a classical example for the evolution of conjugate passive continental margins based on the “simple shear model” that Wernicke et al. (1985) established for the Basin and Range Province in the USA. A modified “detachment-model” has been proposed by Etheridge et al. (1989) to explain the characteristic asymmetric features observed in the South Atlantic by means of a lithospheric inclined shear zone (fig. 3-1). South of the Rio Grande Rise – Walvis Ridge the South American margin appears to be relatively wide with pronounced synrift-structures and thick postrift sediments which are typical features of a “lower plate margin” (Davison, 1997). The “upper plate margin” of southern African, on the other hand, is much narrower and relatively unstructured. Upper plate margins are characterised by uplift due to magmatic underplating establishing and focussing a continental drainage divide that evolves into a “Great Escarpment” (fig. 3-1). Furthermore, the zone of maximum lithospheric thinning is offset landwards of the sediment depocentre which is also resembled by gravity data (Stewart et al., 2000; chapter 3.4). The polarity of these features appears to change north of the Rio Grande Rise – Walvis Ridge which therefore is interpreted to represent a major accommodation zone (Etheridge et al., 1989).

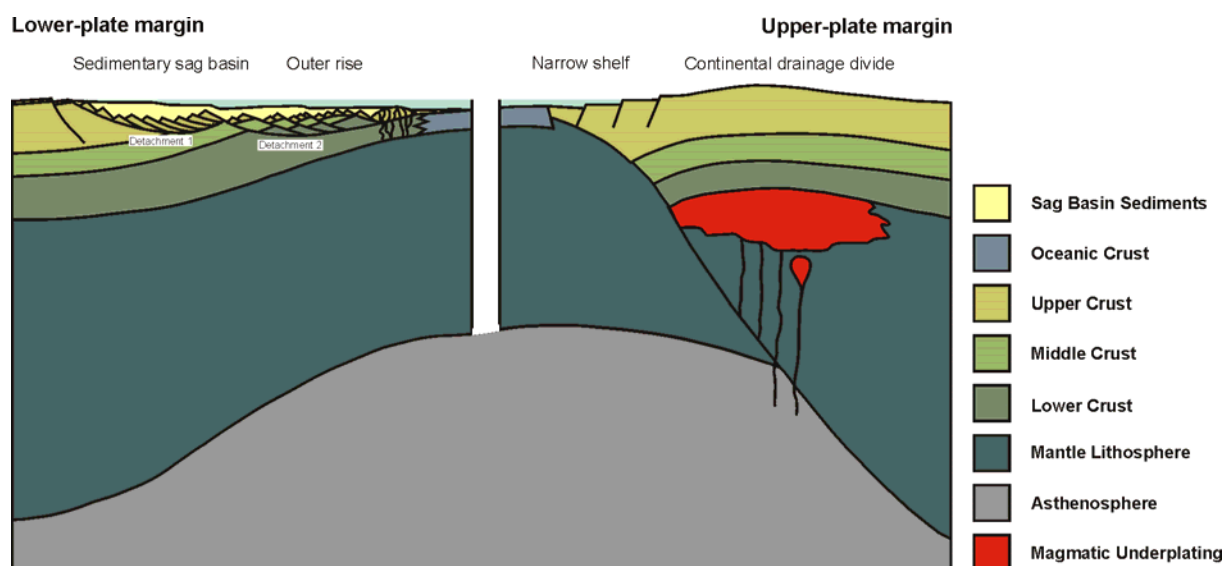


Fig. 3-1. Gross architecture of asymmetric conjugated upper-plate and lower-plate margins resulting from continental extension by detachment faulting. The lower plate margin (left) has a complex structure, with tilt-block remnants of the upper plate above bowed-up detachment faults. Multiple detachment has led to two generations of tilt-blocks. The upper-plate margin (right) is relatively unstructured and is uplifted by magmatic underplating to form passive margin mountains (“Great Escarpment”). From Etheridge et al. (1989).

More recent studies, however, have doubted this significant asymmetry of conjugate rifted margins. Paradoxically, all rifted margins appear to show “upper plate” characteristics in terms of detachment models (Driscoll & Karner, 1998; Kusznir et al., 2002). Estimations of crustal extension on the Namibian margin resulted in an amount of about 125km giving a stretching factor of $\beta=2,05$ (Stewart et al., 2000). Chang et al. (1992) calculated 137km of crustal extension and thus an only insignificantly higher stretching factor of $\beta=2,15$ for the conjugate Pelotas Basin in southern Brazil. Although extension is suggested to be laterally displaced by a low angle crustal/ lithospheric detachment, very similar amounts of extension on both margins are observed. According to Kusznir et al. (2002), depth-dependent stretching with differential amounts within crust and mantle lithosphere might be able to explain this observation; they infer that significant amounts of extension may rather be related to early seafloor spreading than to pre-breakup intracontinental rifting.

Magmatic underplating and increased melt potential is normally associated with the upper plate margin (fig. 3-1). Considering the much more voluminous Paraná basalts on the South American margin in contrast to the Namibian Etendeka volcanics, Stollhofen (1999) proposed a reviewed interpretation of the polarity of the crustal detachment.

3. 2 Rifting and breakup chronology

Pre-drift plate reconstructions of the South Atlantic Ocean cannot be accurately achieved if rigid lithospheric behaviour is assumed; gaps and overlaps indicate that rifting seems to have propagated from south to north (e.g. Rabinowitz & La Brecque, 1979; Nürnberg & Müller, 1991).

Evaluation of seismic data from offshore Namibia reveal that faulting in the synrift-sequences becomes progressively younger further north. Furthermore, the pre- and synrift successions offshore southern Namibia are extremely thick, whereas north of the Walvis Ridge the Tertiary succession is relatively thick compared with the synrift deposits (Light et al., 1992). Gerrard & Smith (1982) have shown that the depocentre of Upper Cretaceous sandstones shifted northwestwards, which is consistent with the overall northward propagation of rift systems.

Differences in rates and directions of extension along the rift axis had therefore to be compensated by transfer/ transform fault systems bounding individual rift segments (fig. 3-2). The Namibian and South African continental margin is bounded to the north by the Torres-Walvis Transform and to the south by the Agulhas-Falkland Transform (Dingle 1992/93). In between, the Colorado-Orange Transform intersects the central Orange Basin at c. 32°S. At the latitude of the Kudu boreholes (c. 28°S), offshore the

mouth of the Orange River, the Salado-Orange Transform matches its onshore continuation in the form of the Karasburg-Orange fault zone (Stollhofen, 1999). Most of the syn- and post-breakup structures offshore and onshore SW-Africa appear to be controlled by pre-existing basement features and match equivalents on the South American side (e.g. review of Brown et al., 2000). This seems not to be the case for the landward continuation of the Walvis Ridge which is a purely plume related aseismic ridge oriented obliquely to the oceanic transform zones. The intracontinental branch of the Pan-African Damara Orogen, for example, can be correlated with the Dom Feliciano Belt of the Brazilian margin.

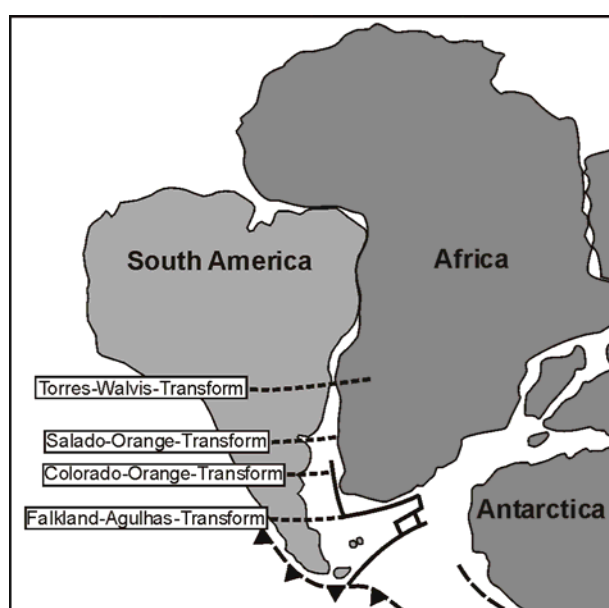


Fig. 3-2. Jurassic pre-drift reconstruction of the South Atlantic Ocean including major transform zones which compensated differential extension during northward prograding oceanic onset in the Early Cretaceous. Modified from Dingle (1992/93).

The chronology of oceanic onset following rifting in the South Atlantic is best preserved in magnetic seafloor anomalies. An overview of the geodynamic evolution is given in figure 3-3. Oceanic onset in the Indian Ocean started in the Late Bathonian (from c. 161Ma; Harland et al., 1990) and thus somewhat earlier than in the South Atlantic Ocean (e.g. Dingle & Scrutton, 1974).

The onset of seafloor spreading was preceded by a long period of intracontinental lithospheric extension prior to breakup and oceanic onset. Harry & Sawyer (1992) and Gladchenko et al. (1997) infer an extensional period of 25Ma before breakup; Stewart et al.

(2000) suggest 17 Ma of rifting for their gravity model (see chapter 3.4).

According to Rabinowitz & La Brecque (1979) oceanic onset offshore South Africa, south of the Agulhas Fracture zone (fig. 3-4) started as early as in the Berriassian, with magnetic anomaly M13 (c. 135Ma); the timescale of Gradstein & Ogg (1996) is used in this section. Between the Agulhas Fracture zone and the Salado-Orange Transform the Valanginian anomaly M11 (c. 132Ma) appears to represent the oldest seafloor (Rabinowitz & La Brecque, 1979; Austin & Uchupi, 1982; Gerrard & Smith, 1982). Dingle (1992/93), however, interpret M10 (c. 130Ma) to be the oldest anomaly in this rift segment. Oceanic onset proceeded northward across the Waterberg-Omaruru fault zone to the Walvis Ridge with anomaly M4 (c. 126Ma), at the latest, as it is illustrated in an enlarged and more detailed version of figure 3-3f given in figure 3-4.

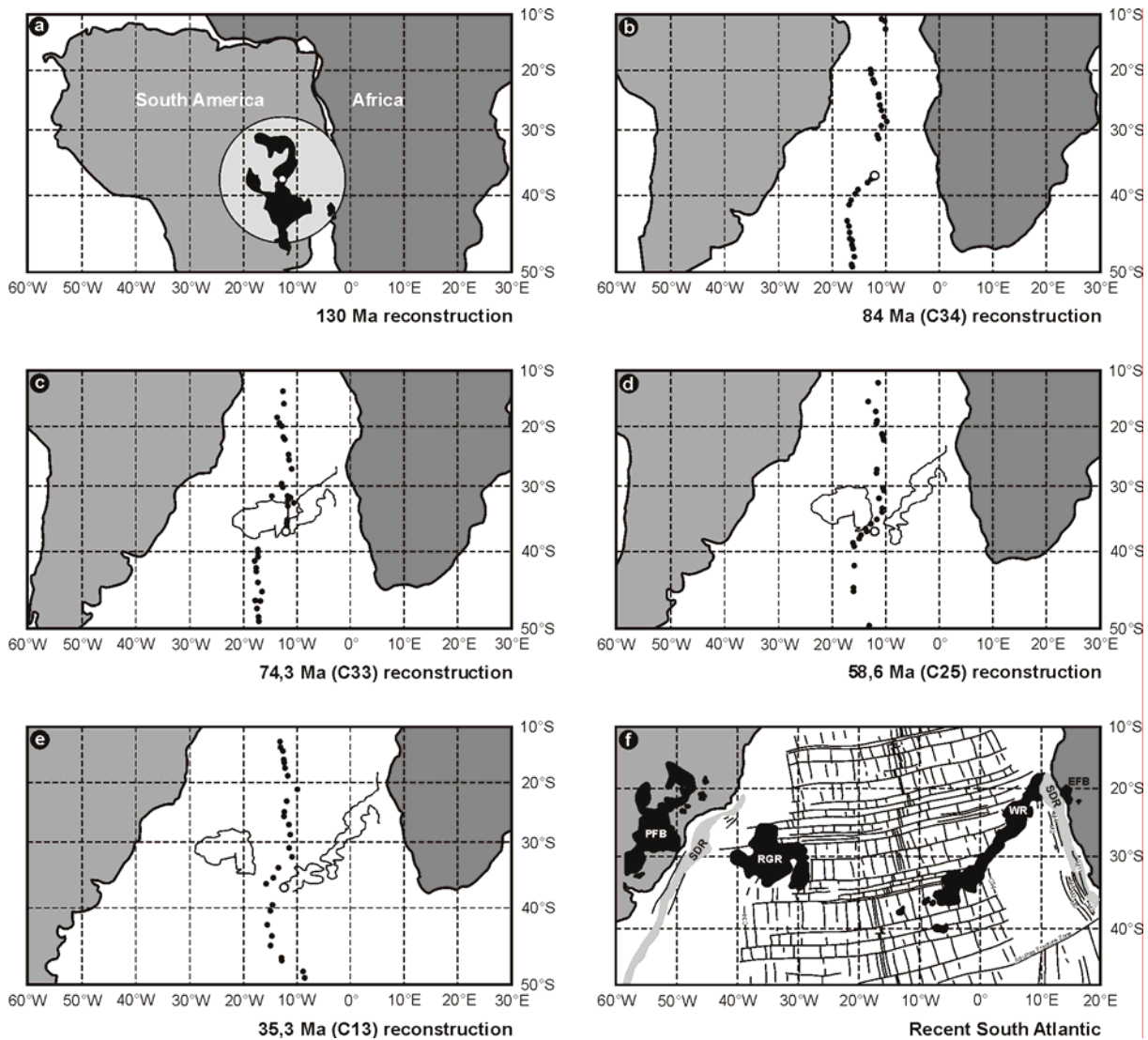


Fig. 3-3. Reconstruction of the spatial relationship between the Tristan da Cunha hot spot, the South Atlantic spreading axis, and the evolving structure of the Rio Grande Rise (RGR) - Walvis Ridge (WR) volcanic system. The Mercator projections are centred on the island of Tristan da Cunha represented by the open circle (a)-(e); modified from O'Connor & Duncan (1990). (a) 130Ma reconstruction; the light grey circle represents a hypothesised large-diameter hot spot above the upwelling Tristan plume and comprises the surface relicts of the Paraná-Etendeka flood basalt system (black). (b)-(e) Reconstructions for selected spreading anomaly times. Bathymetry of Rio Grande Rise and Walvis Ridge is indicated by thin black lines. Small black circles represent magnetic anomaly picks from Cande et al. (1988). (f) Magmatic and magnetic features of the recent South Atlantic (see fig. 3-4 for details).

Offshore Walvis Bay, in the northern Walvis Basin off NW-Namibia, the magnetic anomalies M2 and M4, as well as the magnetic anomaly G, appear to be sinistrally offset (Rabinowitz & La Brecque, 1979; Austin & Uchupi, 1982; Gerrard & Smith, 1982). Stollhofen (1999) delineates in detail the importance of the Waterberg-Omaruru fault zone (fig. 3-4) as a reactivated Pan-African basement structure that represents the onshore continuation of this potential transform fault. Likewise seem the location and structural style of the continental Permian to Jurassic Karoo basins to be controlled by pre-existing structures (e.g. Hegenberger, 1988).

The magnetic anomalies immediately north of the Waterberg-Omaruru fault zone are largely obscured by the Walvis Ridge volcanic feature that results from the passage of the African plate over the Tristan da Cunha mantle plume. Although often published, the exact position of these anomalies has long been questioned. According to Müller et al. (1997) there is no offset of magnetic seafloor anomalies immediately south of the Walvis Ridge.

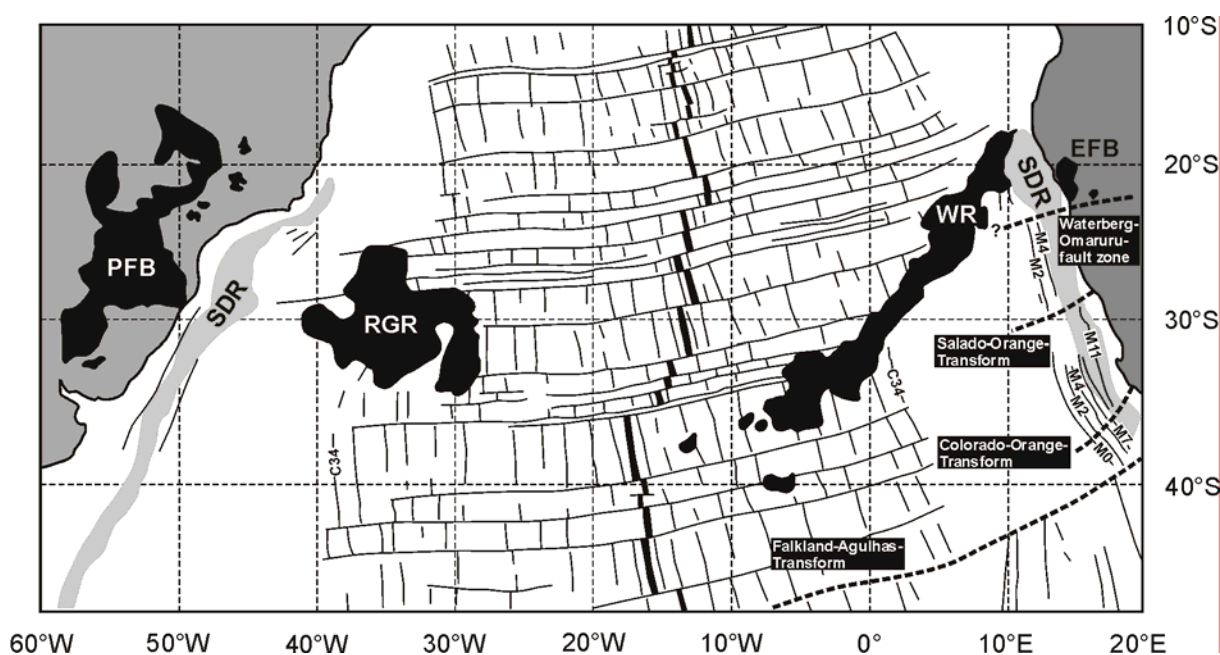


Fig. 3-4. Magmatic and magnetic features of the recent South Atlantic (Modified from Bauer et al., 2000). Labelling of magnetic anomalies after Rabinowitz & LaBreque (1979) and Cande et al. (1988). Rio Grande Rise, Walvis Ridge, Parana Flood Basalt Province, and Etendeka Flood Basalt Province are indicated by RGR, WR, PFB, and EFB, respectively. Coastal regions that are underlain by seaward dipping reflectors (SDR) are shaded in light grey.

The magnetic anomaly G that occurs landward of the oldest seafloor anomaly is a common feature of volcanic rifted margins and is interpreted to be assigned to the landward boundary of extended transitional crust (Bauer et al., 2000). Anomaly G is the most landward magnetic anomaly that can be traced along the South African and Namibian margin over large parts north to the Walvis Ridge. It is controversially discussed in terms of its geophysical origin and the implications for the position of the continent-ocean-boundary (COB; Bauer et al., 2000; Gladchenko et al., 1997; Stewart et al., 2000). Rabinowitz (1976) suggested that G might represent magnetic anomaly M12 (c. 134Ma) which would make large parts of the southwestern African margin significantly older.

However, the figures 3-4 & 1-1 indicate that M2 and M4 are located about 350-400km from the coast in the northern Walvis Basin, suggesting that there might older seafloor be preserved. Extrapolating the half-spreading rate of c. 2,8cm/a between M2 and M4 in that area towards the proposed landward limit of normal oceanic crust

(TNOB in fig. 3-5, located 300-320km from the coast) would imply that oceanic onset in the northern Walvis Basin started as early as 128-129Ma ago. Oceanic onset in the southern part of southwestern Africa therefore occurs slightly before or coeval with Paranà-Etendeka volcanism (see chapter 2.4) whereas offshore northern Namibia it slightly postdates flood basalt extrusion thus indicating an “active” rift mechanism.

As outlined below (fig. 3-5), the entire transitional crust features a strong overprinting by basaltic magmatism. If this effect was completely attributed to the process of oceanic onset, the continent-ocean boundary might be placed on the landward termination of the transitional crust located c. 120km from the coast (COB in fig. 3-5). Extrapolating the half spreading rate of c. 2,8cm/a from M4 towards the COB would imply an age of 134-136Ma for the initiation of oceanic onset. This, in turn, not only corresponds to the inferred age of the magnetic anomaly G or M12, as suggested by Rabinowitz (1976), but also indicates a “passive” rift mechanism, as the Etendeka flood basalt volcanism would postdate oceanic onset.

3. 3 Deep structure of the margin

Some 14300km of high resolution seismic as well as gravity and magnetic data were acquired offshore Namibia between 1989 and 1991 on behalf of *NAMCOR*, the Namibian National Oil Company. The seismic character of the margin sediments has been intensely studied by Light et al. (1992, 1993) and by Bagguley & Prosser (1999). On the basis of this dataset Gladczenko et al. (1997) focussed on the volcanic character of the Namibian continental margin and the related seismic features. They revealed gross similarities with other volcanic margins in tectono-magmatic style, crustal units and dimensions. Massive transient magmatic activity during final breakup and seafloor spreading is attributed to the Tristan da Cunha hot spot (O'Connor & Duncan, 1990) and makes the Namibian volcanic margin part of the “South Atlantic Large Igneous Province” (Coffin & Eldholm, 1994; Gladczenko et al., 1997).

Austin & Uchupi (1982) have already recognised the presence of high-amplitude magnetic anomalies over the SW-African continental slope and have related them to igneous material within a seaward dipping wedge beneath. Seaward dipping reflector wedges occur similarly along the rifted margin of South America (fig. 3-4, Chang et al., 1992; Mohriak et al., 1990).

Gladczenko et al. (1997) interpreted a regional grid of seismic lines in the Walvis Basin offshore NW-Namibia and established four breakup-related tectono-magmatic zones beneath the postrift sedimentary wedge. From the west towards the coast they recognised (1) normal oceanic crust, (2) thickened oceanic crust covered by seaward dipping reflectors (SDR), (3) a c.150km wide rift zone covered with SDRs in the west

and lavas and intrusives in the east, and (4) normal continental crust. Gladczenko et al. (1997) place the continent ocean boundary (COB) on the western edge of their breakup-related zone 3 which corresponds to the inner SDR wedge presented in figure 3-6. Magnetic anomaly G appears to be related (or caused) by the SDRs. However, immediately south of Walvis Bay anomaly G seems to be bended landwards of the SDRs (Rabinowitz & LaBrecque, 1979).

Since seismic resolution is poor beneath SDRs (Eldholm et al., 1995) there is ongoing discussion on the deeper structure of the Namibian margin. Based on their data, Gladczenko et al. (1997) infer magmatic underplating associated with the intense breakup magmatism as well as a high-density lower crustal body, indicated by the deepest reflectors.

The seismic line BGR 95-11 (fig. 1-1 & fig. 3-5), interpreted by Bauer et al. (2000), is located c. 150km to the South of the central Walvis Basin and provides information on crustal thickness and velocity variations across the margin on the basis of seismic reflection and refraction/ wide-angle reflection data. Combined with line ECL89-41 (fig. 3-6), a detailed crustal-scale analysis of the margin architecture and stratigraphic record is possible.

Bauer et al. (2000) observed a 150 to 200km wide zone of up to 25km thick igneous crust (fig. 3-5). It is interpreted to represent a wide transition zone between normal oceanic crust of 12km thickness in the west and up to 35km thick continental crust to the east.

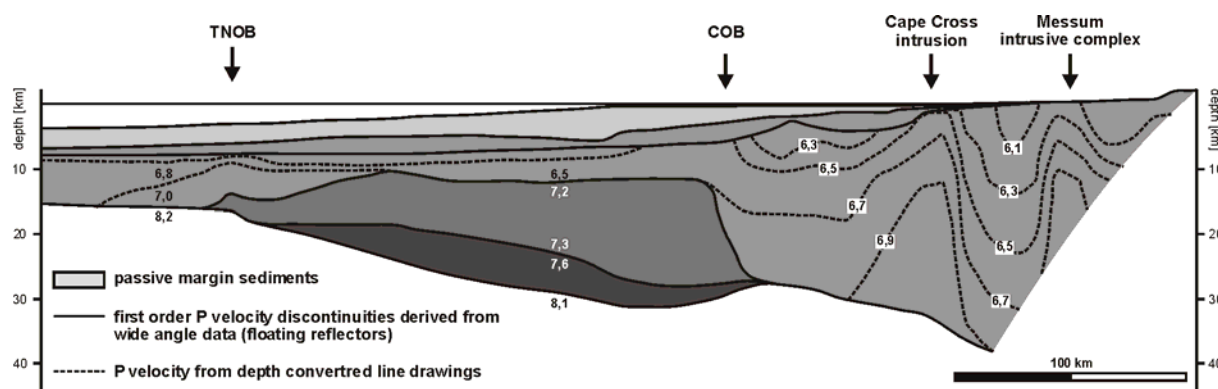


Fig. 3-5. Interpreted p-velocity distribution for the entire crust in the central Walvis Basin area. Solid lines represent first order discontinuities derived from wide-angle reflection data; dashed lines are isovelocity lines interpreted from depth converted line drawings. COB=continent ocean boundary; TNOB=transitional-normal oceanic crust boundary. Modified from Bauer et al. (2000). See figure 1-1 & 4-2 for location of section BGR 95-11.

In contrast to Light et al. (1992, 1993) and Gladczenko et al. (1997) who discuss the transition zone in terms of rifted relict crust, Bauer et al. (2000) regard this zone as consisting almost exclusively of igneous material without any evidence for synrift tectonism. Rift-related structures in the middle and lower crust might be completely

overprinted and obscured by mafic intrusions. P-velocity modelling resulted in values between 7,2km/s and 7,6km/s (fig. 3-5) and corresponding densities of 3,0-3,3g/cm³ which is higher than normal MORB-like igneous material. The velocities correspond to olivine-rich, high-Mg magmas that require more than 20-25% of partial melting of peridotite (Bauer et al., 2000). Taking into consideration that the amount of decompressional melting depends on the potential temperature of the asthenosphere and on the timing and degree of lithospheric thinning (White & McKenzie, 1989), higher than normal mantle-temperatures during breakup can be suggested. For the central and northern Walvis Basin, at least, these can be ascribed to the Tristan da Cunha mantle plume.

The mid- and lower crustal high-velocity zone is overlain by two distinct SDR wedges separated by a zone of flat lying lava flows. These features are very well developed in the central Walvis Basin (fig. 3-6). P velocity modelling indicates values of 4,8 to 5,5km/s which is typical of extrusive basalts (Bauer et al., 2000).

Seaward dipping reflector wedges near the continent-ocean transition spatially related to lower crustal high-velocity bodies ($v_p > 7$ km/s) are typical for volcanic rifted margins; the latter are commonly interpreted as magmatic underplated material that represents the intrusive counterpart (and magma source) of the overlying extrusives (Eldholm et al., 1995; White & McKenzie, 1989; Skogseid et al., 1992).

The landward termination of the mid- and lower crustal high v_p -body is marked by an abrupt decrease in velocities and densities (fig. 3-5) and is defined as proper continent ocean boundary (COB) by Bauer et al. (2000). It is suggested that the Namibian volcanic margin formed by continental rupture focussed over a relatively narrow rift zone. The transition to normal oceanic crust appears to be more gradual and is defined as transitional-normal oceanic crust boundary (TNOB).

In figure 3-6a a seismic section through the central Walvis Basin is presented (line ECL 8941); figure 3-6b below displays a detailed linedrawing of the section and the interpretation of five distinct seismo-stratigraphic zones. Zones 1 and 2 represent the postrift basin fill and are elaborately referred to in chapter 3. 6.

Corresponding to Planke et al. (2000) and Bauer et al. (2000), zone 4 (outer SDR wedge) is interpreted as shallow to deep marine flood and pillow basalts; zone 5 (inner SDR wedge) represents subaerial flood basalts with intercalated sediments; zone 3 may consist of shallow marine hyaloclastic flows and mounds (fig. 3-6b). The SDR sequences are related to intense magmatism during breakup and initial seafloor spreading.

SDR wedges often appear to be fault bounded (Planke & Eldholm, 1994; Eldholm et al., 1995). These features on the Namibian margin have therefore been controversially discussed. Clemson et al. (1999) related them to prerift halfgrabens of Karoo age;

Swart and Cartwright (2002) discussed them in terms of synrift halfgrabens with thick volcanic and clastic infill. The latter would afford enormous synrift subsidence which in turn is not easy to correlate with the volcanic nature of the margin as thermal uplift, at least in the early phases of margin evolution, should be expected. Additionally, the modelled v_p -structure of the SDRs makes major clastic contributions in the central Walvis Basin less probable.

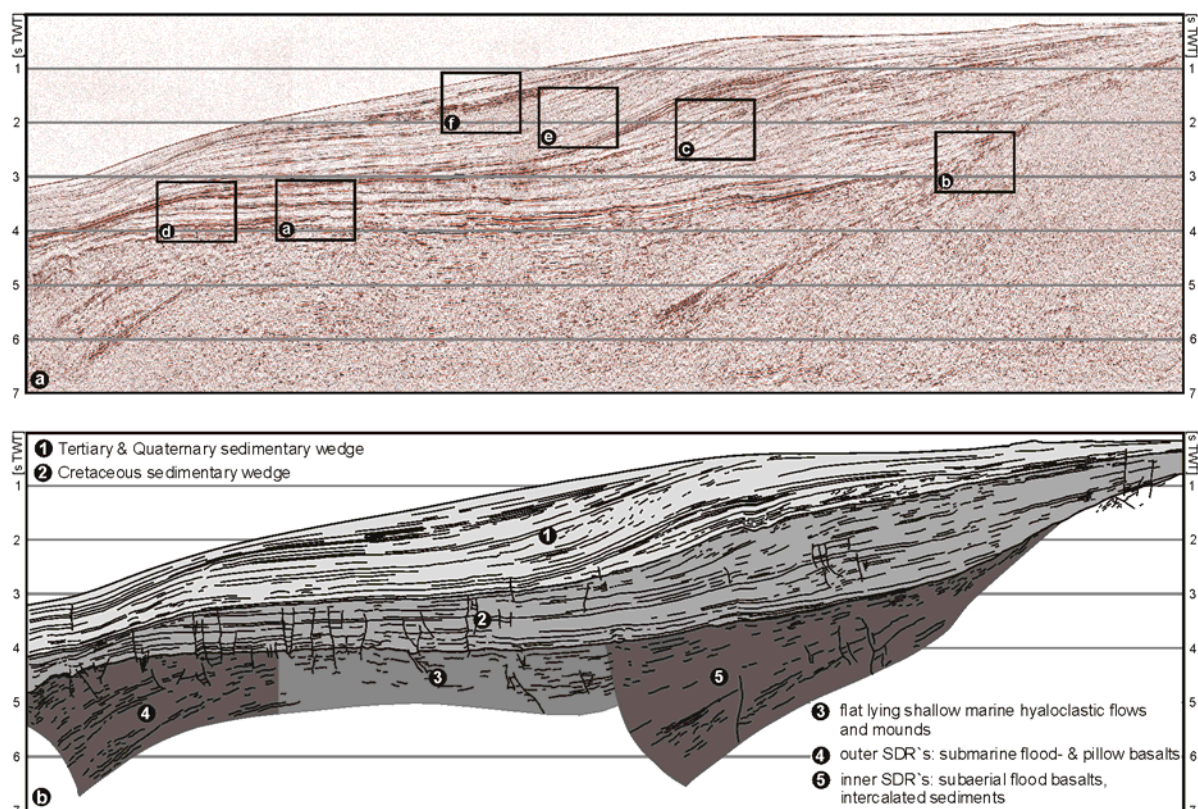


Fig. 3-6. Seismic section ECL 89-41 through the central Walvis Basin. (a) Seismic section down to 7s (TWT) showing the postrift succession in high resolution and significant, breakup-related seaward dipping reflectors; most of the basement is transparent or obscured by overlying strata; boxes labelled a – f indicate locations for detailed seismic interpretations examined in chapter 3.6.4 and figure 3-15. (b) Linedrawing of the section and interpretation of the main seismo-stratigraphic elements. See legend and text for discussion. See figure 1-1 & 4-2 for location of the seismic section.

Planke et al. (2000) established an emplacement model for the major extrusive facies related to volcanic margins on the basis of the extensive database of the Norwegian continental margin. SDR-emplacement models typically focus on the process of subaerial seafloor spreading. However, Planke et al. (2000) emphasise the importance of re-sedimentation processes, water-magma-interaction and tectonism.

The inner SDR-wedge corresponds to the magnetic anomaly G along large parts of the Namibian margin (Austin & Uchupi, 1982). Both features do not extend north of the Walvis Ridge. Bauer et al. (2000) attribute them to the COB; magnetic modelling

supports these interpretations. Schreckenberger (1997) showed that subaerial basalts intercalated with sediments are prone to acquisition of strong magnetic remanence comparable to that of “normal” ocean floor anomalies produced by pillow basalts. The lack of a similar anomaly related to the TNOB is therefore somewhat surprising. However, anomaly G appears to be an effect of the near surface geology and may not be caused by an “edge effect” related to deep crustal contrasts.

Bauer et al. (2000) tested their interpretation by calculating the gravity response of the density-converted crustal v_p -model and came to a very good agreement. The Namibian continental margin south of Walvis Bay is characterised by a distinct positive gravity anomaly about 150km offshore which is followed by a less pronounced positive anomaly farther offshore. They are interpreted as edge effects due to juxtaposition of the wide igneous ocean-continent transition zone with normal oceanic and normal continental crust, respectively, and are thus correlated with the COB and TNOB (chapter 3.4; fig. 3-7).

3. 4 Gravity structure of the margin

Rifted continental margins around the Atlantic Ocean are generally characterised by a positive free-air gravity anomaly (“edge effect”) associated with the juxtaposition of oceanic and continental crust. Usually this gravity high occurs over the shelf break and it is accompanied by a gravity low over the continental slope. Since free-air gravity is very sensitive to the complexity of the continent-ocean transition, the idealised edge effect is often disturbed in nature by sedimentation and magmatism modifying the initial crustal structure (Watts & Fairhead, 1999).

The west African margins seem to be segmented in terms of their gravity signature. Offshore Angola and South Africa, a typical “high-low pair” is developed; the Namibian margin appears to be much more complex. South of 22°S a broad gravity high is developed with a distinct positive peak on its landward edge and a less pronounced peak on its seaward edge; it is displaced landward of the maximum sediment thickness (fig. 3-7, inset). The two branches merge to a single gravity high between 22°S and the Walvis Ridge at c. 19°S (Sandwell & Smith, 1997; fig. 3-7). The Namibian margin lacks a distinct offshore gravity low, which is typical for other underplated margins like the Hatton Bank west of the British isles.

Stewart et al. (2000) utilised 3D subsidence analysis and gravity modelling to explain these features. Thereby, the observed gravity signature is compared with the combined gravity effects of the rift crustal structure (derived from determining the crustal stretching factor β from isolation of the tectonic subsidence/ “backstripping”), sediment thickness (derived from extensive seismic data) and magmatic underplating

to put constraints on the mechanical properties of the lithosphere. Lithospheric response to loading is modelled by an elastic plate model (Karner & Watts, 1982). Figure 3-8 summarises the results of forward gravity modelling in the central Walvis Basin (see fig. 3-7 for location). An unusually high elastic thickness of the lithosphere of $T_e=25$ km throughout modelling best fits the observed data (Stewart et al., 2000).

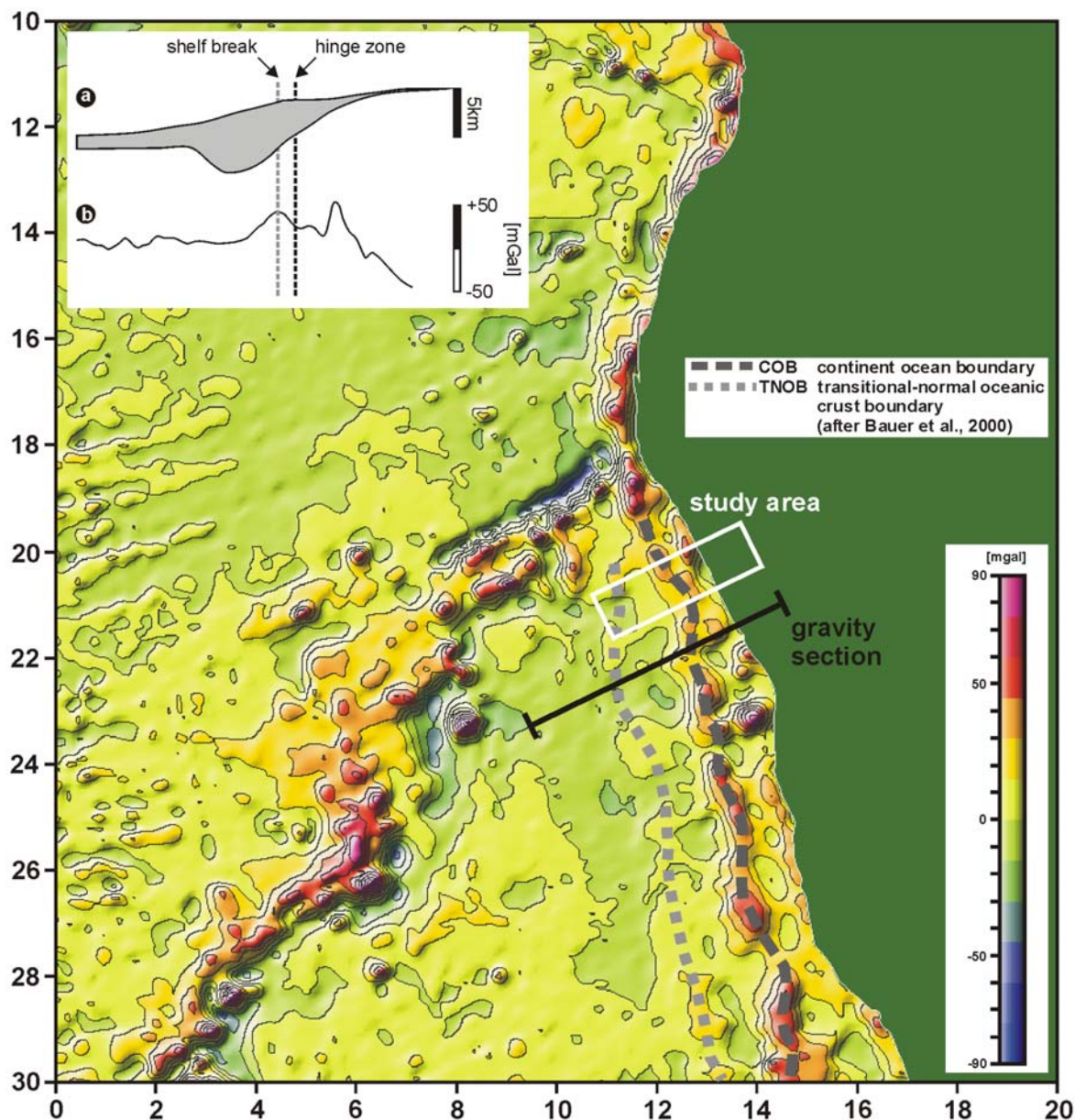
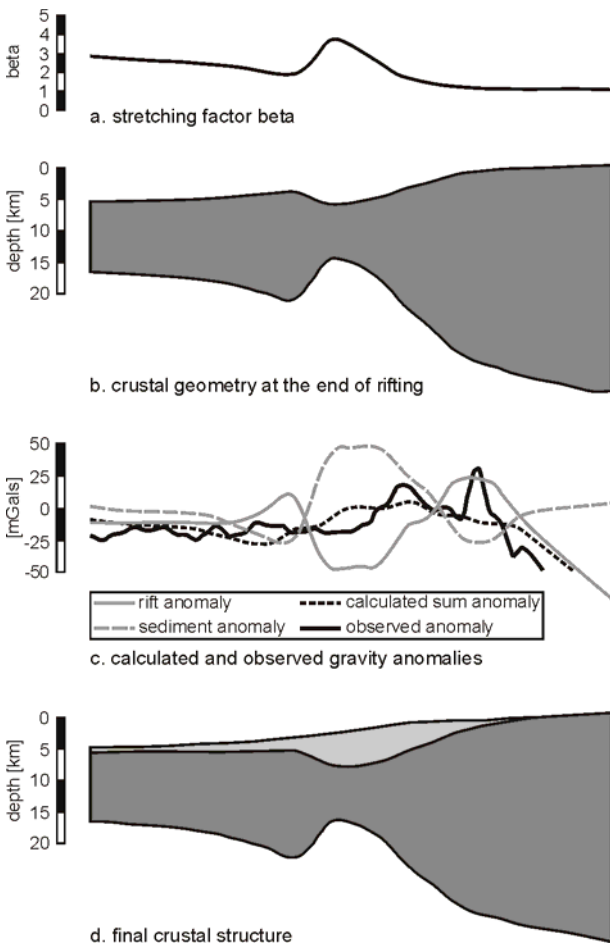


Fig. 3-7. Free-air gravity anomaly map of the Walvis Ridge area offshore NW-Namibia/ SW-Angola. The inset shows a 2D gravity section as indicated by the black line. (a) Thickness of the postrift sedimentary wedge derived from depth-converted seismic sections. (b) 2D gravity profile over the Namibian continental margin showing a pronounced offset of the gravity high landward of the sediment-depocentre (modified from Stewart et al., 2000). A significant coast-parallel gravity high is followed seaward by a less distinct high (grey dashed lines). These are correlated with the COB and TNOB, respectively, by Bauer et al. (2000).

Flexural strength of extended lithosphere is controversially discussed. On the one hand, surface and subsurface magmatism during rifting as well as synrift faulting fundamentally weakens the lithosphere (Watts, 1988). The observation of long-lived uplift of the “old” continental margin around southern Africa (“Great Escarpment”), on the other hand, supports the idea that rifted margins are able to maintain significant flexural strength.

Figure 3-8c indicates that the observed gravity low related to stretched/ rifted crust (“hinge zone”) is flanked by two gravity highs. This is partly compensated by the sediment anomaly which is due to the replacement of water by denser sediment. Assuming magmatic underplating additionally improves the model in terms of the amplitude of the gravity high. However, all gravity models fail to fully explain the observed anomalies, especially in the Walvis Basin off NW-Namibia (Stewart et al., 2000); the exact position of shelf gravity high and the absence of a distinct seaward low remain unexplained.

Comparison of the modelled sum anomaly with the observed anomaly (black dashed line and black solid line in figure 3-8c) illustrates that there remain significant residual anomalies. According to Stewart et al. (2000), these could be reduced by either low density pre-rift basins in the hinge zone south of 22°S, by high-density volcanics in the eastern pinch-out of the synrift succession (MS20/30 of Bagguley & Prosser, 1999; SDR-wedges of Gladchenko et al., 1997 & Bauer et al., 2000), or by lateral sediment density variations across the shelf.



the eastern pinch-out of the synrift succession (MS20/30 of Bagguley & Prosser, 1999; SDR-wedges of Gladchenko et al., 1997 & Bauer et al., 2000), or by lateral sediment density variations across the shelf.

Fig. 3-8. Backstripping and crustal scale gravity modelling for a section through the central Walvis Basin. A high elastic thickness of $T_e = 25\text{km}$ is assumed throughout rifting, backstripping, and modelling. (a) Stretching factor beta obtained from backstripping the sediment megasequences. (b) Rift geometry at the end of rifting. (c) Comparison of modelled gravity anomalies with observed gravity anomaly (see legend for details). Large residual anomalies remain between the modelled sum anomaly and the observed gravity anomaly. (d) Final modelled margin geometry. Modified from Stewart et al. (2000).

Integral part of gravity modelling is 3D backstripping of the sediments on the basis of a depth-converted seismic grid which allowed the reconstruction of a significant depocentre shift in the Walvis Basin (Stewart et al., 2000; fig. 3-9). The basement to Turonian succession (sequences 1 and 2 in figure 3-9a) is much thicker in the Orange Basin than in the Walvis Basin. In contrast, the Late Cretaceous L to seafloor succession (sequences 3 and 4 in figure 3-9a) is much thicker in the Walvis Basin than in the south, reflecting a S-N-oriented depocentre shift along strike of the Namibian continental margin. Within the Walvis Basin, however, an initial landward shift of the subsidence maximum is observed before the main depocentre appears to migrate oceanward in the Late Cretaceous (fig. 3-9b-f). This corresponds strongly to the evolution of the shelf edge as observed in detailed seismic studies in the central Walvis Basin outlined in chapter 3.6.

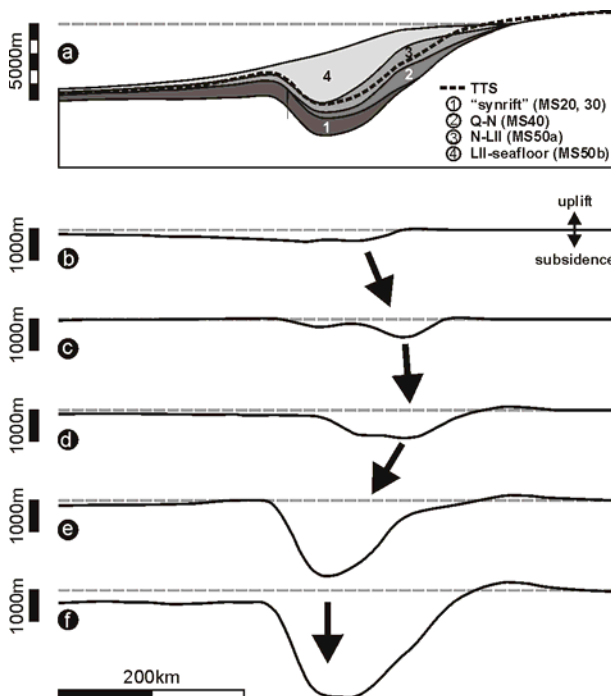


Fig. 3-9. 2D section through a 3D backstripped model of the central Walvis Basin. (a) The megasequences 1-4 represent the synrift, early drift, late Cretaceous, and Tertiary/ Quaternary succession, respectively (see legend for corresponding major seismic horizons). Total tectonic (unloaded) subsidence (TTS) is indicated by the black dashed line. (b)-(e) Individual backstrips for the units 1-4. (f) Cumulative backstrip without sediment and water loading. Black arrows indicate lateral variations of subsidence. The main depocentres to shift landwards before migrating oceanward in the Tertiary. This corresponds to the evolution of the shelf edge. Modified from Stewart et al. (2000).

3. 5 Offshore basins and their seismic features

The Namibian offshore region was imaged by more than 14300km of high resolution seismic data on behalf of the Namibian National Oil Company *NAMCOR* in 1989 and 1991. These data enabled not only the assessment of the deep structure of the margin (chapter 3.3) but also the evaluation of the temporal relationship between rifting and volcanism as well as the seismic character of the passive margin sediments. According to Light et al. (1992, 1993), the Namibian passive continental margin can be subdivided along strike into four depositional centres as illustrated in figure 6-1 (chapter 6.1). The Namibe Basin is located north of the Walvis Ridge and extends into Angolan waters. The Walvis Basin, Lüderitz Basin, and Orange Basin,

respectively, are arranged south of the Walvis Ridge. However, as the subdivision of the latter two is rather arbitrary, some authors use the term “Orange Basin” to describe the entire southern part of the Namibian offshore area (e.g. Dingle, 1992/93).

These basins and the South Atlantic in general owe their formation to the breakup of Westgondwana in the Late Jurassic and Early Cretaceous. The onset of continental extension is not well defined but may have started as early as 160Ma ago. The loci of rifting as well as the detailed structural inventory were strongly controlled by pre-existing weaknesses inherited from the preceding Pan-African geodynamic evolution (e.g. Lawrence, 1989; Porada, 1989; Stanistreet et al., 1991; Tankard et al., 1982). In particular, thrusts became reactivated as transfer faults (Stollhofen, 1999). The Walvis Basin, for example, is bounded to the south by the Waterberg-Omaruru fault zone which represents a reactivated basement structure (Stollhofen, 1999); the Lüderitz Basin is internally complexly structured by the Lüderitz Arch (Light et al., 1992; see fig. 1-1). However, the subdivision of the Namibian continental margin into depositional centres along strike is primarily based on the subsidence/ sediment thickness distribution of the Cretaceous postrift succession.

On the basis of abundant geophysical data, Light et al. (1992) distinguished from the coastline to the west five general structural elements of the margin. These include (a) an Eastern Graben Province on the shelf-platform; (b) a Medial Hinge Line where rift sequences are truncated and which can be traced with good confidence along the entire Namibian margin because it corresponds to a distinct gravity anomaly (chapter 3.4 & fig. 3-7); (c) a Central Half Graben which is bounded to the west by (d) a Marginal Basement Ridge. A major postrift sedimentary wedge due to thermal subsidence covers these pre- and synrift features of the margin. The most prominent structural elements within the study area are illustrated by fig. 3-6, 3-13, and 4-13a. Major depositional sequences were identified and seismically mapped by Light et al. (1992, 1993) on the basis of Gerrard & Smith (1982). The Kudu wells offshore southern Namibia and well A-J1 in the Orange Basin offshore South Africa provided constraints for their interpretation. Several exploration wells in the Lüderitz Basin and Walvis Basin have not been drilled at that time. The extrapolation of interpreted seismic horizons northward to the Walvis Ridge should therefore be well considered if the model of a stepwise northward prograding oceanic onset is accepted (see Stollhofen, 1999 & chapter 3.2).

Five main tectono-stratigraphic megasequences (MS) bounded by seismic marker horizons (given in parenthesis) were defined by Light et al. (1992; tab. 3-1): (1) Prerift (T, top horizon), (2) Synrift I (T – R), (3) Synrift II (R – Q), (4) Transitional (Q – P) and, (5) Thermal Sag (P – seafloor).

Tertiary	Neog.	Thermal Sag	P
	Paleoc.		
Cretaceous	C	Transitional	Q
	L		
		Synrift II	R
		Synrift I	
	Jurassic	U	T
M			
L			
Triassic		Prerift	
Permian	U	Prerift	
	L		

Horizon T is the top Prerift and base Synrift I marker and is interpreted to be a Late Jurassic angular unconformity. Stollhofen (1999), however, suggests a Lower to Upper Triassic age for horizon T (Beaufort/ Stromberg Group) on the basis of detailed stratigraphic work in the Namibian onshore area. Additionally, he proposes to avoid the term “prerift” because these sequences are more related to a phase of early intra-continental rifting than to a precursor of the final oceanic onset of the South Atlantic in the Early Cretaceous.

Horizon R is leading over to the Synrift II megasequence which is preferentially developed in the northern part of the Namibian margin. R has been given a Valanginian age by Light et al. (1992) and corresponds to the unconformity between the Triassic-Jurassic and the Cretaceous megasequence of Stollhofen (1999) onshore (see chapter 2). Horizon Q (Hauterivian; McLachlan & McMillan, 1979) represents the base of a transitional sequence that marks the end of synrift fault activity in the southern offshore area. Based on the stratigraphic work of Wickens & McLachlan (1990) and McMillan (1990), Stollhofen (1999) suggests that Q might define the onset of the Barremian marine transgression which affected the entire Namibian continental margin north to Walvis Ridge. Considering that the oldest seafloor anomaly offshore NW-Namibia, M4, is also Barremian in age (c. 126 Ma, see chapter 3. 2), horizon Q is interpreted to be the “breakup unconformity” (e.g. Braun & Beaumont, 1989) between the Salado-Orange Transform and the Walvis Ridge (fig 3-2, 3-4). Seismic horizon P, however, represents the breakup unconformity north of the Walvis Ridge (Light et al., 1992). P initiates the postrift/ thermal sag phase in the northern Namibian offshore area and is suggested to be mid-Aptian in age (McMillan, 1990).

Tab. 3-1. Major tectono-stratigraphic sequences and regional seismic horizons of the Namibian continental margin. After Light et al., 1992.

Several major unconformities are identifiable within the thermal sag megasequence. Among those the Turonian horizon N (labelled All by Austin & Uchupi, 1982) which is related to a global sea level highstand (Haq et al., 1987; see fig. 3-12), and the base Tertiary horizon L (labelled D by Austin & Uchupi, 1982) are prominent; both occur on the top of prograding wedges with overlying beds downlapping in the west and onlapping in the east, respectively. In the central Walvis Basin which is examined in more detail in chapter 3.6, L is suggested to display a base Eocene unconformity. Generally, the interpretations of Light et al. (1992, 1993), largely based on geophysical data from the southern Namibian margin, are to a considerable degree consistent with the observations made in the central Walvis Basin offshore NW-Namibia (fig. 3-13).

Prerift MS (basement – T)

The prerift-megasequence consists essentially of Karoo deposits and correlates largely with the Permo-Carboniferous MS of Stollhofen (1999). Due to poor seismic character and the lack of well control offshore Namibia, this interval is difficult to interpret. Most probably, the reflectors display N-S-trending arid continental deposits including subaerial lavas to the west of the Medial Hinge Line. Deltaic and shallow marine systems, possibly equivalent to the deltaic Nossob and Auob Members preserved onshore, may have formed in the Central Half Graben.

Synrift I MS (T – R)

This wedge-shaped sequence thickens to the west and pinches out at the Medial Hinge Line in the east. Again, there is no well control offshore Namibia. To the west of the Hinge Line there may be alluvial fans feeding westward into fluvial wadi-systems and shallow marine sequences. There are indicators of aeolian dune sands that may have formed by southwesterly winds that prevailed in the Mesozoic (Martin, 1965). In the Central Graben area of the Lüderitz subbasin a shallow marine sand-shale facies may have developed, bordered by fluvial and shoreline clastics.

Synrift II MS (R – Q)

Intense volcanism related to the Tristan da Cunha mantle plume is associated with this interval which can therefore be ascribed to an active rifting mode. The onshore equivalents of these volcanics are represented by the Etendeka Group flood basalts; basal intercalation with aeolian deposits (Jerram et al., 1999) indicates arid climatic conditions with westerly paleowinds (Martin, 1965).

In the Central Graben of the Orange- and Lüderitz Basins no prominent shelf break seems to have developed. The basin fill is interpreted to consist of moderate energy fluvial sands and shales, passing distally into braid plain sands and lower energy lacustrine siltstones and shales with patches of aeolian dunes displaying an intracontinental basin environment.

Seismic facies in the Walvis Basin to the north of the Namibian margin is much more distinct. Rapid westward and northward thickening of the sequence is indicated due to low to moderate angle aggradational progradation and rapid deposition of sands, silts and shales. A zone of listric faulting to the west observed by Light et al. (1992) might be related to the formation of seaward dipping reflectors in this volcanic-dominated interval as discussed by Bauer et al. (2000), Gladchenko et al. (1997) and Planke et al. (2000) and as outlined in chapter 3.3 (fig. 3-6).

Transitional MS (Q – P)

Initial effects of thermal sag following the end of rifting and first indicators of a developing shelf break are documented within the transitional megasequence. For most of the Q – P interval the Kudu boreholes provide well control (e.g. McMillan, 1990). Basalts and aeolian to fluvial sands grading into shallow marine sands, shelly sandstones, lagoonal shales, deeper marine siltstones, and sapropelic shales on top indicate the Aptian major marine transgression culminating in a global sea level highstand around 116Ma (Haq et al., 1987; fig. 3-12). A mid-Aptian stratigraphic break (horizon P) terminates this interval.

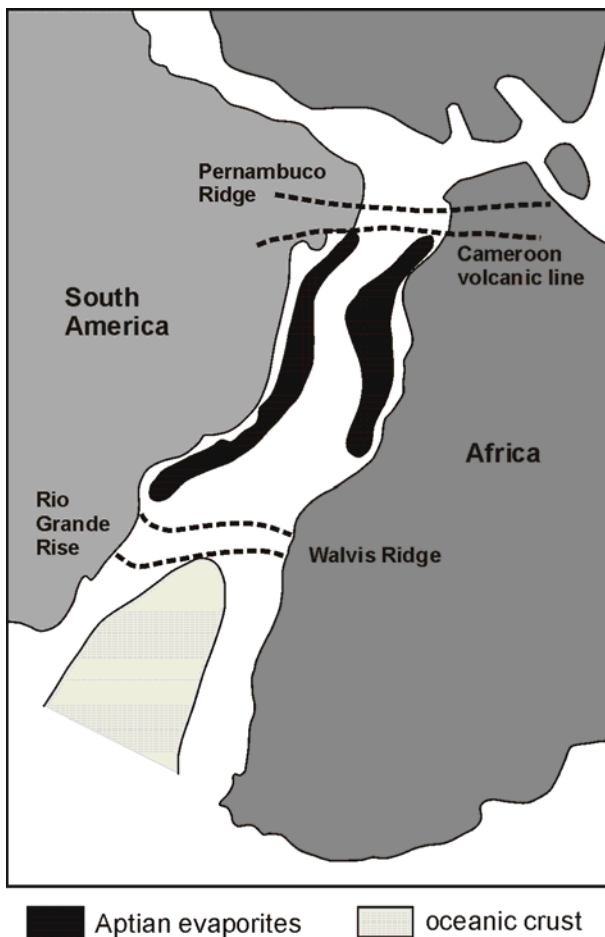
The Lower Aptian organic-rich interval dated by McMillan (1990) on the basis of foraminiferal biostratigraphy is commonly regarded as the oil-prone to wet gas-prone marine source rock for the hydrocarbon shows in the Kudu wells (Davies & van der Spuy, 1990). The stratigraphic position of the Kudu source rocks, however, has been doubted by Schmidt et al. (2002) on the basis of geochemical data (see chapter 6).

Dingle (1992/93) suggests that oceanic isolation during the early phases of continental separation resulted in a period of anoxic marine sedimentation until the Late Aptian. Stein et al. (1989), for example, performed detailed organic geochemical investigations of the amount and type of organic matter in Cretaceous black shales from the Atlantic Ocean. The authors assess the relative importance of terrigenous supply of organic matter and oceanic productivity, as well as the preservation potential of anoxic deep water conditions and rapid burial by turbidites.

Shallow water connections across the Walvis Ridge barrier have been established in Late Cenomanian/ Early Turonian times. Hu et al. (1988), however, suggest on the basis of geochemical data that the Walvis Ridge–Rio Grande Rise acted as a significant divide for oceanic circulation even until the Paleocene. Zimmerman et al.

(1987) tested paleocirculation models of the early South Atlantic in terms of the preservation potential of organic matter in sapropelic sediments. They presume a generally dysoxic condition and restricted circulation for the warm saline bottom-water throughout the early and mid-Cretaceous. A mid-Cenomanian hiatus in the sedimentary record is related to a global sea level fall resulting in eustatic regression, erosion, and a more vigorous deep ocean circulation.

According to Zimmerman et al. (1987), the primary cause for this eustatic sea level fall is climatic cooling in the Cenomanian leading to an increased temperature gradient in the Wedell Basin that produces cool, oxygenated bottom waters penetrating northward into the South Atlantic. This “ventilation event” may have stimulated vertical mixing and diffusion. Almost coeval with that, southward migration of marine ostracods in the Early Cenomanian and/ or Turonian times is observed (Dingle, 1999), indicating the breakdown of the Walvis Ridge as a physical barrier to north-south migrations.



The west African basins and the eastern South American basins to the north of the Rio Grande Rise-Walvis Ridge, however, are dominated by evaporitic deposits (e.g. Clifford, 1986) during Aptian times; the distribution of Aptian salt is bounded to the north by the Pernambuco Ridge and the Cameroon volcanic line, respectively (fig. 3-10).

Fig. 3-10. Aptian paleogeographic reconstruction of the South Atlantic. Control on the distribution of evaporites is exerted by the Rio Grande Rise-Walvis Ridge barrier and the Pernambuco Ridge-Cameroon volcanic line, respectively. Modified from Clifford (1986).

Thermal Sag MS (P – seafloor)

The oldest sequence that is purely related to thermal sag of the margin is represented by a progradational succession downlapping onto horizon P and being itself topped by the Turonian unconformity N (see fig. 3-13). Horizon N is a major transgression related to the global eustatic sea level highstand around 95 Ma (Haq et al., 1987; fig. 3-12). Based on seismic velocity interpretations, Bauer et al. (2000) interpret the succession from N to seafloor as proper open marine drift-sediments. Between the mid-Turonian (N) and the base Tertiary (L) a thick marine sequence developed. Especially in the Late Cretaceous rapid progradation of the shelf formed a distinct shelf break. Related to that, complex slump structures with listric head scarp structures, basal detachment planes and toe areas occur (Light et al., 1992; see chapter 3.6). The potential Maastrichtian reservoir sandstone of well 2012/13-1, examined in chapter 6.4.2, might be associated with such a gravity-driven turbidite.

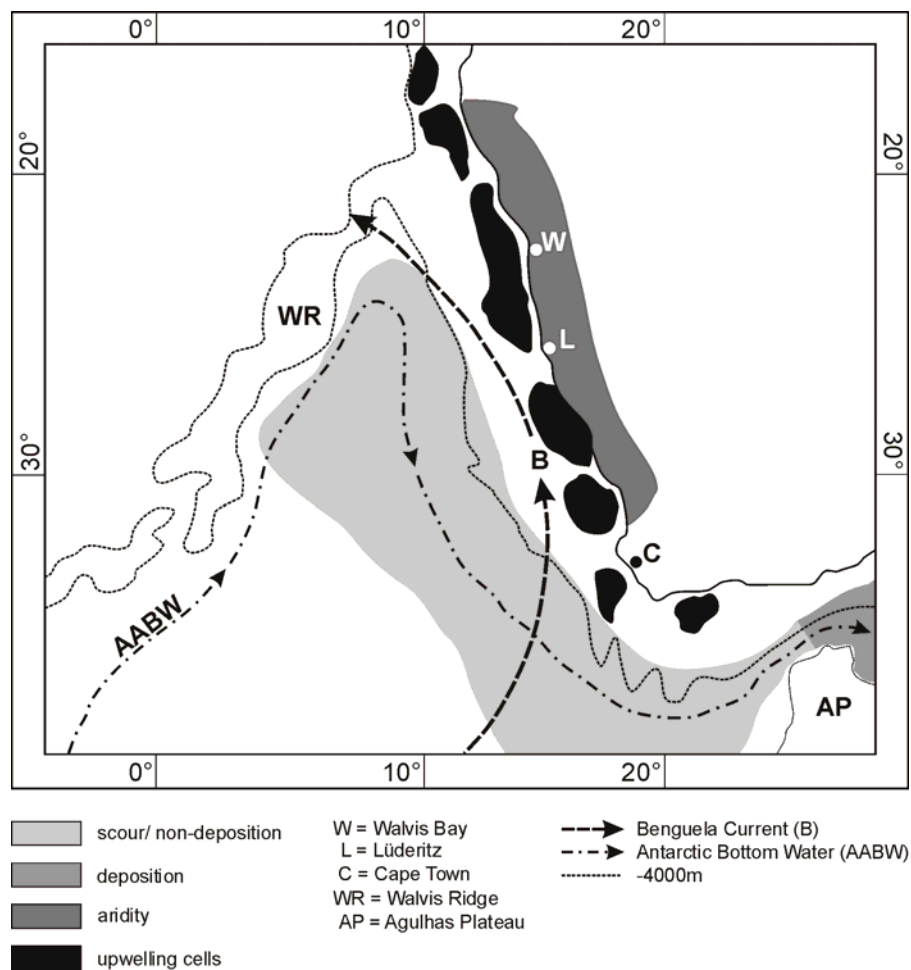


Fig. 3-11. Sedimentary regimes, oceanographic climate and current systems in the eastern South Atlantic during Miocene to Holocene times. Modified from Dingle (1992/93).

Tertiary and Quaternary sediments (L to seafloor) are generally thinner offshore Namibia than north of the Walvis Ridge. A low energy depositional environment is indicated by their mostly transparent seismic character. Few high amplitude and continuous reflectors might represent occasional limestone beds or erosional events due to coast-parallel marine currents. Bagguley & Prosser (1999) give examples of major slump scars rapidly healed by longshore currents; the contourite deposition offshore Namibia is largely restricted to the Upper Tertiary succession. This is in close temporal correspondence to the establishment of the anti-clockwise Benguela Current in the South Atlantic. Siesser (1980) and Dingle (1992/93) suggest that the Benguela system has become important in the Late Miocene, at the latest. Figure 3-11 illustrates sedimentary regimes, oceanographic climate and current systems in the eastern South Atlantic during Miocene to Holocene times.

3. 6 Detailed seismic and stratigraphic characterisation of the postrift strata

Detailed seismic stratigraphy based on section ECL8941 is combined with the interpretation of seismic marker horizons of known age to place constraints on the timing and geometric pattern of sedimentation in the central Walvis Basin (fig. 3-6 & 3-13). The seismic horizons Q, N, K, LII, and L are inferred from a compilation of literature (Gerrard and Smith, 1982; Light et al., 1992, 1993) and are calibrated with biostratigraphic age data from well 2012/13-1. Seismic horizon Q is of Hauterivian/Barremian age and marks the breakup unconformity south of the Walvis Ridge (Stollhofen, 1999). N is an unconformity related to the mid-Turonian eustatic sea level fall around 90Ma (Haq et al., 1987). The unconformity K is attributed to an intra Upper Campanian eustatic event around 75Ma. Horizon LII marks the base Tertiary (66,5Ma) whereas L is interpreted to resemble the Lower/ Middle Eocene boundary. All major stratigraphic events of well 2012/13-1 generally appear to be associated with prominent eustatic sea level falls as indicated by figure 3-12.

It should be kept in mind that the nomenclature of these major seismic sequences has been established on the basis of well data from the Orange Basin (e.g. McLachlan and McMillan, 1979; Gerrard and Smith, 1982; Wickens and McLachlan, 1990; Light et al., 1992, 1993). If the model of a stepwise northward prograding oceanic onset is accepted, seismic horizons might become slightly younger towards the Walvis Ridge (see Stollhofen, 1999).

In order to make the seismic interpretation and stratigraphic subdivision comparable to previous studies, the nomenclature for seismic marker horizons of Austin & Uchupi (1982) and Dingle (1992/93; "All" and "D") as well as the stratigraphy-based nomenclature of Holtar & Forsberg (2000; "W-Groups"; see fig. 6-3) is given for the particular sequences.

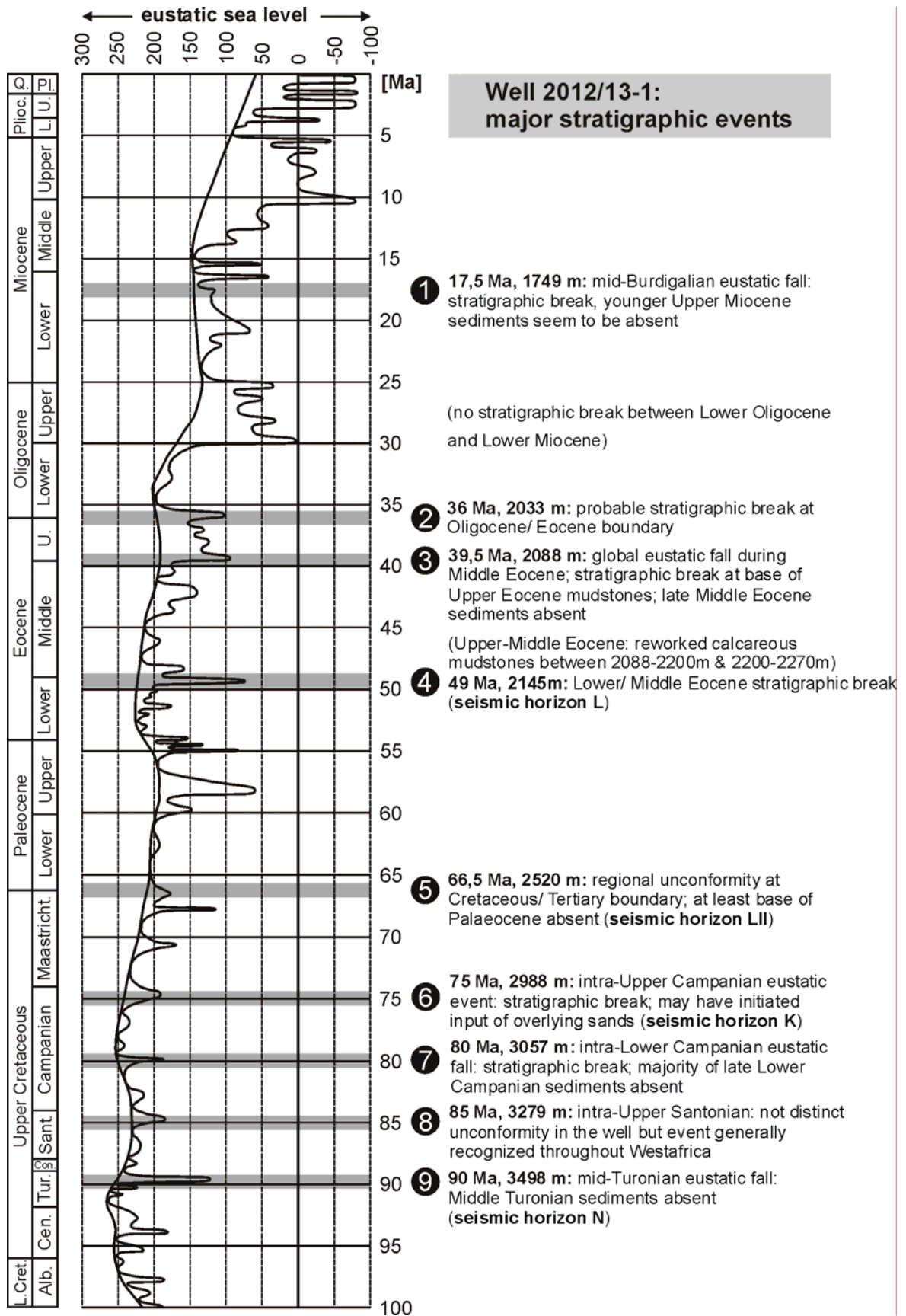
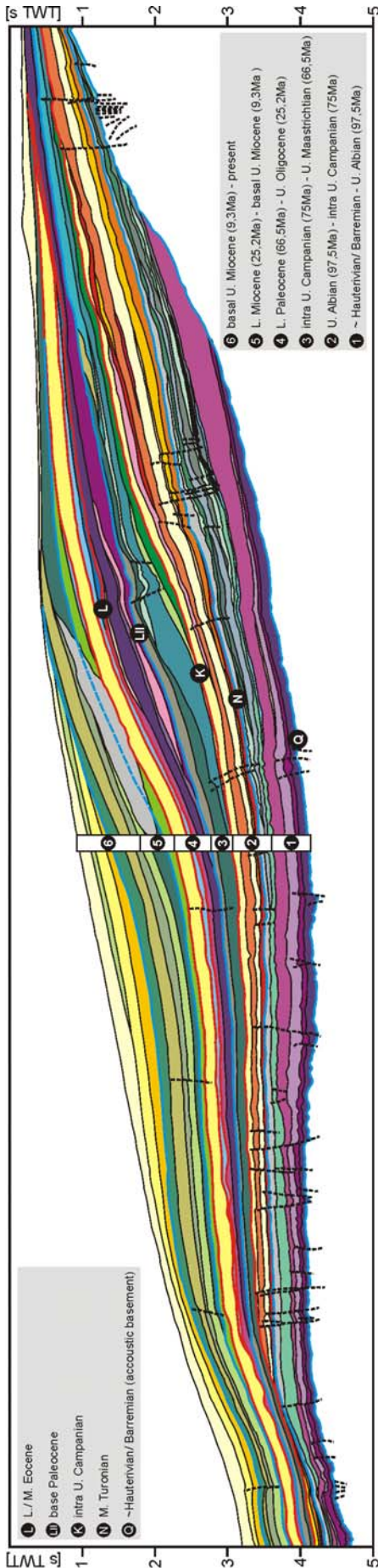


Fig. 3-12. Major stratigraphic events encountered in well 2012/13-1 related to eustatic sea level changes. Compiled from the Final Well Report of well 2012/13-1 (*Sasol Petroleum Namibia*) and Haq et al. (1987).



3. 6. 1 Q to N/ All (W1 to W4-1)

The Q-N-succession records the early drift stage and the initial effects of thermal sag. The lower part is dominated by very strong and continuous, mostly parallel but occasionally mounded reflectors that onlap onto the basement high in the east (fig. 3-14 & 3-15b). Continental beds (aeolian to fluvial sands, basalts?) and shallow marine clastics may have been deposited. In the northern Walvis Basin, shallow marine carbonates dominate this depositional phase (Holtar & Forsberg, 2000). Towards the North, the seismic reflectors remain subparallel and become more semi-continuous and significantly weaker. Micropalaeontological data indicate that deposition of deep marine shales has prevailed at least from the Late Albian.

3. 6. 2 N/ All to K (W4-2 to W5-4)

Between N and K subparallel continuous reflectors of high amplitude dominate in the slope area which appears to be condensed. First signs of an evolving shelf edge can be recognised closer to the coast. Reflectors are weaker and more semi-continuous there. Onlap onto the coast-parallel hinge line becomes successively displaced by progradational downlap (fig. 3-14).

Fig. 3-13. Detailed interpretation of marker horizons, seismic sequences, and syndimentary fault activity of the postrift succession in the central Walvis Basin derived from seismic section ECL 8941. See legend and text for discussion.

3. 6. 3 K to LII (W5-5 to W5-6)

The Upper Campanian to Maastrichtian section from K to LII is clearly dominated by the evolving shelf edge, probably initiated by the intra Upper Campanian stratigraphic event K at c. 75Ma. Downlapping and rapidly prograding wedges indicate high accumulation rates which is recognised in the onshore denudation history as well (Gallagher & Brown, 1999; Raab, 2001). Reflectors are generally semi-continuous and partly wavy in the shelf area; they become relatively transparent in the zones of most rapid progradation (fig. 3-15c). However, parallel and more continuous reflectors of high amplitude can be observed in the slope area. These may possibly be related to sand-rich, gravity-driven mass flows sourced from the upper shelf. The potential reservoir rock of Maastrichtian age which is examined in chapter 6.4.2 is interpreted to be of such origin.

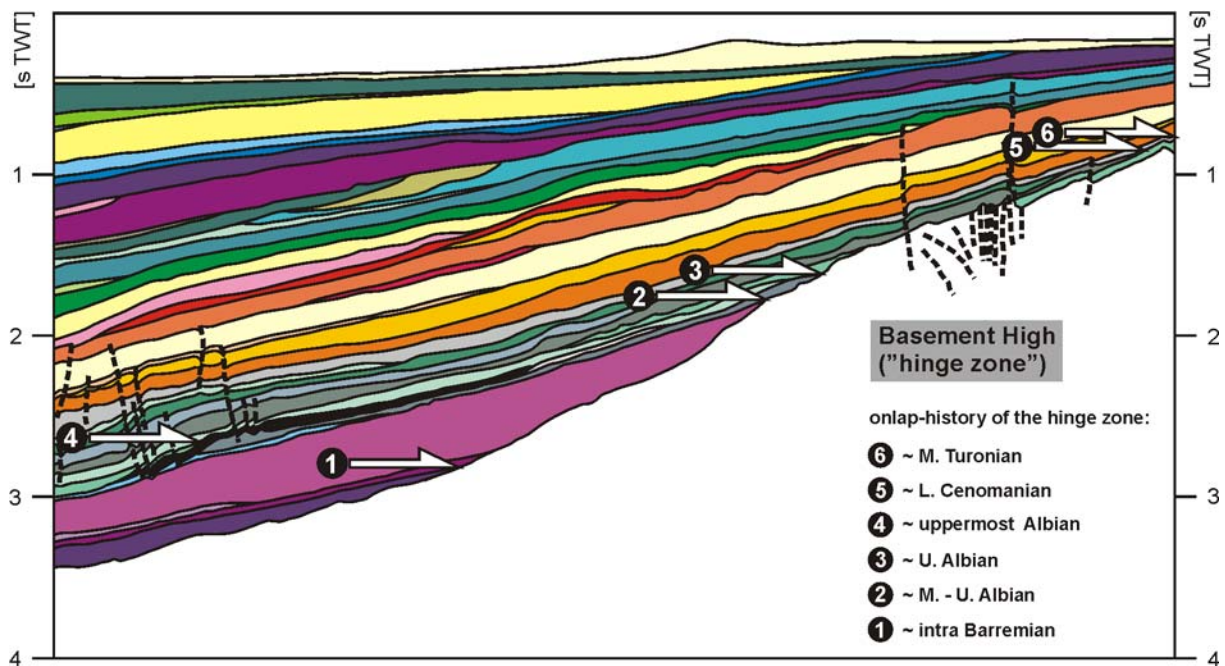


Fig. 3-14. Detailed section of the seismic sequence interpretation displaying the onlap history onto the eastern marginal basement high ("hinge zone"). Onlap starts as early as in the Barremian and is accomplished by mid-Turonian times.

3. 6. 4 LII to L/ D (W6-1 to W6-3)

The lower Tertiary succession from LII to L is characterised by further propagation of the shelf. Progradational downlap dominates on the shelf and slope followed by onlap onto the shelf in the uppermost part of the section. The seismic reflectors are generally semi-continuous and subparallel to wavy. They show a relatively high amplitude which may be due to occasional sandstones and siltstones that are observed in the overall shaly succession of well 2012/13-1. Holtar and Forsberg

(2000) interpreted carbonaceous reef-like features in the Lower Paleocene of well 1911/15-1 in the northern Walvis Basin (see chapter 6.4.3). However, the LII to L succession becomes very thin and wavy in the distal part of the slope indicating sediment starvation.

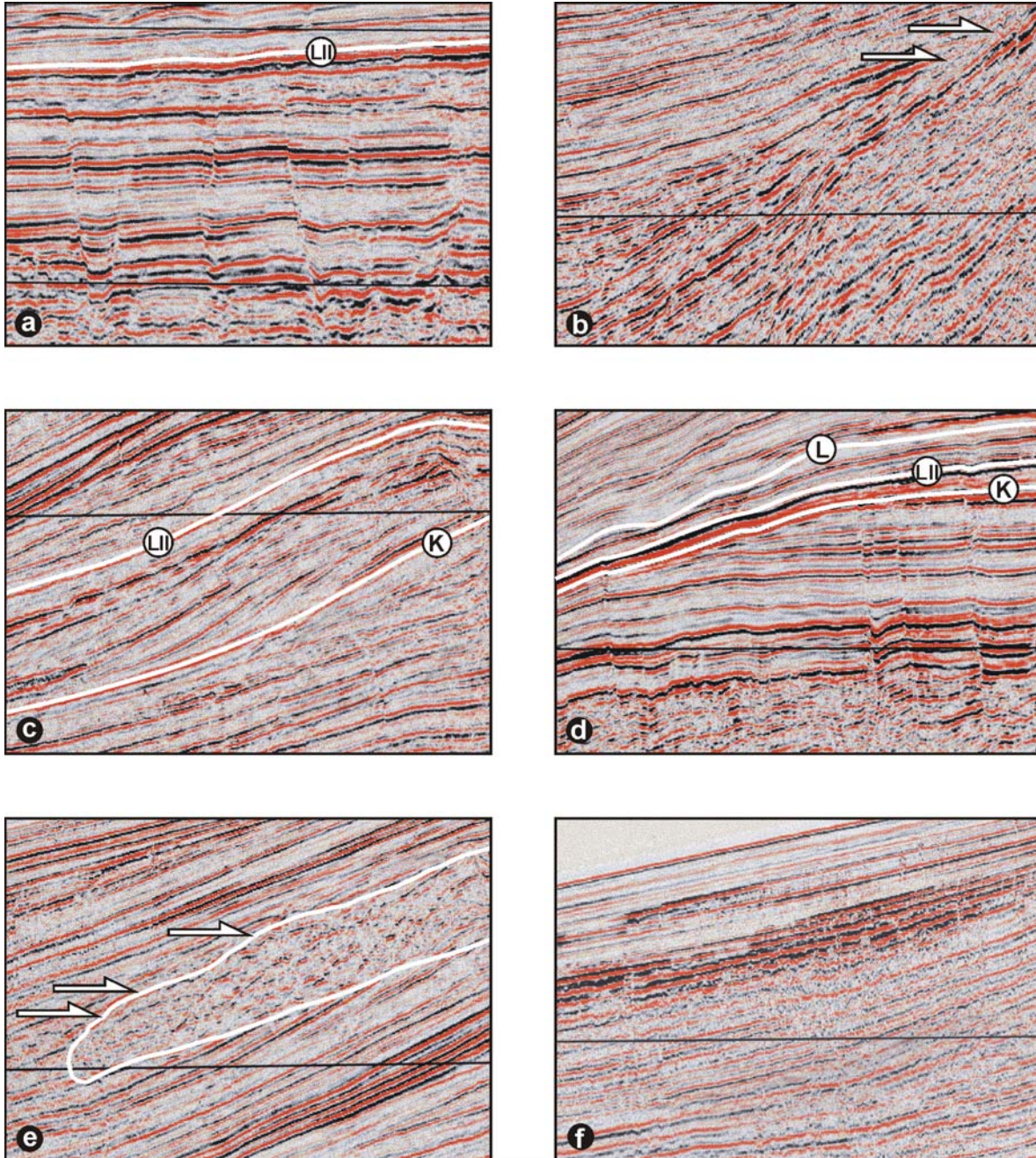


Fig. 3-15. Significant seismic features as indicated by the boxes in fig. 3-6a. (a) Late Cretaceous synsedimentary fault activity. (b) Late Albian onlap onto the eastern basement ridge. (c) Downlap and rapid shelf propagation in the Maastrichtian. (d) Significant truncation of older strata during the latest Cretaceous/ Early Paleocene. (e) Toe area of a major Miocene slump sourced from the shelf edge; it cuts deeply into older strata and is immediately onlapped again. (f) Lens-shaped infill of a Neogene depression on the outer slope by high-amplitude parallel reflectors which is possibly due to longshore current activity.

Erosion of the base Paleocene and reworking of older Cretaceous strata is common in the central and northern Walvis Basin (fig. 3-12). Massive truncation of older sections occurs in the area of a potential Marginal Basement Ridge (see fig. 4-13a; Light et al., 1993) during the Paleocene LII to L interval (fig. 3-15d).

3. 6. 5 L/ D to seafloor (W6-4 to W7)

Large parts of the L to seafloor succession unfortunately lack a detailed age control as no cuttings could be received from well 2012/13-1 due to heavy mud loss. The seismic character is generally transparent; occasional higher amplitudes may be due to limestone stringers in the overall shale-dominated interval (fig. 3-6a). The reflectors become more distinct on the distal slope over the outer SDR-wedge reflecting distal sediment starvation. Relatively young synsedimentary faulting occurs in this section. The shelf is clearly dominated by onlapping grading into aggradational downlapping over the shelf edge.

A major slump of probably Lower to Middle Miocene age sourced from the shelf edge is the most prominent seismic feature of this interval; it is gravitationally or seismically triggered and cuts deeply into older strata. The internal seismic reflector pattern is chaotic but immediate and distinct onlap onto the toe-area of the slump can be recognised (fig. 3-15e).

In the area of the Late Tertiary to Quaternary depocentre on the central slope a flat depression infilled by a condensed stack of strong parallel reflectors is noted (fig. 3-6a & 3-15f). As suggested before, this might be a feature related to the activity of coast-parallel currents with erosion as well as accumulation potential. Rapid scar infill by contourites deposited by longshore currents (fig. 3-11) has already been suggested by Bagguley & Prosser (1999) for the Walvis Basin.

3. 7 Subsidence history of the central Walvis Basin

3. 7. 1 Database and basic principles of backstripping

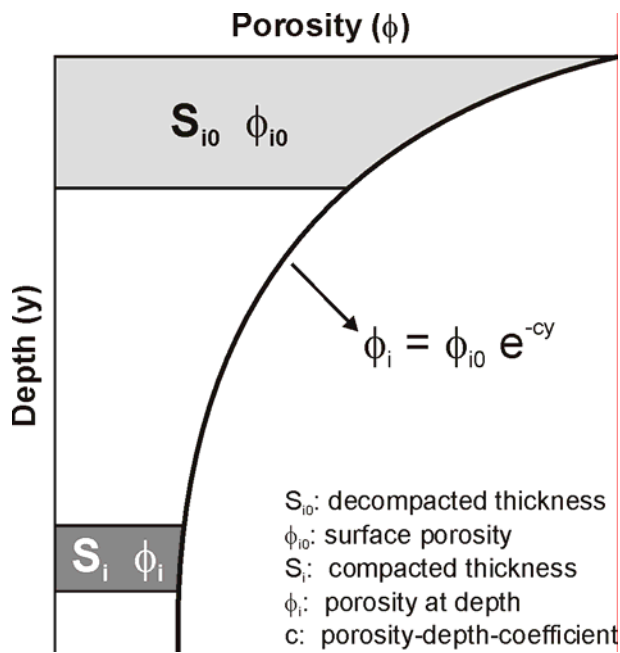
Extensional basins are subjected to subsidence. Stratigraphic thicknesses in basins resulting from this process are a product of cumulative compaction through time. Quantitative analysis of basin subsidence provides information on the basin forming mechanisms by comparison with theoretical (modelled) subsidence curves (e.g. Sclater & Christie, 1980). Primary target of quantitative geohistory analysis is the determination of the depth of basement as a function of time, termed total subsidence (or uplift, Y_{tot}). To infer from that curve the contribution of sediment and water loading (Y_{sed}) is a procedure termed “backstripping” (Watts et al., 1982) which can therefore be regarded as a progressive reversal of the depositional process. Backstripping results in the isolation of that part of the total basement subsidence which is due to tectonic processes or thermal contraction by cooling (Y_{tect}):

$$Y_{tect} = Y_{tot} - Y_{sed} \quad \text{eq. 3-1}$$

A basic assumption in 1D backstripping, as it is performed in this study, is that loads on the lithosphere are compensated isostatically by local/ Airy isostasy. Isostatic equilibrium is achieved separately in each vertical lithospheric column which is equivalent to assuming that the lithosphere has no elastic strength. Roberts et al. (1998), however, emphasise that the results of 1D Airy backstripping are very dependent on the quality of paleobathymetric estimates (fig. 3-18 & 3-20). Airy isostasy cannot acknowledge the effects of laterally varying loads; 1D Airy backstripping therefore tends to overestimate the degree of extension inferred for the basin.

Roberts et al. (1998) formulated 2D backstripping as a reverse postrift modelling process for which flexural isostasy of the lithosphere should be assumed in order to produce more satisfactory geological predictions.

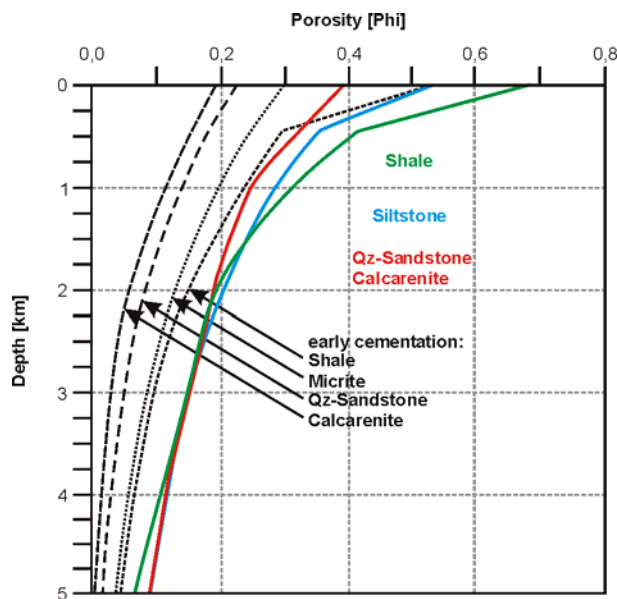
Subsidence analysis relies primarily on the decompaction of stratigraphic units to their correct thickness at a certain time in basin evolution. This “compaction correction” assumes that compaction is mechanical and non-reversible, all changes in porosity are due to compaction, and no early cementation or alteration of grains does affect the porosity. Overpressuring of trapped porefluids would hamper compaction as well. A general porosity-depth relationship is illustrated in figure 3-16. The essential factor, the porosity-depth-coefficient or compaction-coefficient c , is lithology-specific (see tab. 3-2) and is generally derived from empirical studies (e.g. Bond & Kominz, 1984; fig. 3-17).



Two further corrections need to be made in order to plot subsidence as a function of time related to a fixed datum such as present day sea level. Estimations of the variations of water depth through time (paleobathymetry) need to be considered. Additionally, long-term global fluctuations of sea level through time are inferred to assess the effect of water loading on the lithosphere through time. A concept of sea level changes, paleowater depth and total subsidence is displayed in figure 3-18.

Fig. 3-16. General porosity-/ thickness-depth relationship.

Allen & Allen (1990) suggest that a simple transferral from the short-term eustatic sea level curve of Haq et al. (1987; fig. 3-12) is not recommended; the correction for the widely accepted long-term variation of sea level, however, appears to be justified. Figure 3-19 schematically illustrates how a compacted sequence of sediment layers can be backstripped by progressive decompaction.



Primary data required for the 1D subsidence analysis of a basin fill are:

- thickness of each stratigraphic unit
- type of lithologies
- age of each stratigraphic unit
- estimation of paleowater depth
- eustatic sea level changes
- porosity-depth relationships

Fig. 3-17. Porosity-depth relationships specified for different lithologies and early cementation. Modified from Bond & Kominz (1984).

All of these informations are available for the central Walvis Basin, particularly in the form of data from well 2012/13-1 that were kindly provided by *NAMCOR*. Thicknesses and lithologies of the stratigraphic column of well 2012/13-1 are indicated by figure 6-3. Reliable estimations of paleowater depths as well as the ages of the particular stratigraphic units can be deduced from a high-resolution biostratigraphic study conducted by *Time Trax Ltd.* on behalf of *NAMCOR*.

Figure 3-20 illustrates the bandwidth of paleobathymetry estimations based on micropalaeontological analysis, primarily of foraminifera. In this study, the minimum estimation (Wd_{min} , blue curve) is favoured for several considerations; above all, because a too excessive rise in sea level observed since the Late Miocene is rather implausible.

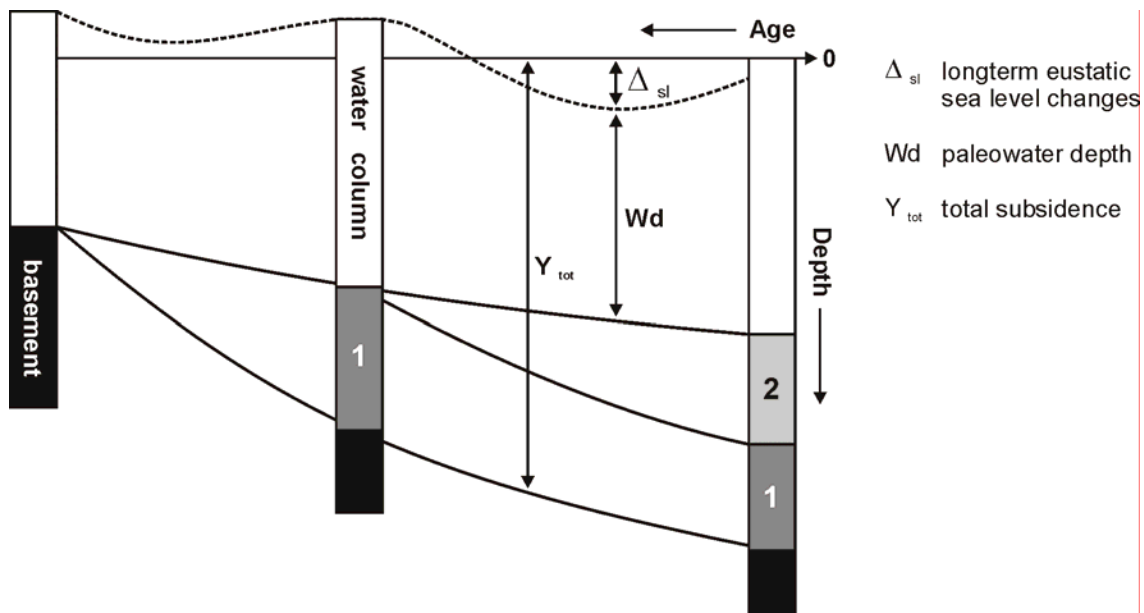


Fig. 3-18. Concept of water loading - longterm eustatic sea level changes combined with estimations of paleowater depth - and total subsidence.

Changes in global sea level are inferred from the long-term curve established by Haq et al. (1987) which is predominantly caused by changes mid-ocean ridge volume (fig. 3-12). Lithology-specific parameters such as compaction-coefficients, densities, and surface porosities are inferred from the extensive petrophysical database included in the *PetroMod2D* software package (see chapter 6).

A 20-layer 1D model comprising the entire postrift succession has been established in order to assess the subsidence history of the central Walvis Basin. The stratigraphic column of well 2012/13-1 has been subdivided into 18 layers for which detailed stratigraphical, lithological, and petrophysical information is available. Since this well reaches TD at 3712m in Late Albian shales, the early drift evolution of the

margin (layers A, B) has been inferred by analogy with well 1911/15-1 from the northern Walvis Basin (see fig. 6-3). The backstripped sedimentary column has thus been extrapolated to a total depth of 4712m resembling the begin of margin evolution about 130Ma ago.

A detailed listing of all parameters required for the backstripping procedure is given in table 3-2 below; this includes lithologies, thicknesses, depositional ages, surface porosities, densities, compaction-coefficients, paleowater depth estimations as well as long-term eustatic sea level changes, respectively.

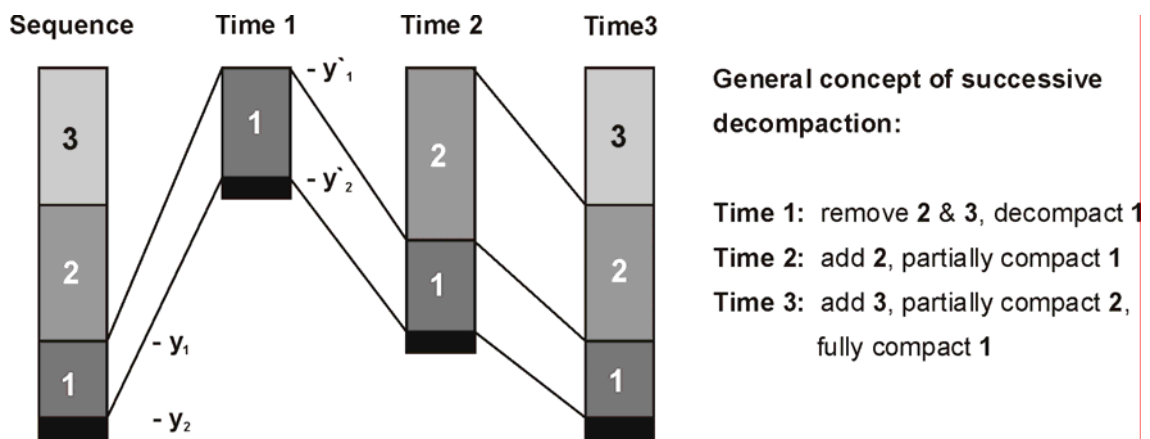


Fig. 3-19. Schematic diagram illustrating how a sequence of multiple sediment layers can be backstripped by successive decompaction.

The procedure of subsidence analysis as performed in this study refers to the methodology described in detail in chapter 8 of Allen & Allen (1990). The purpose of backstripping is to use the stratigraphic record to quantitatively estimate the depth that basement would have in the absence of sediment and water loading.

The general backstripping equation (eq. 3-2) allows the tectonic driving forces responsible for basin subsidence (or uplift, Y_{tect}) directly to be calculated from the database outlined above.

$$Y_{tect} = C \left[S_n \left(\frac{\rho_m - \bar{\rho}_{s_n}}{\rho_m - \rho_w} \right) - \Delta_{sl} \left(\frac{\rho_w}{\rho_m - \rho_w} \right) + (Wd - \Delta_{sl}) \right] \quad \text{eq. 3-2}$$

The general backstripping equation is composed of three terms which are:

a sediment loading term:
$$S_n \left(\frac{\rho_m - \bar{\rho}_s}{\rho_m - \rho_w} \right) \quad \text{eq. 3-3}$$

a sea level loading term:
$$\Delta_{sl} \left(\frac{\rho_w}{\rho_m - \rho_w} \right) \quad \text{eq. 3-4}$$

and a water depth term:
$$(Wd - \Delta_{sl}). \quad \text{eq. 3-5}$$

Since backstripping attempts to correct the stratigraphic record for the effects of loading in the past, thickness and bulk density of the sedimentary column as well as the porosity of a sediment layer i at its current depth at time n have to be corrected for the effects of post-depositional compaction. Progressive decompaction of the sedimentary column through time is the most fundamental process in subsidence analysis; all stratigraphic units in a sequence need to be restored for each time step by decompacting the younger units and successively compact the older ones (fig. 3-19).

The average porosity of a sediment layer i at its current depth is given by equation 3-6:

$$\phi_i = \frac{\phi_{i0}}{c} \frac{e^{-cy^1} - e^{-cy^2}}{y^2 - y^1} \quad \text{eq. 3-6}$$

Backstripping involves the successive unloading of decompacted layers. Therefore, not only the current thickness but also an estimate of its decompacted density is required. The bulk density of the entire sedimentary column consisting of i layers at a distinct time step n is given by equation 3-7:

$$\bar{\rho}_{s_n} = \sum \left[\frac{\phi_i \rho_w + (1 - \phi_i) \rho_{Si}}{S_n} \right] y^1 \quad \text{eq. 3-7}$$

The general decompaction equation formulated in equation 3-8 represents mathematically the exercise of sliding a sediment layer up the exponential porosity-depth curve as illustrated in the figures 3-16 & 3-17. Its calculation requires a circular reference (y^2) which can be solved by numerical iteration; if performed in an Excel-spreadsheet, it is fundamental to define the maximum number of iteration steps (e.g. 100) in the menu bar in advance.

$$y^2 = y_2 - y_1 - \frac{\phi_0}{c} e^{-cy^1} - e^{-cy^2} + \frac{\phi_0}{c} e^{-cy^1} - e^{-cy^2} + y^1 \quad \text{eq. 3-8}$$

The parameters that were utilised in the equations 3-2 to 3-8 are listed below:

Y_{tect}	tectonic (thermal) subsidence
C	degree of local (Airy) vs. regional (flexural) isostatic compensation (here: $C = 1 = 100\%$ local isostasy)
S_n	total thickness of the sedimentary column corrected for compaction at time step n
ρ_{Si}	sediment grain density of layer i
$\bar{\rho}_{s_n}$	bulk density of the entire sedimentary column at time step n
ρ_m	mantle density (3300 kg/m^3)
ρ_w	water density (1030 kg/m^3)
Wd	paleowater depth
Δ_{sl}	longterm eustatic sea level change
y_1, y_2	top & base of compacted layer i
y'_1, y'_2	top & base of decompacted layer i
C	porosity-depth-coefficient
ϕ_{i0}	decompacted surface porosity of layer i
ϕ_i	average porosity of compacted layer i

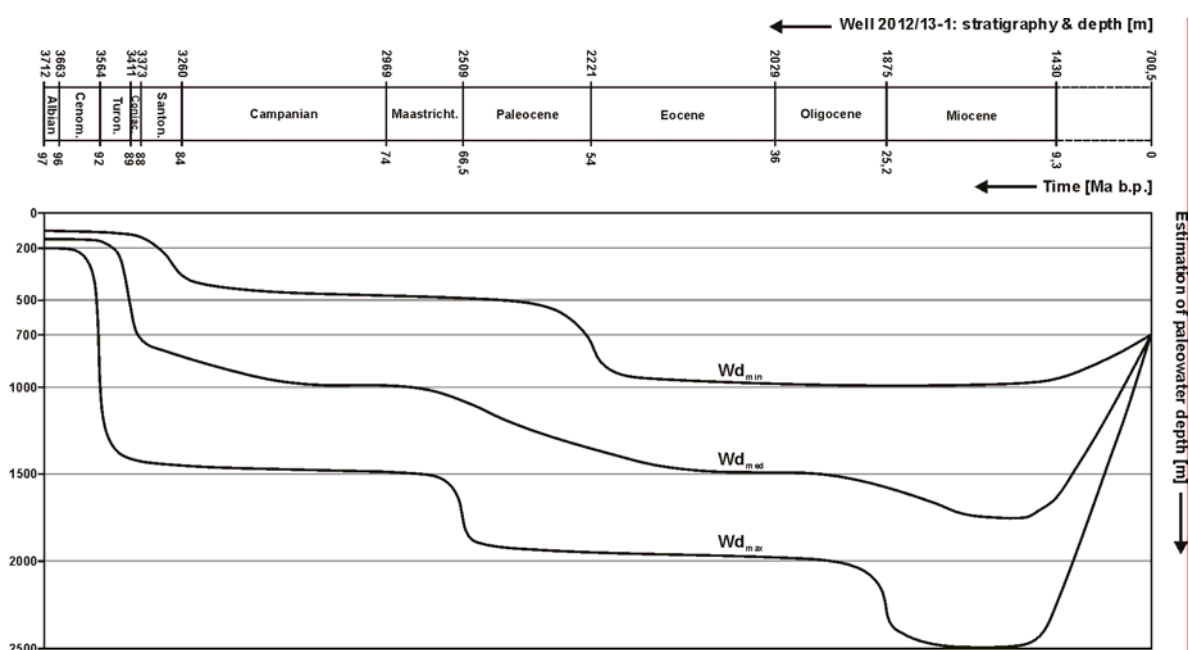


Fig. 3-20. Bandwidth of paleobathymetry estimations based on a high-resolution biostratigraphic study of well 2012/13-1 conducted by *Time Trax Ltd.* on behalf of *NAMCOR*.

Specific parameters from the postrift succession of the central Walvis Basin that were incorporated into the geohistory analysis based on the methodology described above are listed in table 3-2.

Subsidence analysis - parameter listing

layer	lithology	y_1 [m]*	y_2 [m]*	deposition age [Ma] from to	ϕ_{10}	ρ_{st} [kg/m ³]	c [km ⁻¹]	Wd_{min} [m]	Wd_{med} [m]	Wd_{max} [m]	Δ_{sl} [m]
18	Shale, carb.	700,5	920	5,0 0,0	0,62	2655	0,51	785	1000	1200	75
17	Shale, carb.	920	1430	9,3 5,0	0,62	2655	0,51	930	1520	2045	110
16	Shale	1430	1749	16,0 9,3	0,65	2680	0,51	985	1755	2490	140
15	Shale	1749	1875	25,2 16,0	0,65	2680	0,51	995	1640	2460	140
14	Shale	1875	2029	36,0 25,2	0,65	2680	0,51	987	1495	1985	175
13	Shale, carb.	2029	2221	53,6 36,0	0,62	2655	0,51	950	1435	1955	215
12	Shale, silty	2221	2509,5	65,0 53,6	0,62	2677	0,45	492	1115	1895	190
11	Shale, silty	2509,5	2520	65,2 65,0	0,62	2677	0,45	477	1000	1495	205
10	Sandstone, shaly	2520	2969	73,7 65,2	0,48	2666	0,39	470	989	1485	220
9	Sandstone, dolom.	2969	2988	74,0 73,7	0,43	2715	0,27	465	988	1480	240
8	Shale, silty	2988	3057	79,0 74,0	0,62	2677	0,45	450	973	1474	250
7	Shale, silty	3057	3260	84,3 79,0	0,62	2677	0,45	430	895	1464	240
6	Shale	3260	3373	88,0 84,3	0,65	2680	0,51	300	800	1442	230
5	Shale	3373	3411	89,0 88,0	0,65	2680	0,51	150	745	1435	235
4	Shale	3411	3498	89,5 89,0	0,65	2680	0,51	130	685	1425	250
3	Shale	3498	3564	92,0 89,5	0,65	2680	0,51	119	270	1380	265
2	Limestone, shaly	3564	3663	96,0 92,0	0,37	2700	0,51	110	153	230	255
1	Shale, silty	3663	3712	97,5 96,0	0,62	2677	0,45	104	150	202	250
B	Shale, silty	3712	3962	105 97,5	0,62	2677	0,45	80	140	200	195
A	Limestone	3962	4712	130 105	0,24	2710	0,16	40	90	150	175

* 700,5 m water depth at well site included

Tab. 3-2. List of parameters required for the backstripping procedure described by Allen & Allen (1990). Data predominantly compiled from the final well report of well 2012/13-1 kindly provided by NAMCOR and the petrophysical database included in the PetroMod2D software package; additional data from Holtar & Forsberg (2000) and Friedinger (1988).

3.7.2 Results of the subsidence analysis

Application of the general decompaction equation to the stratigraphic column, as schematically illustrated by figure 3-18, enables the reconstruction of the burial history for each layer. The decompacted subsidence history for the postrift succession in the central Walvis Basin can be plotted on a diagram of depth versus age (figure 3-21). The bottom line represents the subsidence of the top of the basement (total subsidence, Y_{tot}). Paleobathymetric or eustatic corrections are not incorporated in this plot.

The overall burial history of the sequences deposited during the postrift phase of basin evolution follows an exponential decay curve. No major erosional events of uplift phases can be deduced from the burial history. Minor irregularities between 75Ma and 65Ma are discussed below.

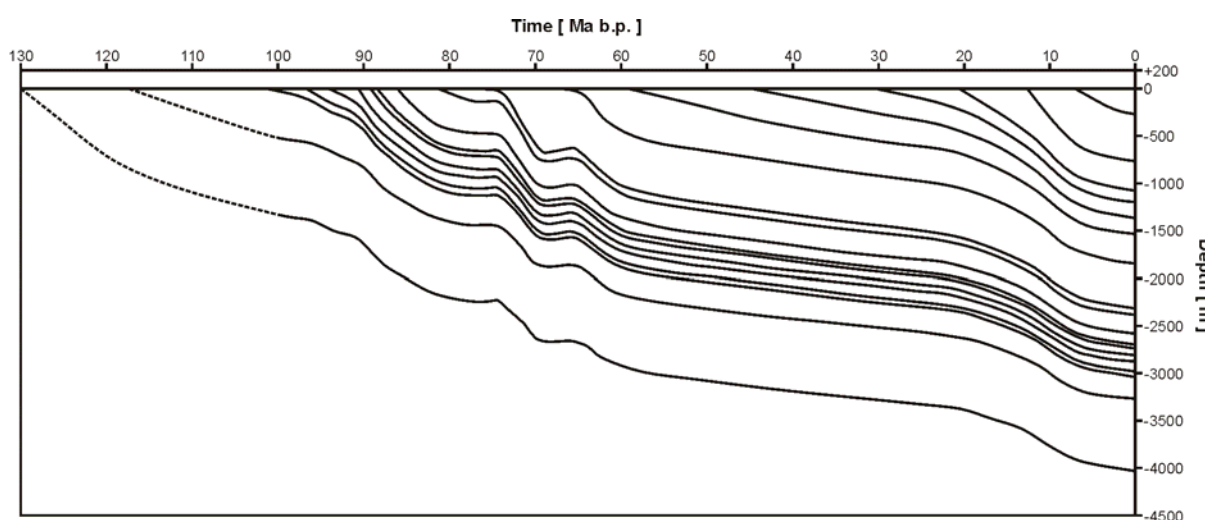


Fig. 3-21. Decompacted burial history for a 20-layer 1D model of the postrift succession in the central Walvis Basin. Dashed line represents early drift section inferred from well 1911/15-1 (see Holtar & Forsberg, 2000). Seafloor serves as reference level.

A backstripped tectonic (thermal) subsidence plot for the central Walvis Basin based on equation 3-2 is illustrated in figure 3-22. Subsidence is corrected for longterm eustatic sea level changes (Δ_{sl}). The error bars as well as the grey shading account for the correction for minimum and maximum estimations of paleowater depths (Wd_{min} , Wd_{max} ; fig. 3-20); the medial black solid line indicates a medium water depth estimation (Wd_{med}). Loads on the lithosphere are compensated by local/ Airy isostasy.

If the tectonic (thermal) subsidence of a basin is compared with the total basement subsidence, the effects of sediment loading can be visualised (eq. 3-1). The upper curve in figure 3-23 indicates the tectonic subsidence of the basin corrected for

medium paleowater depth estimations; error bars account for minimum and maximum paleowater depth estimations, respectively (Wd_{min} , Wd_{max}); the lower curve represents the total subsidence of the basin floor corrected for Wd_{min} which is suggested to display the most plausible paleobathymetric evolution (fig. 3-20). Those parts of the curves that are older than c. 100Ma represent early drift sediments inferred from well 1911/15-1 in the northern Walvis Basin. It is apparent from the comparison of both trends that sediment loading effects contribute up to 50% to the subsidence of the basin floor. The northern Namibian margin is therefore not as sediment starved as other volcanic margins like the Rockall Trough or the Hatton Basin in the North Atlantic have been throughout most of their postrift evolution in the Late Mesozoic and Cenozoic (e.g. O'Reilly et al., 1995).

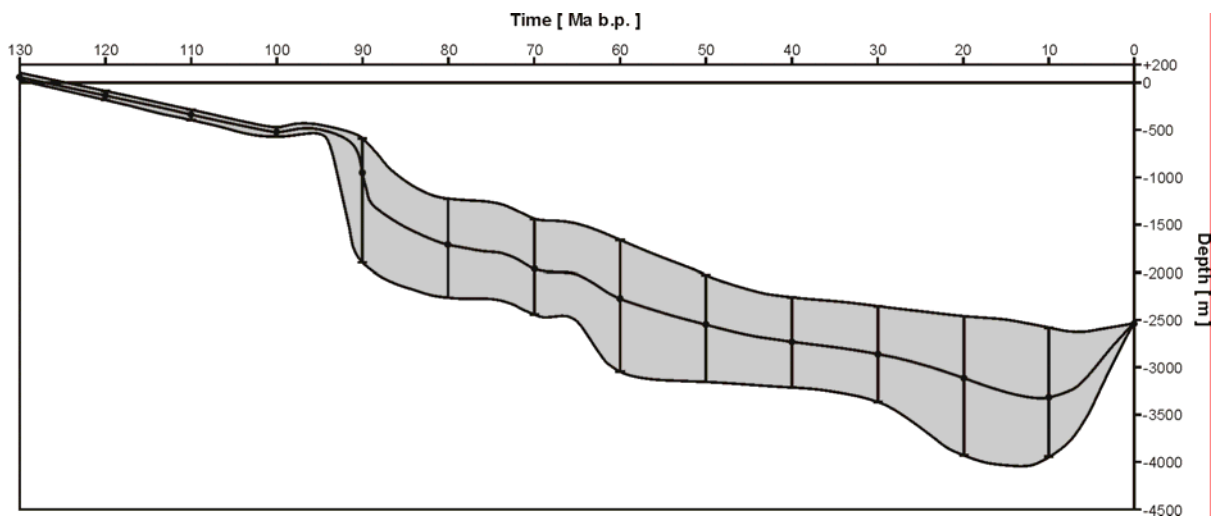


Fig. 3-22. Backstripped tectonic subsidence plot for the central Walvis Basin. Subsidence is corrected for long-term eustatic sea level changes. The error bars account for the correction for minimum and maximum estimations of paleowater depths. Loads on the lithosphere are compensated by local/ Airy isostasy.

The overall subsidence history appears to be relatively continuous without major distortions. This is preferentially the case from 130Ma to 90Ma and during the Tertiary and Quaternary succession from 65Ma to 0Ma, respectively. Major phases of uplift and erosion of previously more deeply buried strata seem to be absent; a certain non-linearity can be recognised between 90Ma and 65Ma as indicated by the grey box in figure 3-23.

A significantly accelerated subsidence can be derived for the time span from c. 90Ma to 80Ma; this might correspond to peaks in denudation and sedimentation as it is suggested by the observation of sedimentation-/ accumulation-rates in well 2012/13-1 (see fig. 4-7) as well as by the denudation history of the NW-Namibian margin (Gallagher & Brown, 1999; Raab, 2001).

Around 75Ma a subsidence-“plateau” can be observed and around 65Ma even slight uplift of the basin floor seems to occur. Both phases may correspond to unconformities that are observed by biostratigraphy and by seismic stratigraphy, respectively (fig. 3-12 & 3-13). The 75Ma event might be indicated by the intra-Upper Campanian seismic marker horizon K which appears to be responsible for the deposition of the overlying sands. A significant stratigraphic break is associated with Cretaceous-Tertiary boundary at 65Ma. The base Paleocene is missing due to erosion, as indicated by biostratigraphic data. This event corresponds to the marker horizon LII observed in the seismic.

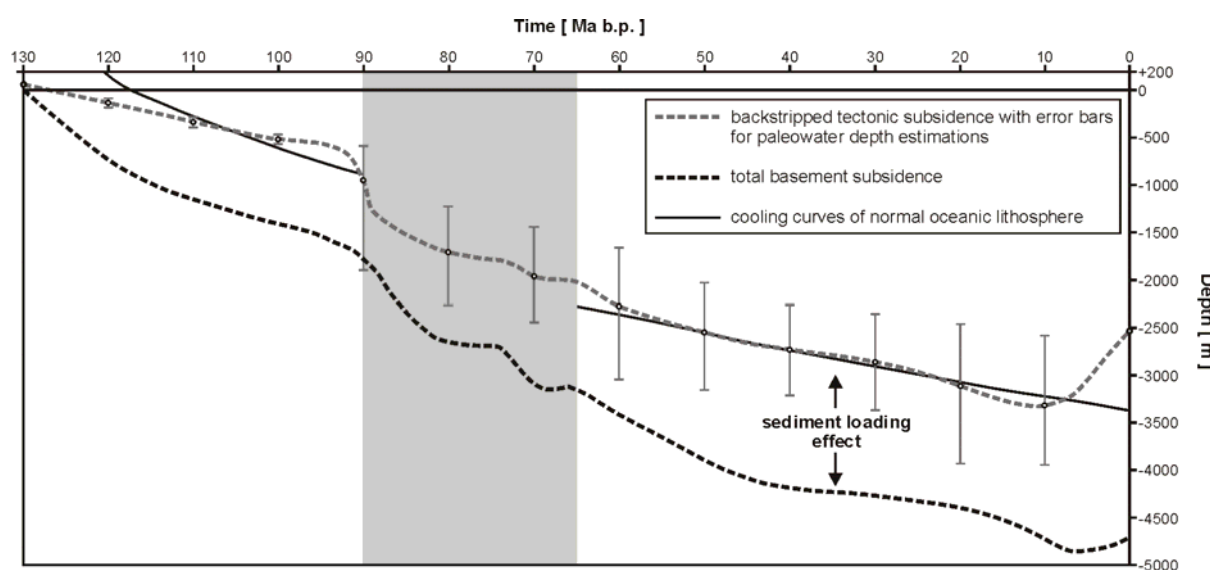


Fig. 3-23. Backstripped tectonic subsidence compared with the total basement subsidence of the central Walvis Basin, thus illustrating the effect of sediment loading. Tectonic subsidence is related to cooling curves of normal oceanic lithosphere (see legend and text for details).

Extrapolation of the tectonic subsidence back to breakup-times at c. 130Ma reveals that the land-surface shortly after the rift-related Etendeka volcanism (c. 132Ma; Renne et al., 1996) has been in the order of 100m above sea level. Subsidence below sea level and thus sedimentation started as early as around 126Ma ago (fig. 3-23). This, in turn, implies that significant subsidence which should be associated with crustal thinning during the rifting process is completely compensated and even slightly overprinted by contemporaneous uplift. The most suitable process to produce uplift of such spatial and temporal dimensions is magmatic underplating and/ or dynamic support of a plume (e.g. Cox, 1989; White & Lovell, 1997). Its effects should be even more distinct closer to the Walvis Ridge where thicker magmatic underplating due to the Tristan plume can be expected (fig. 3-1 & 3-4).

Assuming an intensely underplated and intruded crust of almost basaltic character suggests a comparison of the subsidence curves with theoretical cooling curves of

normal oceanic lithosphere. Age-specific depth of the lithosphere d can be approximated by the equation

$$d[m] = 2500 + 350\sqrt{\text{age}[Ma]} \quad \text{eq. 3-9}$$

after Renkin & Sclater (1988). An array of cooling curves has been evaluated by variation of the initial topography of the basaltic (“oceanic”) lithosphere. The most suitable segments are illustrated by the solid black line in figure 3-23.

The averaged tectonic (thermal) subsidence curve corresponds very well to a cooling curve for normal oceanic lithosphere from 130Ma to 90Ma and from c. 65Ma to 0Ma, respectively, thus supporting the idea of a heavily intruded “basaltic” crust due to underplating.

Local events that might be responsible for the subsidence anomalies observed between 90Ma and 65Ma (grey box) have been discussed above. More global causes for the modification of the overall linear cooling pattern by accelerated marginal uplift, denudation, and sedimentation might be represented by dramatic plate kinematic reorientations in the South Atlantic between the magnetic anomalies C34 (83Ma) and C31 (67Ma), respectively (Cande et al., 1988; Nürnberg & Müller, 1991). These changes were accompanied by a significant increase in the number of fracture zones, by a general decrease in the half spreading rate (34mm/a to 16mm/a), and by the onset of asymmetry in spreading rates in the South Atlantic.

4 Morphotectonic evolution of the margin – a mass and process balance

Studies on passive margin evolution have primarily concentrated on the evaluation of the offshore sedimentary record. Analysis of the deep structure of passive margins revealed their subsidence history and resulted in models expressing the development of basins in terms of the isostatic response to lithospheric thinning. Gallagher & Brown (1997) pointed out that the onshore region of passive margins has relatively been neglected, yet as this is the dominant source region for the offshore sediments; there is a clear generic link between the geomorphologic, tectonic, and sedimentological evolution of both regions.

The high-elevation type passive margin of NW-Namibia has undergone long-lived uplift and erosion as indicated by the development of the Great Escarpment (e.g. Gilchrist & Summerfield, 1990; see fig. 2-1). A variety of mechanisms has been proposed to explain highly elevated (Atlantic-type) passive margins among those are depth-dependent extension (Royden & Keen, 1980; Watts et al., 1982), flexural response to unloading during rifting (Braun & Beaumont, 1989; Weissel & Karner, 1989; Brown et al., 2000), and plume-induced magmatic underplating (Cox, 1980; White & McKenzie, 1995; Turner et al., 1996). All of these mechanisms are genetically related to the rifting process itself and result in transient uplift with a timescale in the order of the thermal time constant of the lithosphere (c. 60Ma).

The uplift and denudation history of the NW-Namibian passive margin has started as early as 130Ma ago. Gilchrist & Summerfield (1990) emphasised that denudational unloading and the associated isostatic rebound may contribute to persistent uplift and erosion by modification of an initially rift-related topography (fig. 4-8).

From reverse and forward structural and stratigraphic modelling of the Norwegian continental margin, Kuszniir et al. (2002), however, emphasised the importance of depth-dependent stretching for the thermal history of the margin. The effects of magmatic underplating are regarded as rather small. They suggest that rifted margins are rather formed by early seafloor spreading than by pre-breakup intra-continental rifting.

Ten Brink & Stern (1992) suggest that erosion itself is not sufficient to cause rift flank uplifts of the dimensions observed at the southern African margins. Magmatic underplating may explain part of the uplift, although the link between temporally restricted magmatism and permanent uplift is unclear. Ten Brink & Stern (1992) emphasised the mechanical coupling between the onshore and offshore regions of passive margins due to laterally varying flexural strengths of the lithosphere; they modelled the uplift of the Great Escarpment as an upward deflection of a continuous elastic plate that is modified by the downward load of sediments on the continental margin (fig. 4-1). Lateral variations in elastic thickness of the lithosphere are inferred to model the observed dimensions of marginal basin subsidence, isostatic rift flank

uplift, and a flexural hinterland basin which is located far inland due to the high flexural rigidity typical of Gondwana cratons.

The convex erosional surface in the area between the Great Escarpment and the coast which is predicted by the model (fig. 4-1) can be recognised on the coastal plain of NW-Namibia in the area NW of Torrabaai (c. 20°S, 13°E; Partridge & Maud, 1987). A narrow band of coast parallel recent cover unconformably overlies “bowed up” Karoo and Etendeka deposits. The geological map of NW-Namibia presented in figure 2-2 gives an overview of the outcrop geology in the study area. Figure 2-3 provides information on the catchment areas of the Hoanib, Uniab, Koigab, Huab, Ugab, and Omaruru ephemeral rivers, respectively, which represent the exterior catchment that drains the study area in a westerly direction. Ten Brink & Stern (1992), however, conclude that not only one of the forces outlined above is responsible for the observed uplift of the Namibian continental margin, but a combination of forces with varying relative contributions.

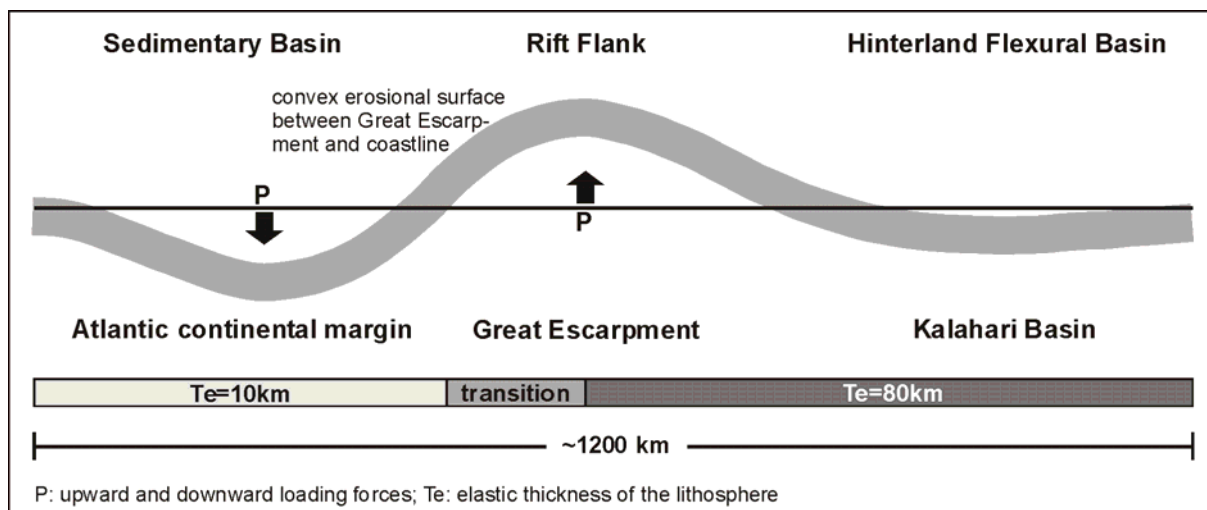


Fig. 4-1. Continuous elastic plate model of the SW-African continental margin that is subjected to upward and downward loads. Flexural rigidity increases from oceanic towards the continental lithosphere with a narrow transition zone in the coastal plain area. Modified from Ten Brink & Stern (1992).

The model approach

Quantitative studies of margin evolution normally focus on the evaluation of the offshore sedimentary record: the denudational history is deduced from the depositional history. The model approach presented in this study, however, follows the sedimentary cycle more consequentially as it begins with the consideration of the sediment source within a 2D reference frame across the passive margin of NW-Namibia. Primarily, the thickness of erosion is estimated and distributed over time by means of independent data derived from quantitative denudation studies on

stratigraphic markers and apatite fission tracks (chapter 4.1). In a first step, rather simple mass balance calculations are presented that compare the amount of sediment supplied to the examined basin segment during the postrift evolution of the margin with the amount of sediment effectively encountered offshore (chapter 4.5).

Secondly, a more sophisticated process-oriented approach to passive margin evolution is performed. Estimations of volumes eroded onshore are combined with the denudation chronology deduced from fission track analysis in order to serve as sediment supply rates over time for a stratigraphic forward-model of the margin evolution (see chapter 5). This model approach not only allows to control the quality of the mass balance calculations but also provides quantitative insights into the feedback mechanisms between sediment supply rate, basin subsidence, and global sea level changes, respectively. Forward modelling intends to reproduce the basinal geometry and stratigraphy observed offshore by application of independently determined parameters.

Misfits in volumes arising from the mass balance may be contributed to a differential transportation component parallel to the coast. Evaluation of a 2D section may therefore even allow to put quantitative constraints on processes in the third dimension. Provenance analysis based on detailed petrographic and geochemical studies on offshore clastic sediments (chapter 4.3 & 4.4) helps to support and refine this aspect. The ultimate goal of the model approach presented here is to attain a quantitative link between uplift and erosion onshore with contemporaneous subsidence and sedimentation offshore.

4. 1 Calculation of the material eroded onshore

Figure 4-2 gives an overview of the model traverse for which the mass and process balance is presented. The traverse is oriented perpendicular to the coast at a latitude of about 20-21°S. It is obvious that the onshore part of the section lies almost completely within volcanic rocks of the Etendeka Group. Any sediment eroded onshore and transported into the adjacent basin segment by a pure transversal drainage system can therefore be attributed to a volcanic source region. Although this assumption is rather simplifying, it provides the opportunity to quantify the effects of a differential transport component perpendicular to the model traverse (i.e. coast-parallel) by considering the non-volcanic detritus observed offshore.

The onshore part of the traverse is chosen so that it comprises the well defined catchment areas of the ephemeral Koigab and Uniab rivers, respectively (fig. 4-27). These two drainage regimes cover the entire coastal plain which is bounded to the Northeast by the Great Escarpment with an elevation of c. 1600m in that area. Assuming a rather “degradational” landscape evolution in the area of the exterior catchments, as it is outlined in chapter 4.1.2 below (fig. 4-8), suggests a relative

stationary drainage pattern in the study area, even in terms of long-term margin evolution. The traverse is 107km in width and c. 400km in total length; it might therefore be regarded as a 2,5D model section. The onshore part comprises an area of 10091km², whereas the offshore proportion covers an area of 30292km² (chapter 4.2).

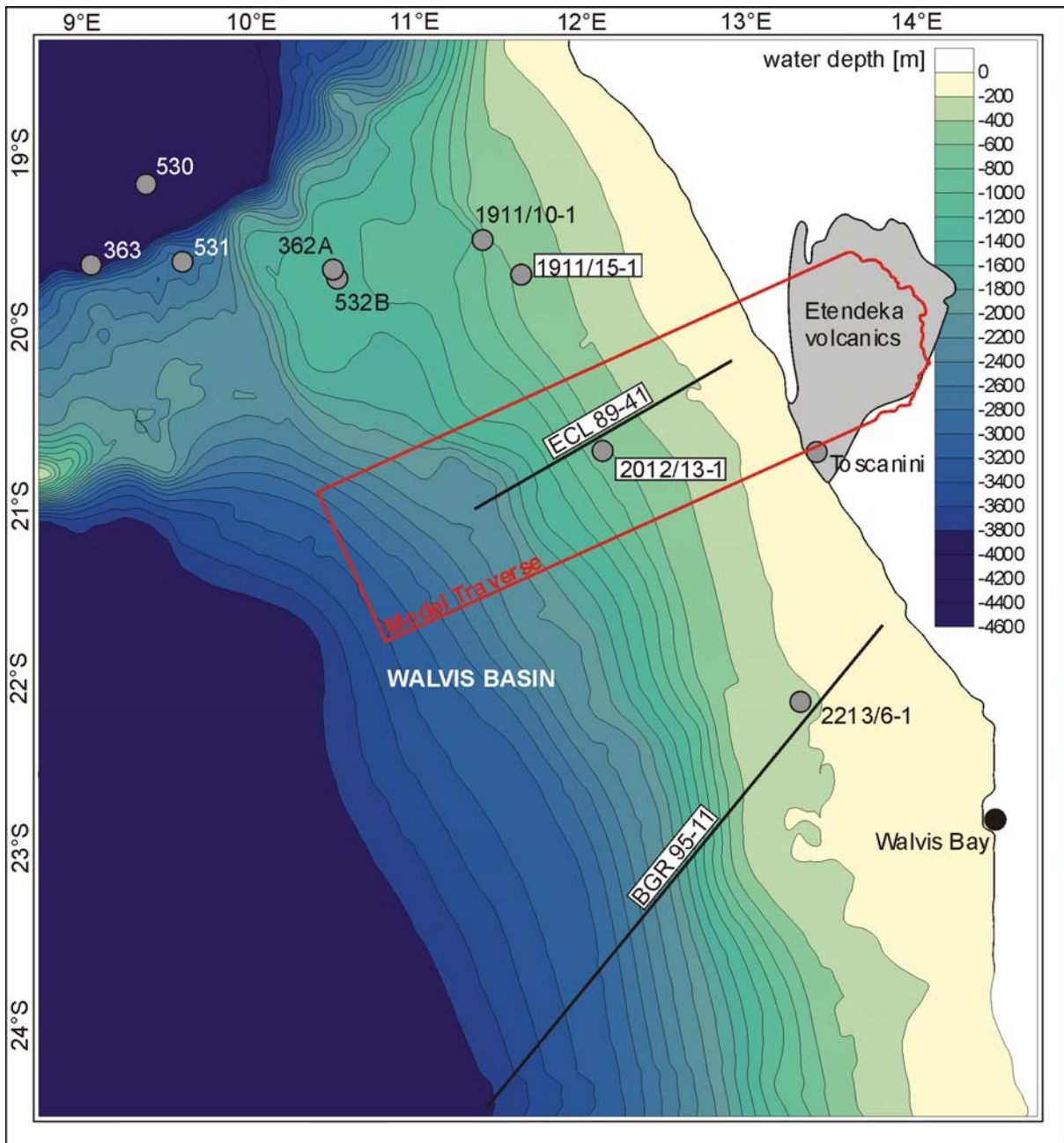


Fig. 4-2. Digital bathymetric model of the Walvis Basin generated with *SURFER*. The available offshore database (well and seismic data) is indicated by white boxes; red box outlines the model traverse for which postrift-denudation onshore is quantitatively linked with contemporaneous sedimentation offshore. Compiled from <http://www.namcor.com.na/pdfs/seismap.pdf>.

An accurate digital elevation model of the proper Uniab and Koigab catchment areas and adjacent coastal regions has been digitised and gridded with *SURFER* on the

basis of topographic maps 1:250000 (fig. 4-3). Possible thicknesses of erosion in this area during passive margin evolution are estimated by inferring different paleo-landsurfaces deduced from a variety of indicators that are discussed in the chapters 4.1.1 & 4.1.2.

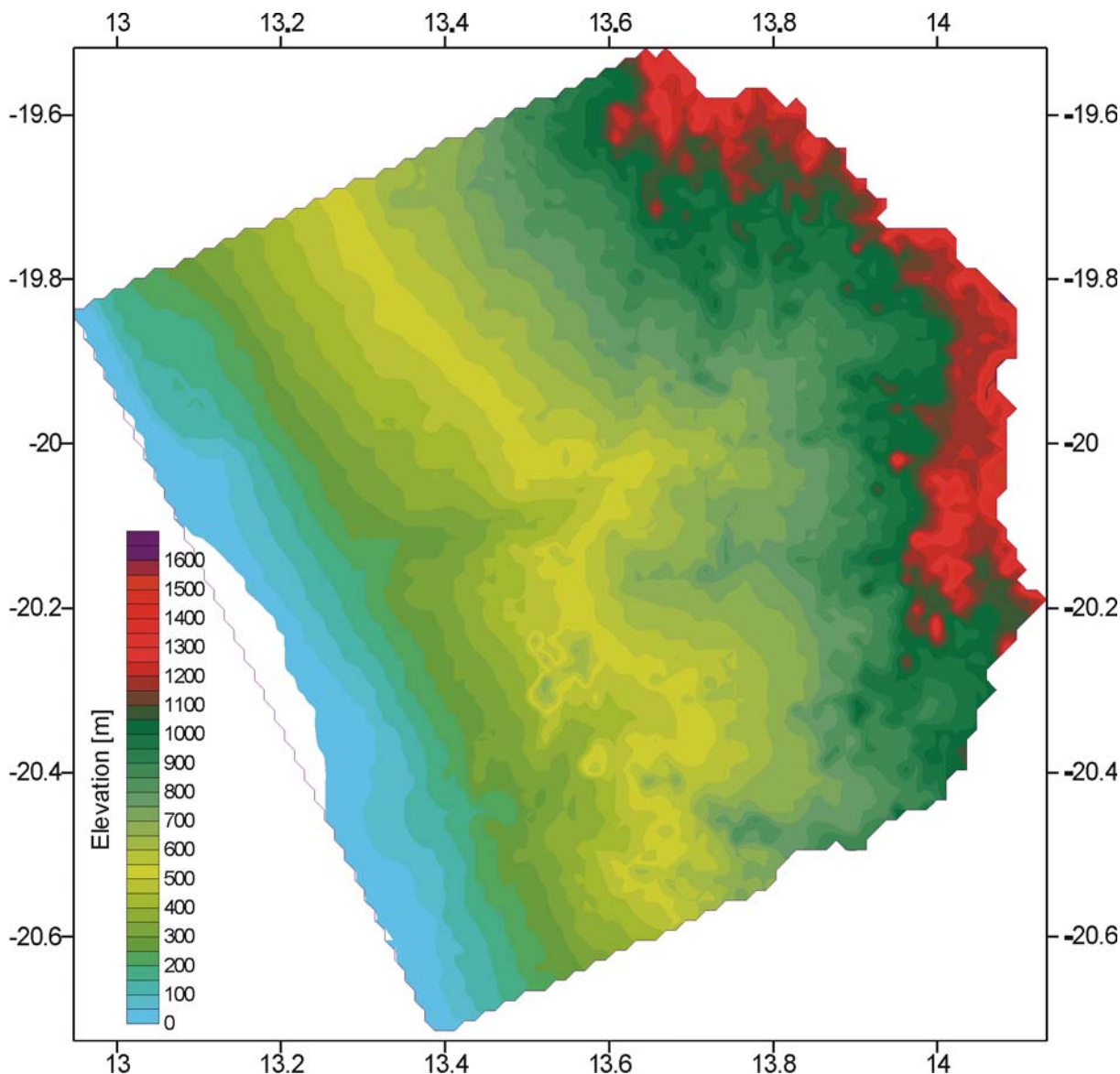


Fig. 4-3. High-resolution digital elevation model of the onshore part of the model traverse, generated with *SURFER* on the basis of topographic maps 1:250000. Area comprises the catchment areas of the Uniab and Koigab ephemeral rivers and adjacent areas in the coastal plain. The Great Escarpment terminates the model in the NE.

SURFER is capable of calculating the volume between the present day topography and any higher level if the horizontal resolution of both the lower and the upper surface is identical; calculation is based on the trapezoidal rule, Simpson's rule, and Simpson's 3/8 rule, respectively (see *SURFER* help menu for details). However, it is essential to transform the dimensions of the reference frame from "degrees longitude/ latitude" into "metres" in order to attain reasonable values; this can be

achieved by converting the respective grid-files into an ASCII-format and by changing the model dimensions in the header-lines in an appropriate manner.

Extensional synsedimentary faulting during rifting has affected near coastal areas of the model traverse. The apparent volume loss associated with extensional faulting led to exaggerated calculations for the volumes eroded during postrift denudation. A misfit of 2316km^3 has been calculated for the model section by restoring major synsedimentary faults; it has been subtracted from each of the volumes computed in chapter 4.1.1.

4. 1. 1 Implications from topography and stratigraphic remnants

Geomorphological features, stratigraphic remnants and estimations of intrusion depths allow first approximations of the thickness of the lithologic column that covered the NW-Namibian study area at the time of breakup. The reconstruction of former landscapes is outlined in a somewhat wider scope in conjunction with Gilchrist et al.'s (1994) model of escarpment evolution (fig. 4-8).

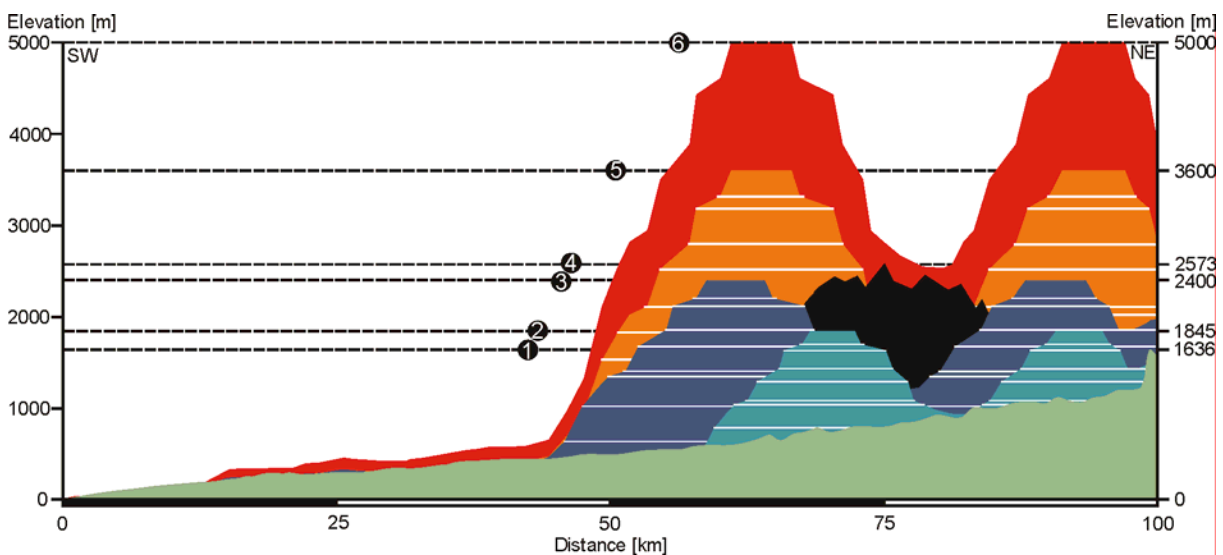


Fig. 4-4. 2D section through the onshore part of the model traverse. The reference levels 1-6 schematically indicate estimations of the topographic elevation of the paleo-landscape at the time of breakup inferred from a variety of stratigraphic and quantitative clues. Green section represents a profile of the Uniab ephemeral river in the coastal plain area. See text for details.

Figure 4-4 illustrates a 2D section perpendicular to the coast line through the catchment area of the Uniab ephemeral river that has been extracted from the northwestern part of the digital elevation model presented in figure 4-3. The lowermost (green) area indicates the gentle and even downward slope of the Uniab drainage regime which is representative for the entire coastal plain to the west of the Great Escarpment.

The additional 2D sections labelled 1-6 that are staggered behind the Uniab river profile (green in fig. 4-5) schematically represent indicators for an estimation of the thickness of the former cover. Rock volumes that have been eroded since the Early Cretaceous times of breakup are inferred from the volumetric difference between the present day topography in the study area (fig. 4-3) and a hypothetical even plain covering the same area at a topographic level indicated by the labels 1-6 in figure 4-4 & 4-5, respectively.

Level 1 represents a hypothetical minimum estimation of postrift denudation; it simply assumes the topography drained by the Uniab and Koigab rivers to be “filled” with rock volume up to the elevation of the escarpment at 1636m in that area.

If the cumulative preserved thickness of the volcanics of the southern Etendeka Group (1245m; Milner et al., 1994; see fig. 2-6) is placed upon the average elevation of the base of the Etendeka in that area at c. 600m, a pre-denudational topographic level of 1845m might have been reached (*level 2*). Plate VI-2 gives an impression of a typical Etendeka landscape on Farm Wêreldsend with isolated volcanic remnants in a deeply eroded coastal plain. Plate VI-3 is located in the Springbok River valley which is the major tributary of the Koigab River; a volcanic relict mountain capped by quartz latites of the Springbok Member (see fig. 2-6) is illustrated. It has been mentioned above that the onshore part of the model traverse has been chosen so that it only covers Etendeka Group volcanics with the exception of a narrow coastal strip. Plate VI-4 represents the Achab River valley which is the major tributary of the Uniab River. This is the location where the interior part of the Etendeka volcanic plateau is most deeply eroded and it can therefore be shown that even there the Etendeka plateau has not been denuded below its base; this feature becomes important in conjunction with provenance studies outlined in chapter 4.3.

Level 3 considers the combined cumulative thicknesses of the Etendeka and Paraná volcanic succession that reaches up to 1800m (Stollhofen, 1999). Placed upon the base of the Etendeka at c. 600m, a topographic level of 2400m might so have been reached in the Early Cretaceous.

The most impressive geological marker that provides constraints on the denudational history of the NW-Namibian margin is the Early Cretaceous Brandberg intrusive complex (e.g. Schmitt et al., 2000) which is located to the South of the study area (Plate VI-1; see fig. 1-1). The top of the Brandberg reaches an elevation of 2573m (*level 4*) which is about 2000m above the surrounding coastal plain. This value indicates a minimum depth of erosion consistent with the average postrift denudation inferred for the entire SW-African margin from offshore sediment volume data (Rust & Summerfield, 1990; Brown et al., 2000). Thereby, the original intrusion depth is still neglected.

Estimations of the thickness of the cover that reached up to 3600m or even 5000m above the present day topography during times of breakup (*levels 5 & 6*) are inferred

from apatite fission track data (Ten Brink & Stern, 1992; Bauer et al., 2000; Brown et al., 2000; Raab, 2001; Raab, pers. comm., 2002). Since these data yield not only maximum estimations of the depth of postrift denudation but also provide a quantitative idea of the denudational history which is fundamental for the basin model examined in chapter 5, fission track analysis is outlined in some more detail in the following chapter. Furthermore, assuming a maximum cover of 5000m thickness provides the most suitable results both in terms of mass balance calculations (chapter 4.5) as well as in terms of sediment supply to the basin model (chapter 5.3).

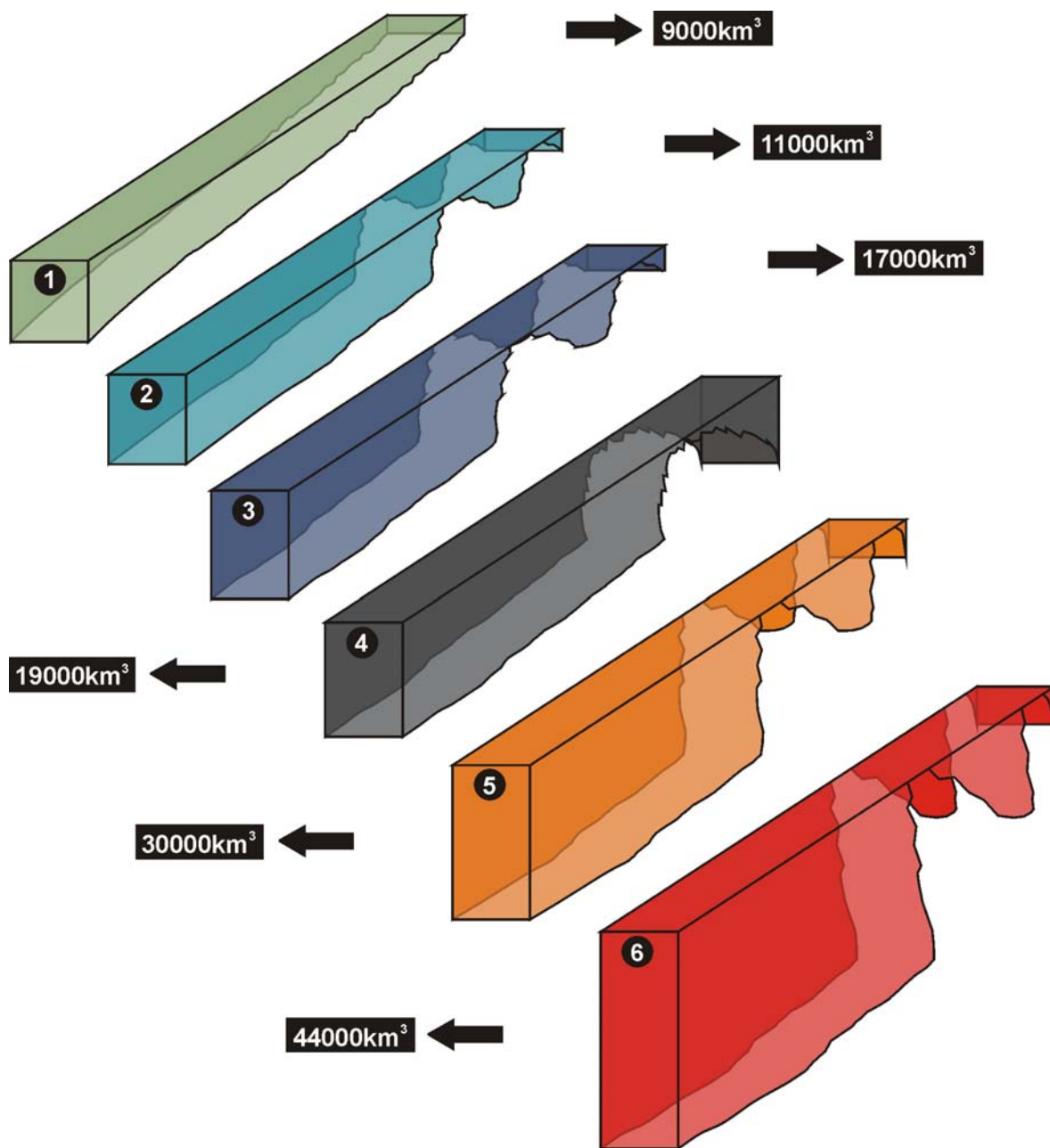


Fig. 4-5. Schematic 3D view of the volumes eroded from the onshore part of the model traverse. Colours are related to different estimations of the elevation of the paleo-landscape at the time of breakup. See text for details.

Figure 4-5 schematically illustrates the volumes of rock eroded during the postrift evolution of the onshore part of the model traverse if the variety of estimations of former covers outlined above is considered. Potential paleo-landsurfaces indicated by the levels 1-6 result in eroded rock volumes of 9000, 11000, 17000, 19000, 30000, and 44000km³, respectively, whereby the latter of which is suggested to represent the most reasonable value.

4. 1. 2 Quantitative denudation history inferred from AFT analysis

While the indicators outlined above attempt to explain the depth of denudation and thus present day topography and exposed stratigraphy, they do not generally address the evolution of topography over time. Apatite fission track (AFT) analysis is capable of considering the denudation chronology of continental margins which provides improved input parameters for more complete stratigraphic models of passive margin evolution (e.g. Tucker & Slingerland, 1994; see chapter 5).

Apatite fission track analysis (AFTA) is a low-temperature thermochronologic technique that provides quantitative estimates of the depth of rock removal over time (Gallagher, 1995; Gallagher & Brown, 1997, 1999). Denudational uplift due to erosional or tectonic processes causes rocks to cool as they approach surface. Since AFTA is sensitive to a temperature range of about 60°C to 110°C, which is characteristic of the upper 4-5km of continental crust, the method is suitable to constrain long-term denudation chronologies on timescales in the order of 1-100Ma. In order to convert AFT data into estimations of denudation, some constraint on the paleogeothermal gradient is required. This information can be either obtained from vertical profiles of samples (e.g. over a range of topographic elevations) or from a series of samples from deep boreholes.

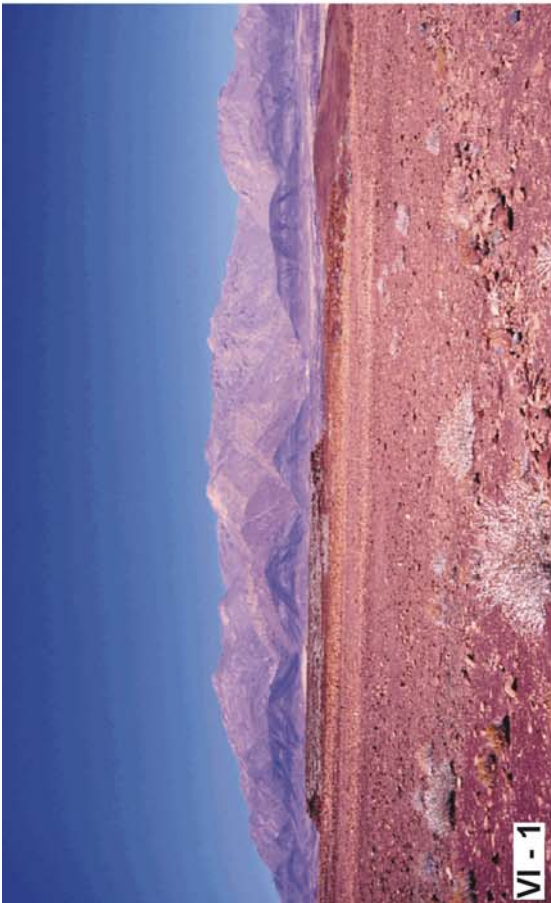
Legend Plate VI

VI-1. View of the Brandberg - a deeply eroded Early Cretaceous igneous complex; the top of the Brandberg reaches an elevation of 2573m which is about 2000m above the surrounding coastal plain; view from the "Tafelkop" to the east; location of viewpoint: 21°04,297' S, 14°15,883' E.

VI-2. Typical Etendeka landscape with isolated volcanic remnants in a deeply eroded coastal plain; location: Farm Wêreldsend (Torra Conservancy), c. 20°11' S, 13°53' E.

VI-3. Volcanic relict mountain capped by quartz latites of the Springbok Member; height of section: c. 200m; location: Springbok River valley which is the major tributary of the Koigab River, c. 20°20,5' S, 13°34,5' E.

VI-4. Locality where the interior part of the Etendeka volcanic plateau is most deeply eroded; it can be shown that even there the Etendeka plateau has not been denuded below its base; scale: step in river bed is c. 1,5m; location: Achab River valley which is the major tributary of the Uniab River, Farm Wêreldsend/ Rooiplaat (Torra Conservancy), c. 20°7' S, 13°52' E.



Fission tracks are discrete linear zones of damage within the crystal lattice of apatite or zircon due to spontaneous fission of ^{238}U present in trace amounts in the mineral; since the rate of fission is constant, an apparent fission track age can be determined by counting the number of fission tracks and by measuring the uranium content.

Fission tracks are revealed with a standard chemical etching procedure; AFT are considered to have a constant initial etchable length of 17-20 μm (pers. comm. M. Raab). Since the maximum etchable track length is a sensitive function of temperature and tracks shorten or anneal at temperatures in excess of 110-120°C (“total annealing temperature”, Gallagher & Brown, 1999), the mean track length (MTL) distribution provides information on the temperature variations experienced by the host rock. The apparent fission track age, however, provides information on the timing and duration of these variations. Plotting the apparent fission track age as a function of MTL, commonly referred to as “boomerang plot”, is a suitable method to interpret the cooling history.

Below a temperature of 110°C the fission tracks shorten with a progressively decreasing rate until they become stable below 60°C; the cooling history through this “partial annealing zone (PAZ)” may be complex and has therefore to be interpreted very carefully (Gallagher & Brown, 1997, 1999; Brown et al., 2000; Raab, 2001). Gallagher (1995) provides the modelling software *MONTE TRAX* to infer an ideal time-temperature-path of samples through the PAZ.

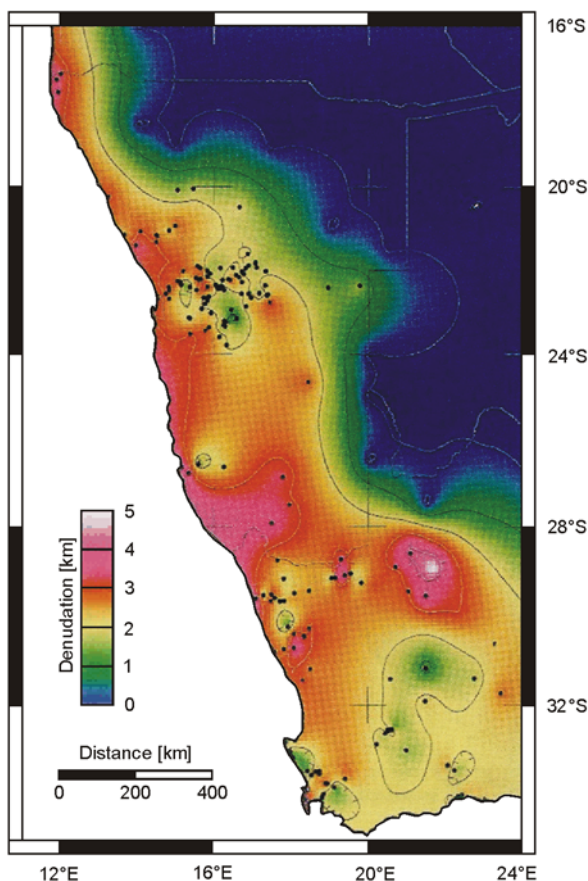
However, young AFT ages associated with long track lengths of $\geq 14\mu\text{m}$ indicate that the sample cooled rapidly from temperatures in excess of 110-120°C; effectively all of the tracks formed after cooling and the AFT age roughly dates the cooling event. Shorter mean track lengths (MTL) $< 14\mu\text{m}$ associated with more variable AFT ages indicate a complex and protracted cooling history through the PAZ; MTL distribution may be wider and more bimodal due to a component of longer tracks forming after the cooling episode and a component of shortened tracks formed prior to cooling. The AFT age therefore represents a minimum age of cooling below 110°C.

Gallagher & Brown (1999) and Brown et al. (2000) demonstrated the construction of quantitative denudation maps based on a regional fission track data set of southwestern Africa (fig. 4-6). Primarily, the AFT data have to be modelled in terms of paleotemperature maps for selected times following the method described by Gallagher (1995), incorporating the fission track annealing algorithm of Laslett et al. (1987). The result of this modelling process is an optimal thermal evolution of each sample. Conversion of paleotemperature maps to equivalent depths of erosion requires some information on the temperature gradient over time.

The depth of erosion z equivalent to modelled paleotemperatures is given by equation 4-1 (Gallagher & Brown, 1999)

$$z = \frac{k(T_p - T_s)}{Q} \quad \text{eq. 4-1}$$

where k is the thermal conductivity, T_p is the paleotemperature estimated from AFT modelling, T_s is the assumed surface temperature, and Q is heat flow. According to Buck et al. (1988) the thermal effects of rifting are unlikely to be significant within the shallow crust of the onshore region of passive margins. A temporally constant but spatially varying heat flow of 53mW/m^2 for southern Africa (Ballard et al., 1987; Pollack et al., 1993) has been used for the modelled denudation map presented in figure 4-6; additionally, a constant thermal conductivity of $2,5\text{W/mK}$ and a constant surface temperature of 20°C has been assumed.



The most striking feature of the modelled postrift denudation of the Namibian passive margin is a significant amount of erosion of 2,5-5km (3-4km on average; see fig. 4-4 & 4-5, levels 5 & 6) parallel to the coastline since the Aptian (118Ma; fig. 4-6). Cooling and thus denudation of the continental interior is closely related to pre-existing crustal structures (Brown et al., 2000). Particularly in NW-Namibia, the trend of preferential denudation is clearly associated with the coastal plain which is drained by the exterior river catchments (see fig. 2-3) and which is terminated by the Great Escarpment to the northeast (see fig. 2-1).

Fig. 4-6. Map of the estimated postrift denudation of southwestern Africa in [km] from 118-0Ma b.p. derived from apatite fission track analysis. Modified from Brown et al. (2000).

A similar and even more distinct pattern is documented in contour plots of apparent fission track ages of NW-Namibia as well (Raab et al., 2000, 2002). The youngest AFT ages, the higher paleotemperatures and consequently higher cooling rates occur within a c. 150km wide coastal zone and decrease systematically inland. This coastal trend is modified by a SW-NE trending zone of young AFT ages that coincides with the continental branch of the Damara orogen (see fig. 2-4).

Since young apparent AFT ages (90-60Ma) are associated with relatively long mean track lengths of c. 14 μ m, these ages roughly date a discrete phase of accelerated Late Cretaceous denudation (grey curve in fig. 4-7; Gallagher & Brown, 1999; Raab et al., 2000); the young ages thus indicate that present day land surface remained under substantial burial adequate to a paleotemperature in excess of 110°C (depending on the paleotemperature gradient) until the Late Cretaceous. Samples from the Early Cretaceous Brandberg intrusive complex exclude any AFT ages older than 132Ma which may otherwise disturb this distinct pattern because intrusion temperatures would have “reset” the AFT ages effectively to zero. This indicates that even the Brandberg, which protrudes out of the surrounding peneplain by 2000m at the present day, remained buried under a considerable cover until the Late Cretaceous. The majority of denudation unequivocally post-dates the time of rifting by 40Ma to 70Ma and is therefore unrelated to the initial formation of the margin.

Raab (2001) who extended and refined the data set of Gallagher & Brown (1999) combined the temperature information derived from AFT data with the spatial information inherited in the samples obtained from a “vertical” section along the Brandberg intrusive complex in order to estimate the paleotemperature gradient. This approach does not only allow to attain a Late Cretaceous paleotemperature gradient of 22-26°C/km for the Brandberg area which is only marginally higher than the present day value of 20°C/km; local denudation rates of up to 120m/Ma in the Late Cretaceous could be inferred as well; furthermore, a calculated paleogeothermal gradient is a suitable means to avoid the uncertainties associated with the extrapolation of present day heat flow values into the geological past as indicated in equation 4-1.

Gallagher & Brown (1999) present a spatially integrated denudation chronology by summing up the depth differences calculated for successive time intervals over the area illustrated in figure 4-6. A generalised cumulative denudation curve can thus be constructed for the Namibian margin by utilising the optimal thermal history models inferred from *MONTE TRAX* (Gallagher, 1995; grey curve in figure 4-7). This curve is of fundamental relevance as it allows the volumes eroded onshore to be distributed over time in order to serve as one of the most important input parameters for the stratigraphic models presented in chapter 5.3. The quality of the model results

utilising these sediment supply rates can be controlled by comparison with the stratigraphic architecture observed in offshore seismic and wells (see fig. 5-17).

Denudation rates increase continuously from the time of breakup to c. 75Ma (fig. 4-7). The most striking feature is a distinct denudation peak in the Late Cretaceous around 80Ma. This phase of accelerated denudation is coincident with a phase of major plate tectonic reorientations observed offshore between the magnetic anomalies C34 (83Ma) and C31 (67Ma; Cande et al., 1988; Nürnberg & Müller, 1991). These may have initiated new relief and a new erosional base-level onshore by rejuvenation of Late Proterozoic basement structures that are clearly reflected by the denudation distribution (fig. 4-6).

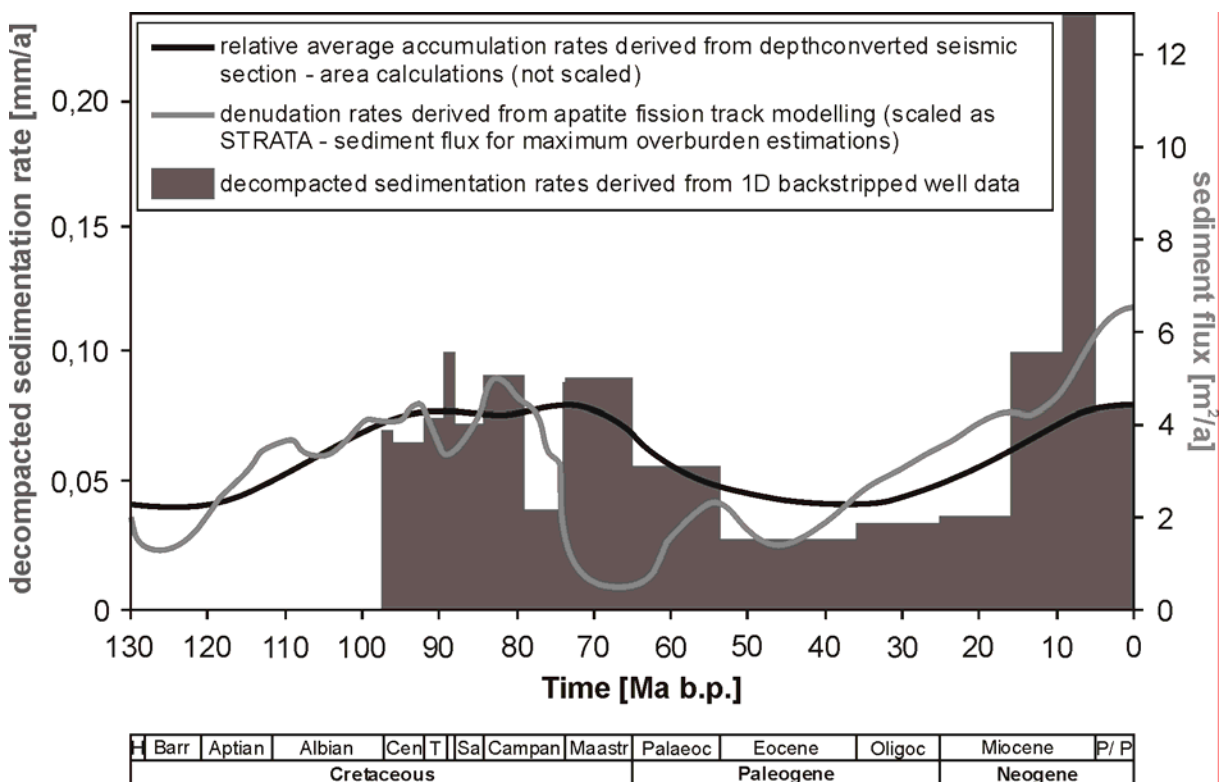


Fig. 4-7. Sedimentation rates, accumulation rates, and denudation rates for the central Walvis Basin and adjacent onshore areas since the time of breakup. Although inferred and modelled from different data sets, a broad correspondence between the curves can be depicted. See legend and text for discussion.

It seems to be appropriate to compare the denudational history with the contemporaneous depositional history offshore. The grey boxes in figure 4-7 illustrate the decompact sedimentation rate [mm/a] for the time span from 97,5Ma to the present inferred from the backstripping process of well 2012/13-1 in the central Walvis Basin (see chapter 3.7). Both trends are roughly parallel; two peaks in the middle and Late Cretaceous are followed by a distinct low; a smaller Early Tertiary denudation peak is not reflected by the sediment data; both curves rise again

throughout the Tertiary until the present day. Although the strong increase in denudation rates from 20Ma is suggested to be attributable to an artifact inherited in the applied AFT annealing model for low temperatures (<50-60°C) on long timescale scenarios (Gallagher & Brown, 1999), a similarly strong increase is observed in the Upper Miocene sedimentation rates (fig. 4-7).

However, the peaks and lows of the sedimentation rates appear to be systematically shifted by c. 15Ma towards younger ages compared to the denudation rates. This might be due to a certain delay in sediment transport associated with the affection of river catchments reaching farther inland. The Ugab chatchment, for example (see fig. 2-3) reaches far inland and it is spatially related to the SW-NE-trending zone of preferential denudation that coincides with the Damara inland branch, as outlined above.

Additionally, relative average accumulation rates based on volume calculations with a depthconverted seismic section through the central Walvis Basin (chapter 4.2) have been incorporated into figure 4-7 (black curve). Although the resolution is not sufficient to visualise more distinct peaks, the trend of the accumulation rates is very similar to both the denudation rates and the sedimentation rates, respectively. The three curves refer to totally different and independent bases of calculation which provides favourable control mechanisms.

Implications for the escarpment evolution

As mentioned above, the temporal and spatial resolution of AFT data is generally insufficient to put constraints on denudation rates and landscape development over more recent geological time scales. However, cosmogenic isotope analysis which includes the measurement of depth-dependent in-situ accumulation of particular isotopes in near-surface material through interactions of target elements with cosmic radiation enables site-specific estimations of denudation rates over time scales in the order of 10^3 - 10^6 a. Cockburn et al. (2000) have integrated AFT analysis with ^{10}Be and ^{26}Al cosmogenic isotope analysis in order to assess the long-term landscape evolution of the central Namibian continental margin. In that area, a gently inclined coastal plain is seperated from the continental interior by a well-defined escarpment which is coincident with the major drainage divide; the escarpment reaches its maximum elevation of 2347m at the top of the Gamsberg (c. 23,3°S, 16,3°E).

Cockburn et al. (2000) deduced average degradational denudation rates of 40m/Ma for the coastal plain from the time of breakup to the end of the Eocene; this is consistent with the rates inferred from AFT analysis, if a thickness of erosion of 5000m over 130Ma is assumed (38m/Ma). Average denudation rates fall to 5m/Ma up to the present. Cosmogenic isotope analysis revealed a mean rate of escarpment retreat of 10m/Ma for the Gamsberg area integrated over the past 80000a; the

coastal plain has been denuded by 5m/Ma on average during that time span. Semi-arid to arid climatic conditions are suggested to have prevailed across the coastal plain for the past 10-15Ma which is coincident with the onset of the Benguela upwelling system in the SE-Atlantic (Siesser, 1980; Ward et al., 1983; Ward, 1987); it is suggested that these climatic conditions have persisted throughout much of the Tertiary and possibly throughout the entire Cenozoic.

Van der Wateren & Dunai (2001) analysed the denudation history of roughly the same area by surface exposure dating based on cosmogenic ^{21}Ne obtained from fluid inclusions in quartz veins. Their data generally confirm the results of Cockburn et al. (2000); a slow long-term denudation history of the central Namibian margin interrupted by pulses of rapid denudation (e.g. in the mid-Pliocene, 2,8Ma ago) is deduced.

Previous morphotectonic models of the Namibian margin have assumed that landscape evolution is dominated by the retreat of a major escarpment at rates approaching 1km/Ma (e.g. King, 1953). Models of landscape development that fundamentally concentrate on the more efficient erosional capacity of the exterior drainage regime in response to marginal upwarp (e.g. Gilchrist & Summerfield, 1990; Gilchrist et al., 1994; Ollier & Pain, 1997) have questioned the simple concept of escarpment retreat.

Gilchrist et al. (1994) presented an approach to the landscape development of southwestern Africa (fig. 4-8) utilising the observation of stratigraphic markers combined with numerical modelling. Reconstruction of the intrusion depths of subvolcanic complexes as well as the consideration of erosional remnants of Karoo sediments and Etendeka volcanics resting unconformably on paleo-landsurfaces of Permo-Carboniferous age, respectively, indicate significant denudation of the margin in the order of 0,5-3,5km. This corresponds to the amount of denudation inferred from AFT analysis as outlined above.

Estimations of total volumes of sediment along the SW-African margin derived from seismic-based isopach maps indicate an average denudation of at least 1,8-2km since the time of breakup (Rust & Summerfield, 1990; Brown et al., 2000).

Kimberlite plugs and pipes of latest Cretaceous age (67Ma) are located inland of the Great Escarpment of southern Namibia; since they still exhibit their original crater infill of lacustrine sediment (Smith, 1986) they provide excellent control on the timing of denudation: landscape in that region has not been significantly eroded during the entire Cenozoic. Additionally, the Namib sand sea of western central Namibia, which is suggested to have originated as early as in the Late Cretaceous (Ward et al., 1983), is bounded to the East by the Great Escarpment. This indicates that the coastal plain must have been substantially eroded by the end of the Cretaceous.

Both features broadly correspond to the quantitative denudation chronology obtained from AFT data modelling (fig. 4-6 & 4-7).

Considering the field observations outlined above, Gilchrist et al. (1994) simulated the evolution of escarpments particularly investigating the control exerted by lithology, climate, antecedent topography at the end of rifting, and baselevel lowering of the interior catchment, respectively. Transport is modelled as linear diffusion or as a function of local discharge and local downstream slope. The location of initial drainage divides and differential denudation in rivalling major catchment areas turned out to fundamentally determine landscape evolution as indicated by the revised model illustrated in figure 4-8. Escarpments may form by regular retreat but degradation and destruction of an initially rift-related escarpment due to incision of the exterior catchment appears to play a fundamental role for the Namibian margin (Gilchrist et al., 1994); the escarpment reforms some at distance inland close to the initial drainage divide.

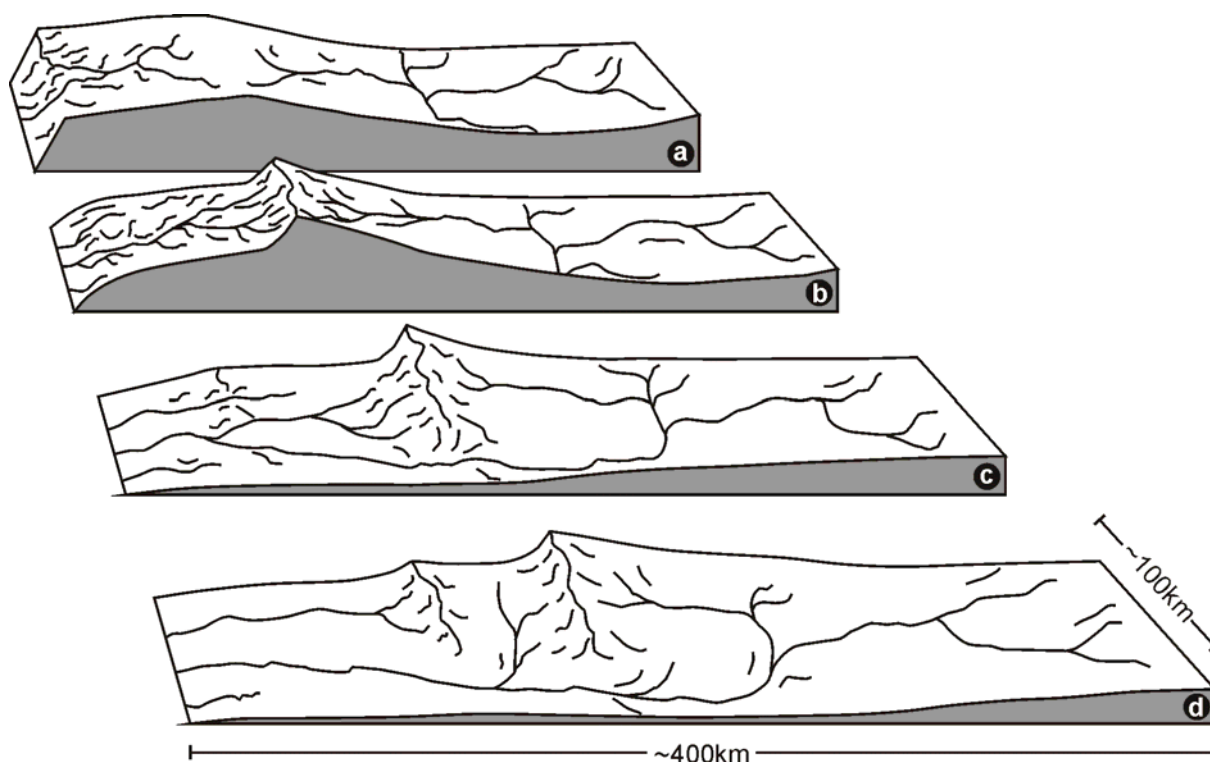


Fig. 4-8. Conceptual model of landscape evolution for the Namibian margin emphasising the degradational morphological evolution of the exterior river catchments (a) at the time of rifting, (b) some time after rifting, (c) when the marginal upwarp is breached by a major river system, and (d) when a stepped landscape due to the exposure of resistant lithology is formed. The location of the initial drainage divide controls the position of the later escarpment rather than rift-related faults. Redrawn from Gilchrist et al. (1994).

Quantitative methods like combined AFT and cosmogenic nuclide data indicate a significant landscape stability over at least the past million years as well; very low rates of retreat support the idea of the Great Escarpment of Namibia to have initiated

only a few kilometers oceanward of its present location. The initial location of the present Great Escarpment may have been controlled by a major inland drainage divide separating a low-gradient interior drainage regime from a higher-gradient exterior river system rejuvenated by marginal uplift due to flexural isostatic rebound (Cockburn et al., 2000; Bierman & Caffee, 2001; Van der Wateren & Dunai, 2001).

4. 2 Calculation of the material deposited offshore

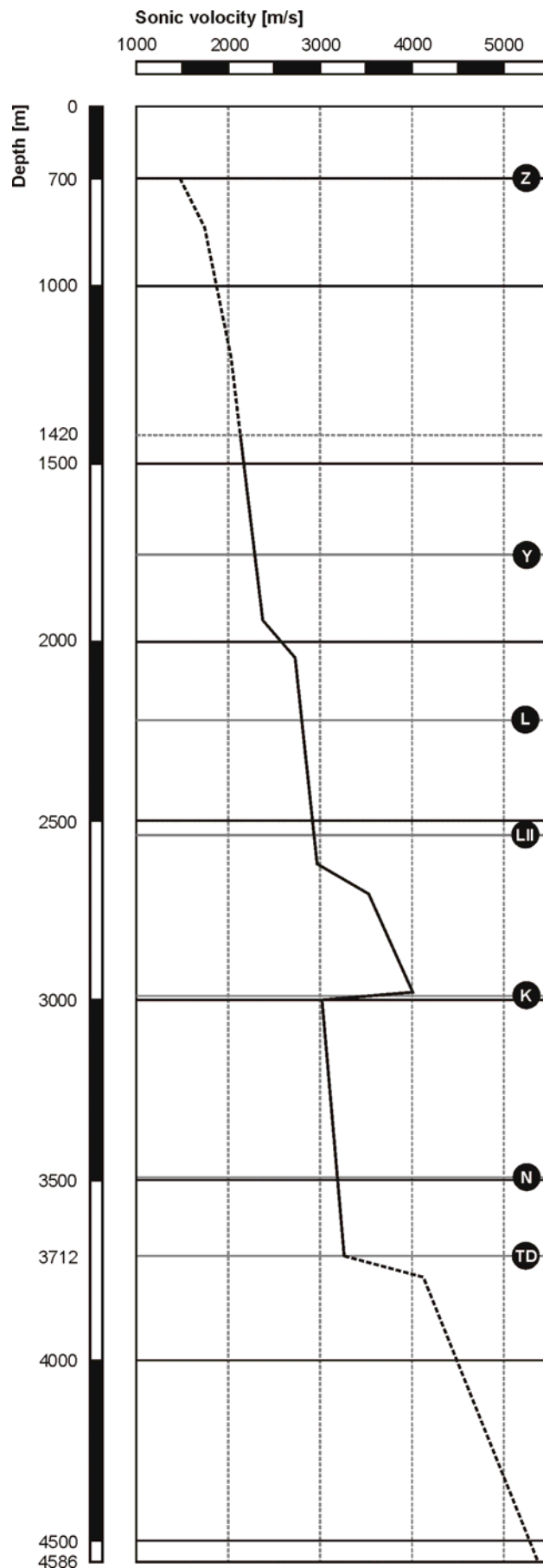
The offshore proportion of the model traverse is located in the central part of the Walvis Basin (fig. 4-2) for which abundant calibration data are available from well 2012/13-1 (see chapter 6) and from the seismic section ECL 89-41 (see chapter 3.6). Additional information can be projected into the section from the seismic line BGR 95-11 and well 1911/15-1 (fig. 4-2; Holtar & Forsberg, 2000). The ultimate goal of this approach is to link quantitatively uplift and erosion onshore with contemporaneous basin subsidence and sedimentation offshore within the framework of a well defined model traverse.

Seismic features and geodynamic aspects of the evolution of the central Walvis Basin are evaluated in chapter 3.6 in great detail. A quantitative view of sedimentation based on digital elevation models of selected depthconverted seismic marker horizons is presented here. The approach outlined above allows to compare the denudation history with the corresponding sedimentary evolution of the basin segment both qualitatively and quantitatively.

The offshore part of the model traverse receives the detritus supplied by the Uniab and Koigab rivers, respectively, if a pure transversal fluvial transport is assumed. The oceanward termination of the evaluated segment has been chosen so that the postrift sediments are supposed to have reached a negligible thickness, as derived from an extrapolation of the seismic section illustrated in figure 4-11a.

Depthconversion

2D information on the postrift succession in the central Walvis Basin is available in the form of a high-resolution seismic section displayed with a depth-scale in “seconds Two-Way-Traveltime (sTWT)”. In order to extract volumetric data from that, a depthconversion of the section has been performed. The essential information required for the depthconversion process is an idea of the depth-dependent sonic velocities of the basin fill. A point source for this type of data is the calibration well 2012/13-1 located close to the centre of the seismic section. The Final Well Report kindly made accessible by *NAMCOR* provides a detailed sonic log for the section from 1420m to 3712m of well 2012/13-1; a simplified version of this log is illustrated by the solid black curve in figure 4-9.



The uppermost and lowermost part of the sonic velocity profile has been inferred from well 1911/15-1 (dashed line in fig. 4-9; Holtar & Forsberg, 2000).

The simplified sonic log depicts a general increase in velocity from values of 1500m/s at seafloor to values of 5000m/s at 4,5km depth. This pattern is considerably modified by particularly high velocities in the intervals between 2600m and 3000m, and from 3800m downward, respectively. The upper interval clearly refers to the Maastrichtian sandy proportion of the overall shaly succession of well 2012/13-1; it represents a potential good quality reservoir rock for hydrocarbons (see chapter 6.4.2). An erratic increase in sonic velocity and thus an inverse velocity profile with depth characterises the base of the Maastrichtian which is also marked by the seismic horizon K.

Fig. 4-9. Simplified sonic velocity log of the postrift sedimentary succession in the central Walvis Basin. The interval from 1420m to 3712m is inferred from the Final Well Report of well 2012/13-1 kindly provided by *NAMCOR*; the uppermost and lowermost intervals, respectively, are derived from well 1911/15-1 in the northern Walvis Basin (Holtar & Forsberg, 2000). Seismic horizons are referred to in the text.

The lower interval with relatively enhanced sonic velocities is related to the basaltic and carbonaceous units W1 and W2 that have been inferred from well 1911/15-1 in the northern Walvis Basin (see fig. 6-3; Holtar & Forsberg, 2000); the basalts are suggested to represent the uppermost proportion of seaward dipping reflectors in that area.

Due to the lack of a 2D velocity section for the seismic line ECL 8941 (see fig. 3-6a) the 1D velocity log described above has been utilised to convert the depth-axis of the section from a TWT-display into a metric system. A number of 12 pseudo-wells has been evenly distributed along the entire offshore part of the model traverse parallel to the seismic section. Among those, well 2012/13-1 served as a reference well located in the centre of the seismic section (fig. 4-13a). The respective depths of the seafloor have been inferred from the bathymetric map illustrated in figure 4-2.

The velocity profile illustrated in figure 4-10 has then been applied to the basin fill by positioning its trend from the seafloor downward to the postrift sedimentary column in each of the pseudo-wells. This procedure accounts for the depth-dependency of the sonic transit time arising from increasing densities with burial depth of the sedimentary pile.

In chapter 3.6 the seismic features of the postrift succession of the central Walvis Basin have been discussed in detail (see fig. 3-13). Interpreted seismic marker horizons have been projected into the pseudo-wells in order to structure the basin fill seismically. The intervals between individual marker horizons in each of the pseudo-wells were transformed from their particular thickness in [sTWT] into their effective thickness in [m] by applying the corresponding segment of the velocity log to the individual interval. Calculation of the cumulative thickness below seafloor thus allows to construct the effective thickness of the postrift succession in each pseudo-well incorporating depth-dependent velocity variations.

Two types of depthconverted sections have been created with the procedure outlined above: (1) a rather simple 3-layer model that covers the entire offshore part of the model traverse and (2) a 7-layer model with higher stratigraphic resolution that is restricted to the length of the original seismic section.

The latter data set additionally allows to model the sonic velocity distribution within the seismic section geometrically (fig. 4-10). The gridding of the data has been performed with *SURFER* on the basis of the kriging-method (see Cressie, 1991 for the mathematic background). An anisotropy-variogram is incorporated into the gridding procedure in order to account for the anisotropy in the spatial distribution of crosspoints between pseudowells and seismic marker horizons which build the reference frame for the velocity model. The velocity contours are roughly parallel to the seafloor; slight modifications only occur below 3000m in the depositional centre

of the section. These might reflect a rather patchy distribution of carbonates in the early drift section whereas the majority of the basin fill is dominated by rather uniformly distributed shales.

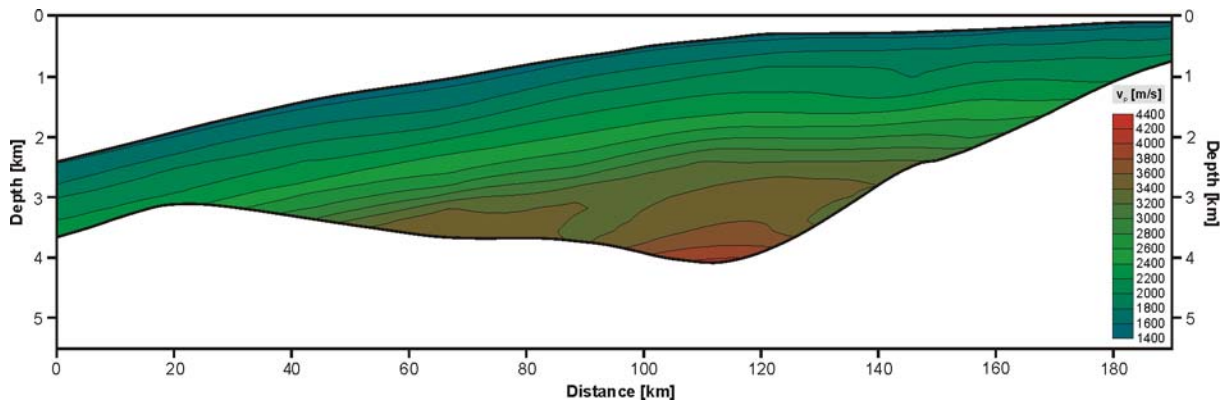


Fig. 4-10. Modelled sonic velocity section of the depthconverted seismic line ECL 89-41 as derived from the depthconversion-procedure; generated with *SURFER*. See text for details.

3-layer model

Four distinct seismic marker horizons have been depthconverted in order to obtain a wedge-shaped model of the postrift succession in the model traverse (fig. 4-11a). The horizons Q (Hauterivian/ Barremian acoustic basement), N (M.-Turonian), L (L./M.-Eocene), and Z (seafloor) subdivide the basin fill into wedges of roughly the same temporal extension (fig. 4-11b). Those parts that are not covered by the seismic line ECL 89-41 (fig. 4-2) have been extrapolated towards the coastline in the east as well as towards the west, until negligible thicknesses of postrift sediments are reached. In order to calculate the volume of each of these wedges, a 3D-digital elevation model of the seismic horizons Q, N, L, and Z has been established with *SURFER* corresponding to the width of the onshore part of the traverse (fig. 4-12). Since the volumes calculated between the individual horizons still possess significant porosity, a depth-dependent correction for pore space had to be performed so as to balance effective masses; the porosity-depth relation of Sclater & Christie (1980) has been applied (fig. 4-11c). The volume of the postrift sedimentary wedge had to be reduced for 17,5% porosity, on average.

The offshore masses computed for the wedges I, II, and III come up to 26000, 17800, and 14100km³, respectively (fig. 4-11a). Figure 4-11b illustrates the relative distribution of the accumulated sediments over time since breakup; the relative denudation chronology derived from AFT analysis (black line, see chapter 4.1.2) is displayed for comparison.

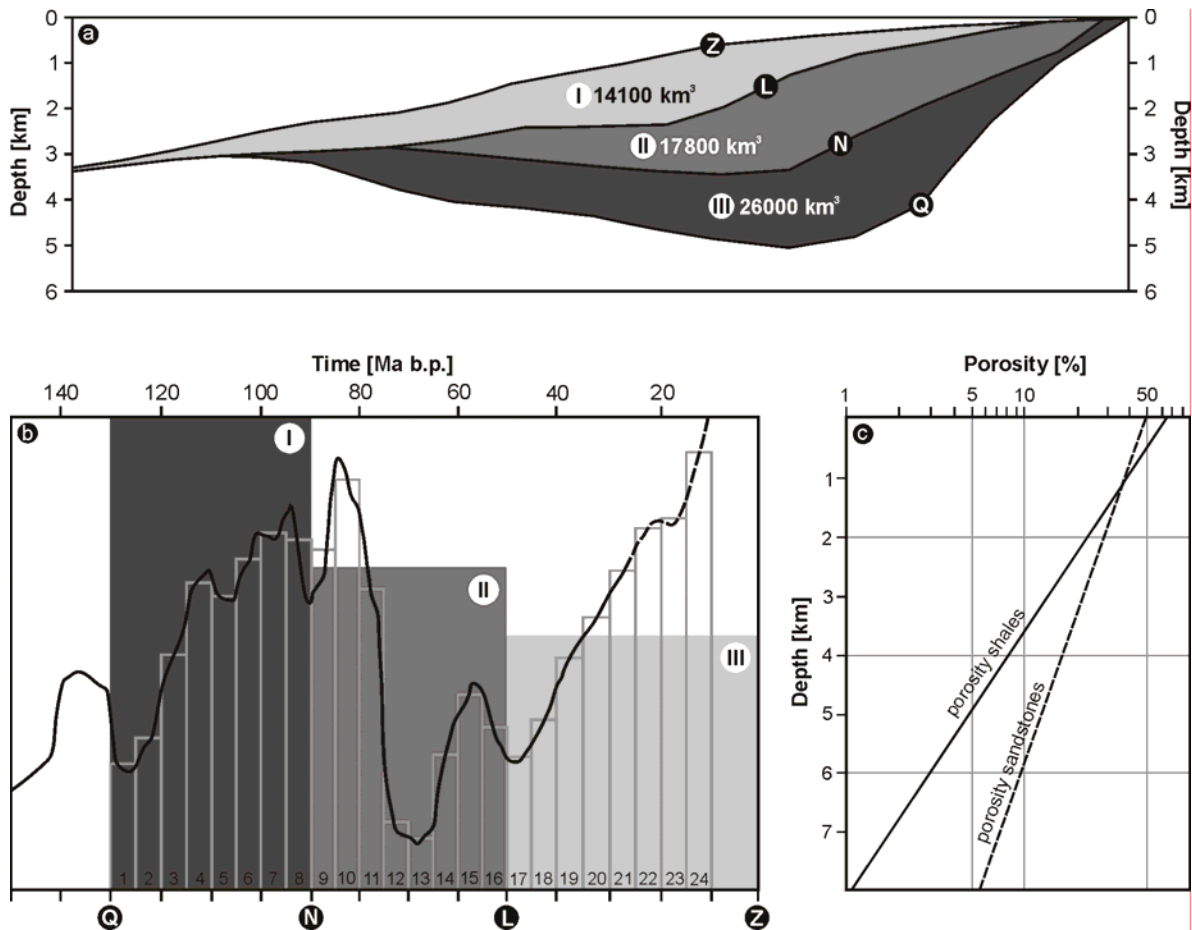


Fig. 4-11. Calculation of the material deposited in the offshore part of the model traverse during passive margin evolution. (a) wedge-shaped 3-layer model (I-III) of the postrift succession in the central Walvis Basin separated by seismic marker horizons; corresponding volumes are given in [km³]; (b) distribution of the accumulated volumes over time (grey boxes) compared with the relative denudation chronology (black line) inferred from AFT data (Gallagher & Brown, 1999, not to scale); (c) porosity-depth-relation after Sclater & Christie (1980) that was applied to reduce computed volumes for depth-dependent porosity in order to obtain effective masses. See text for discussion.

Depthconversion of the postrift succession not only reveals a pronounced wedge-shaped geometry of the basin fill with a very distinct depocentre and a marginal basement high to the West; it also indicates that the vast majority of sediment has been accumulated until the Early Tertiary (wedges I and II) and much of it even until the Late Cretaceous. This corresponds well to the quantitative denudation history discussed above. However, the total volumetric amount of postrift sediments calculated for the offshore part of the modelled section is as much as 57900km³. It is clear from the estimation of material eroded onshore, as discussed above, that even assuming a maximum thickness of the former cover of 5000m the sediment supplied to the adjacent basin segment (44000km³) is not sufficient to reproduce the stratal geometry observed offshore. The onshore contribution to the offshore deposition may therefore not exceed 76% if a pure transversal transportation system is assumed within the traverse.

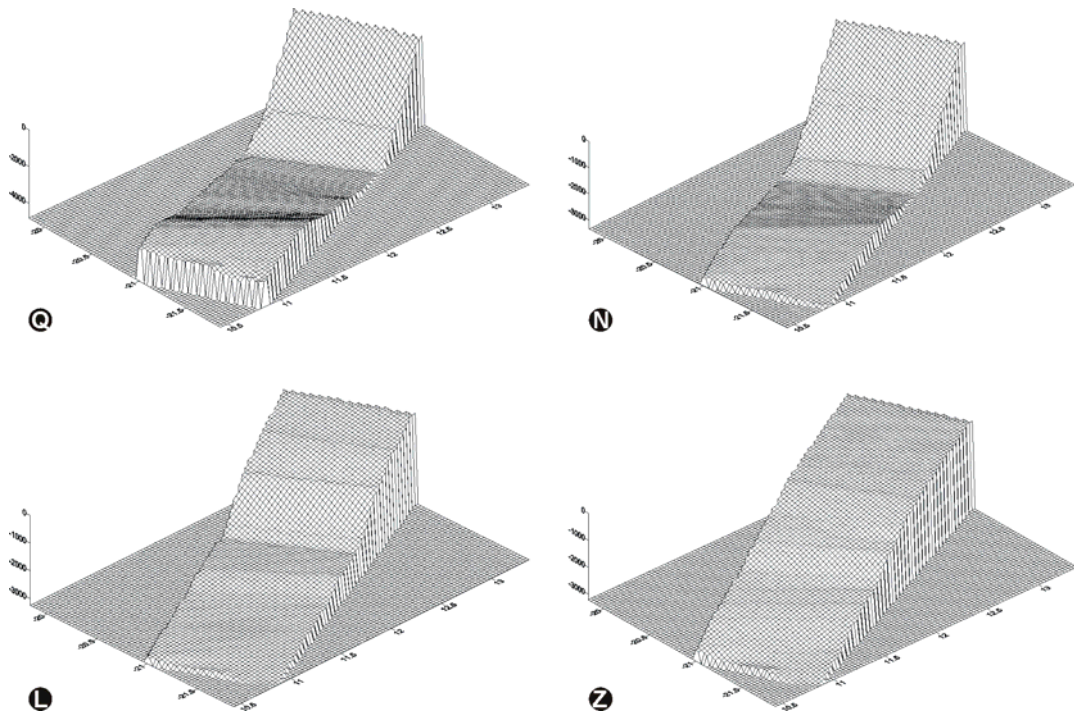


Fig. 4-12. Digital elevation models of the depthconverted seismic marker horizons Q, N, L, and Z within the model traverse which were used as reference surfaces for volume computations with *SURFER*.

7-layer model

Following the method described above, a depthconverted 7-layer model of the postrift succession has been established that is restricted to the length of the seismic section. The layers are bounded by the seismic marker horizons Q, N, K, LII, and L discussed in chapter 3.6; X and Y are auxiliary horizons; horizon Z represents the seafloor.

This approach enables a higher stratigraphic resolution for the volumetric quantification of the basin fill. Volumes of sediment deposited within the individual intervals have been calculated not by means of digital elevation models of the horizons but by calculation of areas of the single wedges that were transferred into volumes by incorporating the width of the model traverse.

The volumes of the individual wedges come up to 7540, 4540, 8980, 6070, 4980, 5630, and 9620km³, respectively (fig. 4-13a). As it has been outlined above, a correction for depth-dependent porosity has been applied in order to balance effective masses. A total volume of 47360km³ of postrift sediments is therefore represented by the seismic section ECL 89-41. Although the proportion covered by the seismic line is significantly smaller than the entire offshore part of the model traverse (fig. 4-2) the amount of postrift sediments is still in excess of the volumes provided by the onshore part of the margin segment. Furthermore, the temporal resolution of the 7-layer model allows to infer the relative accumulation rates of the

basin fill over time (fig. 4-13b). A good correspondence to both the denudation rates derived from AFT analysis as well as with the decompacted sedimentation rates inferred from 1D backstripped well data can be observed (fig. 4-7). Although the trend is somewhat smoother, a broad Late Cretaceous accumulation peak can be detected; it is followed by Early Tertiary low accumulation rates which rise again in Miocene times. Figure 4-7 therefore conspicuously demonstrates the quantitative link between denudation onshore and contemporaneous sedimentation offshore within the model traverse in one, two, and three dimensions.

A further stratigraphic refinement based on this model enabled the establishment of the highly resolved 15-layer model that has been applied in maturity modelling with *PetroMod2D* (see chapter 6.2.3.2).

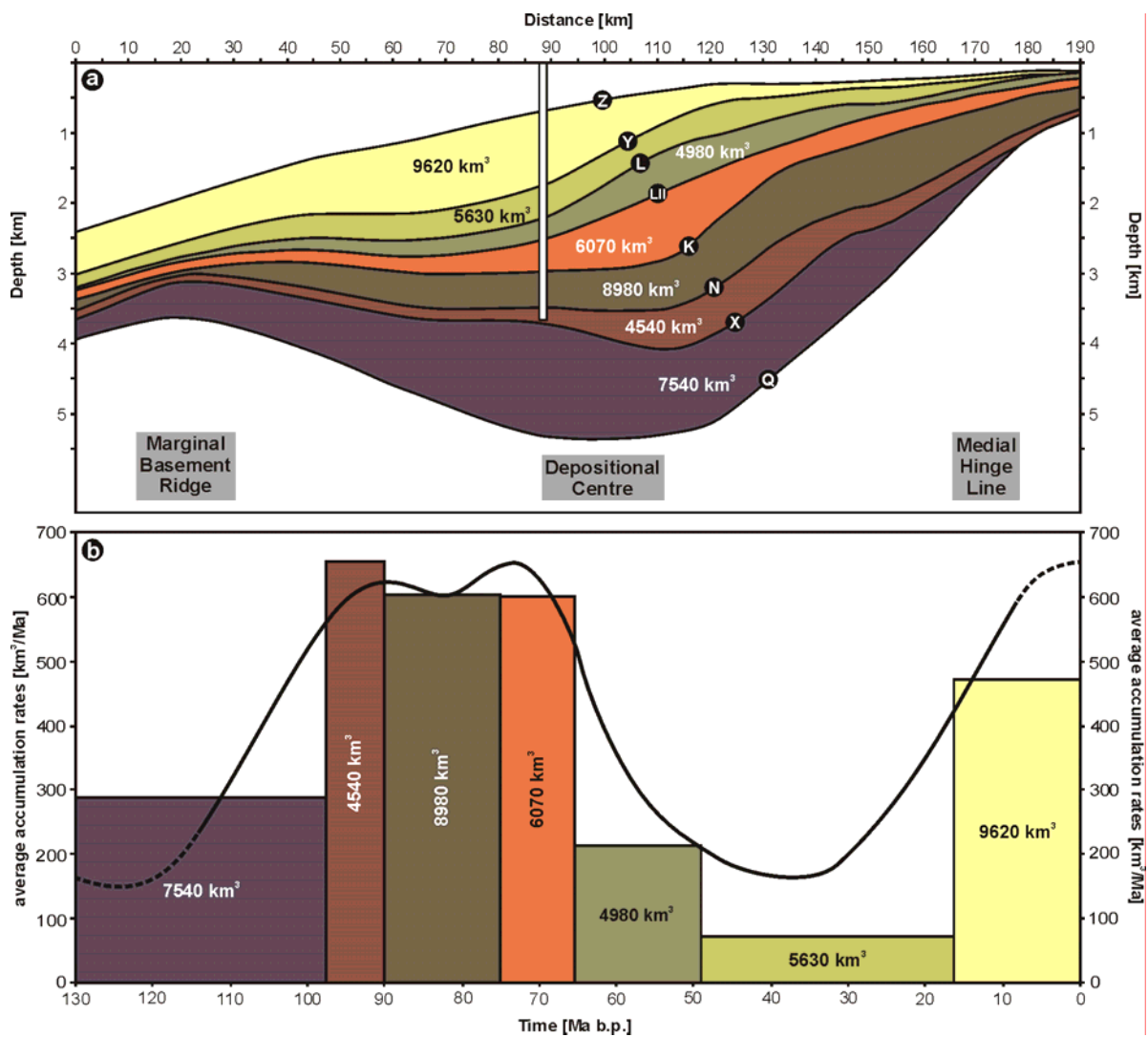


Fig. 4-13. (a) Depthconverted 7-layer model of the seismic section ECL 89-41 subdivided by the seismic marker horizons Q, X, N, K, LII, L, Y, and Z; corresponding volumes of accumulated material are inferred from area-calculations of the 7 wedges by incorporating the width of the model traverse; white bar indicates calibration well 2012/13-1. Major structural elements are inferred from Light et al., 1993. (b) Relative distribution of the accumulated volumes over time and calculation of the average accumulation rates (black curve) scaled in [km³/Ma]. See text for discussion.

4. 3 Petrography of Maastrichtian deep sea turbidite sands and implications for provenance

4. 3. 1 Microscopical analysis

The sedimentary postrift succession encountered in well 2012/13-1 (fig 4-2) is particularly dominated by deep-water shale deposition. Only minor silty interlayers and limestone stringers occur (see fig. 6-3). In the latest Campanian and Maastrichtian, however, fine to coarse-grained sandstones of turbidite origin prevail. Since these sands reveal promising porosity-permeability characteristics, they are discussed in terms of their reservoir potential for hydrocarbons in chapter 6.4.2. Additionally, as it has been outlined above, the Upper Cretaceous interval is a phase of outstanding relevance for both the denudational and depositional history of the Namibian margin as well.

Since the Maastrichtian sands apparently represent the only coarse clastics within the postrift succession, a microscopic evaluation regarding its composition and potential provenance is presented in this chapter. The gross sand interval ranges from 2660m to 2994m in well 2012/13-1. Ten cutting samples (K4, K5, K7, K9, K10, K12, K13, K14, K16, K18) that were kindly made accessible by *NAMCOR* have been taken between 2695m and 3000m; the corresponding depths for each sample are indicated in figure 4-15.

Detritic components	Volume range [%]
Quartz, monocrystalline, volcanic	5 – 35
Quartz, monocrystalline, plutonic	11 – 42
Quartz, polycrystalline, plutonic	0 – 2,3
Quartz, metamorphic	0 – 13
Potassium feldspar (microcline)	0 – 8
Plagioclase	2 – 14
Lithic fragments	2 – 12
Muscovite	0 – 1
Biotite	0 – 2,3
Chlorite	0 – 1
Opaque	0 – 5
Heavy minerals	0 – 1
Authigenic components	
Microcrystalline quartz	0 – 26
Dolomite	2 – 32
Pyrite	traces

Tab. 4-1. Overview of the petrographic composition of the Upper Campanian/ Maastrichtian gross sand interval within the postrift succession of well 2012/13-1.

A representative variety of cuttings of each sample has been embedded in epoxy resin and prepared as thin section. The petrographic composition of a selected rock fragment of each sample has been evaluated by means of a reticule-overlay that comprises 304 cells. Each cell has been analysed in terms of its prevailing petrographic composition which is roughly equivalent to the point counting method of Gazzi-Dickinson.

The most common framework grains include monocrystalline volcanic quartz, monocrystalline plutonic quartz, quartz of metamorphic origin, lithic fragments, and plagioclase. A list of all occurring mineralogical components including their volumetric spectrum is given in table 4-1; a detailed listing of the petrographic composition of each sample can be found in appendix 1.

The composition related to the particular sample depth is also illustrated in figure 4-14; detritic components as well as authigenic cementation are thereby considered. First-generation microcrystalline quartz-cementation dominates the upper part of the sampled section, whereas second-generation dolomite prevails in the lower part. Authigenic clay mineralisation appears to be negligible. Pore space and authigenic mineralisation are referred to in chapter 4.3.2 in more detail.

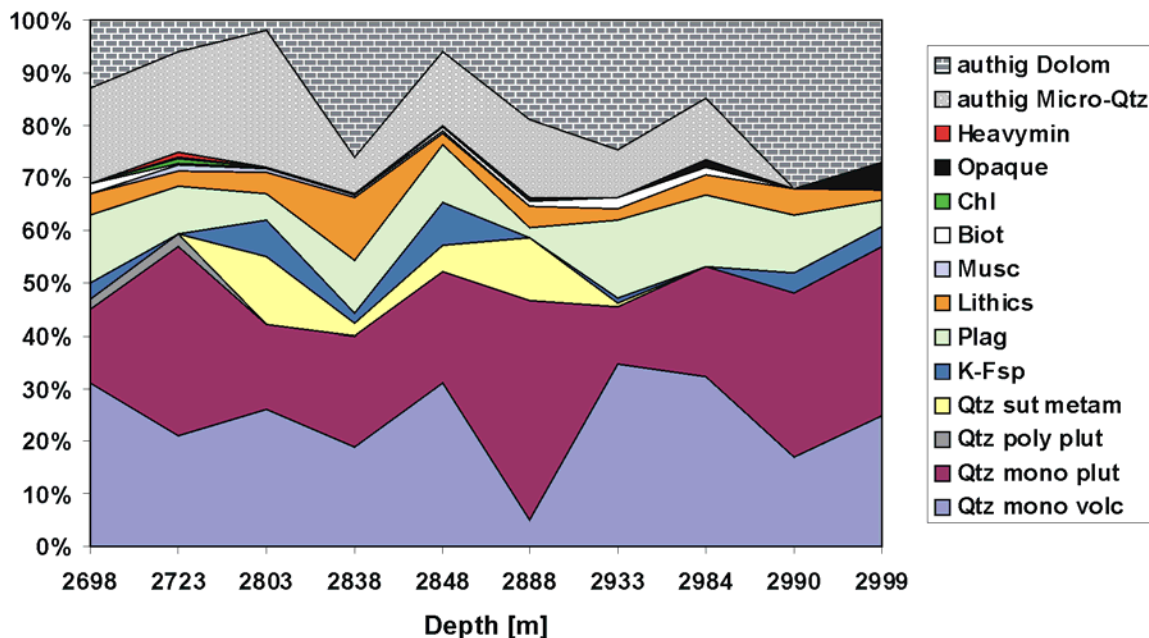


Fig. 4-14. Graphic overview of the cumulative petrographic composition [%] of the Upper Campanian/Maastrichtian gross sand interval from c. 2700-3000m within the postrift succession of well 2012/13-1. Abbreviations in legend related to table 4-1.

In the appendices 2-1 to 2-10 a general graphic overview of the petrographic features observed in the Upper Cretaceous sandy succession of well 2012/13-1 is presented; the width (w) of each photomicrograph is given in mm, respectively. All photos have been taken under crossed nicols, with the exception of appendix 2-8 (14_4). Volcanic monocrystalline quartzes can exemplarily be observed in the appendices 2-7 (13_8), 2-8 (14_3) and 2-9 (16_7). They are typically small, clear and show straight extinction; the angular habit reflects a proximal source. Corrosive grooves are also characteristic of volcanic quartzes (appendix 2-4, 9-7). Monocrystalline plutonic quartzes normally show undulose extinction combined with tracks of fluid and micro-

crystallite inclusions crossing under angles of c. 60° as visible in appendix 2-2 (5_4), 2-3 (7_9), and 2-10 (18_9).

In the appendices 2-5 (10_15) and 2-6 (12_6) the characteristic sutured contacts of recrystallised sub-grains of metamorphic quartzes can be observed. Plagioclase with polysynthetic twinning that makes up to 14 vol.% of the components is displayed in appendix 2-2 (5_8), 2-6 (12_5), and 2-9 (16_8), for example. Microcline, however, which is characteristic of a plutonic source is illustrated in appendix 2-8 (14_8) and 2-9 (16_1). One of the rather rare biotites is shown in appendix 2-1 (4_8); sample 4_5 on the same plate gives an impression of extensive second-generation cementation by dolomite which is preferentially restricted to coarse-grained intervals. Unfortunately, lithic fragments which would have been helpful source rock indicators are rather rare. Two rock fragments of fine-grained siliciclastic origin are presented in appendix 2-1 (4_6) and 2-5 (10_13). They might be attributable to the low-grade metamorphic siltstones and sandstones of the Late Proterozoic to Cambrian Damara Group. Further indicators for a sedimentary source are given by very well-rounded quartz grains in appendix 2-2 (5_4), 2-4 (9_9), and 2-10 (18_3), respectively. These grains are suggested to be of fluvial or even aeolian origin. Appendix 2-3 (7_5 & 7_9) displays well-rounded quartz grains showing quartz overgrowth which is a clear feature of sedimentary reworking.

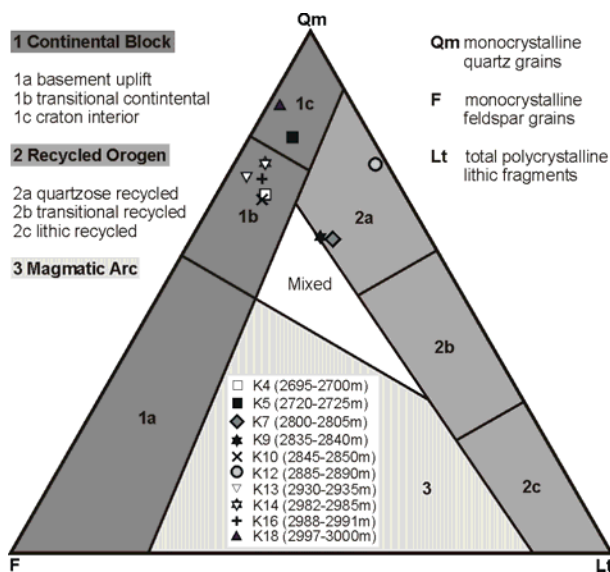
The Etendeka volcanic plateau is suggested to have covered a much more extensive area of NW-Namibia than its remnants do at present day (pers. comm. M. Raab, 2002). Therefore, sedimentary as well as metamorphic or plutonic sources indicate that the plateau must have already been eroded below its base when the Upper Cretaceous turbidite sands have been deposited; if not in the onshore part of the proper model traverse, then at least in a wider area that has influenced deposition in the central Walvis Basin by sediment supplied across the evolving margin. Furthermore, if the well-rounded quartz grains discussed above could have been unequivocally attributed to an aeolian source, even implications for potential aridification and thus for the origin of the Namib desert and the initiation of the Benguela current system would have been possible.

However, the deposition of the Upper Campanian to Maastrichtian coarse clastics in the central Walvis Basin document a phase of increased accumulation rates that corresponds to accelerated denudation rates onshore as it has been discussed before (fig. 4-7; chapter 4.1.2).

Triangular compositional diagrams are suitable to reflect the derivation of sandstones from various provenance terranes. Point counts of sandstones can be subdivided into fields that are characteristic of different kinds of plate tectonic settings. The petrographic composition analysed above has been plotted into a ternary Qm-F-Lt-

plot after Dickinson et al. (1983) in order to infer additional provenance information (fig. 4-15). Qm is the pole for exclusively monocrystalline quartz grains, F represents feldspar grains, and Lt is the pole for the total polycrystalline lithic fragments including quartzose varieties with more than three individual sub-grains. The positions of the boundary lines are empirical. All required information is included in the individual petrographic composition of each sample listed in appendix 1 from which the particular groups have been inferred and recalculated to 100%.

Figure 4-15 reflects a wider distribution of the Upper Cretaceous cutting samples around the Qm-pole of the ternary plot. Stable cratons with low relief (field 1c) generally produce quartzose sands from granite-gneiss basement and recycling of older strata (samples K5, K18). Quartzo-feldspathic sands are predominantly sourced from basement uplifts (field 1a) which are referred to as areas of high relief along rifts and strike-slip zones where erosion has cut deeply into the continental crust. Field 1b therefore indicates a transitional source rock area between a low-relief cratonic interior setting and a marginal basement high (samples K4, K10, K13, K14, K16). The occurrence of lithic fragments reflects some degree of recycling of orogens, either dominated by lithics (field 2c) or by quartz (field 2a); the samples K7



and K9 therefore indicate that at least in part metamorphic basement levels have been uplifted and exposed to erosion.

Fig. 4-15. Provenance analysis of Upper Cretaceous sands of well 2012/13-1. Ternary Qm-F-Lt-plot modified from Dickinson et al. (1983). Sample names, symbols, and related depths are given by the inset in field 3. See appendix 1 for counted and recalculated parameters. The majority of samples reveals a basement or cratonic source (field 1a, 1b); 3 samples indicate recycling of orogens (field 2a).

Although relatively general, these provenance settings support the idea of a source rock area that is not dominated by the denudation of a huge volcanic plateau alone. The petrographic signature displayed by the ternary plot of figure 4-15 clearly indicates a clastic contribution supplied by basement or cratonic source rock areas that must be older than the Etendeka flood basalts and quartz latites. A variety of source rocks relatively similar to the geology exposed at the surface at present day (see fig. 2-3) is suggested to have already existed in the Upper Cretaceous.

Due to a lack of more significant provenance information reflected by individual lithic rock fragments, quartz grain varieties have been evaluated in order to refine the source rock information inherited in the Upper Cretaceous turbidite sands of well 2012/13-1. Quartz grains of definite volcanic, plutonic, and metamorphic origin have been extracted from the petrographic composition illustrated by figure 4-14 and were recalculated to 100% (fig. 4-16). Although volcanic rocks of the Etendeka plateau are expected to serve as predominant source rocks during the entire postrift evolution of the margin, only 10-75% (less than 50% on average) of the quartz grains found in the Upper Cretaceous sands can unequivocally be attributed to a volcanic source. Roughly 50% of the quartzes are derived from a plutonic origin and locally up to 20% are metamorphic quartzes.

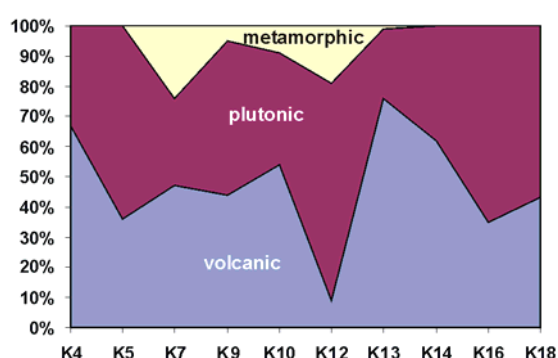


Fig. 4-16. Provenance analysis of Upper Cretaceous sands of well 2012/13-1 using quartz grain varieties (cumulative percentages). Although the Etendeka volcanic plateau is suggested to be the prominent source area, less than 50% on average are of volcanic origin. Plutonic and metamorphic quartzes of probably basement origin constitute a major contribution.

This observation does not only support the idea of a rather diverse geology exposed to erosion in Upper Cretaceous times, it also provides first quantitative constraints on relative contributions of volcanic or non-volcanic rocks. Rather less than 50% of the detritus observed in the offshore part of the model traverse (fig. 4-2) appears to be sourced from Etendeka volcanics, whereas rather more than 50% might possibly be derived from metasedimentary rocks of the Damara Group or by granitoid rocks that intruded into the Damara basement in the Late Proterozoic (e.g. Torrabay Granite, Mile 110 Granite, Durissa Bay Granite) or during Early Cretaceous breakup (e.g. Cape Cross Granite, Brandberg intrusive complex).

This quantitative approach to the denudation history of the margin inferred from basic provenance studies corresponds well to the concept of a very efficient Cretaceous denudation that arises from fission track analysis (chapter 4.1.2). Furthermore, the conclusion that a proportion of roughly 50% of the Upper Cenomanian and Maastrichtian detritus encountered in the offshore part of the model traverse can probably not be related to the adjacent onshore source area, can explicitly be supported and reproduced by basin modelling with *STRATA* (see chapter 4.5 & 5.4).

4. 3. 2 SEM analysis

Scanning electron microscope (SEM) analysis has been utilised to refine the results obtained from microscopic thin section analysis both in terms of the petrographic composition as well as in terms of the potential provenance of the Upper Cretaceous sands encountered in well 2012/13-1. Since the method is capable of attaining 3D grain relationships, SEM analysis is a powerful tool to assess the reservoir properties of sandstones, as briefly outlined in chapter 6.4.2. Combined with an energy dispersive X-ray (EDX) system, SEM analysis is useful to identify the geochemical composition and the distribution of minerals in great detail. Authigenic clay mineralisation in sandstones, for example, is one of the most problematic features affecting permeability in potential reservoir sandstones (e.g. Wilson & Pittman, 1977; Pittman, 1989).

Methodology

A selection of eleven samples (listed below) ranging in depth from 2695m to 3144m has been prepared for SEM analysis. Drill cuttings from 3-10mm in size showing fresh surfaces have been selected. Any fine debris on the surface or artifacts from breaking the rock must be avoided. For best results, the samples should be handled with disposable gloves and tongs throughout the preparation process, because skin oil from fingers would outgas in the SEM vacuum system, thus degrading the image.

Sample name	Sample depth [m]	
K4	2695-2700	Samples are attached to a SEM specimen plug made of aluminium with a carbon adhesive so that an electrical ground from the sample to the plug is provided. The attached samples are then dried overnight in a low-temperature drying oven (50°C). In order to obtain a clear image of the electrically insulating rock material, the sample has to be coated with a thin conductive material such as carbon or gold in a sputter; carbon has been used here to avoid any interference during EDX analysis of minerals.
K6	2770-2775	
K7	2800-2805	
K9	2835-2840	
K10	2845-2850	
K12	2885-2890	
K14	2982-2985	
K15	2985-2988	
K17	2991-2994	
K18	2997-3000	
L20	3141-3144	

The coated samples are placed in the sample chamber which is evacuated to a high vacuum ($>10^{-4}$ mbar); a *ZEISS Digital Scanning Microscope DSM 960* has been applied during this study. SEM images are formed by an internally generated electron beam which is created by heating a “hairpin” tungsten filament until electrons are emitted. The electrons are accelerated by an accelerating high voltage of 5-30kV; in

this study constantly 20kV have been applied. This beam is demagnified and focussed through a series of electromagnetic lenses into a finely focussed electron beam of typically 0,01 μ m in diameter that bombards the sample; the spot size controls the resolution of the image. A stigmator, however, controls the shape of the (ideally circular) beam and apertures minimize lens aberrations.

The interaction of the primary electron beam with the atoms of the sample simultaneously produces various forms of radiation depending on the penetration depth of the electrons. Among those are Auger electrons from the very surface, secondary electrons, backscattered electrons, characteristic X-rays, and continuous or background X-rays. The remainder of the radiation is dissipated into heat. In geologic analysis primarily the secondary electrons (SE image), the backscattered electrons (BSE image), and the characteristic X-rays (EDX spectrum) are used, each collected with a specific detector. The sample is vertically placed in the sample chamber so that it is located in the focus of the electron beam with a distinct distance to the BSE-detector straight above the sample. That distance may vary depending on the aspired magnification factor. In this study, a distance of 20-18mm has been applied.

Collecting the relatively low-energy secondary electrons generated by the primary beam with a SE-detector enables a typical 3D topographic image (SEI) of the sample to be processed. Secondary electrons emitted from relatively close to the surface (a few 10s of nm) are detected with a positively charged metallic net which is located inclined above the sample.

Backscattered electrons (BSE) of relatively higher energy are emitted from somewhat deeper (a few μ m) in the surface of the sample. Since they are faster as well, the emission occurs in straight paths away from the sample following a Gaussian distribution. The related BE-detector (*Robinson detector*) is therefore located straight above the sample. Due to the interference with the orbiting electrons of the sample atoms, the energy of the BSE is the higher, the higher the atomic number of the activated atom is. BSE images (BEI) are therefore capable of illustrating a qualitative chemical contrast of the sample. Ore minerals like pyrite can easily be identified on a BEI by their bright colours.

An energy dispersive X-ray (EDX) system yields a relatively quick and simple semiquantitative elemental analysis by collecting characteristic X-rays produced by ionisation of sample atoms. The primary electron beam ejects electrons from the inner shells of the sample atoms. To regain stability, electrons from the outer shells replace the inner shell vacancies; this transition releases element-specific amounts of energy in the form of X-rays. The strongest and most characteristic of these transitions is produced when a vacancy in the innermost K-shell is replaced from the

proximate L-shell (K_{α} X-ray). Major elements in a sample will yield specific energy peaks (in keV) when plotted against the count rate. Since the majority of peaks found in rock forming minerals will be common elements such as silicon (Si), aluminium (Al), potassium (K), magnesium (Mg), iron (Fe), calcium (Ca), or sodium (Na), the identification of characteristic element peaks can be automated to some degree; the *LINK ISIS* software has been applied in this study. The relative concentration of the identified elements is roughly proportional to respective peak heights. Therefore, a correlation of the peak distribution pattern with the chemical formula of the most common minerals is possible.

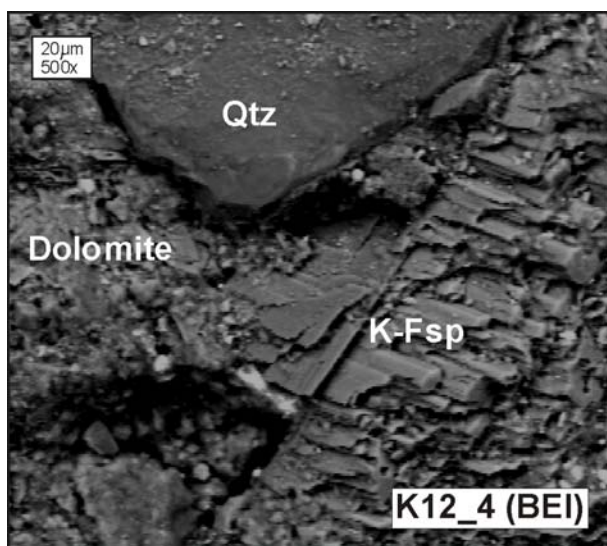
EDX analysis can either be applied as a spot measurement for a quick assessment of the chemical composition of a distinct mineral observed in the SE or BSE mode; additionally, semiquantitative mapping of the concentration of elements in a defined proportion of the sample is possible. Thereby, the primary electron beam scans a specific area with a defined spatial and temporal resolution. The relative concentration of elements is calculated with *LINK ISIS* on the basis of the areas enclosed by the specific peaks; these have to be corrected for the background X-rays. Further corrections have to be made for the atomic number (Z), absorption (A), and the fluorescence (F) of elements (“ZAF correction”).

A brief introduction to SEM analysis combined with an atlas for the identification and interpretation of minerals commonly found in clastic reservoir rocks is given by Welton (1984); see also www.reclot.de for a SEM-short course in German.

Results: petrographic features and implications for reservoir quality

The eleven samples of Upper Campanian and Maastrichtian sandstone listed above have been analysed with the SEM in terms of their composition, pore space properties, and diagenetic features. Additionally, further information on the surfaces of the well-rounded quartz grains (appendix 2-10, 18-3) was expected; unequivocal identification of aeolian quartz grains would have had significant impact on the interpretation of paleoclimate.

As it is illustrated by figure 4-14, quartz grain varieties and authigenic mineralisations of micro-quartz and dolomite constitute the majority of the components found in the Upper Cretaceous sandstones of the central Walvis Basin. This observation corresponds to the topographic impressions provided by SEM analysis of these rocks.

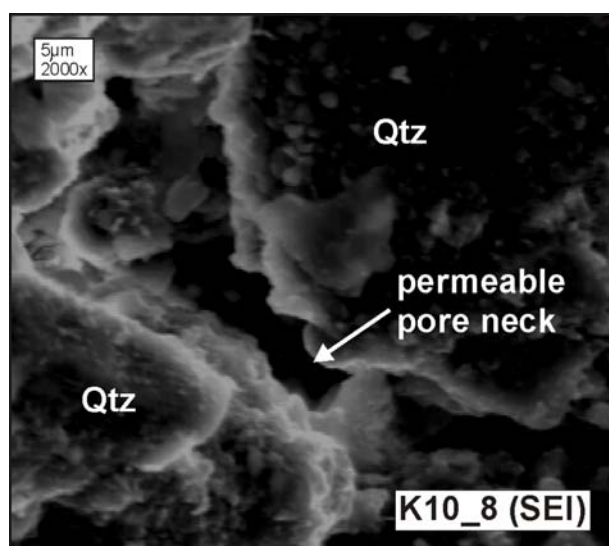


Appendix 3-1 represents an overview of the most common compositional features observed in the SEM. Quartz grains are readily identifiable from their glassy fractured surfaces (appendix 3-1, K14_1, K15_1, K18_2). They form the vast majority of the detrital components.

Fig. 4-17. SEM image (BEI) showing detrital quartz and potassium feldspar, cemented by authigenic quartz. Magnification: 500x. Sample depth: 2885-2890m.

Commonly, the quartzes are embedded in a blocky matrix of diagenetic dolomite (appendix 3-1, K4_2, K17_8). One of the rare examples of clearly identifiable potassium feldspar is displayed in figure 4-17 (sample K12_4, BEI). Feldspar can be recognised by its sparry habit; additionally, an EDX spot measurement revealed a characteristic peak distribution of K, Si, and Al.

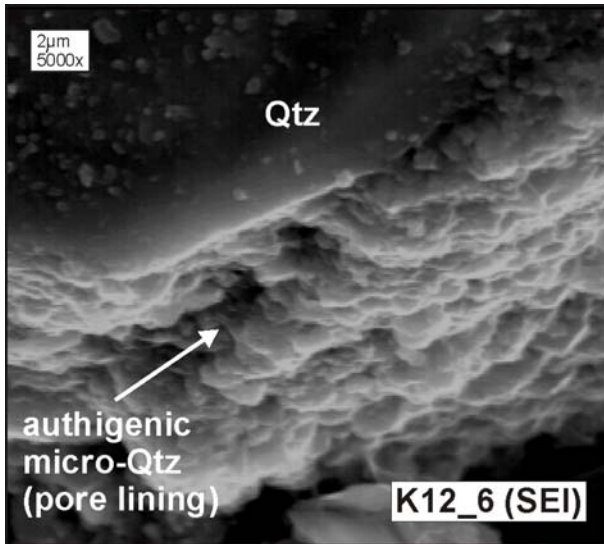
Most of the pore spaces appear to be filled with diagenetic mineralisations of dolomite, as seen above. But nevertheless, an average porosity of 16% within the Upper Cretaceous sandstone indicates that a promising amount of makro- (and micro-) pores remains unfilled by diagenetic minerals (appendix 3-2, K4_3, K10_7, K15_5). Since a first-generation cementation by micro-quartz tends to thinly coat



grains, pore necks remain permeable in intervals where this type of diagenesis prevails (fig. 4-17; appendix 3-2, K7_6, K9_8, K10_8). Second-generation cementation by dolomite seems to be the major limiting factor for permeability.

Fig. 4-18. SEM image (SEI) showing a permeable pore neck between relatively weakly cemented detrital quartz grains. Magnification: 2000x. Sample depth: 2845-2850m.

Appendix 3-2 (K9_1, K12_16, and K12_19) indicates that dolomite rhombohedrons are capable of plugging pore necks. Only locally, authigenic pyrite which can be easily recognised by its white colours on a backscattered electron image (appendix 3-2, K17_4) becomes abundant and fills pore spaces.



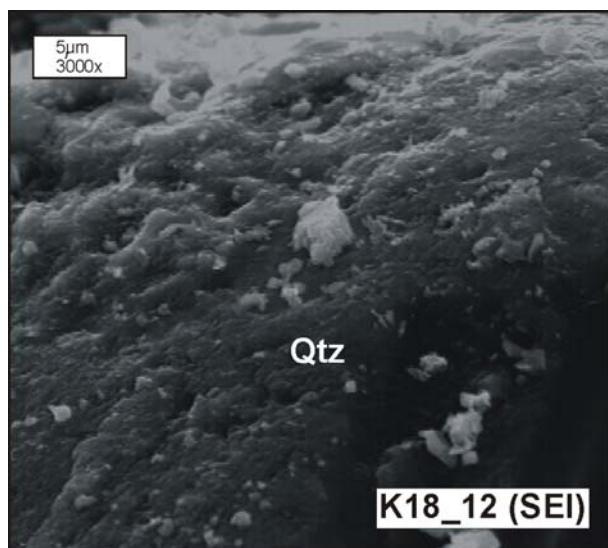
Generally, diagenesis of the Upper Cretaceous sands is characterised by a first generation of cementation by microcrystalline quartz. Although it reaches locally up to 26% of the volume, micro-quartz normally forms isopacous grain coats and rather rarely fills the entire pore space.

Fig. 4-19. SEM image (SEI) showing a detrital quartz grain coated by an equigranular authigenic overgrowth of microcrystalline quartz. Magnification: 5000x. Sample depth: 2885-2890m.

Microcrystalline quartz is suggested to be generated by formation water supersaturated with silica that is derived from pressure solution of radiolaria and diatoms in interbedded mudstones; it influences porosity to a subordinate degree, containing itself abundant microporosity. Figure 4-19 and appendix 3-3 (K6_6, K9_10, K12_6, K15_3, K15_7) illustrates detrital quartz grains rimmed by authigenic equigranular quartz overgrowths of generally rhombic habit; these pore linings reveal thicknesses in the order of 2-5µm.

In a second diagenetic stage, cementation was clearly dominated by authigenic dolomite formation probably derived from pressure solution of calcareous microfossils like planktonic foraminifera. Dolomite is predominantly restricted to the coarse-grained intervals and reaches up to 32 volume% of the components. Since the relatively idiomorphic dolomite rhombohedrons reach sizes in the order of 20-100µm that tend to fill pores (appendix 3-3, K9_2, K10_5, K12_8, K18_8), dolomitic cement is suggested to be the major limiting factor for the potential reservoir properties of these sands. Cementation by authigenic clay minerals like kaolinite or illite could not be identified, neither with the petrographic microscope nor by detailed SEM analysis; their effect on porosity and permeability is therefore suggested to be negligible.

An overview of rather unique features observed during SEM analysis is given in appendix 3-4. The samples K10_13 and K12_13 give very rare impressions of filamentous minerals protruding into the pore space; they could not be identified unequivocally but they are suggested to be rather detrital mica minerals (muscovite or biotite) than authigenic illite.



The samples K18_11 and K18_12 in appendix 3-4 and figure 4-20 exemplarily illustrate surfaces of relatively well-rounded quartz grains. Unfortunately, they lack the characteristic bouncing features that are associated with saltation during aeolian transport.

Fig. 4-20. SEM image (SEI) showing the scarred surface of a well-rounded detrital quartz grain. No indicators of aeolian transport can be observed. Magnification: 3000x. Sample depth: 2997-3000m.

Evidence of a significant degree of aeolian sedimentation in the Upper Cretaceous would have had serious impact on the evaluation of paleoclimate and possibly even on the onset of aridification and the related Benguela upwelling system.

Appendix 3-4 (K12_22, BEI) displays a quartz grain embedded in an intensely weathered plagioclase. A spheroidal feature observed in sample K17_3 (SEI) could not be clearly identified; its shape as well as a distinct calcium-peak in the EDX spot measurement indicates an organic origin (possibly a fecal pellet). Dispersely distributed authigenic pyrite on a fractured surface of a quartz grain can be observed in appendix 3-4 (K18_5, BEI).

Pore spaces of four selected samples (K4, K9, K12, K18) filled with diagenetic cements have been analysed chemically by semiquantitative EDX mappings following the method outlined above (appendices 4-1 to 4-4). Since the detritic (allogenic) and authigenic minerals that were to be expected were already known from the petrographic analysis described above, five preferential elements could be selected for semiquantitative mapping: calcium (Ca), magnesium (Mg), silicon (Si), potassium (K), and iron (Fe); no standard minerals needed to be measured for reference. Each sample has been scanned for c. 8h and was evaluated with *LINK/ISIS*.

The relative frequency of each element is given in grey scales in the appendices 4-1 to 4-4, whereby the darker colours represent the higher content, respectively. A backscattered electron image of each sample is added to provide a general

impression of the element contrast within the scanned area. The rather bad quality of appendix 4-1 (sample K4) is due to problems during scanning which is regretted. The contents of calcium and magnesium, respectively, illustrate very well the distribution and predominance of authigenic dolomite in the pore spaces. Detrital quartz grains can be inferred from the silicon content. Potassium, however, has been mapped in order to assess the significance of detrital micas and authigenic clay minerals; it is obvious from the respective K-mappings that these are very finely dispersed and play a rather subordinate role. Mapping the iron content is a powerful tool to estimate the proportion of ore minerals like authigenic pyrite. Pyrite is indicated by loosely dispersed black spots in the particular Fe-maps. Appendix 4-4 additionally indicates a concentric zonal arrangement of Fe within the dolomite cements of sample K18.

4. 4 Geochemical signature of the basin fill and representative onshore samples – implications for provenance

Methodology

X-Ray fluorescence (XRF) spectrometry is a non-destructive method to analyse the geochemical composition of whole rocks both qualitatively and quantitatively. A high power X-ray tube bombards a sample with primary X-rays; the elements present in the sample as well as their concentrations can be determined by evaluating the secondary (fluorescent) X-rays released by the sample with a wavelength-dispersive spectrometer (e.g. Taggart et al., 1987).

A selection of 19 cutting samples of well 2012/13-1 and 11 samples representative of the geological succession eroded onshore have been prepared for whole-rock geochemical analysis; sample names, lithologies, sample depths as well as stratigraphy and locations of the onshore samples are listed in appendix 5. In order to get a reliable average geochemical analysis of a rock, representative samples have been each milled down to homogeneous rock powders with a jaw crusher and an agate ring pulveriser. The weight loss on ignition (LOI) has been determined for each sample by drying at 105°C and ignition at 1050°C for 1h30min, respectively (appendix 6); the LOI is predominantly due to the calcination of CO₂ out of carbonaceous minerals, either detritic or authigenic.

For analysis, a pressed pellet and a glass disk has been prepared for each sample. Pressed powder pellets generally yield satisfying results for trace elements and volatile elements like S or HG. Glass disks, however, provide excellent homogeneity and reduced particle size effects.

Pressed pellets with a diameter of 33mm have been produced by mixing 4,0000g of powdered and dried sample material homogeneously with 1,0000g of *HOECHST-*

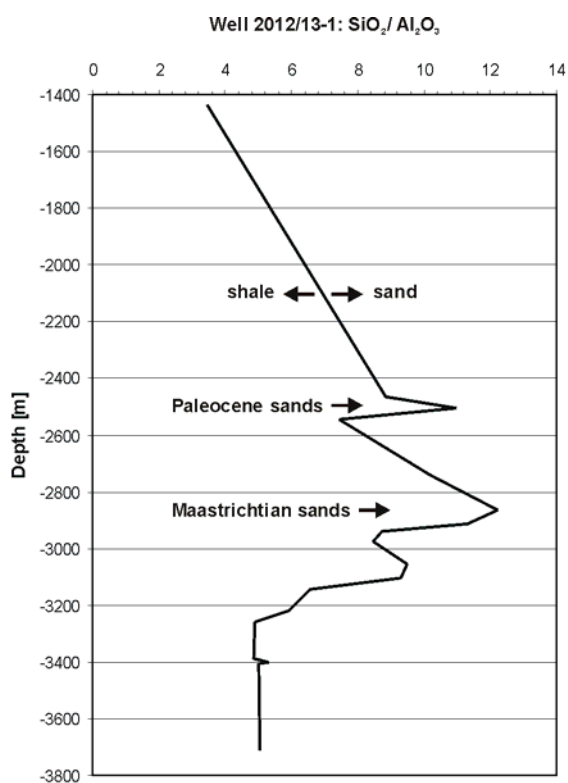
wax C. The sample was then consolidated with a pressure of 294,2kN for 1,5s in a hydraulic press.

For the glass disks an amount of 1,0000g of powdered and dried sample material has been fused with 4,0000g of *MERCK A12* flux (66% $\text{Li}_2\text{B}_4\text{O}_7$ +34% LiBO_2) and melted in a platinum-crucible (95%Pt+5%Au); the melt was then casted into a homogeneous glass disk.

The carefully prepared samples have been analysed with a *Philips PW2404* XRF-facility. Six analyser-crystals allow elements with atomic numbers from 6 (carbon) to 92 (uranium) to be measured. Oxides of major elements are reported in weight-percent [wt%] whereas trace elements are reported in parts per million [ppm]. The detection limit depends on the atomic number, the way of preparation and the configuration of the spectrometer. However, the general limit of detection is in the order of 3ppm; for the volatile elements sulphur (S) and fluorine (F) it is suggested to be 50ppm and 100ppm, respectively.

Appropriate calibration standards similar to the analysed samples need to be chosen in order to control the reproducibility of the results provided by the spectrometer. An ensemble of 40 established standard reference samples have been analysed together with the samples listed in appendix 5; each element has been compared with its specific calibration curve.

Results



An amount of 40 elements has been analysed quantitatively in each of the 19 offshore and 11 onshore samples, respectively (appendices 7 & 8). The 10 major elements are given in [wt%], 30 additional elements are reported in [ppm]. In the appendices 9-1 & 9-2 the results for the offshore samples are plotted versus depth in order to get an idea of the geochemical signature of the sedimentary succession in the central Walvis Basin.

Fig. 4-21. Plot of the $\text{SiO}_2/\text{Al}_2\text{O}_3$ -ratio versus depth to approximate the sand-shale-ratio in well 2012/13-1.

The SiO_2 -content of the overall siliciclastic succession is relatively low which might indicate an effect of dilution by carbonates represented by CaO . A general increase in SiO_2 is recorded with depth culminating within the Upper Cretaceous sands between c. 2600m and 3000m depth; below that interval SiO_2 decreases again. If the $\text{SiO}_2/\text{Al}_2\text{O}_3$ -ratio is plotted versus depth a good quantitative approximation of the sand-shale-ratio in well 2012/13-1 can be determined (fig. 4-21); Paleocene sands at c. 2500m depth as well as the bulk Maastrichtian sands between 2800m and 2900m depth (see fig. 6-3) are clearly indicated.

The general geochemical signature of the cutting samples from well 2012/13-1 is very typical of passive margins. This can be inferred from plotting SiO_2 versus $\text{K}_2\text{O}/\text{Na}_2\text{O}$ after Roser & Korsch (1986; fig. 4-22a) as well as by plotting $\text{K}_2\text{O}/\text{Na}_2\text{O}$ versus $\text{SiO}_2/\text{Al}_2\text{O}_3$ after Maynard et al. (1982; fig. 4-22b); the latter plot has the additional advantage that the dilution effect of biogenic carbonate can be eluded. Passive margin type sandstones are generally enriched in SiO_2 and depleted in Na_2O , CaO , and TiO_2 due to their highly recycled and matured nature. There is a progressive increase in $\text{K}_2\text{O}/\text{Na}_2\text{O}$ and $\text{SiO}_2/\text{Al}_2\text{O}_3$ from oceanic island arc (ARC) to active continental margins (ACM) towards passive margins (PM in fig. 4-22; e.g. Bhatia, 1983; Roser & Korsch, 1988).

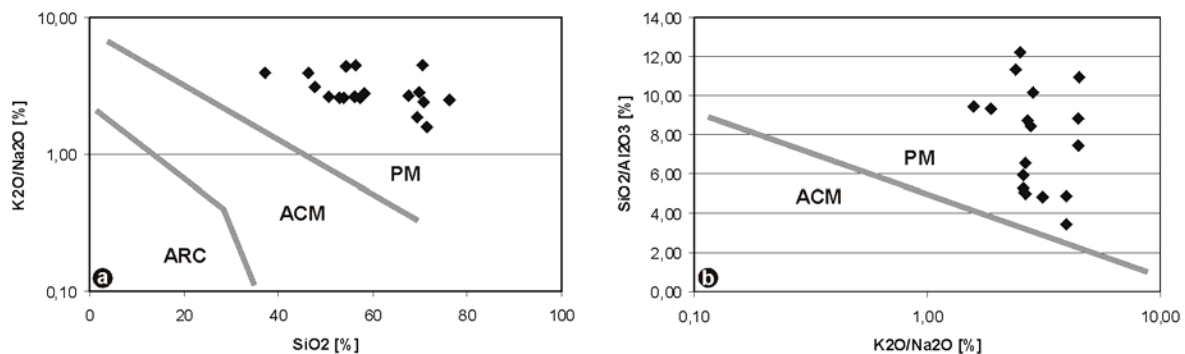


Fig. 4-22. Tectonic discrimination diagrams for sandstones. Both diagrams reveal typical quartz-rich passive margin settings for the offshore samples. (a) Plot of $\text{K}_2\text{O}/\text{Na}_2\text{O}$ versus SiO_2 after Roser & Korsch (1986); ARC = oceanic island margin, ACM = active continental margin, PM = passive margin. (b) Plot of $\text{SiO}_2/\text{Al}_2\text{O}_3$ versus $\text{K}_2\text{O}/\text{Na}_2\text{O}$ after Maynard et al. (1982).

Plotting TiO_2 [%] versus the Ni-content [ppm] enables some more detailed constraints on provenance to be made; passive margin sediments can be attributed to either an acidic or a basic geochemical source area (Floyd et al., 1989). Figure 4-23 clearly depicts a derivation from magmatic rocks of acidic composition for the majority of the offshore cutting samples. At first sight, this appears to be rather inappropriate as the Etendeka flood basalt province is suggested to provide most of the detritus supplied to the central Walvis Basin. However, as microscopical analysis has already shown,

less than 50% on average of the quartz varieties observed in Upper Cretaceous sandstones are of volcanic origin (fig. 4-16). Among those the majority is suggested to be derived from the quartz latite rheognimbrites that are less susceptible to erosion than the tholeiitic basalts of possibly from Damaran metasedimentary rocks. Figure 4-23 might therefore reflect the overall prominent contribution of deeply eroded granitoid rocks emplaced in the Damara basement of the coastal plain to the detritus supplied to the evolving margin.

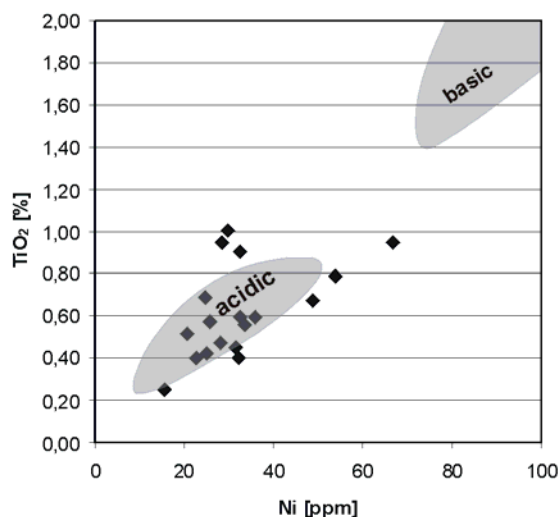


Fig. 4-23. Plot of TiO_2 versus Ni for the offshore samples. Grey fields (after Floyd et al., 1989) indicate magmatic source rocks of acidic composition.

The geochemical signature of the basin fill illustrated in appendix 9 allows relatively analogue conclusions to be drawn. Several indicative elements reveal a distinct increase from depths of 2850m to 2900m downward. Cerium (Ce) which is a rather stable and immobile element that occurs in detrital monazites increases rapidly with depth; it might be derived from granitic sources. Likewise, barium (Ba) shows a distinct increase in the lower proportion of the basin fill. Barium is a typical trace element of potassium feldspars that are abundant in granitoid rocks. However, as Ba is a relatively mobile element, it could

be of diagenetic origin as well but should then be positively correlated with strontium (Sr); this appears not to be the case in well 2012/13-1 (appendix 9-1). Therefore, both elements, Ce and Ba, indicate the affection of granitoid rocks by erosion even during the very early basin evolution.

Titanium (Ti) is an indicative element of ilmenite which is a typical product of the differentiation of basic magmas; it might occur in various magmatic rocks in traces as well. Ti is positively correlated with vanadium (V) and niobium (Nb) which supports the idea of a derivation from ilmenites. The relative contents of Ti, V, and Nb might therefore represent the basaltic contribution to the lower proportion of the basin fill. The strong upward decrease from 3712m to 2850m (appendix 9-1), in turn, may support the idea that the Etendeka flood basalt plateau has already been significantly eroded in the Maastrichtian around 70Ma ago. Above 2850m the basaltic signal as well as the granitoid signal become less distinct. This may be due to the predominant exposure of Damaran metasedimentary rocks to erosion.

A ternary plot of $\text{CaO-Na}_2\text{O-K}_2\text{O}$ commonly used for igneous rocks (Le Maitre, 1976) has been applied to characterise the geochemical signature of selected magmatic rocks that might have been exposed to erosion in the onshore part of the study area

during the morphotectonic evolution of the margin (fig. 4-24; see fig. 2-2 and Miller & Schalk, 1980 for details). Significant sedimentary rocks of the onshore part of the study area as well as the offshore cutting samples have been added for comparison.

The Torrabay and Mile 110 Granites, respectively, are very close to the average

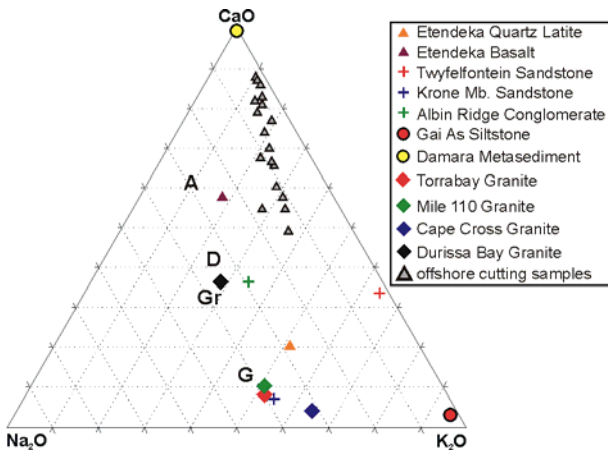


Fig. 4-24. CaO-Na₂O-K₂O ternary diagram. Average composition of andesite (A), dacite (D), granodiorite (Gr), and granite (G) are inferred from Le Maitre (1976) for comparison with magmatic rocks of the study area. Sedimentary onshore samples and offshore cutting samples are plotted for completion.

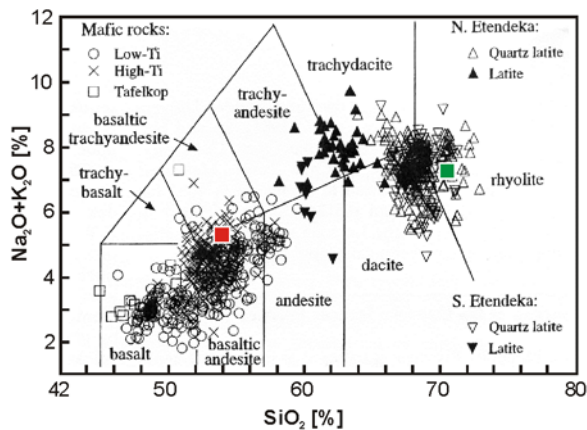


Fig. 4-25. Etendeka volcanic and intrusive rocks plotted on a classification diagram from Le Maitre (1976). The two representative samples of Etendeka basalt (sample 26/2, red square) and Etendeka quartz latite (sample 16/1, green square) analysed in this study fit well into the data set modified from Marsh et al. (2001).

granite composition indicated by G whereas the Cape Cross Granite is slightly enriched in K₂O. The Etendeka quartz latites, however, are slightly enriched in CaO compared to an average granite; Etendeka basalts show higher K₂O-contents than the average andesite composition. The composition of the Durissa Bay Granite plots between the average compositions of average granodiorites and dacites.

Plotting the total alkalis (Na₂O+K₂O) versus silica (SiO₂) is a common diagram to discriminate volcanic rocks (Le Maitre, 1976). Marsh et al. (2001) presented detailed geochemical field data for the Etendeka Igneous Province in order to refine the stratigraphic framework and to infer an improved interpretation of its petrogenetic evolution. One representative sample of the Etendeka basalts (sample 26/2; Achab River; location indicated in plate VI-4) and of the Etendeka quartz latites (sample 16/1; Springbok River/ "Sugar Loaf Hill"), respectively, has been analysed in this study; both are suitable

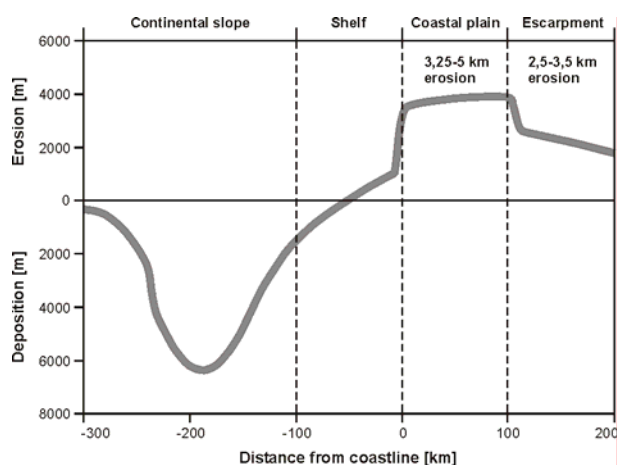
to confirm dataset presented by Marsh et al. (2001) as they reveal a basaltic andesitic to basaltic trachyandesitic composition for the "basalt" sample as well as a rhyolitic composition for the "quartz latite" sample (fig. 4-25).

4.5 Mass balance

The morphotectonic evolution of the passive margin of NW-Namibia can be both qualitatively and quantitatively linked with the depositional and geodynamic evolution of the central Walvis Basin. Unlike most models of margin evolution, the approach towards a quantitative link between uplift and erosion onshore with contemporaneous subsidence and sedimentation offshore which is presented here has been performed by primarily considering the denudational history.

The quantitative reconstruction of the denudation and sedimentation history, respectively, reveals a broad correspondence within the well documented 2D model traverse across the margin that is discussed above; a broad qualitative analogy between the sedimentation rates the central Walvis Basin and the denudation rates in adjacent onshore areas is best displayed by figure 4-7.

Ten Brink & Stern (1992) presented a similar quantitative 2D approach addressing the thickness of erosion and deposition in a section across the southern Namibian margin at the latitude of the Orange Basin. However, they modelled the observed erosional morphology of the rifted margin as well as the depth and the location of the related offshore depocentre as an upward deflection of a continuous elastic plate modified by the downward load of the margin sediments. Thereby, lithospheric rigidity decreases from elastic thicknesses of $T_e=80\text{km}$ inland to $T_e=10\text{km}$ offshore, with the transition occurring far seaward under the continental shelf and slope. The model of Ten Brink & Stern (1992) presented in figure 4-26 does not only predict 2,5-3,5km of denudation at the Great Escarpment and 3,25-5km of denudation in the coastal plain, respectively, which is analogous to the range of estimations of the former cover presumed in this study (chapter 4.1.1 & 4.1.2); the location and depth of the corresponding offshore depocentre is roughly equivalent to that inferred from the depthconversion of a seismic section through the central Walvis Basin, as well (chapter 4.2). Furthermore, Ten Brink & Stern (1992) conclude that uplifted rift flanks do not always need to be underlain by thermal anomalies if the lithospheric flexural



rigidity is distributed like in their model approach briefly outlined here.

Fig. 4-26. Distribution of the total thickness of erosion and deposition (uncorrected for compaction) for a section across the southern Namibian margin at the latitude of the Orange Basin; inferred from an elastic plate model assuming flexural rigidities of the lithosphere decreasing seaward. See text for discussion. Modified from Ten Brink & Stern (1992).

It has been discussed in chapter 4.1 that estimations of the thickness of the lithologic column that covered the onshore part of the model traverse at the time of breakup can be based on a variety of suitable indicators, among those are cumulative thicknesses of stratigraphic remnants, intrusion depths, and quantitative AFT analysis. 5km of postrift erosion in the coastal plain as inferred from AFT analysis (e.g. Raab, 2001), is suggested to be the most probable estimation. This would not only indicate a rather reasonable intrusion depth of the Brandberg intrusive complex of c. 2,5km; a rock volume of 44000km³ provided by 5km of erosion in the study area (figure 4-5, section 6) appears to be well-founded in terms of mass balance considerations as well.

As briefly discussed in chapter 7, the Early Cretaceous landsurface covered by Etendeka volcanics may have reached farther seaward than its erosional remnants at the present day. Estimations of volumes eroded onshore that are terminated by the coastline will therefore underestimate sediment supply to the adjacent basin segment. Assuming that the entire medial hinge line has been buried under 5km of Early Cretaceous cover towards the northeastern termination of the inner SDR wedge (fig. 3-6b & 4-13a), for example, would yield an additional volume of postrift denudation in the order of 22000km³. This is well within the order of magnitude of the mass balance calculations presented here but needs to be ignored due to its highly speculative nature.

Depthconversion of the offshore part of the model traverse yields a postrift sedimentary volume of 58000km³ (chapter 4.2) which is roughly in the order of the volume supplied from within the traverse. However, the fact that the offshore part of the 2D model traverse represents an “open system” and, additionally, the inability to quantify the effects of erosion, suggests that the rock volumes encountered offshore have to be regarded as rather minimum estimations.

This idea is strongly supported by the provenance studies discussed in chapter 4.3. The evaluation of quartz grain varieties in Maastrichtian sandstones of well 2012/13-1 has shown that less than 50% of the quartzes are of volcanic origin (fig. 4-16). Assuming that the onshore part of the model traverse lies almost completely within volcanic rocks of the Etendeka Group, however, suggests that the entire rock volume of 44000km³ supplied to the basin is sourced from volcanics. The second half of the quartz grains might have been sourced from metamorphic and plutonic rocks of the Damara basement which implies a significant contribution from a differential longshore transport component as indicated by figure 4-27. Concluding that Damaran rocks have already been eroded in NW-Namibia in Maastrichtian times has strong impact on the evaluation of the denudational history of the margin which has already been discussed in the chapters 4.1.2 & 4.3.1. A distinct Late Cretaceous denudation and sedimentation peak is readily identifiable in figure 4-7.

Based upon the suggestions derived from the analysis of quartz grain varieties it seems to be appropriate to roughly double the volume of 44000km^3 eroded from the proper onshore part of the model traverse in order to attain reasonable values for the amount of sediment deposited offshore.

This increase by a factor of 2 can independently be inferred from basin modelling with *STRATA* as well (see chapter 5). Applying the denudational history deduced from AFT modelling (fig. 4-7) to the estimated amount of 44000km^3 of rock eroded onshore enabled a temporally varying sediment supply to the basin segment to be calibrated. Since this approach initially yielded rather unfavourable model results, the volume of sediment has been systematically increased in order to reproduce the geometrical and facial evolution of the basin fill. Finally, a volume increase by a factor of 2,3 proved to produce satisfying model results equivalent to the stratigraphic pattern of the central Walvis Basin observed in seismic (see chapter 5.4).

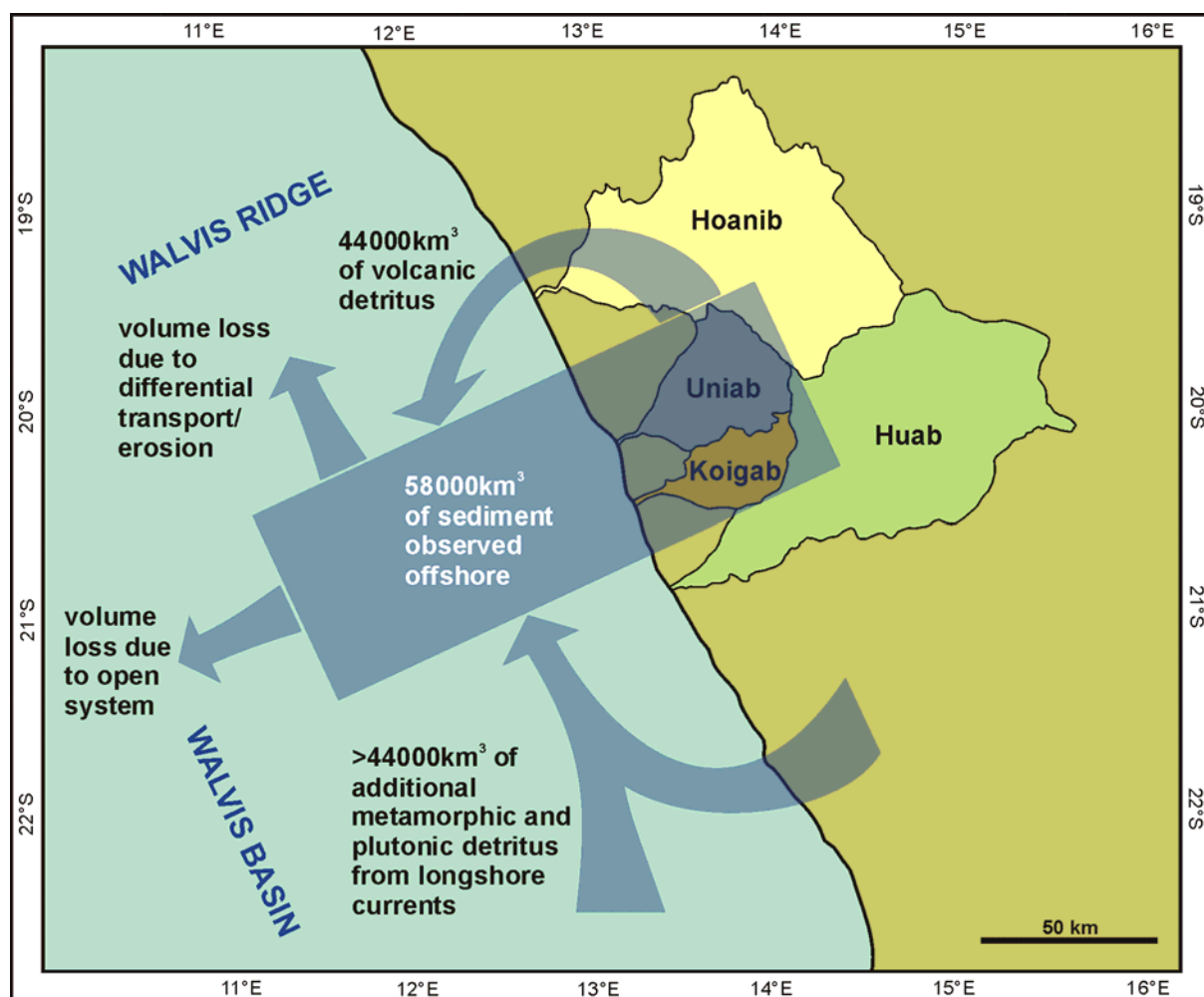


Fig. 4-27. Schematic concept of a mass balance for a segment across the passive continental margin of NW-Namibia. Volumetric constraints can be inferred from estimations of the amount of postrift erosion, from calculations of the volumes deposited offshore, from provenance studies, and from forward basin modelling, respectively. See text for discussion.

In conclusion, it seems to be possible to verify that the amount of 44000km³ of volcanic detritus eroded from within the model traverse during passive margin evolution has been entirely transported into the adjacent basin segment by a purely transversal drainage regime; the volcanic proportion of the basin fill is reflected by the proportion of volcanic quartz grains in Upper Cretaceous sandstones in good approximation.

The volume of 58000km³ calculated for the offshore part of the model traverse appears to be strongly underestimated which might be due to either “volume loss” at the seaward termination of the evaluated margin-segment or to erosion by longshore currents.

Provenance studies as well as basin modelling suggest that an amount of about another 44000km³ of detritus or even more has been introduced to the model traverse by a differential transport component parallel to the coast (Kukulius & Henk, 2003). The source regions may have been Damara metasedimentary rocks or granitoid intrusive complexes from further south (figure 4-27) that were already exposed to erosion in the Late Cretaceous.

The damming effect of the Walvis Ridge volcanic feature located to the north of the model traverse (fig 4-2) might have contributed to the overall accumulation potential of the inferred differential longshore transport component; since it must have already been active in Late Cretaceous times, this current system might be referred to as “Proto-Benguela Current”.

5 Basin modelling

5.1 Sequence stratigraphic framework

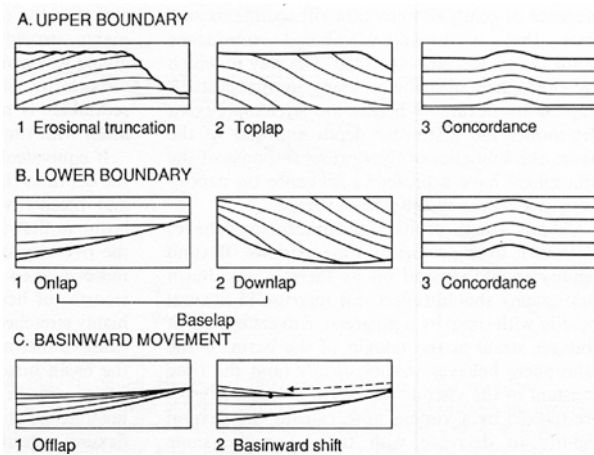
The stratigraphy observed in a marine sedimentary basin is the long-term response of the depositional surface to prolonged subsidence combined with changes in global (i.e. absolute/ true eustatic) sea level. Additionally, the rate of sediment supply and erosion in time and space give rise to characteristic geometries of stratigraphic units. The advent of high resolution seismic stratigraphic methods over the last decades enabled detailed observation, description and interpretation of the stratigraphic record (e.g. Haq et al., 1987; Posamentier et al., 1988; Posamentier & Vail, 1988; Van Wagoner et al., 1988; Christie-Blick & Driscoll, 1995).

Based on that, the concept of “depositional sequences” has been established (Van Wagoner et al., 1988). These are fundamental units of stratigraphy composed of genetically related packets of strata which are bounded by unconformities or their correlative conformities on their bottom and top, respectively. Depositional sequences can be subdivided into smaller units with distinct stacking patterns termed systems tracts (Posamentier & Vail, 1988). They are themselves composed of parasequences, the smallest units identifiable in a basin. Their boundaries are thought to be of chronostratigraphic significance at a small scale and are related to abrupt changes in water depth.

The geometry of depositional sequences and the distribution of related unconformities and conformities is generally controlled by three variables: eustatic sea level change, subsidence, and changes in sediment supply (Christie-Blick & Driscoll, 1995). Stratigraphic forward modelling is capable of illustrating how complex these processes interact through time to produce the observed stratal geometries. Numerical forward modelling provides information on the relative importance of these variables (e.g. Jordan & Flemings, 1991). *STRATA*, the basin modelling tool used in this study, approximates the efficiency of sediment transport (or erosion) by slope controlled diffusion (Flemings & Grotzinger, 1996; chapter 5.2.1).

5.1.1 Geometrical inventory of seismic stratigraphy

The chronostratigraphic significance of depositional sequences is given by the ages of their sequence boundaries where they are conformities; age is reduced where the boundaries are unconformities. Critical for the interpretation and correlation of sequence boundaries are the geometrical relationships of internal subunits to the boundary itself (fig. 5-1).



Onlap and downlap indicate a nondepositional hiatus. The updip termination of initially inclined strata (e.g. foreset bedding) is termed toplap. It may be linked to minor erosion or sediment bypassing. Erosional truncation is the lateral termination of strata, thus indicating an erosional hiatus. Offlap features represent a basinward facies movement (fig. 5-1).

Fig. 5-1. The geometrical relationships of strata to depositional sequence boundaries are critical for the interpretation of seismic sections (from Allen & Allen, 1990).

5. 1. 2 Tectonic mechanisms and sea level concepts

During the tectonically active synrift-phase of margin evolution, the flexural strength of the lithosphere is minimal and the crustal response to thinning is close to Airy isostatic behaviour. Subsequent thermal subsidence is due to cooling and contraction of the thermally disturbed lithosphere. Gently dipping postrift sediments deposited during that phase indicate a broadly distributed subsidence. The lithosphere provides strong support for superimposed sediment and water loads and reacts by flexure. Wavelength and amplitude of this deflection of the passive margin increase through time due to thickening of the lithosphere as it cools combined with the effect of the increasing sediment load (Allen & Allen, 1990). The rift-drift transition in passive margin evolution generally coincides with strong coastal onlap (see fig. 3-14).

Sediment accumulation on continental margins is strongly controlled by tectonic subsidence rates, sediment supply rates, and changes in eustatic sea level. The distance from the centre of the earth to the ocean's surface is termed global or (true) eustatic sea level. Changes in eustatic sea level arise either from changes in the volume of water within the oceanic basins or from changes in the volume of the oceanic basins themselves. Since the volume of sea water is suggested to have not greatly changed during the Phanerozoic (Allen & Allen, 1990), changes in the basin volume may be substantial.

Major and long-term eustatic changes are thought to be caused by changes in mid-ocean ridge volumes which are, in turn, controlled by variations in spreading rates and the total length of spreading axes. Large-scale but more rapid changes are suggested to be caused by glaciation and deglaciation of land based ice-sheets.

Since the lithosphere is also able to move up and down relative to the centre of the earth (uplift, subsidence), the distance from an arbitrarily chosen reference horizon within the lithosphere (e.g. top basement) to the sea surface is called relative sea level or accommodation space. Accommodation space can be filled up with sediment or water. Eustatic sea level rise combined with tectonic subsidence therefore increases accommodation space. Tectonic uplift, erosion, and eustatic sea level fall, on the other hand, reduce accommodation space.

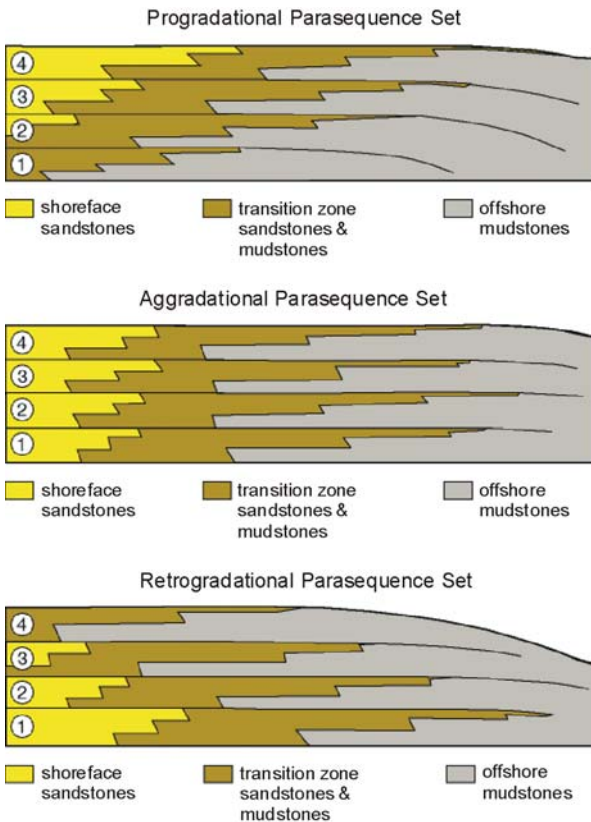
If the rate at which new accommodation space (accommodation potential) is made available exceeds the sediment supply rate, the basin is termed “underfilled” (generally the case in marine basins). In the opposite case, the basin is called “overfilled” (terrestrial basins; not valid for intramontane basins). If both rates are equal, the basin is “filled” which is true for coastal sedimentation (Schlunegger, 2001, pers. comm.)

A rise in relative sea level, which acts as a base level, allows an increment of coastal deposition to be accommodated (Allen & Allen, 1990). Measurement of stratal geometries, facies analysis, and evaluation of coastal onlap- and offlap patterns, therefore, enable the interpretation and reconstruction of absolute sea level changes. Based upon that, Haq et al. (1987) provided a long-term eustatic curve and a detailed short-term eustatic sea level curve; the latter has been slightly smoothed to be used as one major input parameter for the basin model presented in this study (fig. 5-4; chapter 5.2.4).

5. 1. 3 Stratigraphic response to sea level changes

Fundamental indicators of relative changes in sea level are the depositional limits of onlap and toplap within coastal marine sequences (Haq et al., 1987). Coastal onlap generally indicates landward movement of facies during a relative sea level rise. A transgression or regression may result from that rise, depending on the magnitude of sediment influx. Coastal toplap by aggradation to baselevel and subsequent seaward build-out may be due to a relative sea level stillstand. Relative sea level fall is indicated by downward shift of coastal onlap. This may be associated with erosion of underlying strata and sediment bypass across the shelf (Emery & Myers, 1996).

As mentioned earlier, depositional sequences are relatively conformable successions consisting of systems tracts which reflect chronostratigraphic increments (Van Wagoner et al., 1988); they are themselves composed of parasequences which represent single episodes of progradation and thus imply a shallowing upward succession and a seaward movement of the shoreline (fig. 5-2). Once the accommodation space is filled, a flooding surface tops the parasequence and gives rise to new accommodation space.



Crucial for the understanding of the stratigraphic response to sea level changes is the recognition of vertical and lateral facies relationships within parasequences. A single parasequence is composed of shallower water facies updip and a deeper water facies downdip. Parasequence boundaries (flooding surfaces) may be obscured in coastal settings and in deep water settings, respectively, due to a lack of facies contrast.

Fig. 5-2. Depositional sequences are composed of parasequences that represent single episodes of progradation (shallowing upward). The overall stacking pattern of parasequences (progradational, retrogradational, aggradational) reflects the complex interplay of relative sea level change, sediment supply, and subsidence (from Van Wagoner et al., 1988).

The rate at which sea level changes, particularly in combination with the rate of subsidence and the sediment supply, is a critical parameter in determining the related stratigraphic response (Allen & Allen, 1990). The rate of change is highest at the inflection point of the sea level curve (fig. 5-3 & 5-4) whereas the rate of subsidence is relatively constant (fig. 5-5). A combination of both, therefore, gives the rate at which new accommodation space is provided to be filled with sediment. Sea level rises will be amplified by the subsidence, sea level falls, on the other hand, will be damped down by the subsidence in terms of accommodation space.

The period of greatest increase of accommodation space is the rising limb of the sea level curve. If this rate slows down, sediment supply will easily fill the available space; sediment begins to be bypassed across the shelf leading to a progradational stacking pattern of parasequences (fig. 5-2 & 5-3). Progradation is strongest at the inflection point of the falling limb of the sea level curve. During sea level fall the shelf is subjected to erosion and rivers may even be rejuvenated to incise the former shelf; this leads to an (progradational) unconformity bounding the depositional sequence below (*type 1 sequence boundary*).

When the rate of sea level fall decreases and new accommodation space is made available again, the underlying unconformity is progressively onlapped and the parasequences backstep in a retrogradational manner (fig. 5-2 & 5-3) reflecting an overall deepening upward succession. During that transgression sedimentation is

restricted close to the supply point and the shelf is relatively starved of sediments; the relict shelf break may be eroded resulting in a marine (distal) unconformity. This phase is terminated by a *maximum flooding surface*.

In periods where accommodation space is filled about as rapidly as it is created, a aggradational stacking pattern of parasequences will be established (fig. 5-2 & 5-3) reflecting no net vertical trend in water depth.

The spatial and temporal development of unconformities (progradational/ sequence boundary, retrogradational/ marine) related to such an idealised sea level cycle is best visualised by a chronostratigraphic plot termed Wheeler diagram as it is provided by *STRATA* (Wheeler, 1964; e.g. fig. 5-14b).

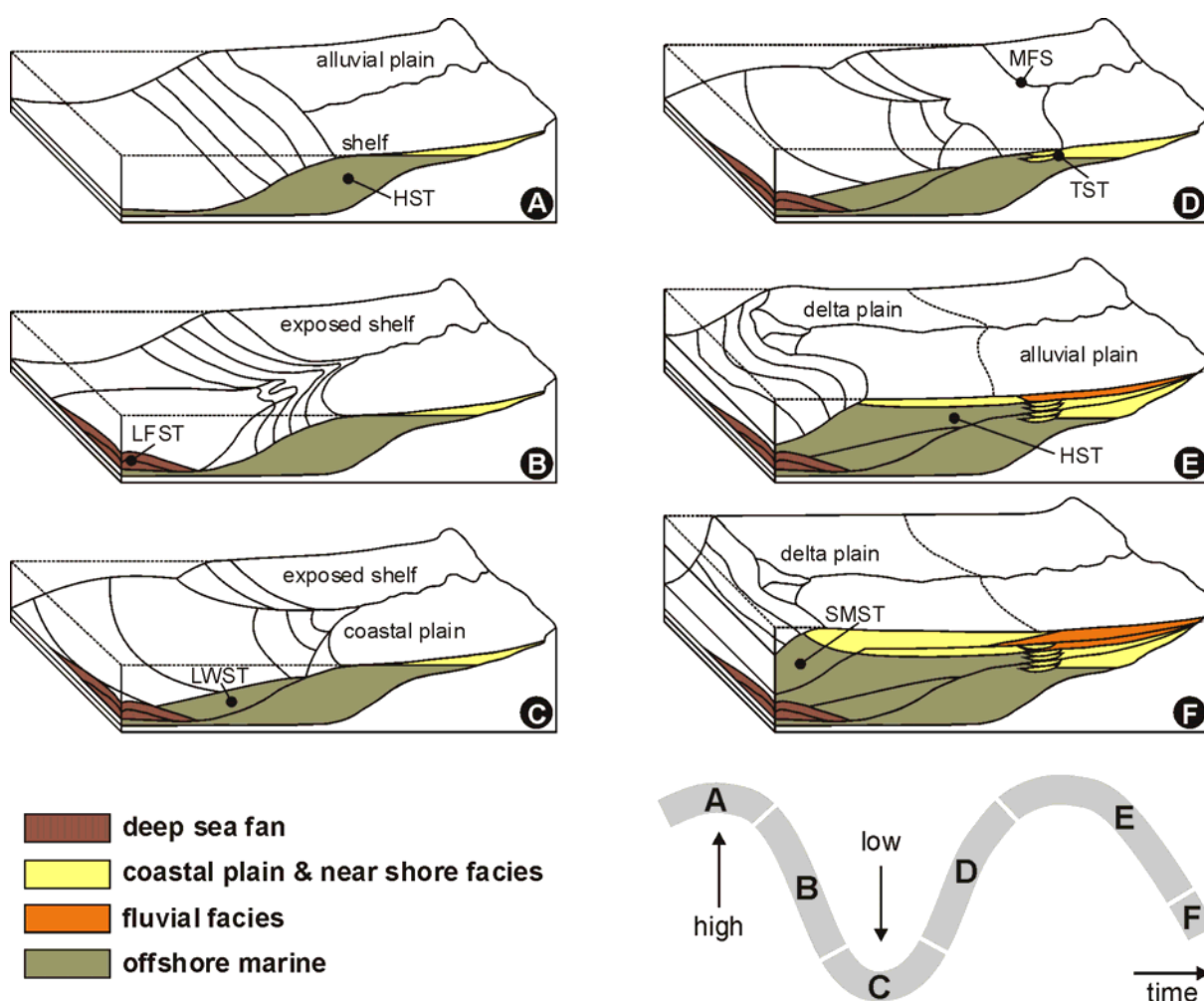


Fig. 5-3. An idealised depositional sequence is the record of one cycle of relative sea level and has a predictable internal structure related to specific segments (A-F) of the sea level curve. The evolution of highstand systems tracts (HST), lowstand fan systems tracts (LFST), lowstand wedge systems tracts (LWST), shelf margin systems tracts (SMST), and marine flooding surfaces (MFS) is illustrated. See text for details (modified from Posamentier et al., 1988).

Every depositional sequence is the record of one cycle of relative sea level and has therefore a predictable internal structure of stratal surfaces and systems tracts related to specific segments of the sea level curve (Van Wagoner et al., 1988; fig. 5-3).

Lowstand systems tracts are active during times of relatively low sea level following the formation of a sequence boundary. They generally comprise lowstand fan and lowstand wedge sediments (LFST, LWST). Lowstand fans are base-of-slope fans fed through incised valleys and canyons and display an aggradational stacking pattern. Lowstand wedges consist of progradational parasequences that onlap successively onto the slope and downlap onto the basin floor and (if developed) onto the lowstand fans. They are formed during low but slowly changing sea level. When sea level fall is not that severe, an aggradational shelf margin systems tract (SMST) may be developed at the shelf edge onlapping landward and downlapping basinward; its base is then termed *type 2 sequence boundary* (Emery & Myers, 1996).

During rapid sea level rise, a retrogradational set of parasequences backsteps onto the margin strongly onlapping in a landward direction and downlapping basinward onto a *transgressive surface*. Condensed sections due to sediment starvation are common in such *transgressive systems tracts* (TST). When the rate of sea level rise decreases, the *maximum flooding surface* (MFS) is reached and parasequences change from being retrogradational to being aggradational.

When the rate of sea level rise slows down after maximum flooding, a *highstand systems tract* (HST) will be developed. The rate of creation of accommodation space becomes successively outranged by the rate of sediment supply and thus progradational stacking is increasingly favoured over aggradational stacking. The maximum flooding surface below represents a prominent downlap surface for a typically clinoform system of parasequences in a highstand systems tract. As relative sea level begins to fall, a new sequence boundary begins to form. Thereby, erosion starts much earlier at the landward side of the basin than at the seaward side which is best displayed in chronostratigraphic Wheeler diagrams (e.g. fig. 5-14b). Naturally, the highstand systems tract is most prone to erosional removal during sequence boundary formation.

5. 2 Model basics and setup

5. 2. 1 The diffusion equation

STRATA is a two-dimensional process-based depositional model that incorporates a basin subsidence model to predict stratigraphic records (Jordan & Flemings, 1991; Flemings & Grotzinger, 1996). Deposition and erosion are each treated as diffusive processes in which sediment transport is proportional to the surface gradient. The

concept of the diffusion equation (eq. 5-1) has been derived from physical heat flow laws and empirical studies have shown that it can be adequately applied to sedimentation processes (Paola, 2000).

Initially, models based on the diffusion equation have been used to describe geomorphological processes and fluvial systems, especially in foreland basin settings (e.g. Flemings & Jordan, 1989, 1990). By analogy, however, with the approach to nonmarine transport the same authors have approximated marine transport, e.g. on passive margins, by the diffusion equation (Jordan & Flemings, 1991):

$$\frac{\delta h}{\delta t} = K \left(\frac{\delta^2 h}{\delta x^2} \right) \quad \text{eq. 5-1}$$

Thereby, the depositional (or erosional) volumetric transport rate is proportional to the change in local slope and volume (mass) is conserved. Nonmarine transport is treated as more efficient transport than marine transport; the shoreface is treated as a boundary between both transport efficiency regimes and therefore traps sediment.

The equation is solved using an implicit finite-difference method (see Incropera & DeWitt, 1985 for details) where h is the elevation of the earth's surface [m], t is time [a], x is the horizontal position [m], and K is a proportionality constant [m^2/a] referred to as the transportation coefficient or transportation efficiency.

Whether sediment is deposited or eroded ($\partial h/\partial t$ positive or negative, respectively) depends upon the change in local slope ($\partial^2 h/\partial x^2$). Therefore, local topography produced by enhanced sediment influx or increased subsidence tends to be smoothed through time due to a balance between deposition and erosion.

The transportation efficiency K is apparently the prominent controlling factor. Nonmarine diffusion constants ($K_{\text{nonmarine}}$) are empirically determined and calibrated with well documented facies distributions in specific fjords and deltas; values range from 2×10^4 to $6 \times 10^5 \text{ m}^2/\text{a}$. Reasonable values for K_{marine} appear to be in the order of 100 to 1000 m^2/a (Jordan & Flemings, 1991; Kaufmann et al., 1991).

STRATA is capable of simulating erosion and resedimentation as an integral part of sediment transport dynamics. However, it is incapable of incising the shelf, which is a three-dimensional phenomenon. The diffusive model does not simulate catastrophic failure of marine slopes that result in turbidity currents either, but creep and debris flow along a delta front or shelf slope are explicitly approximated by downslope diffusion (Jordan & Flemings, 1991).

In *STRATA* models the entire shoreline is treated as a delta, i.e. as a sediment point source. Interdeltaic processes and shore-parallel transport due to currents can therefore not be taken into consideration. Based on geometry rather than on genesis,

however, the diffusion equation provides a valuable gross approach to sediment transport behaviour.

5. 2. 2 Program modules

STRATA is a stratigraphic modelling package that was originally developed at Cornell University (Ithaca, New York) by Flemings & Jordan (1989). Subsequently it was further developed at both Penn State University and Massachusetts Institute of Technology in collaboration with Jamie Morris (Flemings & Grotzinger, 1996). The *STRATA* package should work on UNIX and UNIX-like systems (Linux). Free download and additional information including a detailed manual and exercises can be found on the world wide web (<http://hydro.geosc.psu.edu>).

STRATA is composed of four independent programs: a pre-processor *setbasin* to set the model's parameters, a processor *simbasin* to run the model with the user-defined parameters, a post-processor *plotbasin* to display the results, and a special program *filmbasin* to create a movie. Each module creates specific output-files to be processed in the following module.

Plotbasin is capable of displaying six time slices of the model results with a defined horizontal axis. The program enables the vertical axis to be displayed as depth in metres, as depth in two-way-traveltime, or as a Wheeler plot with chronostratigraphic significance (Wheeler, 1964). A great variety of contoured model results can be displayed as an overlay in plotbasin; among those are water depth at deposition, porosity, diffusion, sediment composition, acoustic velocity, density, impedance, seismic signal, heat conductivity, temperature, temperature gradient, and, additionally, the sumTTI-index as an approach to thermal maturity (see chapter 6).

Filmbasin arranges the results from the processor and the post-processor to create a movie; this might occasionally be afflicted with software problems and a commercial graphics software may produce relief.

5. 2. 3 Constant model parameters

The pre-processor *setbasin* is able to set a great bandwidth of user-defined model parameters which are subdivided into the groups measures, ages, clastics, carbonates, sea level, subsidence, compaction, and heat flow. The very bulk of the parameters can be defined by a single number or simple activation or deactivation; they are briefly described here.

In the measures group the total width (350km) and time (130Ma) of the modelled system as well as the spatial and temporal accuracy of the simulation are defined. Six evenly distributed or user-defined output ages can be defined in the ages group.

Clastic deposition is simulated as diffusive process controlled by the fundamental factor of the diffusion equation (eq. 5-1), the nonmarine and marine diffusion constant, respectively ($K_{nonmarine}$, K_{marine}). They can be defined in the clastics group. The decay coefficient for marine diffusion constant governs the transition from nonmarine to marine sediment transport. These three parameters exert the most prominent influence on the shelfal geometry of the passive margin. Additionally, the clastic influx into the basin (left, right, or both) as well as the pelagic sedimentation rate can be defined here.

Model parameters

total_width	350e3	sea level_file	sea level file
spatial_divisions	1000	sea_time_offset	0
total_time	130e6	sea_datum	0
time_divisions	1000	sea_amp	0
num_timelines	200	sea_period	1e6
even_ages	False	subsidence	subsidence file
age_1	20.0e6	profile_name	passive
age_2	40.0e6	flex_compensate	False
age_3	60.0e6	flex_rigidity	1e23
age_4	80.0e6	density_air	1e-4
age_5	110.0e6	density_crust	2300
age_6	130.0e6	density_mantle	3300
nonmarine_diffusion_constant	0.6e4	density_water	1000
sim_marine_sed	True	local_grav	9.81
marine_diffusion_constant	550	compact_sediments	True
marine_diffusion_decay	0.007	erosion_affects_compaction	True
left_flux	flux file	shale_decay	.51e-3
right_flux	none	shale_phi	.63
pelagic_rate	0.000002	sand_decay	.27e-3
carbonate_file	none	sand_phi	.49
epeiric_max	1e-3	sand_cutoff	-1
epeiric_depth	1.0	compaction_composition_decay	1
oceanic_max	1e-3	thermal_flux	heatflow file
oceanic_decay	0.1	sand_conductivity	3.00
oceanic_depth	1.0	shale_conductivity	3.01
carb_skim	True	fluid_conductivity	0.50
isotope_file	none	surface_temperature	20
isotope_time	0	surface_temp_falloff	0

Tab. 5-1. List of model parameters. Parameters varying through time are indicated by a grey box; they are examined in the next section. Sediment supply (“flux file”) is the only factor that is varied in the model results presented below.

In contrast to clastic deposition, calcium carbonate sedimentation is primarily controlled by the water depth and can occur independently from the horizontal position in the modelled section (carbonates group parameters). Carbonate sedimentation has not been applied in this study.

Amplitude and period of a sinusoidally oscillating eustatic sea level are defined in the sea level group. The possibility of a user-defined sea level varying through time is outlined in chapter 5.2.4.

Flexural properties of the lithosphere, densities, and the subsidence rate can be determined in the subsidence group; subsidence can be varied through time (fig. 5-5). Initial porosities of the lithological end-members (sand, shale) and compaction properties are defined in the compaction group. Finally, rock-specific thermal conductivity, surface temperature, and a constant or temporally varying thermal flux are determined in the heat flow group.

The constant parameters that were applied in this study are listed in table 5-1; parameters varying through time are indicated by a grey box.

A detailed examination of the stratigraphic modelling package *STRATA* with user guidelines and extensive parameter studies has been presented by Junker (2002). The models presented here are fundamentally based on these preliminary studies which are gratefully acknowledged.

5. 2. 4 Variable model parameters

As mentioned above, passive margin stratigraphy is predominantly controlled by changes in global sea level, subsidence of the basin floor, changes in basal heat flow, and, finally, by the rate of sediment supply. *STRATA* is capable of handling these temporally varying parameters. The user-defined input-files outlined below allow for a high temporal accuracy of the individual factors.

Eustatic sea level changes represent the most influential factor in terms of generating depositional sequences. The sea level-file utilised in this study (fig. 5-4; appendix 10) is based on the Lower Cretaceous-to-recent segment of the "Exxon" global sea level change published by Haq et al. (1987). Figure 5-4b illustrates Haq et al.'s (1987) shortterm (black)- and longterm (grey) eustatic sea level curve, respectively. Since *STRATA* is not capable of resolving the extremely abrupt changes of the shortterm-curve (this would lead to artefacts and miscalculations in the model results), the sea level curve has been slightly smoothed by Junker (2002) without loss of characteristic features (fig. 5-4a).

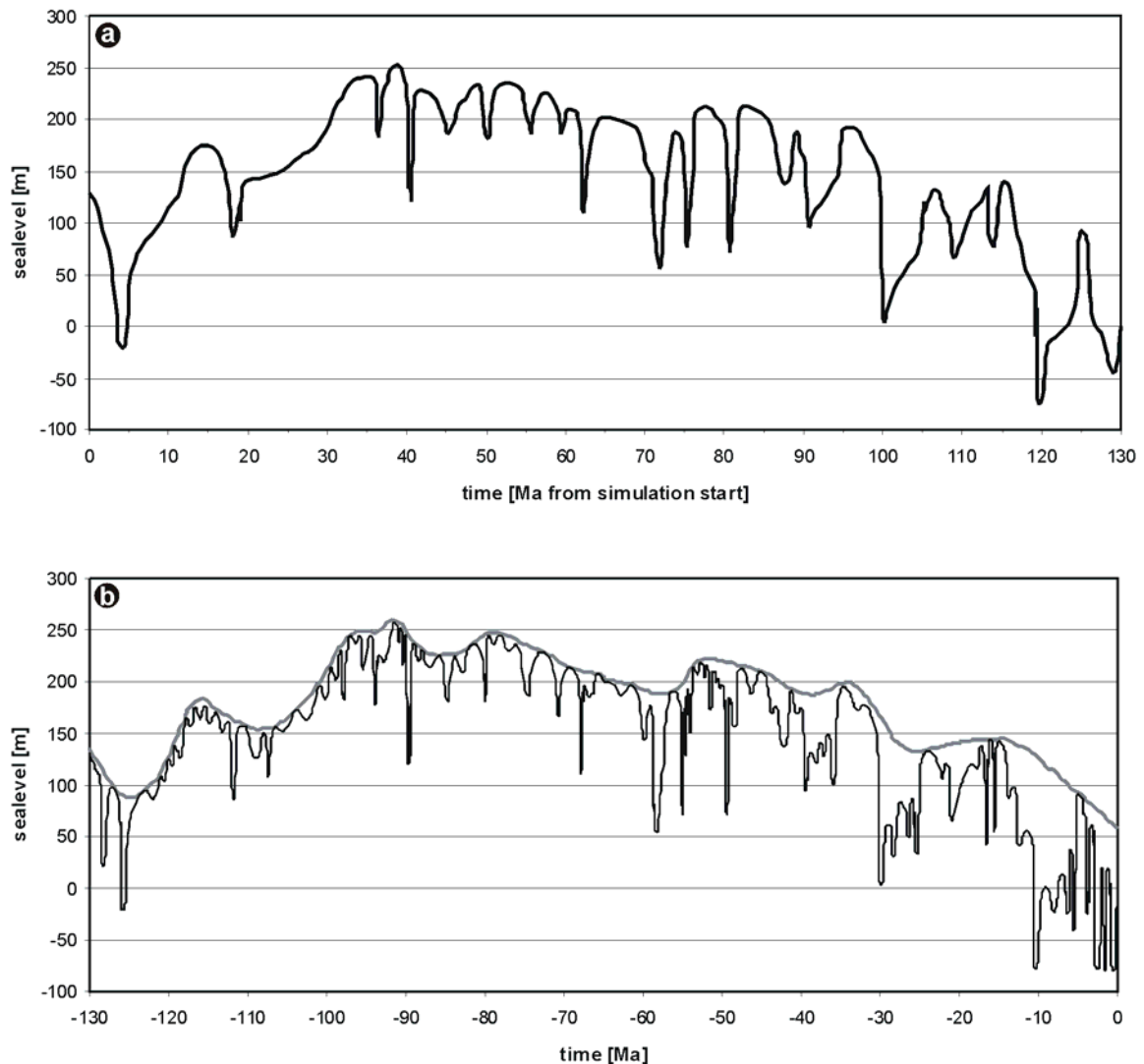


Fig. 5-4. (a) Chart of global sea level changes applied to the basin model as modified by Junker (2002) from (b) the shortterm eustatic sea level changes (black curve) published by Haq et al. (1987). Longterm changes are indicated by the grey enveloping curve.

A significant amount of preparatory work has to be done to extract the subsidence history of a basin. For this study, the interpretation of a seismic section through the central Walvis Basin has been depth-converted from a two-way-traveltime display using specific acoustic velocities for the individual layers (see chapter 4.2; fig. 4-13a). The so obtained basin floor geometry is displayed in figure 5-5b. 1D-backstripping of calibration well data (see chapter 3.7) enables the determination of the temporal evolution of the total basin floor subsidence (fig. 5-5a). A combination of both informations results in the subsidence file applied to the basin model (appendix 11).

Basal heat flow to the basin is another parameter that varies through time during margin evolution (appendix 12). It does not influence the stratigraphic results of the model but has a strong impact on the thermal maturation which can be approximated

by modelling the sumTTI-index of the basin fill. Rock-specific thermal conductivities are inherited in the *STRATA* model. Postrift heat flow values applied in the models presented here are typical of passive margins and are related to the data from Pollack et al. (1993) and Schmidt et al. (2002). Heat flow deteriorates exponentially from 95mW/m^2 at model start to recent values around 50mW/m^2 (fig. 5-6). Heat flow is somewhat more discussed in connection with maturity modelling in chapter 6.

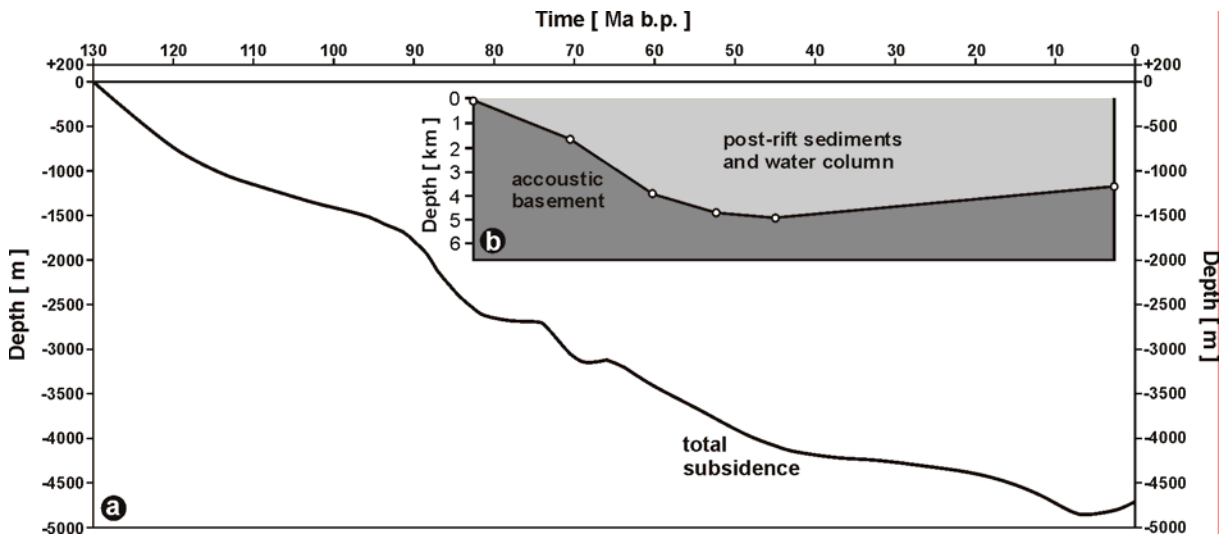


Fig. 5-5. (a) Subsidence history of the central Walvis Basin derived from backstripping of well data. Inset (b) shows the geometry of the basin floor obtained from a depthconverted seismic section of the NW-Namibian passive margin. The subsidence file applied to the basin model is given in appendix 11.

Based on preliminary work of Junker (2002), the sediment supply rate to the central Walvis Basin is the most essential parameter tested in the following studies. The reconstruction of the onshore geology in the Uniab- and Koigab catchment areas, respectively, combined with a denudation model of the NW-Namibian passive margin (Gallagher & Brown, 1999; Raab, 2001) enables the quantification of sediment flux into the modelled section (see chapter 4.5). Primarily, a volume of 44000km^3 of eroded rock has been calculated to be available for sedimentation within the model traverse if a maximum overlay of 5000m above the current land surface is presumed. By utilising a modelled denudation flux curve this volume could be distributed over the model runtime with a 5Ma-resolution (fig. 4-11b) and transferred into a time-dependent flux file for the *STRATA* model (appendix 13).

Mass balance calculations (see chapter 4.5), particularly in combination with elaborate *STRATA* modelling (Junker et al., 2002; Junker 2002), have shown that the amount of sediment provided by erosion is by far not sufficient to produce the passive margin stratigraphy observed in the central Walvis Basin. An amount of 44000km^3 appears to be in the order of 2,3 times too small. Additional sedimentation may be attributed to coast-parallel currents – possibly a “Proto-Benguela current”?

In the model results presented below, intensive parameter studies have been accomplished with the sediment supply rate being the only factor to be varied. Thereby, the sediment supply rate calculated from the onshore denudation rate remains as a basal value; an additional sediment supply curve is placed upon that which represents a potential coast-parallel component and which meets the demand for a clastic flux increased by a factor of 2,3.

The additional sediment flux curve is varied systematically: (1) a sinusoidally shaped curve is placed upon the basal curve and is systematically shifted through time in 5Ma-steps (*sinusoidal runs*); (2) the pre-existing denudation curve is increased by a factor of 2,3. The resulting additional curve is shifted by 20Ma in 5Ma-steps to test the hypothesis of a delayed sedimentation due to erosion of the hinterland and the associated prolonged sediment bypass across the continental margin (*AFT-shift runs*); (3) the additional sediment flux curve is shaped manually in order to obtain a “best fit” model result which allows to interpret the relative importance of a potential coast-parallel current and a quantitative approximation of its sediment transport behaviour (*manual runs*).

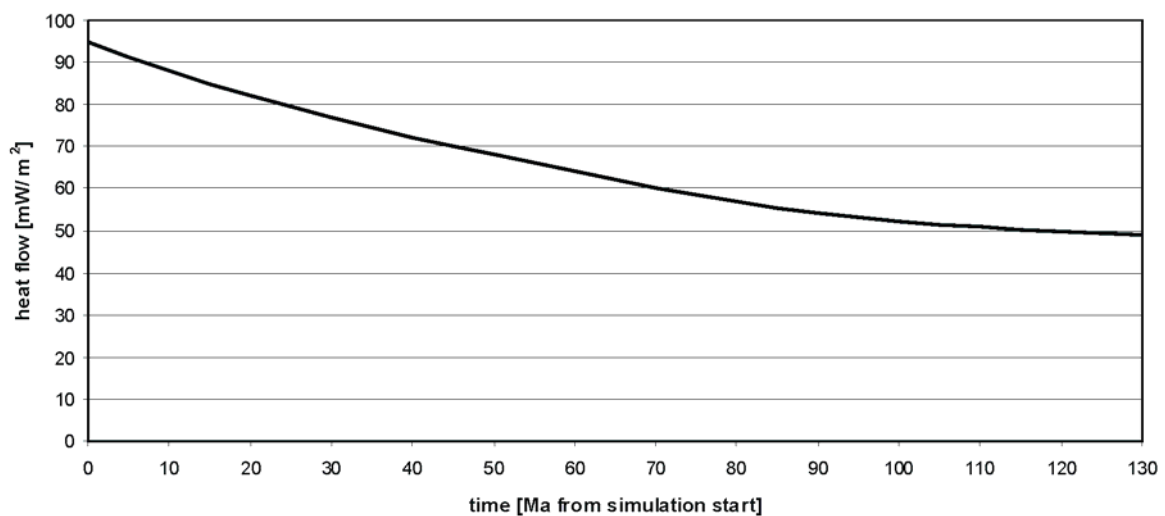


Fig. 5-6. Illustration of the heat flow history applied to the basin model. Data are related to Pollack et al. (1993) and Schmidt et al. (2002).

5.3 Model results

5.3.1 Parameter study (1): sinusoidal runs

In this study the sediment supply rate derived from onshore denudation modelling (grey curve in fig. 5-7) is superimposed by an additional curve that represents a hypothetical longshore transport component (grey dashed curve in fig. 5-7). The resulting combined curve is displayed in black.

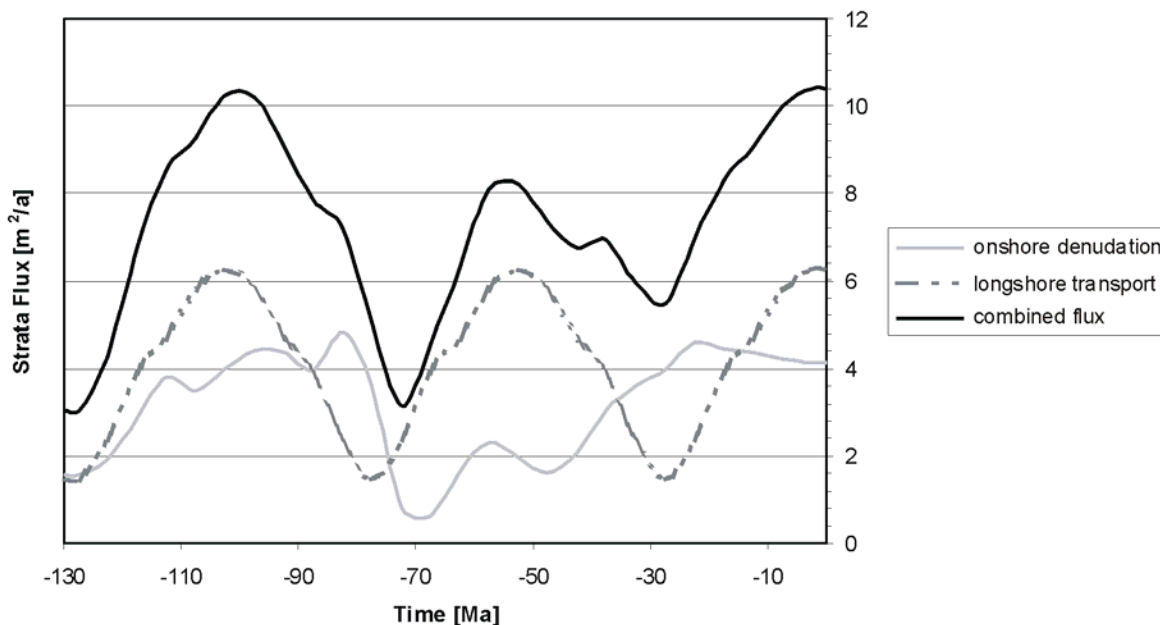


Fig. 5-7. Concept of sediment supply rates applied to the basin model. The grey line represents the supply rate derived from onshore denudation; a hypothetical longshore transport component is indicated by the grey dashed line; a combination of both results in the net sediment flux [m²/a] to the basin model (black curve).

In order to test the model's sensitivity to well defined small-scale changes in one single significant parameter, the additional curve has been given a sinusoidal shape which is shifted systematically in 5Ma-steps parallel to the time-axis. 24 model runs have been performed; an overview is presented in the figures 5-10 & 5-11. The particular sea level curves are given in figure 5-9. Figures 5-10 & 5-11 represent the modelled lithology of the basin fill as well as the modelled water depth at deposition time, respectively.

A clear correlation of sediment supply peaks with coarse-grained (sandy) facies is most obvious, especially when they occur during early basin evolution (e.g. run 2; fig. 5-8). Sedimentation peaks in the late basin evolution are less clearly reproduced in the basin fill due to prolonged subsidence and trapping of sediment close to the supply point. A wide, shallow marine early-drift sedimentation, as it is observed in the

central and northern Walvis Basin (see fig. 6-3), can only be reproduced by *STRATA* if the bulk sediment input is clearly concentrated in the first halftime of passive margin evolution combined with a very early sedimentation peak that keeps pace with early postrift subsidence (e.g. run 23; fig. 5-8).

Unfortunately, none of the models was able to image both early drift shallow marine sedimentation and the Late Cretaceous coarse clastics represented by a Maastrichtian reservoir sandstone (see chapter 6.4.2; fig. 6-3).

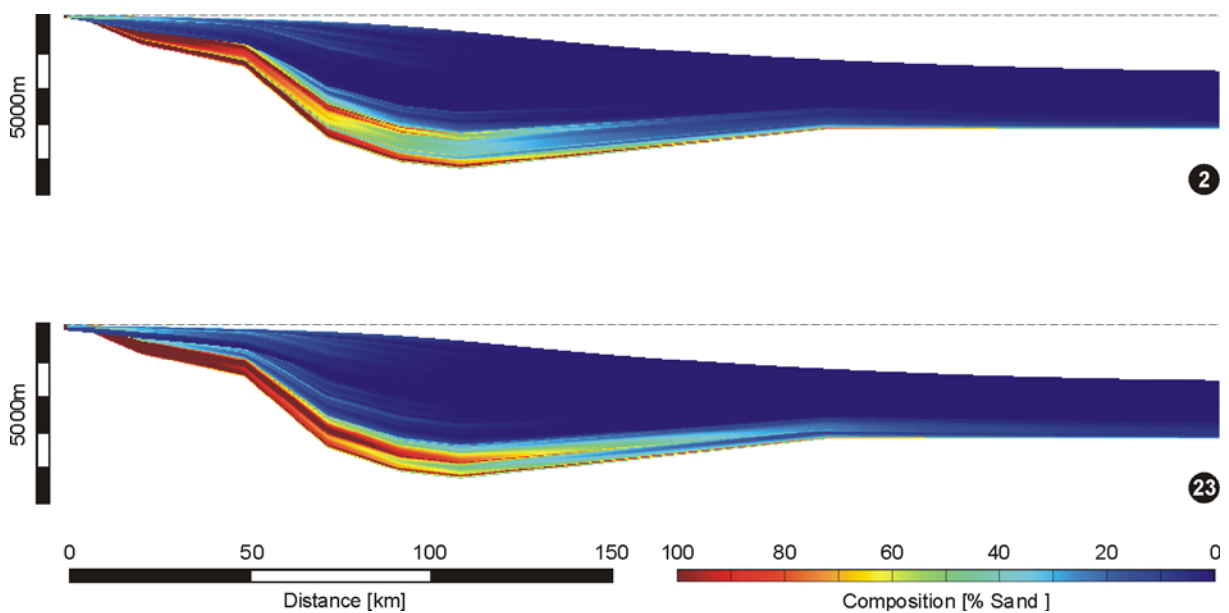


Fig. 5-8. Composition of model runs 2 and 23 displayed as sand-shale ratio [% Sand]. Run 2 illustrates a clear correlation of sediment supply peaks with coarse-grained facies, especially during early basin evolution. Shallow marine early-drift sedimentation can only be reproduced if the bulk sediment input is concentrated in the early margin evolution (run 23).

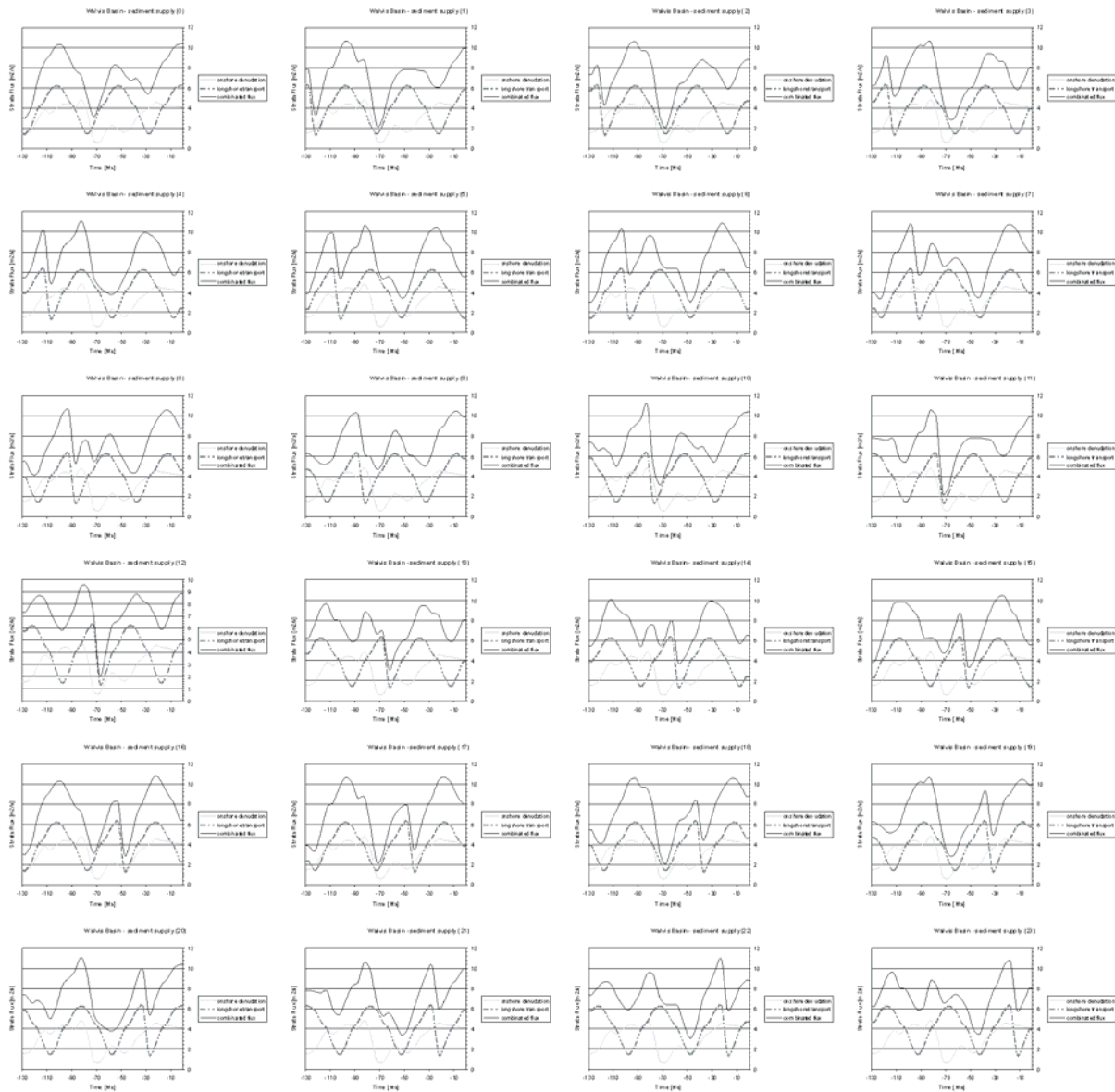
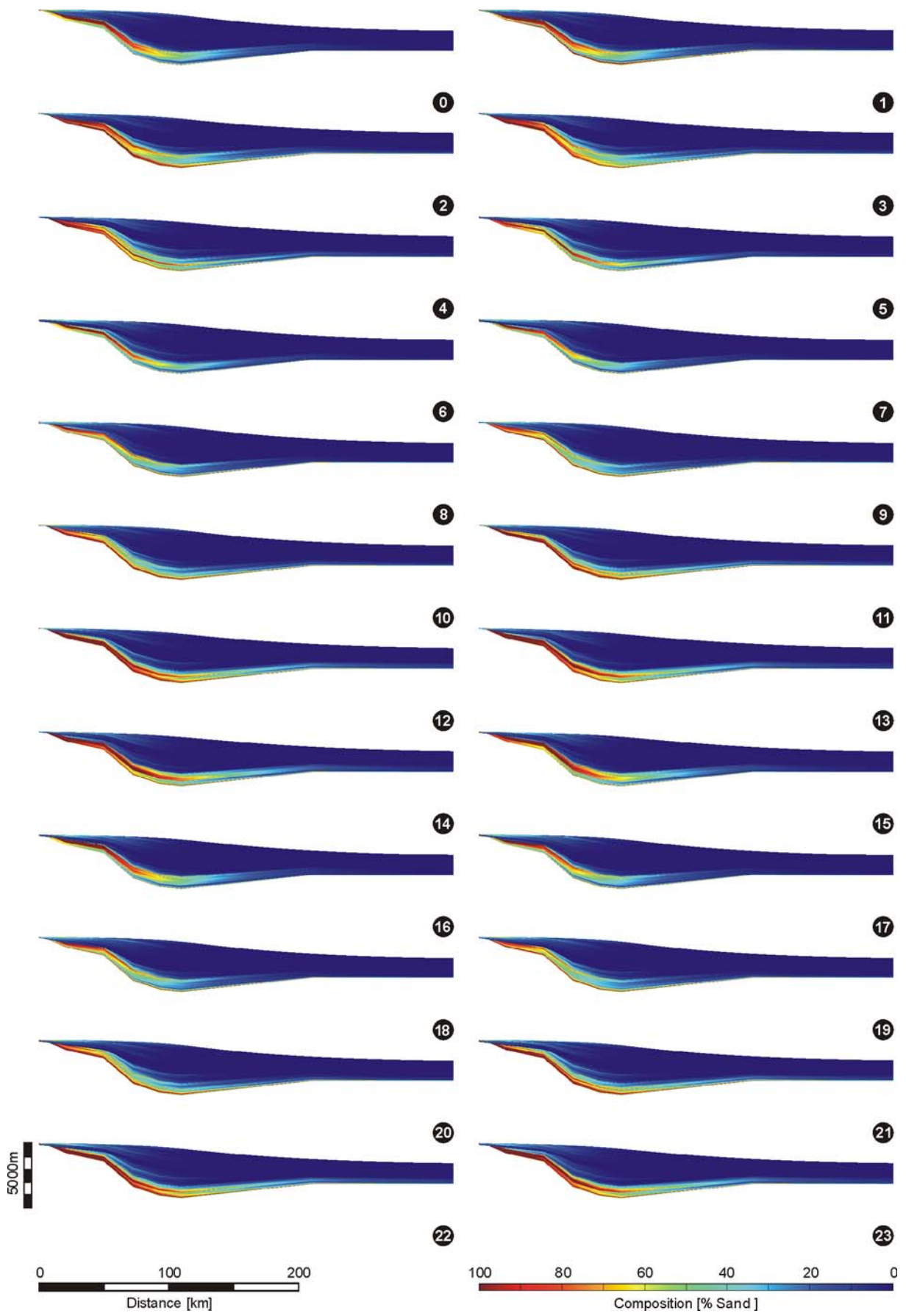


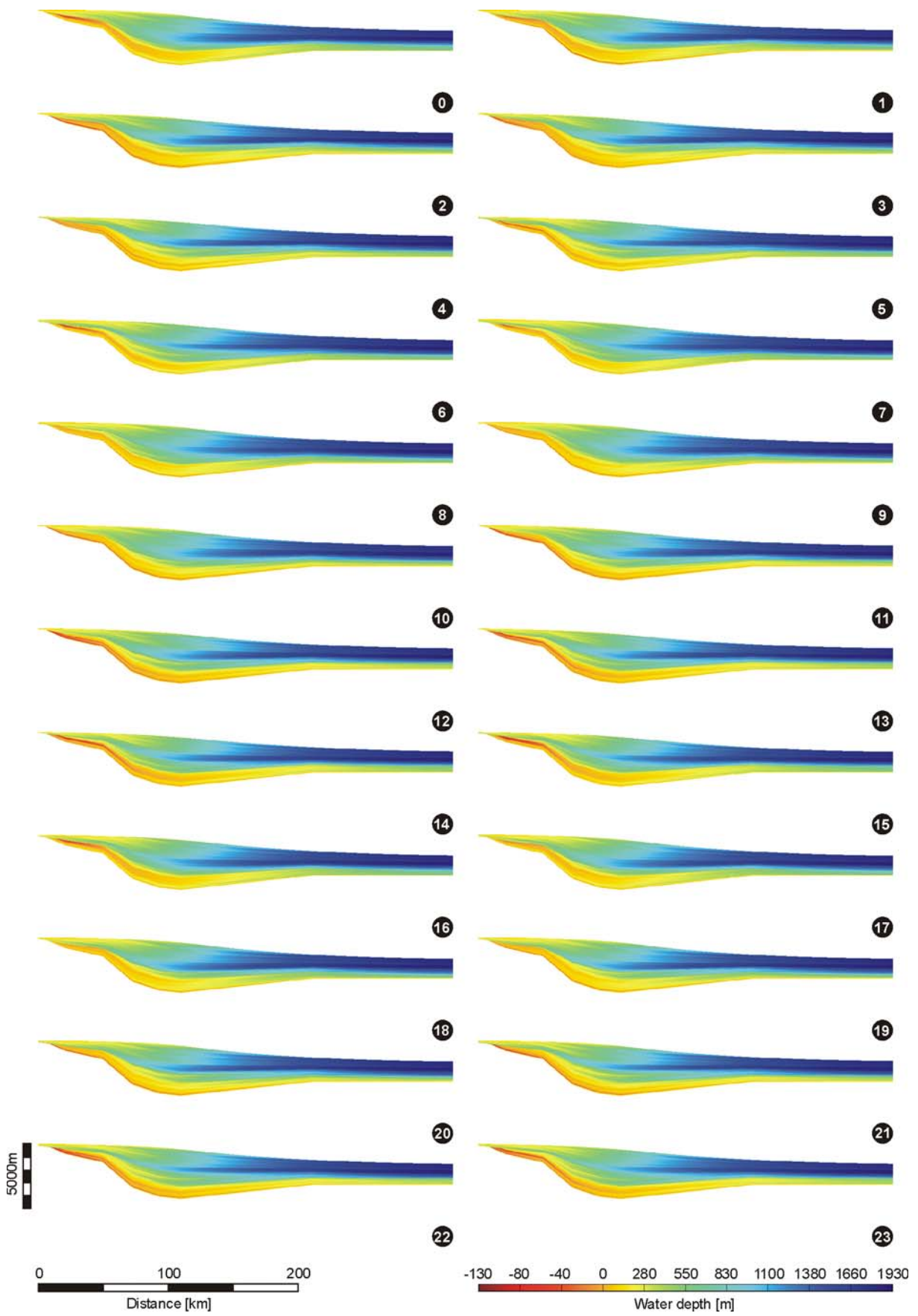
Fig. 5-9. Overview of 24 sediment supply rates (black curves) systematically applied to the basin model (“sinusoidal runs”) by varying the hypothetical longshore transport component (grey dashed line).

Following pages:

Fig. 5-10. Overview of model results 0-23: colours indicate composition of the basin fill [% Sand].

Fig. 5-11. Overview of model results 0-23: colours indicate paleowater depth [m] at time of deposition.





5. 3. 2 Parameter study (2): AFT shift runs

In order to attain model results under as realistic conditions as possible the studies presented here have entirely been established on the basis of a sediment supply rate derived from the denudation history of the NW-Namibian margin. Elaborate apatite fission track modelling by Gallagher & Brown (1999; chapter 4.1.2) provides a detailed denudation curve for the model transect. As mentioned before, the amount of sediment supplied by the Uniab and Koigab rivers, respectively, is insufficient to reproduce the stratal geometry observed in the central Walvis Basin. Considering that the denudation history affects the entire NW-Namibian margin, it might be suggested that a paleo-Huab river system supplies its sediments with a similar rate to the southern central part of the Walvis Basin. The Huab river is located to the south of model traverse (see fig. 4-27) and drains a much larger area that reaches farther inland. Prolonged sediment bypass across the continental margin and longshore transport into the model traverse by potential coast-parallel currents may accommodate the need for additional clastic input in the modelled segment.

To account for the temporal delay associated with such a process, the additional sediment flux curve is shifted parallel to the time-axis in 5, 10, and 20Ma-steps, respectively; a model run without temporal delay is presented for comparison as well. The curve related to the additional transport component has been given the shape of the initial denudation curve and is enhanced so that the resulting combined flux again represents a 2,3 times higher than original clastic influx.

The figures 5-12 & 5-13 document the model results of the “AFT shift runs”. In the upper part of figure 5-12, the essential model parameter “sediment flux” is displayed. A grey line represents the clastic flux derived from onshore denudation modelling; a grey dashed line displays the superimposed longshore transport component applied to the model in order to obtain a combined flux (black line). The four model runs a, b, c, and d reflect a temporal delay of the additional clastic influx of 0, 5, 10, and 20 Ma, respectively.

In the lower part of figure 5-12 the modelled composition of the basin fill is contoured as sand-shale-ratio. Figure 5-13 illustrates the associated paleowater depths in the upper part as well as a modelled seismic response prediction for the case-studies a, b, c, and d in the lower part; the latter display-mode is particularly suitable for comparison with real seismic sections.

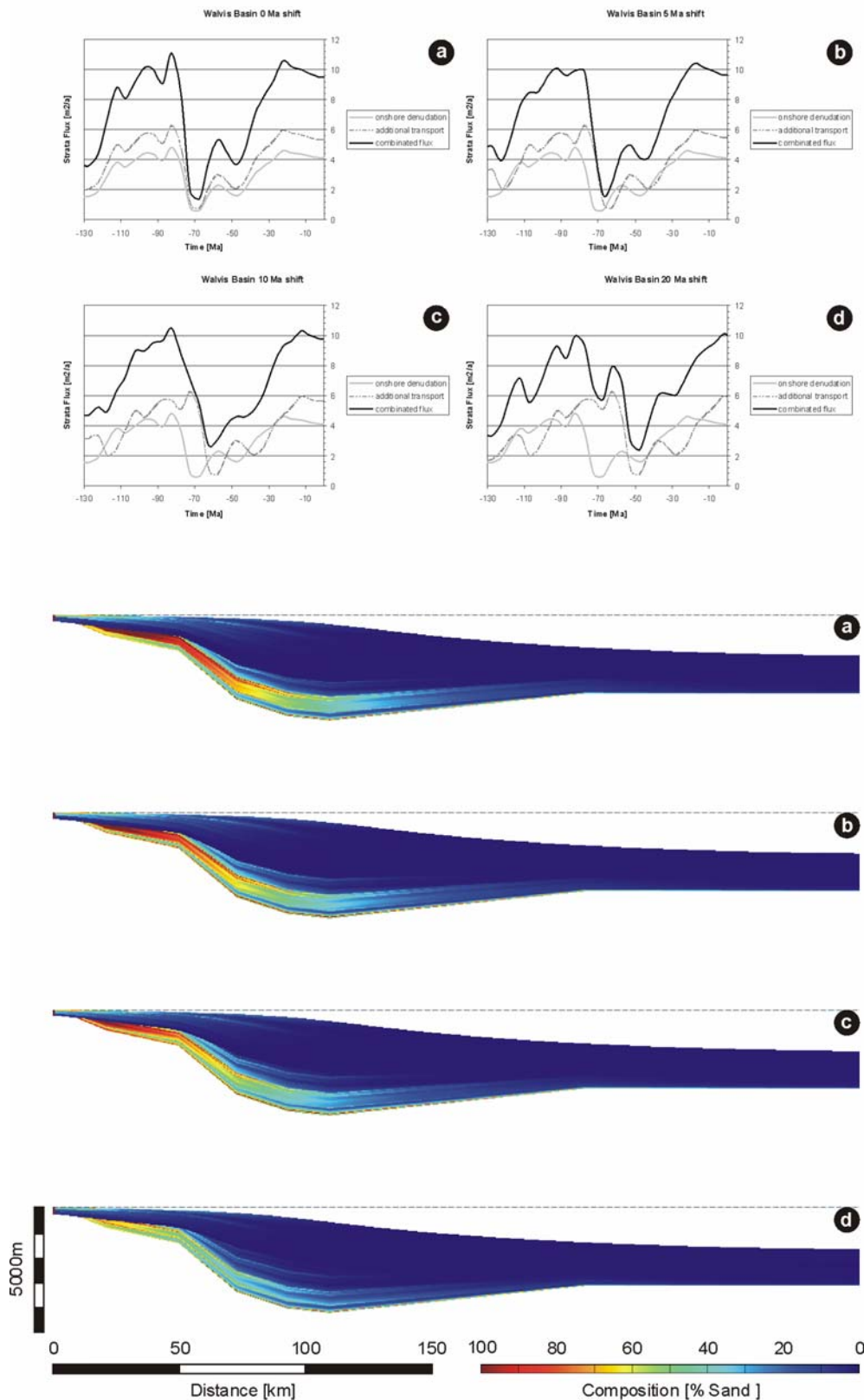
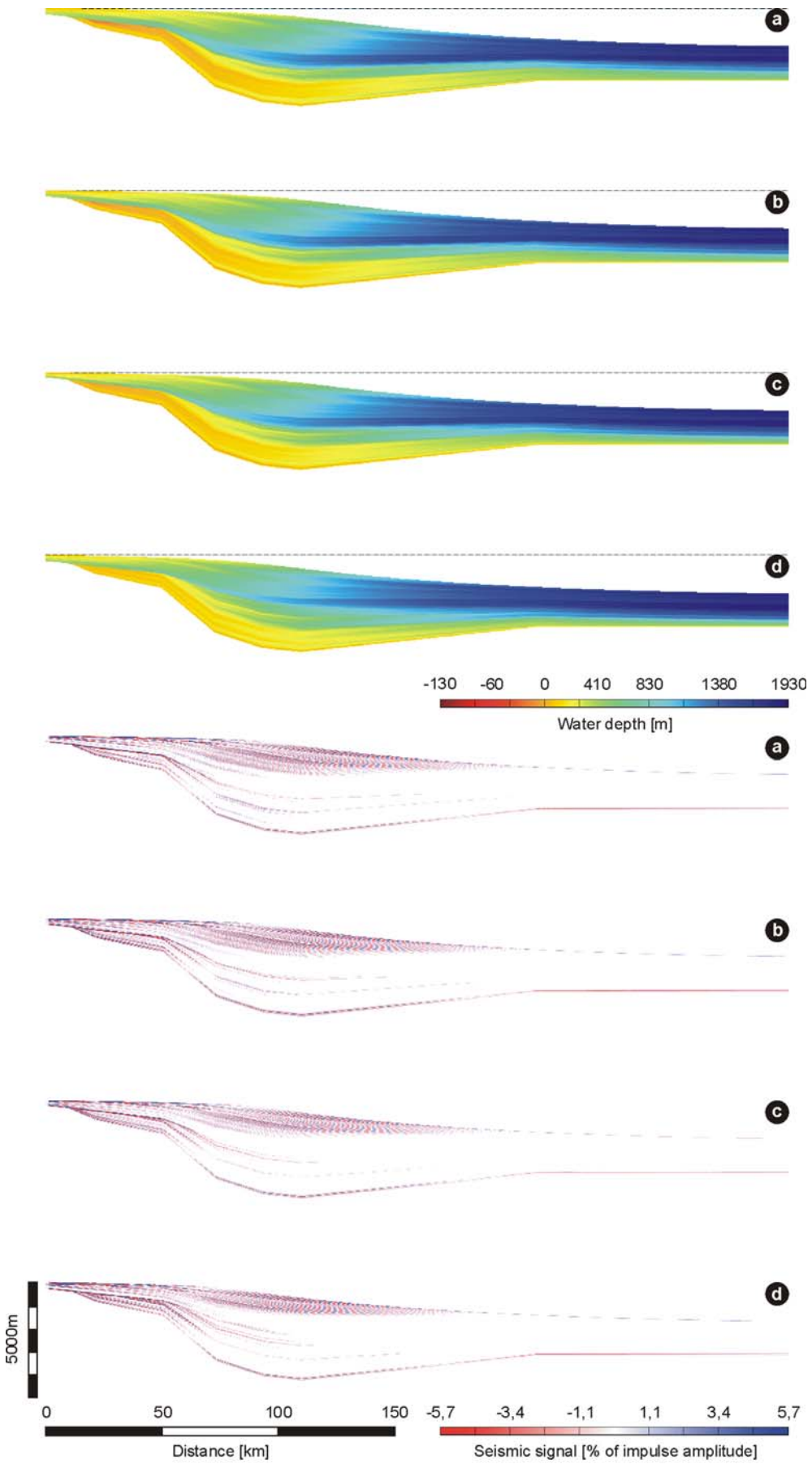


Fig. 5-12. Upper part: sediment supply rates for the AFT shift runs a-d. Lower part: modelled composition of the basin fill [% Sand]. See text for details.

Following page:

Fig. 5-13. Upper part: modelled paleowater depths of the AFT shift runs a-d. Lower part: modelled seismic signal [% of impulse amplitude]. See text for details.



Similarly to the “sinusoidal runs”, the general model approach of a systematically shifted additional flux based on the denudation history of the Namibian margin does not yield model results of sufficient accuracy when compared with a real seismic section (fig. 3-13) and well data (fig. 6-3). None of the models a-d is capable of reproducing the early drift shallow marine facies observed in well 1911/15-1 (fig. 6-3). The model run with no temporal shift applied to the additional flux (fig. 5-12a), however, best displays the Late Cretaceous sedimentation peak 80Ma ago (see chapter 4.1.2), yet the coarse-grained facies appears to be located too deep in section and its distal reach and thickness is still insufficient.

Besides the basin floor, two distinct seismic horizons are developed in the lower half of the basin fill (fig. 5-13a, lower part); these might reflect the Late Cretaceous seismic horizon K that initiates coarse clastic sedimentation above, and the Early Tertiary seismic horizons L or LII (see fig. 3-13) which represent prominent stratigraphic breaks, respectively.

Paleobathymetry modelling (fig. 5-13, upper part) generally provides results well within the range of paleobathymetric estimations derived from micropalaeontological well data (see fig. 3-20). A mid to Late Tertiary paleobathymetric maximum of up to 1900m of water depth which is followed by slight shallowing in the Late Tertiary to Holocene is very similarly indicated by the calibration well 2012/13-1.

Great expectations have been set in this model approach. As outlined above, they could be achieved with the concept of the “AFT shift runs” to a certain degree but there is still a lack of accuracy, especially in reproducing the Early and Late Cretaceous calibration data. Therefore, the means of shaping the significant parameter “sediment flux” manually appeared to be justified.

5. 3. 3 Parameter study (3): manual runs

In order to create a “best fit” stratigraphic model in good agreement with the calibration data from the central Walvis Basin, the general method of a systematically varying additional sediment flux has been skipped. Manual distribution of the additional clastic supply over time according to the demand certainly means a circular statement. But, however, since the proportion of clastic influx related to the denudation of the onshore part of the model traverse remains constant, the establishment of a “best fit” model allows to assess the relative role of the additional transport component quantitatively. Relatively enhanced sedimentation or even relative erosion due to a longshore transport component may be filtered out.

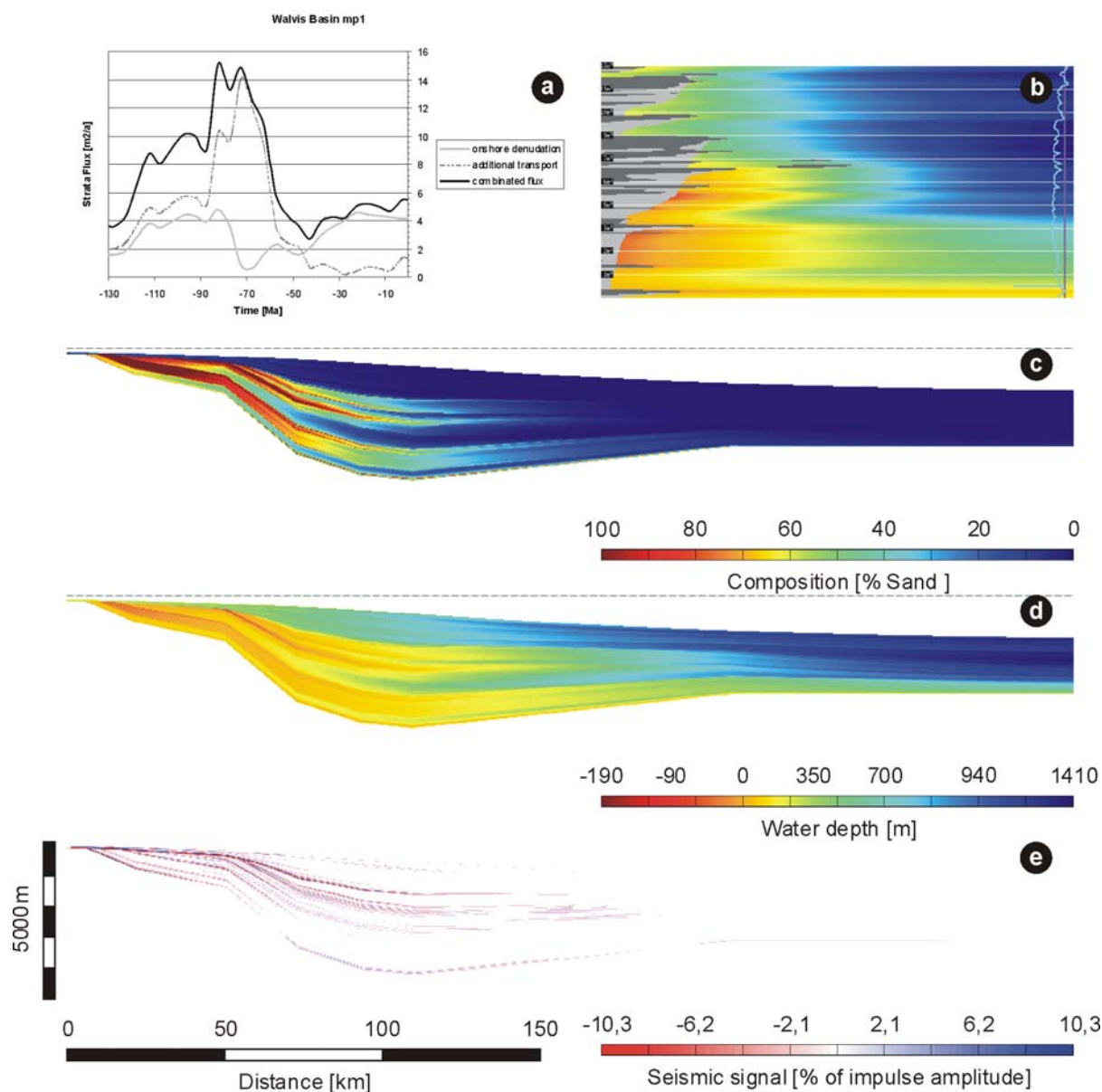


Fig. 5-14. Results of manual run 1 (mp1): (a) the particular sediment flux curve, (b) a chronostratigraphic Wheeler-diagram, (c) the composition of the basin fill [% Sand], (d) a paleowater depth model [m], (e) and a seismic response prediction model [% of impulse amplitude] are illustrated. See text for details.

Four significant model runs (mp1-4) are documented by the figures 5-14 to 5-17. Besides the particular sediment flux curve, a chronostratigraphic Wheeler-diagram, the composition of the basin fill, a paleowater depth model, and a seismic response prediction model are illustrated, respectively. The common feature of all of the four model runs is a decided accentuation of the Late Cretaceous denudation/ sedimentation peak as it is indicated by apatite fission track modelling (Gallagher & Brown, 1999). As suggested before, the entire NW-Namibian margin underwent significant erosion between about 85Ma to 75Ma b.p. Major sediment contributions from outside the model traverse may play a crucial role. The Huab river to the south, and the Hoanib river to the north of the traverse with their large catchment areas (see

fig. 4-27) may serve as important sediment repositories. Simple transversal transport across the margin definitely appears to be modified by a coast-parallel component. Considering the potential additional clastic input from the Huab and Hoanib rivers, respectively, sediment flux to the basin model between 90 and 60Ma has been modified manually in order to achieve a “best fit” model comparable with the calibration data.

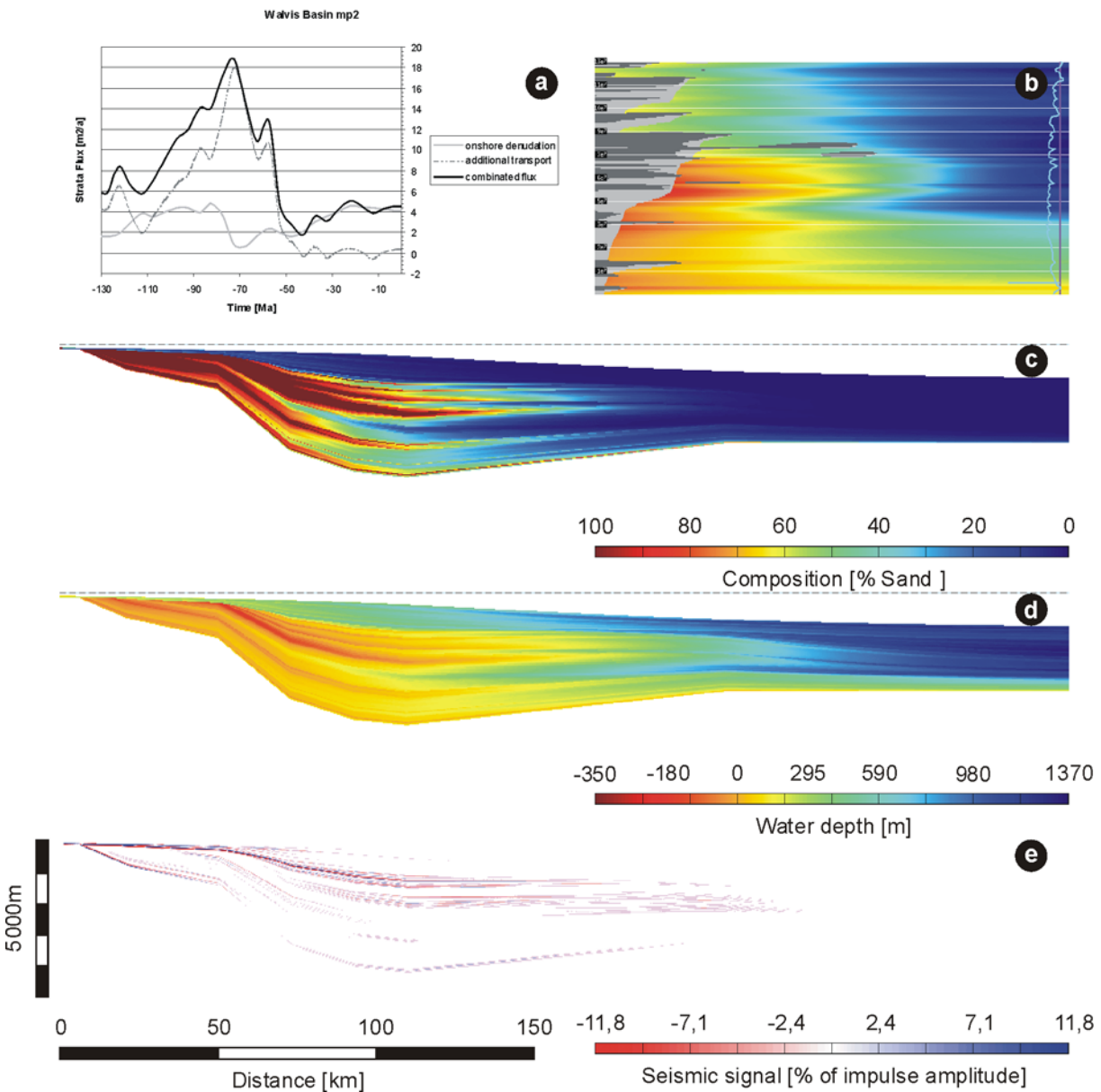


Fig. 5-15. Results of manual run 2 (mp2): (a) the particular sediment flux curve, (b) a chronostratigraphic Wheeler-diagram, (c) the composition of the basin fill [% Sand], (d) a paleowater depth model [m], (e) and a seismic response prediction model [% of impulse amplitude] are illustrated. See text for details.

The first model (mp1, fig. 5-14a) exhibits two distinct sedimentation peaks about 80 and 70Ma ago (black curve). Despite the prolonged subsidence in the Late Cretaceous and, other than in the “AFT shift run” models outlined above, both peaks are well displayed in the composition model (fig. 5-14c); they are slightly too high in section. Early drift shallow marine sedimentation is pronounced but still insufficient. Additionally, the basinward extent of both of these most striking calibration features is not far enough.

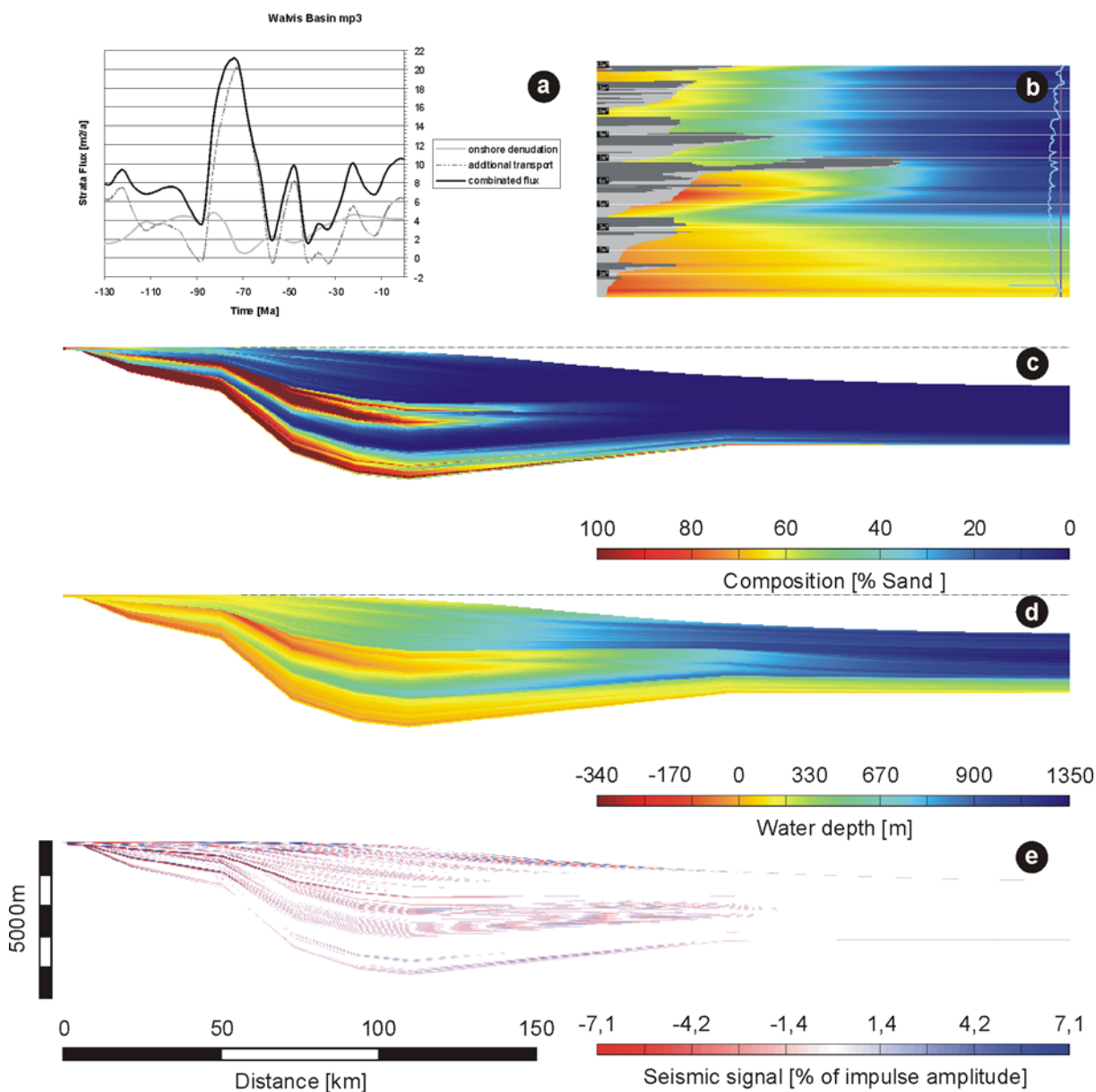


Fig. 5-16. Results of manual run 3 (mp3): (a) the particular sediment flux curve, (b) a chronostratigraphic Wheeler-diagram, (c) the composition of the basin fill [% Sand], (d) a paleowater depth model [m], (e) and a seismic response prediction model [% of impulse amplitude] are illustrated. See text for details.

In model mp2 the temporal extent of the clastic flux peak (fig. 5-15a) has been widened at the expense of Tertiary and Holocene sedimentation. Thereby, Late Cretaceous to Early Tertiary sedimentation is largely overestimated, notably in terms of thickness (fig. 5-15c). Its lateral extent, however, as well as the distal condensation of strata above the marginal basement ridge (see fig. 4-13a) which is best displayed by the paleobathymetric model (fig. 5-15d) is in good agreement with the original seismic data.

A single and very pronounced sedimentation peak between 90 and 60Ma ago has been applied in model mp3 (fig. 5-16) which turned out to be very favourable. Smaller peaks have been added in the early drift phase, in the Paleocene, and in the Miocene basin evolution, respectively (fig. 5-16a). Thickness, lateral extent, and the isolated character of Maastrichtian and Early Paleocene coarse clastics are very well displayed (fig. 5-16c); their vertical position in section is in good agreement with the well data. Early drift shallow marine facies and condensation of strata is well imaged by model mp3 (fig. 5-16c & d) but is still underestimated in terms of its lateral extent.

5. 3. 4 The best fit model

Model mp4 is only slightly different from model mp3 discussed above and is interpreted to be the most favourable model run ("best fit model"). Again, a pronounced sedimentation peak between 90Ma and 60Ma is applied to the basin model. The smaller sediment flux peaks of model mp3 are slightly reduced and smoothed. Early drift sedimentation is somewhat favoured at the cost of Tertiary and Holocene sedimentation (fig. 5-17a; appendix 13). A sand-rich interval of 400m thickness observed in the Late Campanian and Maastrichtian succession of well 2012/13-1 can be reproduced by model mp4 (fig. 5-17c) as well as a sandy to silty facies in the Early Paleocene. Early drift shallow marine facies is well reproduced in thickness and lateral extent and can best be calibrated with the basal units of well 1911/15-1 (see fig. 6-3). The distal condensation and even erosion of strata above the marginal basement ridge (see fig. 4-13a) is imaged by the paleobathymetric model (fig. 5-17d) as well as by the chronostratigraphic Wheeler plot (fig. 5-17b); the related prominent erosional event is indicated by grey colours in figure 5-17b reaching far offshore. Thereby, light grey documents non-deposition, grey reflects effective erosion.

Furthermore, the Wheeler diagram displays the evolution of six major erosional events interpreted as progradational unconformities (sequence boundaries SB1 to SB6; fig. 5-17b) resulting from the interplay of subsidence, relative sea level changes and sediment supply and each bounding a depositional sequence. The Wheeler plot illustrates that the unconformities generally evolve basinward very slowly to be overlapped again quite quickly during a rising sea level associated with retrogradation

and the deposition of rather condensed deep water facies. The sea level file applied to the model is indicated by the blue curve on the right margin of the Wheeler plot (fig. 5-17b) where rises are oriented to the left, and falls are oriented to the right, respectively.

Sequence boundaries are developed after model runtimes of about 28, 39, 58, 67, 94, and 108Ma, which is related to ages of 102 (Albian, SB1), 91 (Turonian, SB2), 72 (Cenomanian, SB3), 63 (base Paleocene, SB4), 36 (Late Eocene, SB5), and 22Ma (Lower Miocene, SB6), respectively. This corresponds well to stratigraphic events observed in well 2012/13-1 (see fig. 3-12).

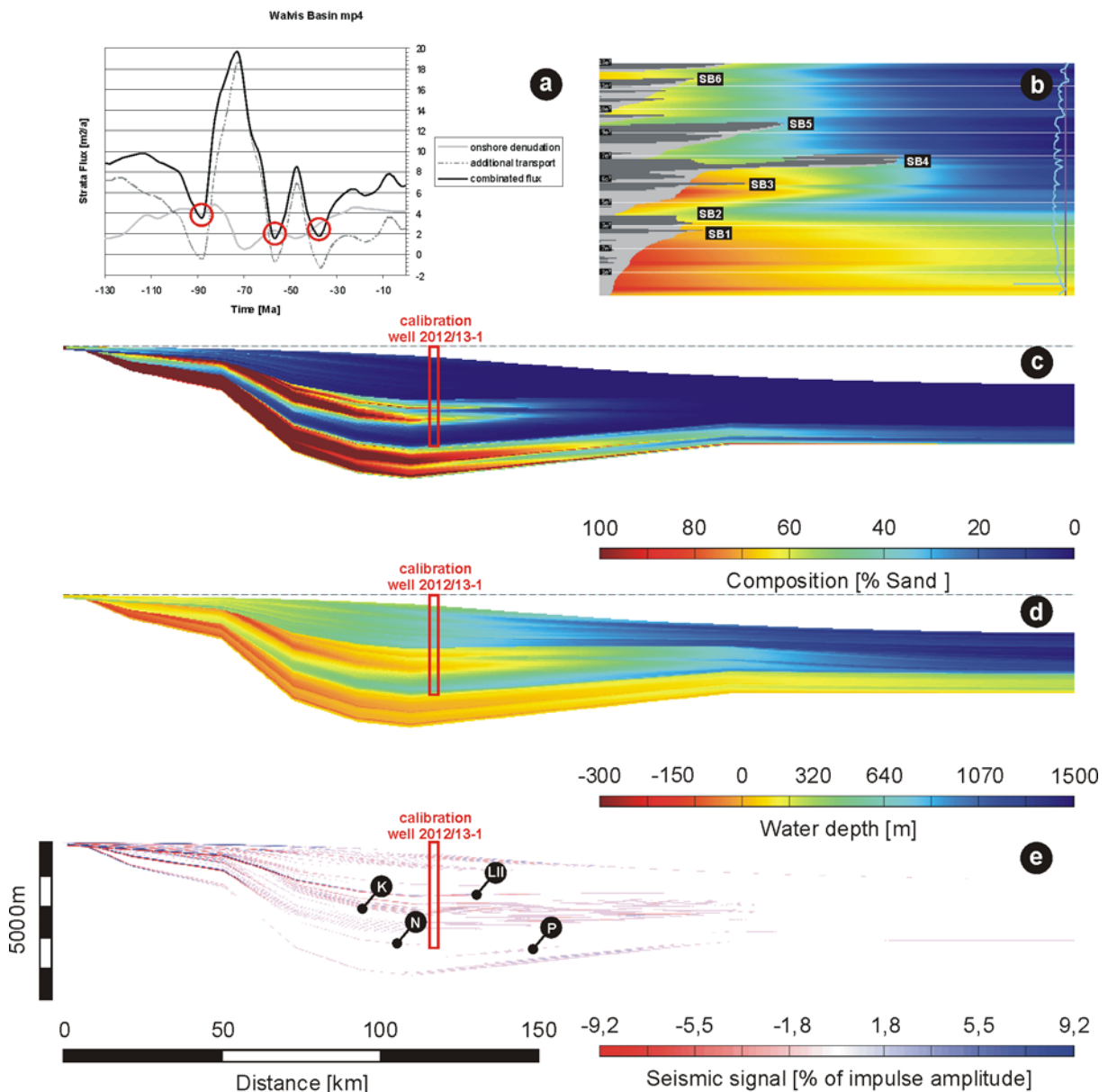


Fig. 5-17. Results of the “best fit” model run (mp4): (a) the particular sediment flux curve, (b) a chronostratigraphic Wheeler-diagram, (c) the composition of the basin fill [% Sand], (d) a paleowater depth model [m], (e) and a seismic response prediction model [% of impulse amplitude] are illustrated. Additionally, interpretations and correlations with calibration data are indicated. See text for detailed discussion.

Additionally, the modelled sequence boundaries partly bear analogy to seismic marker horizons observed in the central Walvis Basin (see chapter 3.6; fig. 3-13). SB1 might be related to seismic horizon P which marks the base of the late drift phase; the prominent Turonian stratigraphic break N may be resembled by SB2; seismic horizon K (SB3?) is suggested to have initiated the deposition of the overlying coarse clastics of Maastrichtian age; finally, the significant base Paleocene marker horizon LII may correspond to SB4. The analogy outlined here can be roughly reproduced by the modelled seismic response prediction illustrated in figure 5-17e. The establishment of a “best fit model” by application of the modified sediment supply curve displayed in figure 5-17a suggests that at least three periods of significant effective erosion have influenced passive margin evolution. These periods are characterised by a net clastic flux (black curve in fig. 5-17a) less than the flux derived from mere onshore denudation (grey curve) as indicated the by red circles. Again, these major erosional events are quite consistent with major stratigraphic breaks in mid Turonian (c. 90Ma), base Paleocene (c. 60Ma), and Late Eocene (c. 38Ma) times derived from biostratigraphic well data (see fig. 3-13).

5. 4 Discussion of the model results

In the previous chapter the evolution from systematic parameter studies, based on elaborate preliminary work of Junker (2002), to a “best fit” model of the NW-Namibian passive margin has been outlined. The basic idea of simulating the observed geometry and stratigraphy of the margin by stratigraphic modelling with independent parameters turned out to be rather unfavourable. By reproducing the marginal stratigraphy “manually”, the application of a circular statement could not be avoided; however, this approach enabled the additional transport component that needed to be introduced to be assessed quantitatively.

In connection with the “best fit” model run mp4 the good correspondence of the basin model to the stratigraphy and the internal (facial) geometry observed in seismic and well data has been discussed. Three distinct erosional events could be identified. The Late Cretaceous denudation peak derived from apatite fission track modelling (Gallagher & Brown, 1999; Raab, 2001) appeared to be still underestimated. This is a phenomenon similarly observed in independent petrographic data. Analysis of quartz varieties showed that about 50% of the quartz grains in the Maastrichtian bulk sand interval of well 2012/13-1 are related to source areas from outside the model traverse (see fig. 4-27). A distinct shift of the Late Cretaceous as well as of the Early Tertiary sediment supply peak compared to the denudation peak in the order of 10-15Ma towards younger ages needs to be incorporated into the model; this delay effect between denudation and sedimentation has already been discussed in chapter 4.1.2. The increase of the sediment supply rate by factor of about 2 (2,3) therefore appears

to be justified for several independent reasons (see chapter 4.5); it is essential not only to reproduce the internal stratigraphy of the Namibian continental margin, but also to image its external geometric features (see fig. 4-11a). A total thickness of the postrift sediments of about 5000m as well as the geometry of the seafloor, the shape and position of the present shelf break, and the present bathymetry of 700m at the well site are reproduced with satisfying accuracy by model mp4. Unfortunately, the bulge-like progradational evolution of the Late Cretaceous shelf break could not be properly reproduced due to the inability of *STRATA* to model gravitational failure of slopes that result in the deposition of turbidites.

The Namibian passive continental margin is dominated by clastic deposition; carbonate sedimentation plays a subordinate role. Pelagic background sedimentation, however, can be incorporated into the *STRATA* model but is very difficult to assess quantitatively. Application of a pelagic background sedimentation that contributes 10% to the entire sediment supply, for example, would decrease the demand for additional clastic flux from a factor of 2,3 to 2,08 in relation to the volume provided by onshore denudation in the model traverse.

The stratigraphic evolution of a passive margin is a 3-D phenomenon; to approximate its depositional history by means of a 2-D basin model affords basic conditions and simplifications to be considered. The basin is treated as homogeneous perpendicular to the modelled 2-D section; sediment supply calculated from a 3-D volume eroded onshore has to be referenced to a 2-D point source. However, considering the insights from a mass- and process balance that integrates all accessible information and comparison of the model results with the reference dataset allows conclusions about the third dimension to be made; Paola (2000) created the term “2,5-D model” for such an approach. In this study, reasonable semi-quantitative statements on a coast-parallel transport component possibly due to a “Proto-Benguela Current” turned out to be possible.

It should always be considered that model results can only be as plausible as their basic assumptions. A broad range of parameters which have been tested in extensive preliminary studies has been applied to the models presented here. Particularly, the time-dependent parameters heatflow, subsidence, sea level changes, and sediment supply have been intensely prepared. They are, however, definitely affected with uncertainties that are transferred into the model results. Additionally, *STRATA* models are treated as closed systems which is incompatible with natural systems. Nevertheless, the “best fit” model mp4 demonstrates that even the complex geologic evolution of a passive continental margin can be reproduced by a rather simple modelling software if the boundary conditions are accurately preprocessed. For future studies, the prediction-potential of the model approach presented here may serve as a useful tool for the exploration and evaluation of less well known margins.

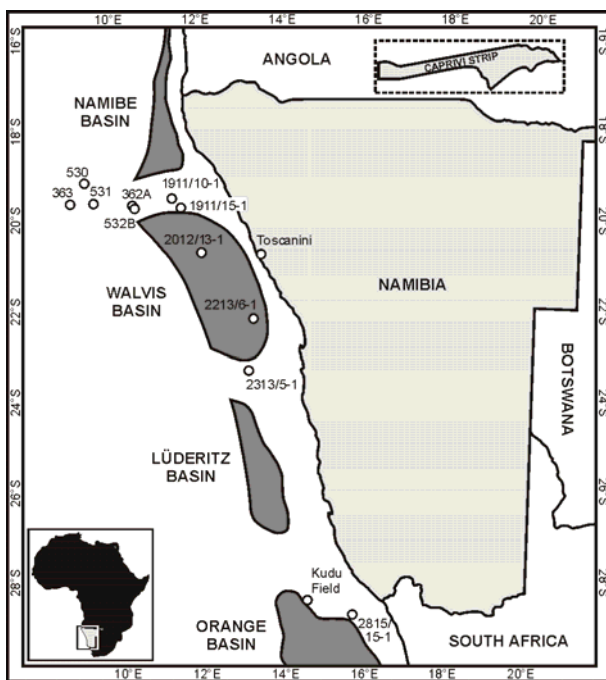
6 Hydrocarbon potential of the central Walvis Basin

6.1 Introduction

South Atlantic passive continental margins have long been object of hydrocarbon exploration. The Angolan Mocamedes- and Kwanza Basins, and the Brazilian Santos- and Campos Basins, respectively, proved to have extensive hydrocarbon potential (e.g. miscellaneous papers in Mello & Katz, 2000, and Cameron et al., 1999).

According to Etheridge et al.'s (1989) detachment model the Pelotas Basin in SE Brazil and the Walvis Basin in NW Namibia represent an exemplary pair of asymmetric conjugate passive margins. Both show typical lower- and upper-plate features, respectively. Driscoll & Karner (1998), however, doubt a marked asymmetric evolution of conjugate passive margins and suggest upper-plate characteristics for both. The structural evolution has, naturally, major influence on the evolution of hydrocarbon systems. But despite their exemplary character these two basins can be regarded as "underexplored" in both respects.

Although the Namibian passive margin has a proven petroleum system in the Kudu



gas field in southern Namibia offshore Oranjemund (e.g. Davies & van der Spuy, 1992/93; Wickens & McLachlan, 1990) only five wells have been drilled into the Walvis Basin in NW Namibia: Norsk Hydro (1911/10-1, 1911/15-1), Sasol (2012/13-1), Ranger (2213/6-1), and Shell/ Shark (2313/5-1) as displayed in figure 6-1. They characterise the postrift succession from c. 130Ma to recent and only the southernmost well 2313/5-1 offshore Walvis Bay penetrates clastic synrift sediments.

Fig. 6-1. Location map showing the Namibian continental margin, offshore depocentres, and well sites (after Light et al., 1993).

Apparently all elements of a working petroleum system are present in the Walvis Basin, even though untested to date. At least two potential source rock intervals are recognised in the postrift succession. Residual oil in Apto-Albian carbonates shows that oil has been generated, although from an uncertain source. Besides this

depleted reservoir, Maastrichtian deep marine fan sands and base Tertiary reef-like features might represent possible reservoirs. Gas chimneys observed on seismic reveal possible migration pathways.

10646 km of good quality 2D seismic have been shot in the Walvis Basin area including the N2R, NWG, and ECL surveys. Additionally, high-resolution aeromagnetic and gravity surveys are available. This study concentrates on a 2D section through the central part of the Walvis Basin and aims towards an integrated evaluation of the hydrocarbon potential with all available data from drilling and seismic.

After a brief general synopsis of potential source rocks developed on the Namibian passive continental margin a detailed analysis of the organic matter in the most favourable source rock interval of well 2012/13-1 with respect to quantity and quality is presented; thermal maturity is assessed by the evaluation of 1D maturity data and 2D maturity modelling with *PetroMod2D*.

The examination of potential reservoir intervals developed in the central and northern Walvis Basin is completed by a discussion of schematic play concepts that let further exploration activities appear worth while.

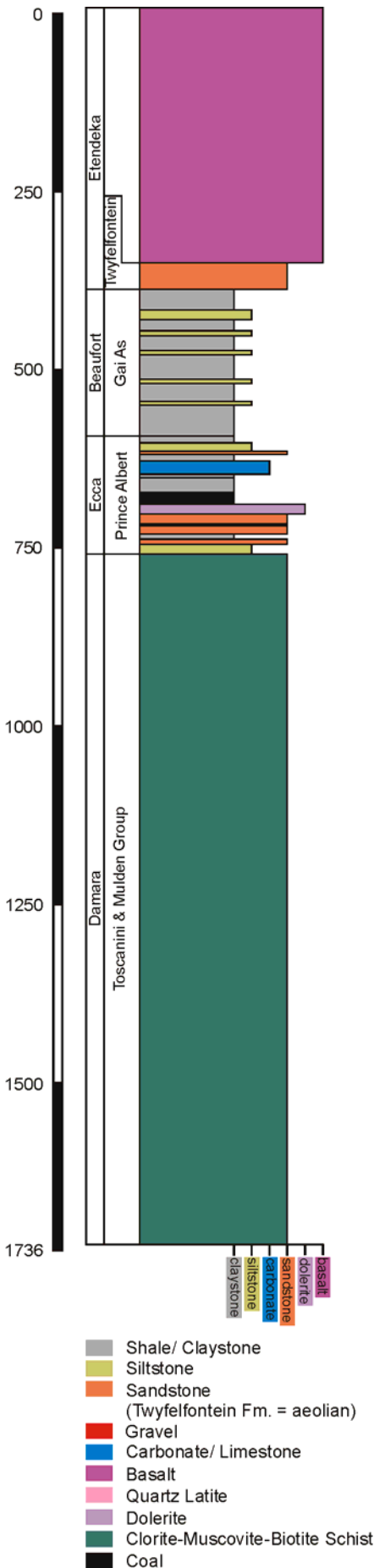
6. 2 Potential source rocks

Longlived and multi-phased extensional tectonics in Westgondwana started as early as in the Permo-Carboniferous and finally led to the formation of the South Atlantic in the Lower Cretaceous. Thereby rifting and seafloor spreading propagated from south to north (Stollhofen, 1999). Four major potential source rock intervals were deposited during the prerift-, synrift-, and postrift evolution of the margin, respectively.

6. 2. 1 Prerift strata

The shallow marine Whitehill Formation in southern Africa was deposited in Permian (Karoo) times and can possibly be linked to a "live oil" seep onshore Namibia (Walter et al., 1996). The equivalent Artinskian Irati shales proved enormous oil generation potential in southern Brazil.

Additionally, the Toscanini borehole onshore NW-Namibia (fig. 6-2) has drilled a total of 120m of carbonaceous shales containing 15m of Artinskian coal (Schommarz, 1988) attributed to the Prince Albert Formation (Ecca Group). Given sufficient spatial distribution and maturity conditions offshore, this interval would be capable of substantial gas generation. However, no wells offshore Namibia have yet reached this stratigraphic interval but it may be discussed in terms of a possible play scenario (chapter 6.5).



6. 2. 2 Synrift strata

Lacustrine environments capable of preserving TOC-rich shales may have developed during early rifting but lack well control on the Namibian margin. Oil-prone source rocks are reported from the Hauterivian synrift succession in the Orange Basin (Muntigh, 1993). Hypothetical synrift halfgrabens in the Walvis Basin would have attained excellent maturity conditions, but this option is yet untested. However, synrift source rocks are schematically incorporated in a *PetroMod2D* maturity model evaluated by Beha (2003; fig. 6-13).

6. 2. 3 Postrift strata

6. 2. 3. 1 Barremian/ Aptian

The passive continental margin of southwestern Africa has significant hydrocarbon potential as proved by the Ibhubesi-field in South Africa and the Kudu-field (fig. 6-1) in southern Namibia, respectively. Marine, oil-prone source rocks of Barremian/ Aptian age are well known from the Kudu wells and DSDP sites 361 (offshore Angola) and 364 (Cape Basin). They have been deposited during the early drift-phase of the opening of the South Atlantic under restricted marine conditions (Jungslager, 1999). Schmidt et al. (2002), however, suggest on the basis of geochemical data and maturity modelling that the Barremian/ Aptian strata are not likely to serve as both source and cap rock for the Kudu gasfield underneath.

Fig. 6-2. Simplified lithostratigraphic log of the Toscanini oil-borehole TO 1/72 (drilled by Du Preez, 1972). See fig. 6-1 for location.

Barremian/ Aptian source rocks have not been encountered in the Walvis Basin (wells 1911/10-1, 1911/15-1, 2012/13-1, 2213/6-1, fig. 6-1) but due to their occurrence in Angolan waters as well as in the Cape Basin, Bray et al. (1998) expect them to be widely distributed along the Namibian margin.

6. 2. 3. 2 Late Cenomanian/ Early Turonian

Cenomanian/ Turonian marine carbonaceous claystones with good source rock potential are present in the central and northern Walvis Basin offshore NW-Namibia, as documented by the wells 2012/13-1, 1911/15-1, 1911/10-1, and DSDP 530 (fig. 6-1). In the central Walvis Basin well 2012/13-1 provides direct access to dark, organic-rich, partially carbonaceous claystones of Late Cenomanian/ Turonian age which were drilled between 3450m and 3650m (fig. 6-3). Quantity and quality of organic matter were analysed by *Robertson Research* on behalf of *NAMCOR*; the provision of these data is gratefully acknowledged.

High gamma ray and sonic transit time readings delineate several zones, up to a maximum thickness of 15m. The highest organic carbon contents (TOC) of 5,45 % were measured in the interval between 3555m and 3567m which is earliest Turonian in age (fig. 6-4, appendix 14). It consists of dark grey, variably calcareous, organic-rich mudstones that contain abundant moderately pyritic sapropelic amorphous organic matter. Thus, the concentration of sedimentary organic carbon in well 2012/13-1 clearly exceeds the average value for deep sea sediments of 0,2% (McIver, 1975).

Well 1911/15-1 in the northern Walvis Basin, however, penetrates carbonaceous claystones of latest Cenomanian age with even higher TOC values of >10% (Holtar & Forsberg, 2000). An initially anoxic paleoenvironment followed by dysoxic conditions with poor to absent bottom water circulation is indicated by the quantity and quality of the organic matter and by a high uranium content. Deposition of this interval may have been related to the Early Turonian sea level highstand and the associated global anoxic event.

Quality of organic matter

Optical methods have been utilised by *Robertson Research* to characterise the organic matter included in the sedimentary pile of well 2012/13-1. Microscopical analysis was carried out from 1435m to TD and three types of organic matter were differentiated: inertinite, vitrinite, and sapropel (fig. 6-5, appendix 15). Inertinite is highly reflecting wood tissue with preserved cell structure and is considered to have no hydrocarbon source capacity. Vitrinite consists of the reflective cell-wall material of higher land plants and is, in contrast, regarded to have significant gas-generating

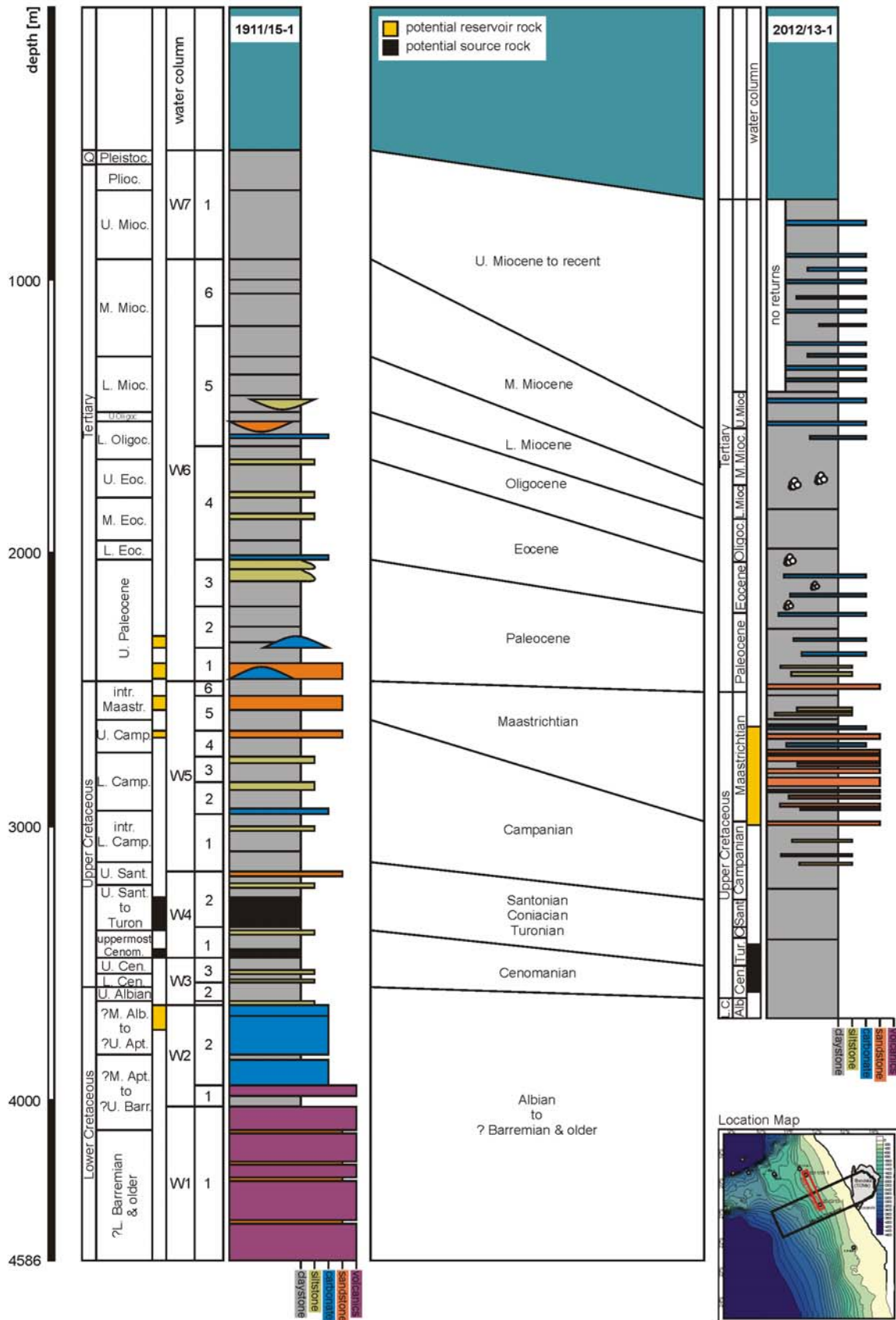
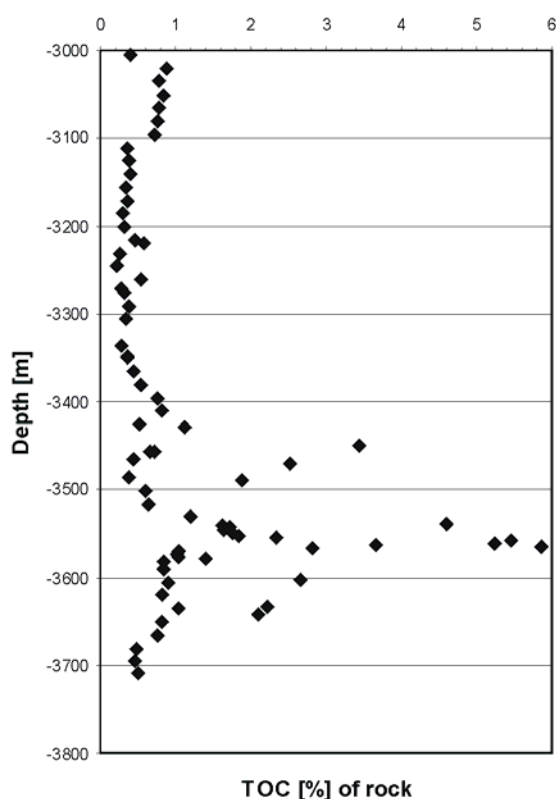


Fig. 6-3. Simplified lithostratigraphic columns and chronostratigraphic correlation of wells 1911/15-1 and 2012/13-1. Potential source rocks are indicated in black; potential reservoir intervals are indicated in yellow. See location map and fig. 4-1 for bathymetry information.

potential. Sapropel is a more general term for mainly phytoplankton and zooplankton which is microscopically amorphous and translucent. During diagenetic processes sapropel and other organic matter is altered to kerogen. The breakdown of labile kerogen and the generation of oil and gas is termed catagenesis (Tissot & Welte, 1984).

In figure 6-5 the distribution of these three types of organic matter is presented. Inertinite occurs preferentially in the upper third and in the deepest part of the measured section whereas sapropelic material is significant in the upper part and dominant in the central part of the sedimentary column between 2638m and 3050m.



Resedimentation of organic matter derived from the erosion of older deposits is documented by the presence of inertinite, preferentially in the Tertiary part of the section. Several peaks reflect the distribution of gas-generating vitrinite (e.g. 2398m, 2959m). The most significant vitrinite occurrence, however, is present between 3231m and 3620m. This interval matches the potential gross source rock interval from 3450m to 3650m very well.

Fig. 6-4. Plot of total organic carbon (TOC) content [% of rock] vs. depth for the interval from 3000m to TD of well 2012/13-1.

The quality of organic matter is characterised by means of Rock-Eval pyrolysis following the method of Espitaliè et al. (1977). Thereby, a finely grinded sample is raised from a temperature of 250°C to a temperature of 550°C in a furnace in an inert atmosphere. The evolving hydrocarbon products are recorded by a flame ionisation detector as a function of time. Appendix 14 contains the measured values for S1, S2, S3, and the S2-related peak temperature T_{max} . Additionally, the Hydrogen-Index HI [mgHC/gTOC] and the Oxygen-Index OI [mgCO₂/gTOC] are calculated from the combined S- and TOC-parameters.

Maximum temperatures determined for the S2-peak average around 429°C. OI values vary between 28 and 231 mgCO₂/gTOC whereas the value for HI reaches a maximum of 620 mgHC/gTOC at a depth of 3564m. The latter matches well the early Turonian potential gross source rock interval.

Comparison of these measured parameters with the commonly used trend lines for oil-prone type I and II kerogens and the more gas-prone type III kerogen after Tissot & Welte (1984) reveals most of the data falling between the trend lines for type II and III kerogen (fig. 6-6a). The majority of the HI vs. OI plots for the potential source rock interval between 3500m and 3600m has HI values of more than 300 (fig. 6-6a, black squares) and shows a trend towards an oil-prone type II kerogen.

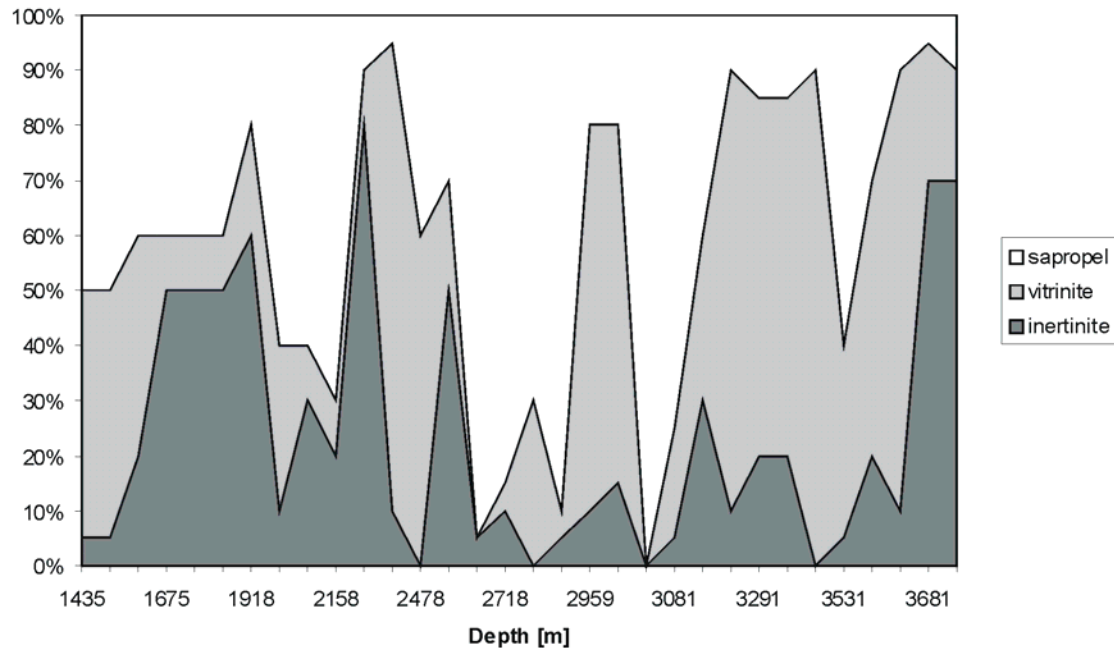


Fig. 6-5. Composition and distribution of organic matter in well 2012/13-1.

The latest Cenomanian claystones of well 1911/15-1 in the northern Walvis Basin with HI values of 600 indicate a very good type II kerogen, as well (Holtar & Forsberg, 2000). While hydrogen-poor type III kerogens are typical for most deep sea sediments, the hydrogen-rich organic matter encountered in the early Turonian claystones of well 2012/13-1 have much in common with upwelling-related sediments. For comparison, the recent upwelling cell offshore NW-Namibia is illustrated in figure 6-7.

As biostratigraphical data suggest deep water bathyal conditions for the early Turonian and the eustatic sea level curve of Haq et al. (1987) shows its historical maximum (see fig. 3-12), the observed HI values might indicate redistribution and affection by mass or turbidity currents sourced from shallower areas of the Namibian shelf. Preservation of organic matter under turbidite sediments is commonly due to rapid burial that inhibits aerobic microbial decay at the sediment-water interface. The high organic carbon concentration in the Late Cenomanian/ Early Turonian interval might be an effect of a “mid-Cretaceous global anoxic event” related to the sea level highstand.

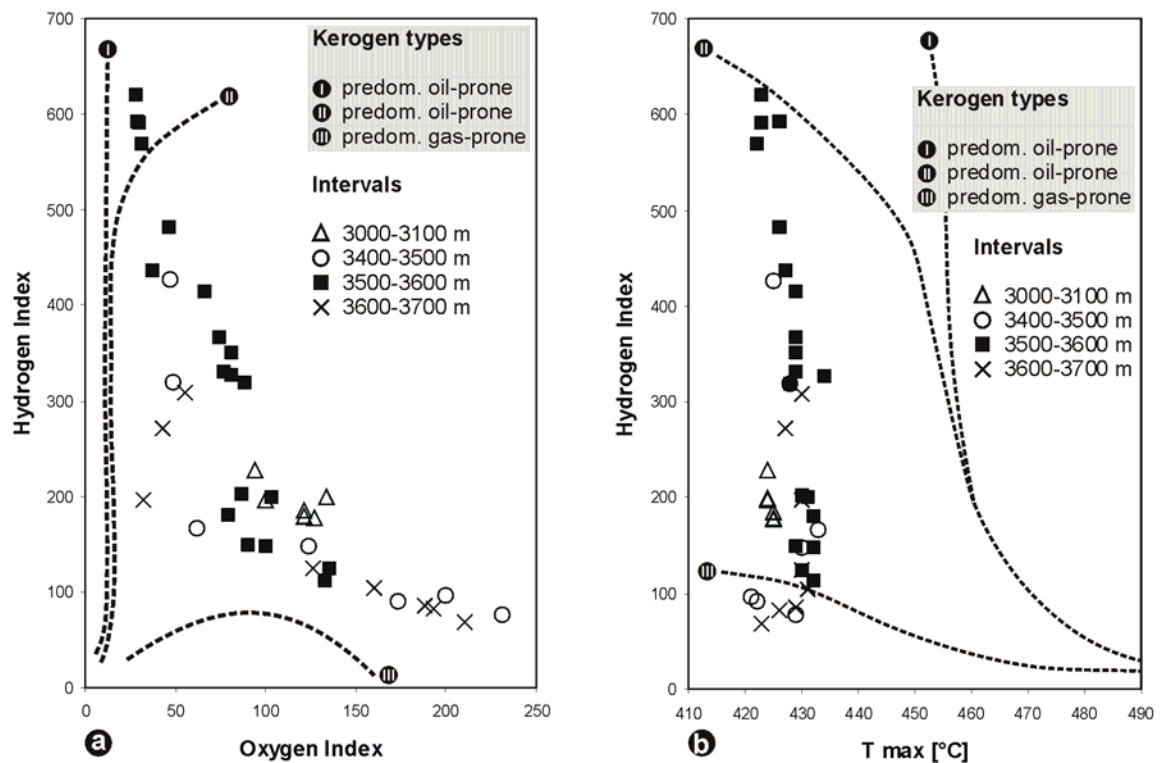
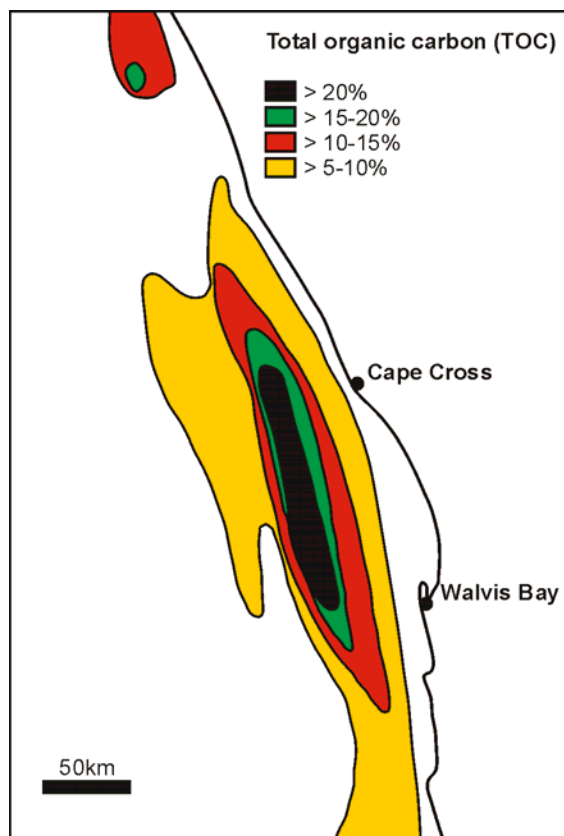


Fig. 6-6. Trend lines for the determination of kerogen types from Rock-Eval pyrolysis data. (a) Plot of Hydrogen index vs. Oxygen index after Tissot & Welte (1984). (b) Plot of Hydrogen index vs. peak temperature (T_{max} , see Holtar & Forsberg, 2000).

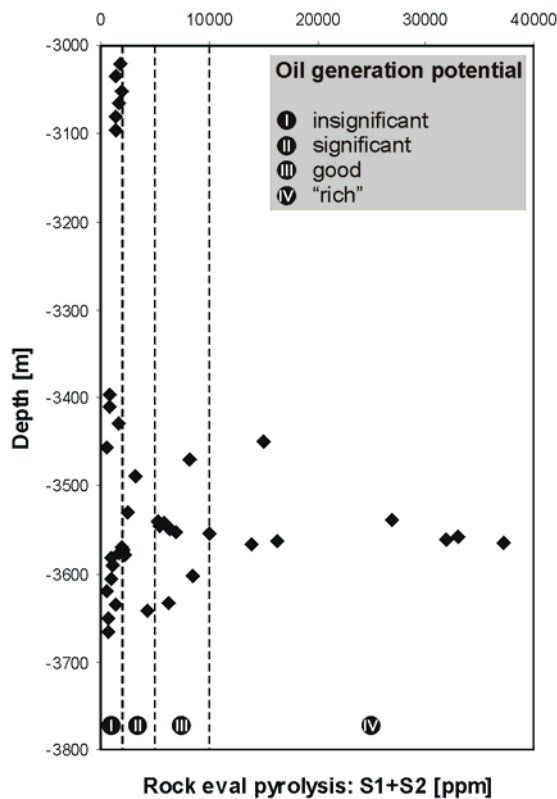


If plotted into a HI- vs. T_{max} -diagram (fig. 6-6b; see Holtar & Forsberg, 2000), the data indicate a similar trend roughly between a type II and the more gas-prone type III kerogen. The tendency towards the oil-proneness of a type II kerogen is not as clear as in figure 6-6a.

The dominance of the more gas-prone vitrinite within the organic matter of the potential source rock section is in slight contrast to the tendency towards an oil-proneness that results from the commonly used discrimination plot of figure 6-6a after Tissot & Welte (1984).

Fig. 6-7. Recent upwelling zone offshore NW-Namibia. Upwelling causes high phytoplankton productivity in surface waters. Seabottom sediments are anoxic beneath highly productive waters (modified from Demaison & Moore, 1980).

Utilising the HI- vs. T_{max} -diagram which provides an intermediate result between a more oil-prone type II kerogen and a more gas-prone type III kerogen (fig. 6-6b) therefore appears to be more reasonable.



Plotting the summarised S1 and S2 peaks from Rock-Eval pyrolysis against depth enables a qualitative assessment of the oil generation potential. Figure 6-8 shows a significant to "rich" potential within the gross source rock interval from 3450m to 3650m with a distinct peak at 3560m.

Fig. 6-8. Plot of S1+S2 vs. depth as a measure of oil generation potential.

1D maturity data

Besides the organic carbon content and the parameters derived from Rock-Eval pyrolysis two indicators were measured that allow first approximations on the thermal maturity level. Both, vitrinite reflectance and spore colour index clearly reveal an increasing thermal maturity with depth which reflects a "normal" burial history (fig. 6-9, appendix 15). Standard procedures for vitrinite reflectance measurements are documented in Stach (1982).

In situ vitrinite values range from 0,27%Ro at 1435m to 0,61%Ro slightly above TD. The Late Cenomanian/ Early Turonian potential source rock interval can therefore be interpreted as marginally mature. Vitrinite reflectance values of 0,55%Ro and higher indicate the beginning oil generation (Allan & Allan, 1990).

Highly reflecting resedimented vitrinites are concentrated below a depth of 2318m which might indicate the degree of redistribution of sediments on the margin during that time span. In contrast to marine organic matter these remains of higher land plants have a higher preservation potential. The values vary between 0,42%Ro at 1755m and 0,9 at 3709m (fig. 6-9a, appendix 15).

Evaluation of the spore colour index, normally referred to as “thermal alteration index (TAI)”, provides quite similar results. According to these data, the earliest maturity stages are reached at a depth of about 2950m. Therefore, the potential gross source rock interval lies well within the early mature stage of oil generation and the deepest section of well 2012/13-1 theoretically even reaches middle mature conditions (fig. 6-9b).

Compared to the vitrinite reflectance data the maturity level derived from the colour of spores within the kerogen seems to be slightly too high. This effect might be due to the subjective nature of TAI determinations as this optical method is not as standardised and reproducible as vitrinite reflectance measurements. A common equivalence to a pyrolysis T_{max} of 430°C is a vitrinite reflectance value of 0,5%Ro and a TAI value of 2,3 the latter of which is clearly exceeded here (appendix 15).

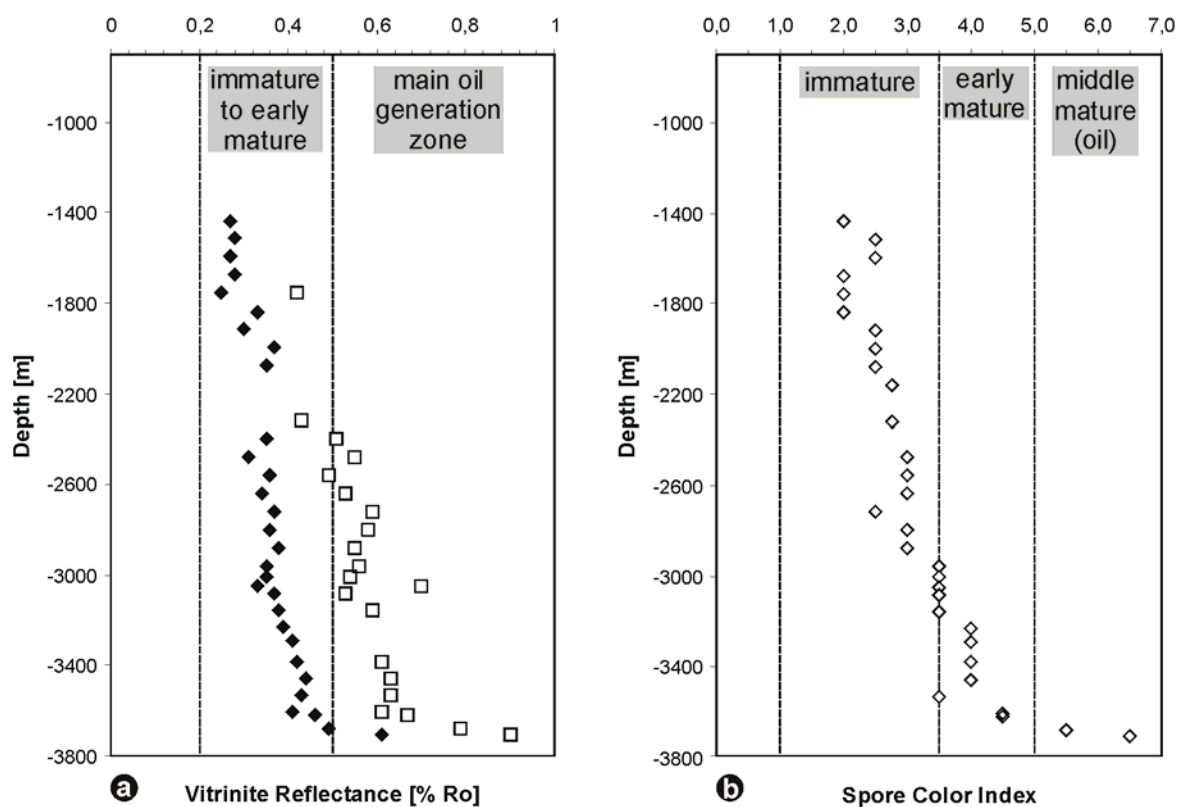


Fig. 6-9. Optical indicators for the thermal maturity level of well 2012/13-1. (a) In situ vitrinite (black diamonds) and reworked vitrinite (open squares) reflectance [%Ro] vs. depth. (b) Spore Colour Index vs. depth.

2D maturity modelling

A depthconverted seismic section through the central Walvis Basin (fig. 4-13a) that can be calibrated with the dataset of the 2012/13-1 exploration well in much detail is used to establish a geological transect across the margin with the professional maturity modelling package *PetroMod2D* (IES, Jülich/ Germany).

Additionally, the results from elaborate basin modelling with *STRATA* (chapter 5; Junker et al., 2002) are taken into consideration to account for lateral changes in geometry and facies within the postrift-succession.

The model consists of 15 layers representing the early drift- and postrift-sediments in the central Walvis Basin since 130Ma b.p. Due to magmatic underplating the basement is intensely modified by intrusions and lava sheets and it is referred to as "basaltic" (see chapter 3.3). This effect leads to a pronounced obscuration of any synrift structures.

Four stratigraphic breaks that affected the burial history in the basin are incorporated into the model at 90Ma (M. Turonian), 75Ma (intra U. Campanian), 65,5Ma (base Paleocene), and 17,5Ma (M. Burdigalian), respectively; all of them are indicated by the seismic and appear to be related to major eustatic sea level falls (fig. 3-12 & 3-13).

The comparison of modelled Easy%Ro-trends and temperature-gradients, respectively, with the calibration data provides excellent control on the basal heat flow applied to the model. Figure 6-10A illustrates that an abnormally low and temporally constant basal heat flow of 40mW/m² best fits the observed vitrinite reflectance data. An exponentially decreasing and spatially varying basal heat flow of 65mW/m² during the early drift evolution of the distal basin to 39mW/m² at the recent coastline, however, better fits the temperature data (fig. 6-10B & fig. 6-11).

These values are much lower than the data Schmidt et al. (2002) applied to their maturity model of the Kudu gasfield in southern Namibia. Assuming that a significant proportion of the heat flow floor at the top of the basement is derived from radiogenic heat production in the lower and middle crust, the strong basaltic overprinting of the wide continent-ocean transition zone offshore NW-Namibia (see fig. 3-5) might provide an explanation for the reduced heat flow inferred in the model. On the other hand, significantly increased heat flow values should be expected at least for the early phases of volcanic passive margin formation. Estimations of the recent surface heat flow in Namibia range from 50 to 55mW/m² (Ballard et al., 1987; Gallagher & Brown, 1999; Pollack et al., 1993). These values might, in turn, be related to enhanced radiogenic heat production of the granitic continental basement exposed on the NW-Namibian coastal plain (e.g. Haack et al., 1983).

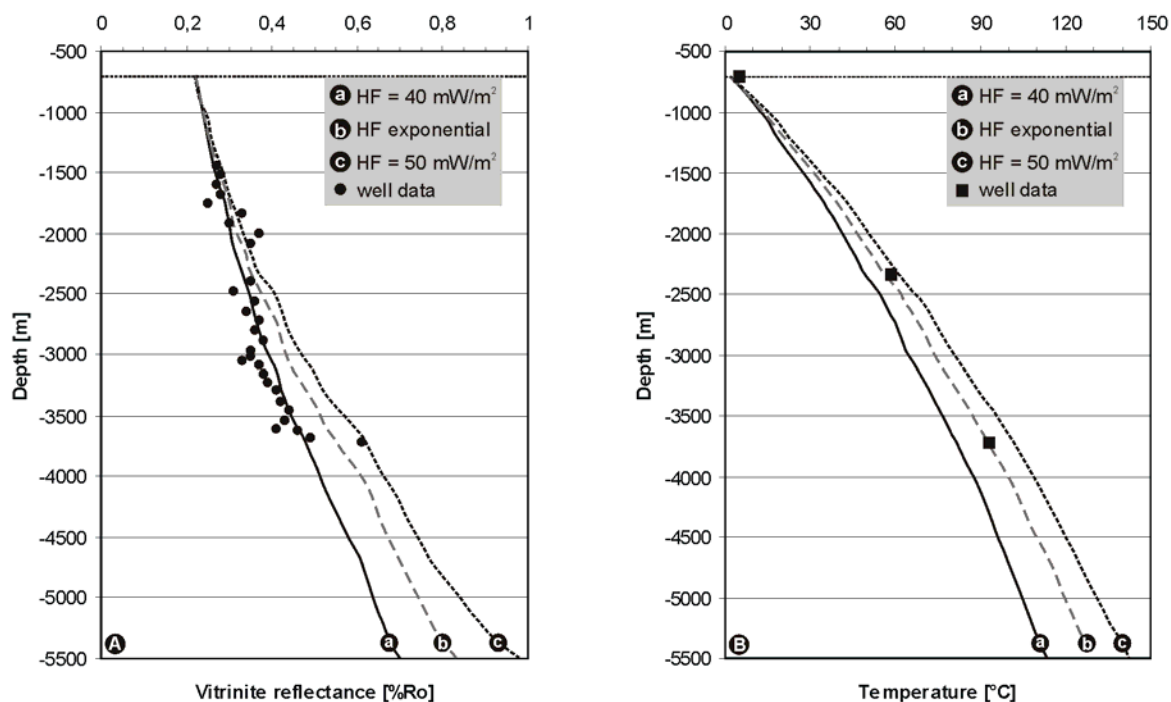


Fig. 6-10. Comparison of modelled Easy%Ro-trends (A) and temperature-trends (B) with calibration data from well 2012/13-1 for different settings of basal heat flow. A low constant basal heat flow of 40mW/m^2 (a) fits the observed vitrinite reflectance data very well. An exponentially decreasing and spatially varying heat flow (b) better fits the measured temperature data.

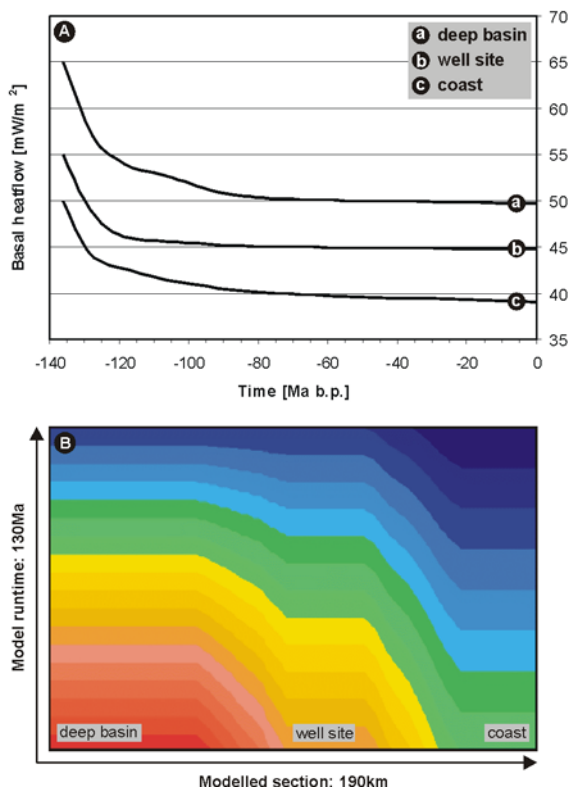
The model results presented in figure 6-12 presume a very low basal heat flow of 40mW/m^2 constant over time for the central Walvis Basin and maturity estimations derived from the model can therefore be regarded as minimum estimations.

In figure 6-12a-d a 2D section through the central Walvis Basin is presented; temperature, vitrinite reflectance, the beginning oil generation window, and the generation potential for hydrocarbons are illustrated. Layer 3 which is accentuated in green in figure 6-12c is referred to as potential source rock interval as it comprises the late Cenomanian/ Early Turonian TOC-rich claystones discussed above (fig. 6-3). An Upper Campanian/ Maastrichtian gross sandstone interval is penetrated by well 2012/13-1 between about 2630m and 2860m; it represents a potential good quality reservoir rock (fig. 6-3; yellow in fig. 6-12c) as outlined below.

Well data like porosities, temperatures, and vitrinite reflectance values are used to calibrate the maturity model; the well location is indicated in figure 6-12. Figure 6-12a visualises a modelled temperature section through the central Walvis Basin. Values range from 5°C at the seafloor to 125°C in the deepest part of the basin. A 1D temperature profile at the well site assuming different heat flow values is given in figure 6-10B.

Figure 6-12b displays a modelled vitrinite reflectance section through the study area. Values reach up to 0,8%Ro in the deepest part of the basin whereas the highest value attained in the source rock layer at the well site is 0,48%Ro. Assuming an oil prone type II kerogen, the onset of effective oil generation is thought to be at 0,5%Ro (Tissot & Welte, 1984). Large proportions of the source rock in the section are thermally immature for hydrocarbon generation; source rocks at the well site can be regarded as very marginally mature. However, approaching the hinge zone (Light et al., 1992) at a distance of c. 120km where a thicker sedimentary pile has been accumulated, the source rock layer reaches conditions well within the oil generation window (up to 0,65%Ro) as illustrated by figure 6-12c.

In figure 6-12d the modelled contours of the transformation ratio (in %) of generated hydrocarbons are presented. Considering the very conservative estimation of basal



heat flow, apparently a very low ratio of the generation potential has been actually transferred into hydrocarbons within the section. At the well site values of only 1,42 to 1,47% are reached within the source rock layer, increasing to 5% at c. 120km distance where the source rock is most deeply buried. In the deepest part of the basin a theoretical transformation ratio of 43% is attained.

Fig. 6-11. Illustration of an exponentially decreasing and spatially varying heat flow applied to the maturity model as a function of time (A) and as a contour plot over the modelled section (B).

It is evident from figure 6-12c that, even assuming a very low basal heat flow of 40mW/m², a significant proportion of the potential source rock interval has encountered the oil generation window. Well 2012/13-1 is located close to the left termination of this 55km wide zone which extends landwards to c. 145km distance and which is clearly associated with the early depocentre of the Walvis Basin. Parameter studies indicate that a slight increase of basal heat flow would increase the potentially oil generating zone significantly.

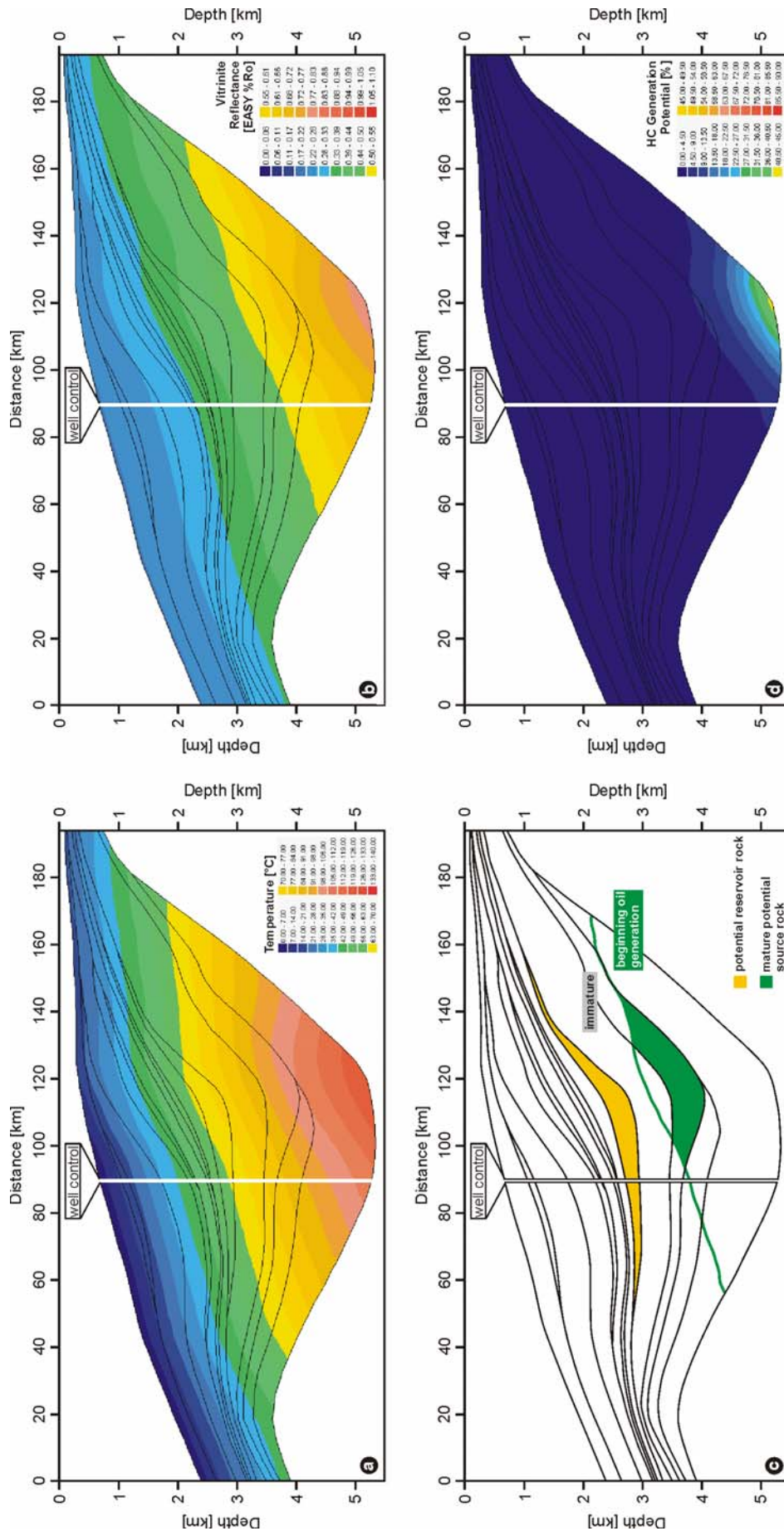


Fig. 6-12. Maturity modelling for a depthconverted seismic section through the central Walvis Basin with *PetroMod2D*. (a) Modelled temperature section. (b) Modelled vitrinite reflectance section. (c) Maturity stage of the potential source rock interval assuming minimum basal heat flow. (d) Modelled contours of the transformation ratio of generated hydrocarbons.

The 2D burial history of the central Walvis Basin (see fig. 3-21) provides important information on the timing of hydrocarbon generation. From 1D burial-shots and well-calibrated vitrinite reflectance curves no significant discontinuities in the sedimentary history like major uplift phases can be deduced. Two distinct sedimentation peaks in the Coniacian to L. Campanian and in the U. Maastrichtian, respectively, are evident from well data (see fig. 4-7). Large proportions of the sediments on the NW-Namibian shelf must have been accumulated by the end of the Cretaceous (Kukulius & Henk, 2002). A long period of low sedimentation rates from base Eocene to mid Miocene times is followed by a pronounced increase from the Upper Miocene onward.

These observations correspond to the timing of the hydrocarbon generation in the central Walvis Basin. The potential source rock interval was deposited in late Cenomanian and Early Turonian times and its base entered the oil generation window in the Late Paleocene (c. 55Ma), slightly after the sedimentation peak. The TOC-rich upper parts of the interval have been affected in the Late Eocene (c. 35Ma), at the latest. Maturity has increased continuously since then and at least 5% of the generation potential should have been transferred into hydrocarbons in the most deeply buried part of the source rock interval.

6. 3 Migration of hydrocarbons

It is quite difficult to comment on the proposed migration route into the most favourable reservoir. There is only very little evidence for migrating hydrocarbons either along faults or updip from Turonian or potential older sources. Gas chromatography analysis on extracts of migrant hydrocarbons from the Maastrichtian gross reservoir section revealed a biodegraded residue and a live oil fraction of unknown provenance containing low maturity biomarkers.

Synsedimentary fault activity is very common during the middle and Upper Cretaceous (see fig. 3-6b). This is possibly due to the high sedimentation rates that result in a destabilisation of the passive margin sediments at that time. Differential compaction might play an additional role. According to Schmidt et al. (2002) these structures can be interpreted as “counter regional faults” for which fully marine conditions and high sedimentation rates of fine-grained clastics are a precondition. Synsedimentary faults might possibly provide migration pathways into the Maastrichtian reservoir but unfortunately, this cannot be proved to date.

Within the scope of a diploma thesis at the University of Freiburg/ Germany (Beha, 2003) parameter studies have been performed in order to assess potential migration pathways in the central Walvis Basin with *PetroMod2D*. Schematic play concepts presented in chapter 6.5 can be evaluated with this extended model.

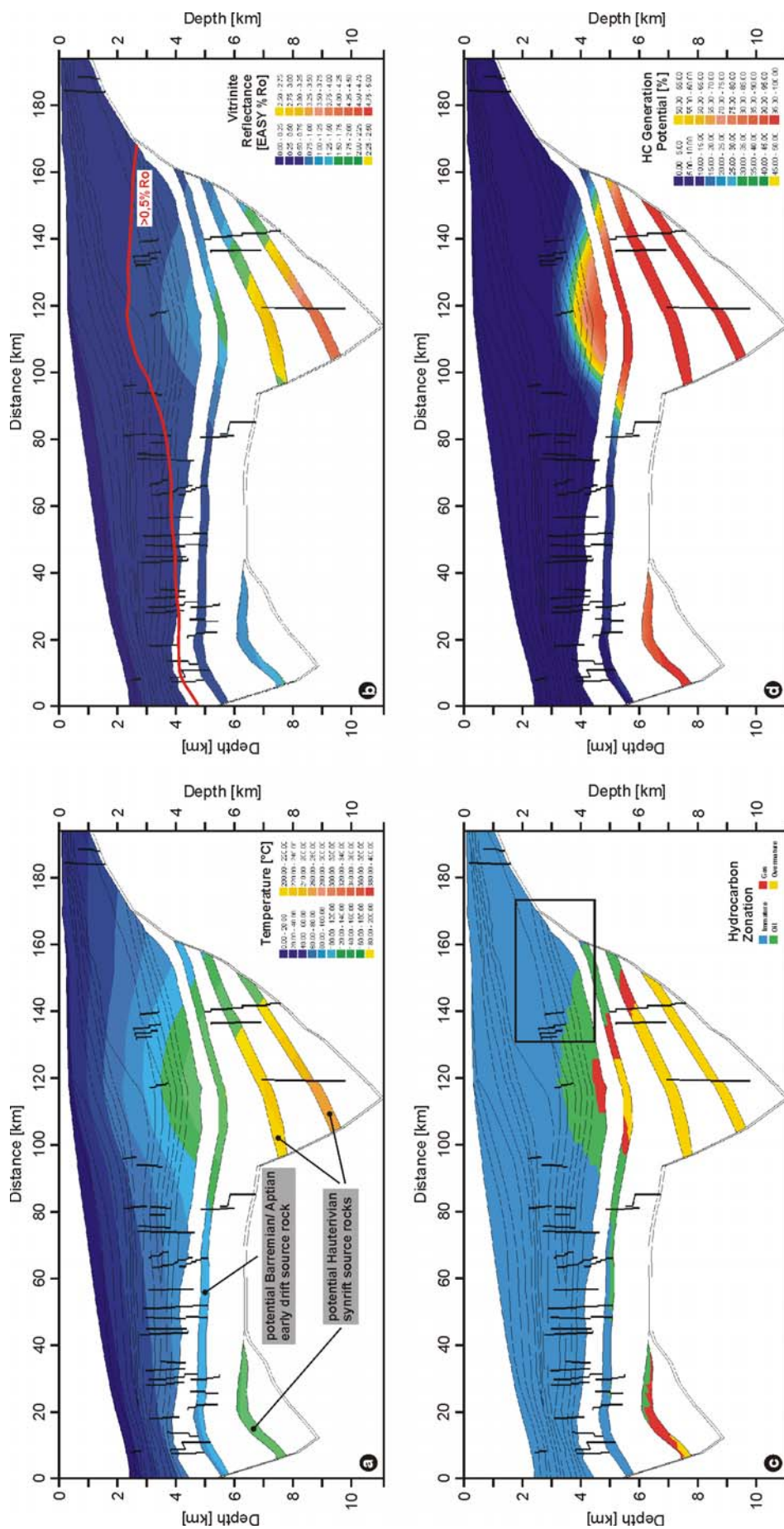


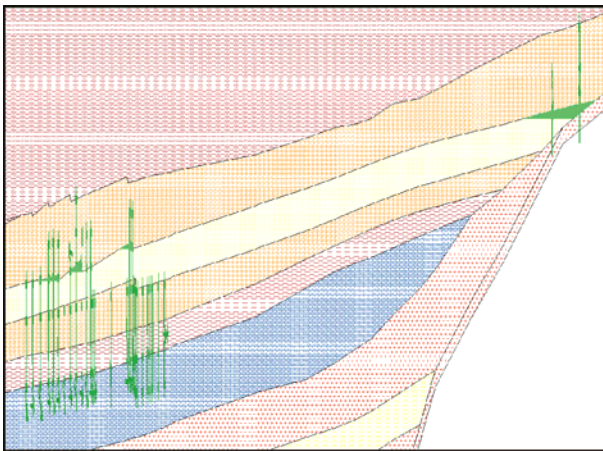
Fig. 6-13. Maturity model of the central Walvis Basin with *PetroMod2D* comprising synrift- and postrift-related structures. The maturity stage of potential synrift and early drift source rocks is evaluated. (a) Modelled temperature section. (b) Modelled vitrinite reflectance section. (c) Modelled hydrocarbon zonation; box indicates location of figure 6-14. (d) Modelled contours of the transformation ratio of generated hydrocarbons. Synsedimentary faults are incorporated to assess their relevance for hydrocarbon migration. Modified from Beha (2003).

The established model does not only include the deeper parts of the margin related to its synrift evolution, but also incorporates synsedimentary faults observed in the seismic section to evaluate their relevance for potential hydrocarbon migration (fig. 6-13).

Synsedimentary faulting appears to be absent in the Tertiary interval of the passive margin deposits; major postsedimentary faulting is not known from the central Walvis Basin, either. The occurrence of gas chimneys observed in seismic, however, indicates that hydrocarbons do have migrated.

In the conceptual maturity model presented in figure 6-13 potential Hauterivian synrift source rocks (chapter 6.2.2) intercalated in the basaltic lava sheets of the seaward dipping reflector wedges (see fig. 3-6b) as well as potential early drift source rocks of Barremian/ Aptian age are incorporated. A heat flow exponentially decreasing from 55mW/m^2 to 42mW/m^2 in the deep basin and from 42mW/m^2 to 32mW/m^2 at the coastline, respectively, has been applied to the basin floor.

As in the model results described above (fig. 6-12), the maturity of the potential source rock intervals is significantly associated with the depositional centre of the margin (fig. 6-13b). Modelled vitrinite reflectance values range from at least $0,5\%R_o$ up to theoretical values of $4,0\%R_o$ in the most deeply buried source rocks. Temperatures vary from 100°C to 260°C within the source rock intervals (fig. 6-13a). The associated modelled hydrocarbon zonation is illustrated in figure 6-13c. Prominent parts of the source rocks are oil prone; large parts, especially within the outer SDR wedge, are gas prone. Very deeply buried sections can even be regarded as overmature. Figure 6-13d suggests that a ratio of at least 10% of the generation potential has actually been transferred into hydrocarbons within the largest proportion of the potential source rock intervals.



Hydrocarbons have not only been generated, they have migrated as well as it is illustrated by figure 6-14 (location is indicated by the black box in figure 6-13c).

Fig. 6-14. Migration and trapping of hydrocarbons (green) associated with synsedimentary faults and updip pinch-out modelled with *PetroMod2D*. Location is indicated in figure 6-13c. Modified from Beha (2003).

Small amounts of mature hydrocarbons have migrated along synsedimentary faults into fault-controlled structural traps proving their relevance as migration pathways. Additionally, stratigraphically controlled onlap onto the marginal hinge line serves as a pinch out trap for generated oil that has migrated updip within this early drift reservoir interval (see chapter 6.5).

In the northern Walvis Basin, Holtar & Forsberg (2000) discovered residual oil of a highly mature source in the Barremian to mid Albian interval of well 1911/15-1 (see fig. 6-3, unit W2). Enhanced oil saturation has been found in low porosity zones of shallow marine carbonates which is characteristic for depleted reservoirs. Unlike the model results discussed above, no distinct source rock interval could be delineated from this occurrence.

6. 4 Potential reservoir rocks

6. 4. 1 Barremian to mid Albian carbonates

Potential reservoir rocks on the Namibian passive continental margin are restricted to three distinct intervals. The postrift development of the northern Walvis Basin has been derived from well 1911/15-1 by Holtar & Forsberg (2000); they delineate a Barremian to mid Albian age for their stratigraphic unit W2 (fig. 6-3). The base of this 371m thick interval is interbedded with the top of the underlying SDR sequences. Muddy limestones and glauconitic claystones prevail in the lower part. The upper 295m consist of shallow marine micritic mudstones with pelloidal grainstones and packstones; oolites are frequent in the upper 60m, indicating a general transgression. Holtar & Forsberg (2000) ascribe a very good reservoir quality with up to 25% porosity to the uppermost 100m of W2. Enhanced oil saturation is recorded in this interval indicating a very mature source that could not yet be established. Barremian/Aptian or even older sources are to be considered. However, the residual oil occurs in low porosity zones which is typical for depleted reservoirs.

The W2 carbonates are not encountered in well 2012/13-1 which terminates slightly higher in section, in the Upper Albian (fig. 6-3). Seismic-based extrapolation of the interval thickness to the south suggests more than 650m of W2 carbonates in the central Walvis Basin (Holtar & Forsberg, 2000).

6. 4. 2 Upper Campanian to Maastrichtian sandstones

A distinctive mounded feature observed on seismic within a deep marine fan complex was the primary target of well 2012/13-1. A 334m thick gross sand interval of deep sea turbidite origin was encountered from 2660m to 2994m (fig. 6-3). The sequence was biostratigraphically dated by *TimeTrax Ltd* on behalf of *NAMCOR* as Late Campanian to Maastrichtian in age.

6. 4. 2. 1 Petrographic composition

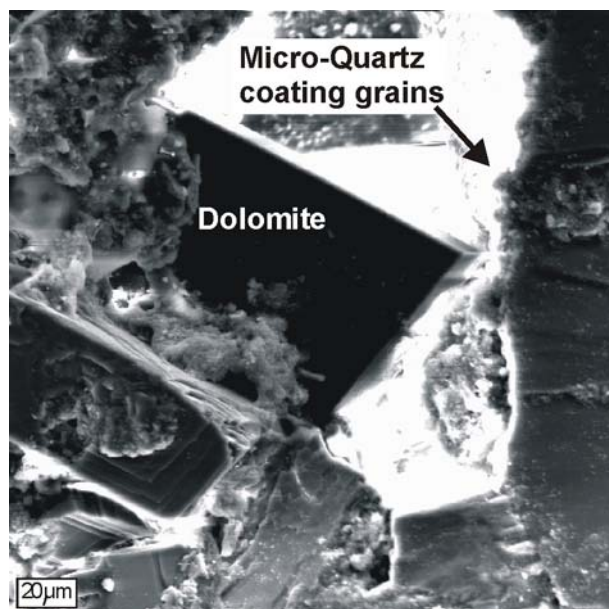
Detailed microscope and scanning electron microscope (SEM) analysis of cutting samples have been utilised to characterise this potential gross reservoir interval (see chapter 4.3). Quartz contributes up to 42% to the detritic components. Feldspar contents vary between 2% and 14% and particularly potassium feldspar may be responsible for a distinctly high gamma ray reading at 2660m depth. Only 2% to 12% of lithic fragments occur, which complicates provenance analysis (see chapter 4.3 and 4.5). Grain sizes range from very fine to coarse whereby the finer grained sands tend to be better sorted.

Quartz varieties were distinguished in order to gather provenance information. Although the onshore catchment areas for the central Walvis Basin lie almost completely within Etendeka Group volcanics, quartz grains of volcanic origin contribute only to about 50% to the quartz grain assemblage. A significant amount is provided by plutonic quartzes and even metamorphic quartz grains are present (fig. 4-16). This observation might reflect that the huge Etendeka plateau has been denuded below its base already in Maastrichtian times, at least in places, to allow for the erosion of the underlying Paleozoic to Precambrian granites and metasedimentary rocks (Kukulius & Henk, 2002; chapter 4.5).

6. 4. 2. 2 Characterisation of pore space and reservoir quality

Microcrystalline quartz and dolomite occur as authigenic minerals within the sands in varying proportions from 2% to 32%. Traces of pyrite could be observed by SEM-analysis. Microcrystalline quartz as a first-generation cement coats grains and fills pore spaces having itself abundant microporosity. It is suggested that formation water supersaturated with silica from radiolaria and diatoms in interbedded mudstones passed through the sand. A second generation of cement is represented by dolomite that can locally become very abundant and massive, especially in coarse grained intervals. Detailed SEM-analysis (chapter 4.2.3) reveals negligible contents, if any, of kaolinite and Illite that would otherwise have significant influence on the permeability.

The SEM-image in figure 6-15 illustrates a representative pore space of this potential gross reservoir interval. Quartz grains forming the pore space are coated by a thin layer of microcrystalline quartz. A second-generation cementation with idiomorphic dolomite appears to affect the reservoir quality to a major degree.



The gross sand interval exhibits an average porosity of 16%. Between 2832m and 2859m a “main” sandstone was encountered that showed even higher values of up to 21% porosity combined with a negligible clay content. Reservoir quality of the single sand units can therefore be interpreted to be good. However, a low net to gross ratio of only 0,3 indicates that these sandstones are generally very thin and the quality of the potential reservoir section as a whole has to be classified as poor.

Fig. 6-15. SEM-image of a representative pore space of the potential Upper Campanian/Maastrichtian reservoir rock interval indicating a first generation microcrystalline quartz-cementation and a second generation dolomite cementation (depth: 2838m, exagg.: 500x).

The prognosed submarine fan model for the depositional environment of this interval could be validated by drilling; however, the prognosed 100m of massive sand were not achieved by far. Additionally, no valid closure was encountered and updip leakage of hydrocarbons might be expected. Minor shows of extremely dry gas were recorded over the reservoir section from 2660m to 2994m. Reservoired hydrocarbons turned out to be absent.

6. 4. 3 Base Tertiary mounded features

The lobate deep marine fan sands of well 2012/13-1 described above appear to be the most promising potential reservoir interval in the central Walvis Basin. By analogy with well 1911/15-1 in the northern Walvis Basin, however, another horizon should be paid careful attention to.

The basal Tertiary unconformity which is observed in both wells marks a period of very limited deposition and is, at least in the proximity of the Walvis Ridge, associated with the occurrence of distinct mounded features. They are interpreted to

represent carbonate reefs or reef-like structures on the paleoshelf edge and are regarded as major objectives of future hydrocarbon exploration (Holtar & Forsberg, 2000).

6.5 Schematic play concepts

Prerift structural traps

Figure 6-16 schematically illustrates source rock–trap relationships that might be developed on the Namibian passive continental margin. Prominent prerift structures are absent in the central Walvis Basin but may be developed further south on the margin. Karoo rifting (Stollhofen, 1999) possibly provides fault traps for hydrocarbons sourced from the Permian Whitehill Formation (fig. 6-16a).

Synrift pinch-out traps

Intensive magmatism related to the Tristan plume and the emplacement of SDR's largely obscure any synrift structures in the Walvis Basin. Sands interbedded within single lava sheets, however, may serve as stratigraphic pinch-out traps truncated by the breakup unconformity (fig. 6-16b). The Permian Whitehill Formation may provide very mature hydrocarbons.

Early drift stratigraphic traps

Onlap onto the hinge zone (see fig. 3-14 & 6-14) during the early drift phase provides considerable potential for stratigraphic traps. Hydrocarbons sourced from the Barremian/ Aptian are known from the Kudu wells and from offshore Angola; these or older sources might be trapped in updip cut offs due to stratigraphic pinch-out or onlapping (fig. 6-16c).

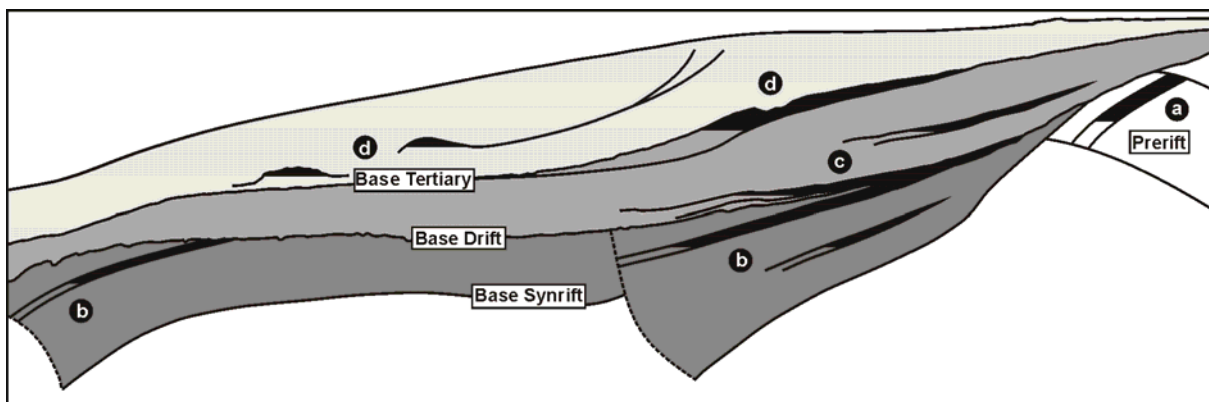


Fig. 6-16. Conceptual illustration of hydrocarbon play types that may have developed in the Walvis Basin during the (a) prerift-phase, (b) synrift-phase, (c) early drift-phase, and (d) late drift-phase of margin evolution. See text for discussion.

Posrift structural traps

Reservoirs in the later posrift succession may host hydrocarbons sourced from the Barremian/ Aptian as well as from Cenomanian/ Turonian TOC-rich shales. Maastrichtian deep marine fan sands proved good reservoir quality and may exhibit updip stratigraphic or slump-scar controlled pinch-out. Synsedimentary faulting and major slumping due to differential compaction and high sedimentation rates on the evolving shelf edge are important processes on the developing margin. Toe-thrust anticlinal structural traps are likely to be present (fig. 6-16d). The mounded reef-like features related to the base Tertiary unconformity outlined above may provide excellent potential as anticlinal traps (fig. 6-16d).

6. 6 Discussion of the hydrocarbon potential

The intention of this chapter is to assess the exploration potential of the NW-Namibian continental margin which is not yet exhausted. Potential hydrocarbon source rocks occur in prerift and synrift strata along the Namibian margin; direct access to data and samples of potential source rocks, however, is restricted to few wells drilled into the posrift succession.

Barremian to Albian shales proved generation potential in the Kudu wells. Cenomanian and Turonian shales containing good-quality organic matter have been drilled in the central Walvis Basin. TOC values of up to 5,45% and HI values of up to 620mgHC/gTOC appear to be rather comfortable. Maturity data and modelling with *PetroMod2D* purely based on well data, however, suggest very marginally mature kerogen at the well site. Yet, maturity of hydrocarbons improves significantly towards the coast where thicker posrift sediments have been accumulated. A hypothetical well there would encounter quite favourable maturity conditions.

Conceptual maturity modelling incorporating hypothetical synrift and early drift source rocks reveals very favourable maturity conditions as well as migration potential within the central Walvis Basin.

Three potential reservoir rock intervals are developed in the early to late drift succession. Samples from Upper Campanian/ Maastrichtian fan sands allow detailed characterisation of the reservoir quality. Porosity reaches 21% in the main sand body but a net to gross ratio of 0,3 is rather unfavourable. Clay mineral content, however, is negligible; the major factor limiting permeability is a locally strong late cementation by dolomite. Although the prognosed structural and stratigraphic closure for the Maastrichtian reservoir could not be proved by well 2012/13-1 it is evident that hydrocarbons do have migrated.

Reservoired hydrocarbons seem to be absent but all major elements of a valid hydrocarbon system are present in the central and northern Walvis Basin which makes further evaluation and exploration worth while.

The mound-shaped features associated with base Tertiary unconformity are interpreted to represent carbonate reefs or reef-like structures on the paleoshelf edge; they can be regarded as major objectives of future hydrocarbon exploration. Furthermore, a marginal basement ridge, which is best visualised by a depthconverted seismic section of the central Walvis Basin (fig. 4-13a), appears to be very prone to produce stratigraphic pinch-out structures and should be considered as a future exploration target as well.

7 Conclusions and discussion

Rifting and breakup of Westgondwana in the Late Jurassic/ Early Cretaceous led to the formation of the South Atlantic and a conjugated pair of asymmetric passive continental margins. The Walvis Basin offshore NW-Namibia is used as a case study to investigate a mass and process balance that links uplift and erosion onshore with contemporaneous subsidence and sedimentation offshore. Quantitative studies of passive margin evolution normally focus on the evaluation of the offshore sedimentary record. The model transect through the central Walvis Basin and adjacent onshore areas presented in this study, however, has shown that denudational unloading of the evolving continental margin by erosion contributes not only to persistent uplift and the maintenance of a high-elevation “Atlantic-type” passive margin; the reconstruction of the denudational history and the volumes eroded onshore within a well-documented 2D model traverse proved to be also a suitable means to control mass and process balance calculations if applied as input for stratigraphic basin modelling.

Volumes eroded onshore are calculated for a well-defined catchment area by assuming possible paleo-landsurfaces for the time of breakup and initial margin evolution; stratigraphic remnants, estimations of intrusion depths, and apatite fission track (AFT) analysis provide reasonable indicators for the thickness of erosion. The onshore part of the model traverse has been chosen so that the associated drainage regime lies almost completely within Etendeka Group volcanics; non-volcanic detritus encountered offshore is therefore attributed to other sources and a differential, coast-parallel transport component is quantitatively assessed.

The offshore part of the 2D model transect is documented by the seismic section ECL 89-41. Basement features are largely transparent and rift-related structures are obscured by intensive magmatism resulting in the emplacement of seaward dipping reflectors. Subsidence analysis, however, enables conclusions on the geodynamic evolution of the margin to be drawn. Thermal subsidence corresponds to cooling curves of normal oceanic lithosphere thus indicating a basaltic character of the basement. Significant crustal thinning and associated subsidence during the earliest phases of margin evolution are suggested to be compensated by magmatic underplating and/ or dynamic support of a plume.

Well 2012/13-1 penetrates much of the postrift succession and is used for a detailed calibration of the seismic section that reveals a typically wedge-shaped geometry for the passive margin sediments. Volumes of sediment deposited offshore are calculated from a depthconversion of the seismic section based on sonic logs. High resolution biostratigraphy combined with the interpretation of seismic marker horizons allows for the reconstruction of the depositional history during passive margin formation; it is in broad qualitative correspondence to the denudation history derived

from AFT analysis thus indicating a clear causal link between erosion onshore and contemporaneous deposition offshore.

However, mass balance calculations reveal that the material eroded onshore is insufficient to produce the stratigraphic architecture encountered offshore even if a maximum thickness of erosion of 5km is assumed; mass balancing suggests a volumetric misfit of at least 25%. These observations are supported by petrographic and geochemical provenance analysis as well as by quantitative basin modelling which all indicate a misfit of even 50%. Only half of the sediments observed offshore can be attributed to nearby volcanic sources. A substantial part of the detritus has been transported into the transect by coast-parallel currents; a precursor of the anticlockwise Benguela Current is suggested which may have already been established in the juvenile South Atlantic south of the Rio Grande-Walvis Ridge bathymetric barrier. Provenance studies and geochemical data furthermore indicate that substantial parts of the Etendeka volcanic plateau have already been eroded by the end of the Cretaceous. Late Proterozoic basement rocks of the Damara Group may have been exposed in the Maastrichtian at the latest. This observation corresponds to a major denudation peak between 85Ma and 75Ma b.p. derived from AFT analysis.

Stratigraphic basin modelling incorporates basement subsidence, basal heat flow, global sea level changes, and sediment supply rates derived from the reconstruction of the denudational history of the margin segment. Geometry and stratigraphic architecture of the postrift succession are quantitatively reproduced thus providing physical explanations for the main sequence boundaries and the lithological composition of the basin fill. In addition to its predictive potential this process-based model is applied as improved input for a thermal maturity model assessing the hydrocarbon potential of the central Walvis Basin. Late Cenomanian to Early Turonian claystones encountered in well 2012/13-1 reveal good source rock quality and show features of both oil- and gas-proneness. Maturity indicators as well as maturity modelling depict a marginally mature kerogen in that interval at the well site. This unexpectedly low maturity is attributed to reduced basal heat flow inferred from the model which may in turn be related to strong basaltic overprinting of lower to mid crustal levels. However, possible future exploration targets can be delineated for the area of pronounced onlap onto the marginal hinge line during early drift evolution.

In conclusion, major aspects of this study are briefly highlighted again:

1. The evolution of the central Walvis Basin started in the Hauterivian/ Barremian and resulted in the formation of a typical volcanic passive margin.
2. Intense magmatism during rifting and oceanic onset largely obscures synrift features.
3. Thermal subsidence corresponds to cooling curves of normal oceanic lithosphere thus indicating a basaltic character of the basement.
4. Synrift subsidence is largely compensated by magmatic underplating or by dynamic support of a plume; the thermal effects may explain prolonged shallow-water conditions until c. 90Ma b.p.
5. Basaltic and/ or carbonaceous deposition keeps pace with reduced subsidence during the early drift-evolution of the margin.
6. The postrift succession in the seismic section ECL 89-41 reveals a wedge-shaped geometry typical of passive margins that can be calibrated with well 2012/13-1.
7. The onshore part of the model traverse lies almost completely within Etendeka Group volcanics; non-volcanic detritus encountered offshore can therefore be attributed to other sources.
8. Reconstruction of the denudation and sedimentation history in the 2D model transect, respectively, shows broad correspondence. A volumetric misfit of 50% is supported by petrographic and geochemical provenance studies as well as by basin modelling.
9. This integrated approach suggests that about half of the sediment observed offshore can be attributed to longshore currents that have already been active during early margin evolution.
10. Substantial denudation of the Etendeka volcanic plateau during early margin evolution exposed Late Proterozoic strata to erosion in the Maastrichtian at the latest; this corresponds to the denudation history independently obtained from AFT analysis.
11. Process-based stratigraphic basin modelling is capable of a quantitative reproduction of the postrift stratigraphic architecture observed offshore.
12. The hydrocarbon potential of the central Walvis Basin is assessed by maturity modelling based on the stratigraphic model. Late Cenomanian to Early Turonian good quality source rocks reveal marginally mature conditions at the well site but significantly improved potential closer to the marginal hinge zone.
13. This integrated approach to quantitative passive margin evolution can serve as a case study implying a strong predictive potential for undrilled intervals or less well documented passive margins.

The quantitative approach to passive margin evolution presented in this study has to cope with certain simplifications that are predominantly owed to the restriction of the available data to a 2D transect. An extension of the seismic database into the third dimension and additional well control combined with a more continuous sampling of drill cuttings would have been helpful especially in terms of the evaluation of coast-parallel features.

Nevertheless, the integration of a series of methodological approaches has yet proven to yield both qualitative and quantitative insights into passive margin evolution with considerable accuracy. This case study on the evolution of the NW-Namibian margin is rather well documented within a 2D scope: mass balance calculations can be supported by provenance studies and controlled by stratigraphic basin modelling, respectively. The integrated approach towards a mass and process balance presented here even allows for semi-quantitative conclusions on differential transport perpendicular to the model transect.

However, some aspects of the evolution of the Namibian passive margin remain unexplained and need further investigation. A detailed temporal assessment of the northward prograding breakup and oceanic onset during margin evolution and the relative role of the Tristan da Cunha mantle plume, for example, is a matter of considerable debate.

Undoubtedly, breakup in the southern part of the margin started as much as 20Ma earlier than in the north and was not associated with plume activity thus rather indicating a plate-mode passive extension. Minimum ages of the formation of oceanic crust are given by seafloor magnetic anomalies. It may be suggested that in the Walvis Basin area offshore NW-Namibia the propagation of rifting and oceanic onset rather accidentally interfingered with the activity of the Tristan plume impinging on lithosphere under extension. Huisman et al. (2001) proposed that weakened or thinned lithosphere may even attract a plume.

The Rio Grande-Walvis Ridge volcanic features represent aseismic ridges resulting from the passive passage of lithosphere over the plume; this is indicated by their V-shaped bathymetric expression illustrated by the gravity map on the front page. Since the volcanic ridges are obliquely crossing oceanic transform faults the plume itself may not have actively triggered the oceanic onset of the related margin segment. However, enhanced asthenospheric melt potential due to plume activity can be clearly associated with magmatic underplating, the strong basaltic overprinting of the crust, and the formation of the huge Paranà-Etendeka flood basalt province, yet the relative timing of rifting and volcanism needs to be discussed.

It has been suggested that oceanic onset at the latitude of the Walvis Basin has started as early as 128-129Ma ago if the age of the oldest well defined normal oceanic crust is estimated. The temporally restricted Etendeka volcanism between

132Ma and 131Ma b.p. would then clearly predate oceanic onset which indicates a diapiric-mode active extension. The majority of the Early Cretaceous igneous complexes that intruded in NW-Namibia between 135Ma and 124Ma ago as well as the Horingbaai dyke swarm (130-125Ma) reveal a geochemical signature that can be related to the Tristan plume; a mantle source magma with up to 20% contamination by Damara crust can be inferred for the Brandberg anorogenic complex.

If this “active model” of margin evolution is accepted, the wide continent-ocean transition zone landward of the well defined normal oceanic crust (fig. 3-5) may rather be interpreted as extended and intensely intruded continental crust. The emplacement of basaltic seaward dipping reflectors (SDR) might therefore be closely related to synrift fault activity. Two distinct SDR wedges can be observed that appear to be bounded by listric normal faults on their seaward termination. Their basaltic character with minor clastic contributions can be inferred from v_p -modelling; in their basal part the SDR wedges might even comprise volcanics of the Etendeka Group that would mark a tilted-down Early Cretaceous land surface. In that case the SDR wedges would document pronounced synrift subsidence as well as intense extrusive and intrusive magmatism for the period between c. 132Ma and 125Ma. This interpretation is consistent with observations from well 1911/15-1 in the northern Walvis Basin where 500m of probably Barremian basalt with minor clastic intercalations have been encountered that are regarded to represent the uppermost SDR units. Subsidence analysis has shown that marine sedimentation started as early as 126Ma ago which is interpreted to roughly mark the transition from a Basin-and-Range-like synrift phase to the postrift phase of margin evolution. Early drift sedimentation may have been characterised by condensed shallow-water carbonate deposition due to restricted subsidence resulting from the thermal effects of magmatic underplating.

In a passive mode of rifting, volcanism generally follows rifting. An alternative model of margin evolution might attribute the wide continent-ocean transition zone to the actual process of oceanic onset. The emplacement of SDR wedges is often interpreted to be a feature of subaerial seafloor spreading. Such a model would relate the onset of the formation of oceanic crust to the landward termination of the basaltic transition zone for which, in turn, an age of 134-136Ma can be determined. This approach would not only make large proportions of the Namibian margin older than suggested before, it would also imply a rather plate-mode passive extension not originally caused but modified by the effects of the Tristan plume. Most basalts of the Etendeka province show isotopic and trace element ratios that are incompatible with a primitive mantle source; if this model of passive rifting with volcanism postdating rifting and oceanic onset is accepted, there would probably be sufficient time for a crustal contamination of a primarily mantle-sourced magma.

Pure end-member models of margin evolution obviously fail to explain all observed features of the NW-Namibian passive margin. The twostage extension model proposed by Huismans et al. (2001) inferring a change from plate-mode passive extension to diapiric-mode active extension when the sphere of plume influence is reached might provide reasonable explanations.

This study has shown that the surface processes of denudation and contemporaneous sedimentation within the model transect can be linked both quantitatively as well as in terms of their particular temporal evolution. Stratigraphic basin modelling is capable of incorporating internal processes like the specific basement subsidence.

The important role of denudational unloading and flexural isostatic rebound of an elastic plate has been discussed repeatedly in conjunction with the formation of high-elevation (“Atlantic type”) passive margins. Figure 4-1 illustrates an elastic plate model which not only emphasises the relevance of denudational unloading but also the integral effect of flexural loading of the lithosphere on the maintenance of a highly elevated margin as well as on the formation of a flexural hinterland basin. The reconstruction of the denudational history and the depositional history, respectively, clearly revealed the causative link between these superficial processes within the model transect (fig. 4-7). The associated flexural feedback mechanisms with the lithosphere, however, are rather difficult to assess.

It has been discussed in chapter 4.1.2 that the temporal evolution of the denudation rates derived from AFT analysis systematically predates the reconstructed sedimentation (and accumulation) history by c. 15Ma; two Late Cretaceous peaks are followed by a distinct low, respectively. This observation might be attributed to a delay effect associated with sediment transport from distal source regions.

However, a distinct Early Tertiary denudation peak between c. 60Ma and 50Ma b.p. (fig. 4-7) is not reflected by the depositional history at all. It might be suggested that this “event” of enhanced denudation may represent the onshore flexural response of the margin to heavy lithospheric loading offshore during the Late Cretaceous. Subsidence analysis indicates an undisturbed and continuous sediment loading effect during the Early Tertiary but rather varying contributions of both thermal and sediment loading effects on the total basement subsidence between 90Ma and 65Ma (fig. 3-23). Enhanced Early Tertiary denudation may thus exemplarily illustrate the general approach of a closed cycle between surface processes and internal processes as proposed in figure 1-2.

The NW-Namibian margin might be regarded as a textbook example of a volcanic passive margin and therefore exhibits a considerable research history. However, especially the strong predictive potential of the case study investigated here may even imply suitable applications for less well documented passive margins in terms of basin evolution and hydrocarbon potential.

A reasonable future development for this integrated approach towards quantitative passive margin evolution would surely be the integration of additional seismic and well data to assess the evolution of the entire Namibian margin in 3D. Furthermore, considering the associated conjugate passive margin of northern Argentina and southern Brazil would help to more fully understand the formation and evolution of the South Atlantic.

8 References

- ALLEN, P. A. & ALLEN, J. R. (1990): Basin analysis: principles and applications.- London (Blackwell), 451pp.
- AUSTIN, J. A. & UCHUPI, E. (1982): Continental-oceanic transition off southwest Africa.- AAPG Bull., 66, 1328-1347.
- BAGGULEY, J. G. & PROSSER, S. (1999): The interpretation of passive margin depositional processes using seismic stratigraphy: examples from offshore Namibia.- In: CAMERON, N.R., BATE, R.H. & CLURE, V.S. (eds.): The Oil and Gas Habitats of the South Atlantic.- Geol. Soc. London Spec. Pub., 153, 321-344.
- BALLARD, S., POLLACK, H. N. & SKINNER, N. J. (1987): Terrestrial heat flow in Botswana and Namibia.- J. Geophys. Res., 92, 6291-6300.
- BAUER, K., NEBEN, S., SCHRECKENBERGER, B., EMMERMANN, R., HINZ, K., FECHNER, N., GOHL, K., SCHULZE, A., TRUMBULL, R. B. & WEBER, K. (2000): Deep structure of the Namibia continental margin as derived from integrated geophysical studies.- J. Geophys. Res., 105, 25829-25853.
- BEHA, A. (2003): Modellierung des Kohlenwasserstoffpotentials im zentralen Walvis- Becken/ offshore NW Namibia.- Diploma thesis Univ. Freiburg/ Germany, in prep.
- BHATIA, M. R. (1983): Plate tectonics and geochemical composition of sandstones.- J. Geol., 91, 611-627.
- BIERMAN, P. R. & CAFFEE, M. (2001): Slow rates of rock surface erosion and sediment production across the Namib Desert and Escarpment, southern Africa.- Am. J. Sci., 301, 326-358.
- BOGGS, S. (2001): Principles of Sedimentology and Stratigraphy.- New Jersey (Prentice Hall), 726pp.
- BOND, G. C. & KOMINZ, M. A. (1984): Construction of tectonic subsidence curves for the early Paleozoic miogeocline, southern Canadian Rocky Mountains: implication for subsidence mechanisms, age of breakup, and crustal thinning.- Geol. Soc. Am. Bull., 95, 155-173.
- BRAUN, J. & BEAUMONT, C. (1989): A physical explanation of the relation between flank uplifts and the breakup unconformity at rifted continental margins.- Geology, 17, 760-764.
- BRAY, R., LAWRENCE, S. & SWART, R. (1998): Source rock, maturity data indicate potential off Namibia.- Oil and Gas Journal, 96/ 32, 84-89.
- BROWN, R. W., GALLAGHER, K., GLEADOW, A. J. W. & SUMMERFIELD, M. A. (2000): Morphotectonic evolution of the South Atlantic margins of Africa and South America.- In: SUMMERFIELD, M. A. (ed.): Geomorphology and Global Tectonics.- Chichester (John Wiley & Sons), 254-281.
- BUCK, W. R., MARTINEZ, F., STECKLER, M. S. & COCHRAN, J. R. (1988): Thermal consequences of lithospheric extension: pure and simple.- Tectonic, 7, 213-234.
- CAINELLI, C. & MOHRIAK, W. U. (1999): Some remarks on the evolution of sedimentary basins along the Eastern Brazilian continental margin.- Episodes, 22, 206-216.
- CAMERON, N. R., BATE, R. H. & CLURE, V. S. (eds.): The Oil and Gas habitats of the South Atlantic.- Geol. Soc. London Spec. Pub., 153, 474pp.
- CANDE, S. C., LABRECQUE, J. L. & HAXBY, W. F. (1988): Plate kinematics of the South Atlantic: Chron 34 to present.- J. Geophys. Res., 93, 13479-13492.

- CARTWRIGHT, J. & SWART, R. (2002): The Subsidence History of Volcanic Margins.- In: GATLIFF, R., WALKER, I., CARTWRIGHT, J. & MITCHENER, B. (eds.): Frontier Exploration of Volcanic Continental Margins, Geol. Soc. London Petroleum Group Meeting, 17th – 18th September 2002, conference abstracts.
- CHANG, H.K., KOWSMANN, R.O., FIGUEIREIDO, A.M.F. & BENDER, A.A. (1992): Tectonics and stratigraphy of the East Brazil Rift system: an overview.- *Tectonophysics*, 213, 97-138.
- CHRISTIE-BLICK, N. & DRISCOLL, N. W. (1995): Sequence stratigraphy.- *Ann. Rev. Earth Planet. Sci.*, 23, 451-478.
- CLEMSON, J., CARTWRIGHT, J. & BOOTH, J. (1997): Structural segmentation and the influence of basement structure on the Namibian passive margin.- *J. Geol. Soc. London*, 154, 477-482.
- CLEMSON, J., CARTWRIGHT, J. & SWART, R. (1999): The Namib Rift: a rift system of possible Karoo age, offshore Namibia.- In: CAMERON, N.R., BATE, R.H. & CLURE, V.S. (eds.): The Oil and Gas Habitats of the South Atlantic.- *Geol. Soc. London Spec. Pub.*, 153, 381-402.
- CLIFFORD, A. C. (1986): African oil - Past, present and future.- In: HALBOUTY, M. T. (ed.): Future petroleum provinces of the world.- *AAPG Memoir*, 40, 339-372.
- COCKBURN, H. A. P., BROWN, R. W., SUMMERFIELD, M. A. & SEIDL, M. A. (2000): A combined fission-track and cosmogenic isotope analysis approach to quantifying long-term landscape change: an example from the central Namibian continental margin.- *Geol. Soc. Austr.*, Abstr. No. 58, 9th International Conference on Fission Track Dating and Thermochronology, 51-54.
- COFFIN, M. F. & ELDHOLM, O. (1994): Large Igneous provinces: Crustal structure, dimensions, and external consequences.- *Reviews of Geophysics*, 32, 1-36.
- COWARD, M. P., PURDY, E. G., RIES, A. C. & SMITH, D. G. (1999): The distribution of petroleum reserves in basins of the South Atlantic margins.- In: CAMERON, N.R., BATE, R.H. & CLURE, V.S. (eds.): The Oil and Gas Habitats of the South Atlantic.- *Geol. Soc. London Spec. Pub.*, 153, 101-131.
- COX, K. G. (1989): The role of mantle plumes in the development of continental drainage patterns.- *nature*, 342, 873-877.
- CRESSIE, N. A. C. (1991): *Statistics for Spatial Data*.- New York (John Wiley & Sons), 900pp.
- DALY, M. C., CHOROWICZ, J. & FAIRHEAD, J. D. (1989): Rift basin evolution in Africa: the influence of reactivated steep basement shear zones.- In: COOPER, M. A. & WILLIAMS, G. D. (eds.): *Inversion Tectonics*.- *Geol. Soc. London Spec. Pub.*, 44, 309-334.
- DAVIES, C. P. N. & VAN DER SPUY, D. (1990): Chemical and optical investigations into the hydrocarbon source potential and thermal maturity of the Kudu 9A-2 and 9A-3 boreholes.- *Communs. Geol. Surv. Namibia*, 6, 49-58.
- DAVIES, C. P. N. & VAN DER SPUY, D. (1992/93): The Kudu wells: Results of a biomarker study related to burial history modelling.- *Communs. Geol. Surv. Namibia*, 8, 45-56.
- DAVISON, I. (1997): Wide and narrow margins of the Brazilian South Atlantic.- *J. Geol. Soc. London*, 154, 471-476.
- DEMAISON, G. J. & MOORE, G. T. (1980): Anoxic Environments and Oil Source Bed Genesis; *AAPG Bull.*, 64, 1179-1209.
- DICKINSON, W. R., BEARD, L. S., BRAKENRIDGE, G. R., ERJAVEC, J. L., FERGUSON, R. C., INMAN, K. F., KNEPP, R. A., LINDBERG, F. A. & RYBERG, P. T. (1983): Provenance of North American Phanerozoic sandstones in relation to tectonic setting.- *Geol. Soc. Am. Bull.*, 94, 222-235.
- DINGLE, R. V., SIESSER, W. G. & NEWTON, A. R. (1983): *Mesozoic and Tertiary geology of southern Africa*.- Rotterdam (Balkema), 375pp.

- DINGLE, R. V. (1992/93): Structural and sedimentary development of the continental margin off southwestern Africa.- *Communs. Geol. Surv. Namibia*, 8, 35-43.
- DINGLE, R. V. (1999): Walvis Ridge barrier: its influence on paleoenvironments and source rock generation deduced from ostracod distributions in the early South Atlantic Ocean.- In: CAMERON, N.R., BATE, R.H. & CLURE, V.S. (eds.): *The Oil and Gas Habitats of the South Atlantic*.- *Geol. Soc. London Spec. Pub.*, 153, 293-302.
- DINGLE, R. V. & SCRUTTON, R. A. (1974): Continental Breakup and the Development of Post-Paleozoic Sedimentary Basins around Southern Africa.- *Geol. Soc. Am. Bull.*, 85, 1467-1474.
- DRISCOLL, N. & KARNER, G. (1998): Lower crustal extension across the Northern Carnarvon basin, Australia: Evidence for an eastward dipping detachment.- *J. Geophys. Res.*, 103, 4975-4991.
- DUNCAN, A. R. & ARMSTRONG, R. A. (1990): MORB-related dolerites associated with the Etendeka volcanics, Northwestern Namibia.- *Abstract Geol. Soc. S. Africa Geocongress 1990, Cape Town*, 143-146.
- DUNCAN, R. A., HOOPER, P. R., REHACEK, J., MARSH, J. S. & DUNCAN, A. R. (1997): The timing and the duration of the Karoo igneous event, southern Gondwana.- *J. Geophys. Res.*, 102, 18127-18138.
- EBERLE, D., ANDRITZKY, G. & WACKERLE, R. (1995): The new magnetic data set of Namibia: Its contributions to the understanding of crustal evolution and regional distribution of mineralization.- *Communs. geol. Surv. Namibia*, 10, 141-150.
- EBERLE, D., ANDRITZKY, G., HUTCHINS, D. G. & WACKERLE, R. (2002): The regional magnetic data set of Namibia: Compilation, contributions to crustal studies and support to natural resource management.- *South African J. Geol.*, 105, 361-380.
- ELDHOLM, O., SKOGSEID, J., PLANKE, S. & GLADCZENKO, T. P. (1995): Volcanic margin concepts.- In: BANDA, E., TALWANI, M. & TORNÉ, M. (eds.): *Rifted Continent Ocean Boundaries*.- NATO ASI Series Volume, Kluwer Academic Publishers, 1-16.
- EMERY, D. & MYERS, K. (1996): *Sequence Stratigraphy*.- London (Blackwell), 297pp.
- ERLANK, A. J., MARSH, J. S., DUNCAN, A. R., MILLER, R. McG., HAWKESWORTH, C. J., BETTON, B. J. & REX, D. C. (1984): Geochemistry and petrogenesis of the Etendeka volcanic rocks from SWA/ Namibia.- *Geol. Soc. South Africa Spec. Pub.*, 13, 195-245.
- ESPITALIÈ, J., LAPORTE, J. L., LEPLAT, P., MADEC, M., MARQUIS, F., PAULET, J. & BOUTEFEU, A. (1977): Méthode rapide de caractérisation des roches mères, de leur potentiel pétrolier et de leur degré d' évolution.- *Rev. Inst. Fr. Pet.*, 32, 23-42.
- ETHERIDGE, M. A., SYMONDS, P. A. & LISTER, G. S. (1989): Application of the detachment model to reconstruction of conjugate passive margins.- In: TANKARD, A. J. & BALKWILL, H. R. (eds.): *Extensional Tectonics and Stratigraphy of the North Atlantic Margins*.- AAPG Memoir, 46, 23-40.
- FLEMINGS, P. B. & GROTZINGER, J. P. (1996): STRATA: Freeware for analyzing stratigraphic problems.- *GSA Today*, 6, 12, 1-7.
- FLEMINGS, P. B. & JORDAN, T. E. (1989): Synthetic stratigraphic model of foreland basin development.- *J. Geophys. Res.*, 94, 3851-3866.
- FLEMINGS, P. B. & JORDAN, T. E. (1990): Stratigraphic modeling of foreland basins: Interpreting thrust deformation and lithosphere rheology.- *Geology*, 18, 430-434.
- FLOYD, P. A., WINCHESTER, J. A. & PARK, R. G. (1989): Geochemistry and tectonic setting of Lewisian clastic metasediments from the early Proterozoic Loch Maree Group of Gairloch, N. W. Scotland.- *Precamb. Res.*, 45, 203-214.

- FOUCHÉ, J., BATE, K. J. & VAN DER MERWE, R. (1992): Plate tectonic setting of the Mesozoic Basins, southern offshore, South Africa: A review.- In: DE WIT, M. J. & RANSOME, I. G. D. (eds.): Inversion tectonics of the Cape Fold Belt, Karoo and Cretaceous Basins of Southern Africa.- Rotterdam (Balkema), 33-45.
- FRIEDINGER, P. J. J. (1988): BASTA - Subsidence and paleotemperature modelling of rift basins.- Computers & Geosciences, 14, 505-526.
- GALLAGHER, K. (1995): Evolving thermal histories from fission track data.- Earth Planet. Sci. Lett., 136, 421-435.
- GALLAGHER, K. & BROWN, R. (1997): The onshore record of passive margin evolution.- J. Geol. Soc. London, 154, 451-457.
- GALLAGHER, K. & BROWN, R. (1999): The Mesozoic denudation history of the Atlantic margins of southern Africa and southeast Brazil and the relationship to offshore sedimentation.- In: CAMERON, N.R., BATE, R.H. & CLURE, V.S. (eds.): The Oil and Gas Habitats of the South Atlantic.- Geol. Soc. London Spec. Pub., 153, 41-53.
- GERRARD, I. & SMITH, G. C. (1982): Post Palaeozoic succession and structure of the southwestern African continental margin. In: WATKINS, J. S. & DRAKE, C. L. (eds.): Studies in Continental Marine Geology.- AAPG Memoir, 34, 49-74.
- GILCHRIST, A. R., KOOL, H., & BEAUMONT, C. (1994): Post-Gondwana geomorphic evolution of southwestern Africa: Implication for the controls on landscape development from observations and numerical experiments.- J. Geophys. Res., 99, 12211-12228.
- GILCHRIST, A. R. & SUMMERFIELD, M. A. (1990): Differential denudation and flexural isostasy in formation of rifted-margin upwarps.- Nature, 346, 739-742.
- GLADCZENKO, T. P., HINZ, K., ELDHOLM, O., MEYER, H., NEBEN, S. & SKOGSEID, J. (1997): South Atlantic volcanic margins.- J. Geol. Soc. London, 154, 465-470.
- GRADSTEIN, F. M. & OGG, J. (1996): A Phanerozoic timescale.- Episodes, 19, 3-5.
- HAACK, U., GOHN, E. & HARTMANN, O. (1983): Radiogenic Heat Generation In Damaran Rocks.- Spec. Pub. Geol. Soc. S. Afr., 11, 225-231.
- HAQ, B. U., HARDENBOL, J. & VAIL, P. R. (1987): Chronology of fluctuating sea-levels since the Triassic (250 million years ago to present).- Science, 235, 1156-1167.
- HARLAND, W. B., ARMSTRONG, R. L., COX, A. V., CRAIG, L. E., SMITH, A. G. & SMITH, D. G. (1990): A geologic timescale.- Cambridge (Cambridge University Press), 263pp.
- HARRY, D. L. & SAWYER, D. S. (1992): Basaltic volcanism, mantle plumes, and the mechanics of rifting: the Paraná flood basalt province of South America.- Geology, 20, 207-210.
- HAWKESWORTH, C. J., GALLAGHER, K., KELLEY, S., MANTOVANI, M., PEATE, D. W., REGELOUS, M. & ROGERS, N. (1992): Paraná magmatism and the opening of the South Atlantic.- In: STOREY, B. C., ALABASTER, T. & PANKHURST, R. J. (eds.): Magmatism and the Causes of Continental Break-Up, Geol. Soc. London, Spec. Pub., 68, 221-240.
- HEGENBERGER, W. (1988): Karoo sediments of the Erongo mountains, their environmental setting and correlation.- Commun. Geol. Surv. Namibia, 4, 51-57.

- HOLTAR, E. & FORSBERG, A.W. (2000): Postrift development of the Walvis basin, Namibia, Results from the exploration campaign in Quadrant 1911. – In: MELLO, M.R. & KATZ, B.J. (eds.): Petroleum Systems of South Atlantic margins. – AAPG Memoir, 73, 429-446.
- HORSTHEMKE, S., LEDENDECKER, S. & PORADA, H. (1990): Depositional environments and stratigraphic correlations of the Karoo sequence in northwestern Damaraland.- *Communs. Geol. Surv. Namibia*, 6, 63-73.
- HU, X., WANG, Y. L. & SCHMITT, R. A. (1988): Geochemistry of sediments on the Rio Grande Rise and the redox evolution of the South Atlantic Ocean.- *Geochim. Cosmochim. Acta*, 52, 201-207.
- HUISMANS, R. S., PODLADCHIKOV, Y. Y. & CLOETHING, S. (2001): Transition from passive to active rifting: Relative importance of asthenospheric doming and passive extension of the lithosphere.- *J. Geophys. Res.*, 106, 11271-11291.
- INCROPERA, F. G. & DeWITT, D. P. (1985): *Introduction to Heat Transfer*.- New York (John Wiley & Sons), 712pp.
- JERRAM, D. A., MOUNTNEY, N. & STOLLHOFEN, H. (1999): Facies architecture of the Etjo Sandstone Formation and its interaction with the basal Etendeka Flood basalts of NW Namibia: Implications for offshore analogues.- In: CAMERON, N.R., BATE, R.H. & CLURE, V.S. (eds.): *The Oil and Gas Habitats of the South Atlantic*.- *Geol. Soc. London Spec. Pub.*, 153, 367-380.
- JORDAN, T. E. & FLEMINGS, P. B. (1991): Large-Scale Stratigraphic Architecture, Eustatic Variation, and Unsteady Tectonism: A theoretical Evaluation.- *J. Geophys. Res.*, 96, 6681-6699.
- JUNGSLAGER, E. H. A. (1999): Petroleum habitats of the Atlantic margin of South Africa.- In: CAMERON, N.R., BATE, R.H. & CLURE, V.S. (eds.): *The Oil and Gas Habitats of the South Atlantic*.- *Geol. Soc. London Spec. Pub.*, 153, 153-168.
- JUNKER, R., KUKULUS, M. & HENK, A. (2001): The Last Outpost of South Atlantic Rifting - The Albin Ridge/ Skeleton Coast, NW-Namibia.- In: ROTH, S. & RÜGGERBERG, A. (eds.): *2001 MARGINS Meeting: Program and Abstracts*, Kiel, 2.-6.10.2001.- *Schriftenreihe d. dt. Geol. Ges.*, 14, 103.
- JUNKER, R. (2002): 2D-Modellierung der Sedimentation an Kontinentalrändern mit "STRATA" – Parameterstudien und Anwendbarkeit auf den passiven Kontinentalrand NW Namibias.- *Diploma Thesis*, Univ. Würzburg, Germany, 125pp.
- JUNKER, R., KUKULUS, M. & HENK, A. (2002): Postrift-Sedimentation im Walvis-Becken offshore Namibia – eine quantitative Analyse.- In: NIEHBUR, B. (Hrsg.): *Geo 2002: Programm und Kurzfassungen*, Würzburg, 1.-5.10.2002.- *Schriftenreihe d. Dt. Geol. Ges.*, 21, 182.
- KARNER, G. D. & WATTS, A. B. (1982): On isostasy at Atlantic-type continental margins.- *J. Geophys. Res.*, 87, 2923-2948.
- KAUFMANN, P., GROTZINGER, J. P. & McCORMICK, D. S. (1991): Depth-dependent diffusion algorithm for simulation of sedimentation in shallow marine depositional systems.- In: FRANSEEN, E. K., WATNEY, W. L., KENDALL, C. G. St. C & ROSS, W. (eds.): *Sedimentary modeling: Computer simulations and methods for improved parameter definition*.- *Kansas State Geol. Surv. Bull.*, 233, 489-508.
- KING, L. C. (1953): *Canons of landscape evolution*.- *Geol. Soc. Am. Bull.*, 64, 721-752.
- KUKULUS, M. & HENK, A. (2002): „Source to Sink“ – Bilanzierung von Erosion und Sedimentation entlang einer Traverse über den passiven Kontinentalrand von NW-Namibia.- In: HÜSSNER, H., HINDERER, M., GÖTZ, A. E. & PETSCHICK, R. (Hrsg.): *Sediment 2002: Kurzfassungen und Programm*, Frankfurt a. M. – Darmstadt, 29.-31.5.2002.- *Schriftenreihe d. Dt. Geol. Ges.*, 17, S. 124-125.

KUKULUS, M. & HENK, A. (2002): „Source to Sink” – Balancing erosion and sedimentation along a traverse across the Namibian passive continental margin.- In: GATLIFF, R., WALKER, I., CARTWRIGHT, J. & MITCHENER, B. (eds.): Frontier Exploration of Volcanic Continental Margins, Geol. Soc. London Petroleum Group Meeting, 17th – 18th September 2002, conference abstracts.

KUKULUS, M. & HENK, A. (2003): Mass transfer across the passive margin of NW-Namibia and evolution of the central Walvis Basin.- *Berichte der Deutschen Mineralogischen Gesellschaft, Beih. z. Eur. J. Mineral.*, 15/ 1, 113.

KUSZNIR, N., ROBERTS, A. & HUNSDALE, R. (2002): Depth-dependent Stretching of the Norwegian Continental Margin: Implications for Subsidence and Hydrocarbon Maturation at Volcanic Rifted Margins.- In: GATLIFF, R., WALKER, I., CARTWRIGHT, J. & MITCHENER, B. (eds.): Frontier Exploration of Volcanic Continental Margins, Geol. Soc. London Petroleum Group Meeting, 17th – 18th September 2002, conference abstracts.

LARSEN, H. C., SAUNDERS, A. D., CLIFT, P. D. et al. (1994): Proceedings of the Ocean Drilling Program. Initial Reports, 152, Ocean Drilling Program, College Station, TX.

LASLETT, G. M., GREEN, P. F., DUDDY, E. R. & GLEADOW, A. J. W. (1987): Thermal annealing of fission tracks in apatite 2. A quantitative analysis.- *Chemical Geology (Isotope Geoscience)*, 65, 1-13.

LAWRENCE, S. R. (1989): Prospects for petroleum in Late Proterozoic/ Early Palaeozoic basins of southern-central Africa.- *J. Petrol. Geol.*, 12, 231-242.

LE MAITRE, R. W. (1976): The chemical variability of some common igneous rocks.- *J. Petrol.*, 17, 589-637.

LIGHT, M. P. R., MASLANYJ, M. P. & BANKS, N. L. (1992): New geophysical evidence for extensional tectonics on the divergent margin offshore Namibia.- In: STOREY, B. C., ALABASTER, T. & PANKHURST, R. J. (eds.): Magmatism and the Causes of Continental Break-Up, Geol. Soc. London, Spec. Pub., 68, 257-270.

LIGHT, M. P. R., MASLANYJ, M. P., GREENWOOD, R. J. & BANKS, N. L. (1993): Seismic sequence stratigraphy and tectonics offshore Namibia.- In: WILLIAMS, G. D. & DOBB, A. (eds.): Tectonics and Seismic Sequence Stratigraphy.- *Geol. Soc. London Spec. Pub.*, 71, 163-191.

MARSH, J. S., EWART, A., MILNER, S. C., DUNCAN, A. R. & MILLER, R. McG. (2001): The Etendeka Igneous Province: magma types and their stratigraphic distribution with implications for the evolution of the Parana-Etendeka flood basalt province.- *Bull. Volcanol.*, 62, 464-486.

MARTIN, H. (1953): Notes on the Dwyka succession and on some pre-Dwyka valleys in South West Africa.- *Trans. Geol. Soc. S. Afr.*, 56, 37-43.

MARTIN, H. (1965): The Precambrian geology of South West Africa and Namaqualand.- The Precambrian Research Unit, Univ. of Cape Town.

MAYNARD, J. B., VALLONI, R. & YU, H.-S. (1982): Composition of modern deep sea sands from arc-related basins.- In: LEGGETT, J. K. (ed.) Trench-forearc geology: sedimentation and tectonics on modern and ancient active plate margins.- *Geol. Soc. Spec. Pub.*, 10, 551-561.

McIVER, R. D. (1975): Hydrocarbon occurrences from JOIDES Deep Sea Drilling Project.- *Proc. Ninth Petrol. Congr.*, 269-280.

McKENZIE, D. P. (1978): Some remarks on the development of sedimentary basins.- *Earth Planet. Sci. Lett.*, 40, 25-32.

McLACHLAN, I. R. & McMILLAN, I. K. (1979): Microfaunal biostratigraphy, chrono-stratigraphy and history of Mesozoic and Cenozoic deposits on the coastal margin of South Africa.- In: ANDERSON, A. M. & VAN BILJON, W. J. (eds.): Some sedimentary basins and associated ore deposits of South Africa.- *Geol. Soc. South Africa Spec. Pub.*, 6, 161-181.

- McMILLAN, I. K. (1990): Foraminiferal biostratigraphy of the Barremian to Miocene rocks of the Kudu 9A-1, 9A-2 and 9A-3 boreholes.- *Communs. Geol. Surv. Namibia*, 6, 23-29.
- MELLO, M. R. & KATZ, B. J. (eds.): *Petroleum systems of South Atlantic margins*.- AAPG Memoir, 73, 451pp.
- MILLER, R. McG. & SCHALK, K. E. L. (1980): *South West Africa/ Namibia geological map 1:1000000*.- Geological Survey of Namibia, Windhoek.
- MILNER, S. C. & EWART, A. (1989): The geology of the Goboboseb Mountain volcanics and their relationship to the Messum Complex, Namibia.- *Communs. geol. Surv., Namibia*, 5, 31-40.
- MILNER, S. C., DUNCAN, A. R. & EWART, A. (1992): Quartz latite rheoignimbrite flows of the Etendeka Formation, north-western Namibia.- *Bull. Volcanol.*, 54, 200-219.
- MILNER, S. C., DUNCAN, A. R., EWART, A. & MARSH, J. S. (1994): Promotion of the Etendeka Formation to Group status: A new integrated stratigraphy.- *Communs. Geol. Surv., Namibia*, 9, 5-11.
- MILNER, S. C., Le ROEX, A. P. & O`CONNOR, J. M. (1995): Age of Mesozoic igneous rocks in northwestern Namibia, and their relationship to continental breakup.- *J. Geol. Soc. London*, 152, 97-104.
- MOHRIAK, W. U., HOBBS, R. & DEWEY, J. F. (1990): Basin-forming processes and the deep structure in the Campos Basin, offshore Brazil.- *Marine and Petroleum Geology*, 7, 94-122.
- MUNTINGH, A. (1993): *Geology, prospects in Orange Basin offshore western South Africa*.- *Oil and Gas Journal*, 91/ 4, 104-109.
- MÜLLER, R. D., ROEST, W. R., ROYER, J-Y., GAHAGAN, L. M. & SCLATER, J. G. (1997): Digital isochrons of the world`s ocean floor.- *J. Geophys. Res.*, 102, 3211-3214.
- NÜRNBERG, D. & MÜLLER, R. D. (1991): The tectonic evolution of the South Atlantic from Late Jurassic to present.- *Tectonophysics*, 191, 27-53.
- OLLIER, C. D. & PAIN, C. F. (1997): Equating the basal unconformity with the paleoplain: a model for passive margins.- *Geomorphology*, 19, 1-15.
- O`CONNOR, J. M. & DUNCAN, R. A. (1990): Evolution of the Walvis Ridge – Rio Grande Rise Hot Spot System: Implications for African and South American Plate Motions Over Plumes.- *J. Geophys. Res.*, 95, 17475-17502.
- O`REILLY, B. M., HAUSER, F., JACOB, A. W. B., SHANNON, P. M., MAKRIS, J. & VOGT, U. (1995): The Erris and Eastern Rockall Troughs: Structural and Sedimentological Development.- In: CROKER, P. & SHANNON, P. M. (eds.): *Petroleum Geology of Ireland's Offshore Basins*.- *Geol. Soc. London Spec. Pub.*, 93, 413-421.
- PAOLA, C. (2000): Quantitative models of sedimentary Basin filling.- *Sedimentology*, 47, 121-178.
- PARTRIDGE, T. C. & MAUD, R. R. (1987): Geomorphic evolution of southern Africa since the Mesozoic.- *S. Afr. J. Geol.*, 90, 179-208.
- PITTMAN, E. D. (1989): Problems related to clay minerals in reservoir sandstones.- In: MASON, J. F. & DICKEY, P. A (eds.): *Oil field development techniques, proceedings of the Daqing international meeting*.- AAPG Studies in Geology, 28, 237-244.
- PLANKE, S. & ELDHOLM, O. (1994): Seismic response and construction of seaward dipping wedges of flood basalts: Voring volcanic margin.- *J. Geophys. Res.*, 99, 9263-9278.
- PLANKE, S., SYMONDS, P. A., ALVESTAD, E. & SKOGSEID, J. (2000): Seismic volcanostratigraphy of large-volume basaltic extrusive complexes on rifted margins.- *J. Geophys. Res.*, 105, 19335-19351.

POLLACK, H. N., HURTER, S. J. & JOHNSON, J. R. (1993): Heat flow from the Earth's Interior; Analysis of the Global Data Set.- *Rev. Geophys.*, 31, 267-280.

PORADA, H. (1989): Pan-African Rifting and Orogenesis in Southern to Equatorial Africa and Eastern Brazil.- *Precambrian Res.*, 44, 103-136.

POSAMENTIER, H. W., JERVEY, M. T. & VAIL, P. R. (1988). Eustatic controls on clastic deposition I – conceptual framework.- In: WILGUS, C. K., HASTINGS, B. S., KENDALL, C. G. St. C., POSAMENTIER, H. W., ROSS, C. A. & VAN WAGONER, J. C. (eds.): *Sea-level changes: an integrated approach*, SEPM Spec. Pub., 42, 109-124.

POSAMENTIER, H. W. & VAIL, P. R. (1988): Eustatic controls on clastic deposition II – sequence and systems tract models.- In: WILGUS, C. K., HASTINGS, B. S., KENDALL, C. G. St. C., POSAMENTIER, H. W., ROSS, C. A. & VAN WAGONER, J. C. (eds.): *Sea-level changes: an integrated approach*, SEPM Spec. Pub., 42, 125-154.

RAAB, M. J., BROWN, R. W., GALLAGHER, K., CARTER, A. & WEBER, K. (2000): Mapping the extent of Late Cretaceous morphotectonic reactivation in northern Namibia.- *Geol. Soc. Austr. Abstracts No. 58*, 9th International Conference on Fission Track Dating and Thermochronology, 267-269.

RAAB, M. J. (2001): The Geomorphic Response of the Passive Continental Margin of Northern Namibia to Gondwana Break-Up and Global Scale Tectonics.- PhD Thesis, Univ. Göttingen/ Germany, 253pp.

RAAB, M. J., BROWN, R. W., GALLAGHER, K., CARTER, A. & WEBER, K. (2002): Late Cretaceous reactivation of major crustal shear zones in northern Namibia, constraints from apatite fission track analysis.- *Tectonophysics*, 349, 75-92.

RABINOWITZ, P. D (1976): Geophysical study of the continental margin of southern Africa.- *Geol. Soc. Am. Bull.*, 87, 1643-1653.

RABINOWITZ, P. D. & LABRECQUE, J. (1979): The Mesozoic South Atlantic Ocean and Evolution of Its Continental Margins.- *J. Geophys. Res.*, 84, 5973-6002.

RENKIN, M. L. & SCLATER, J. G (1988): Depth and age in the North Pacific.- *J. Geophys. Res.*, 93, 2919-2935.

RENNE, P. R., GLEN, J. M., MILNER, S. C. & DUNCAN, A. R. (1996): Age of Etendeka flood volcanism and associated intrusions in southwestern Africa.- *Geology*, 24, 659-662.

ROBERTS, A. M., KUSZNIR, N. J., YIELDING, G. & STYLES, P. (1998): 2D flexural backstripping of extensional basins: the need for a sideways glance.- *Petroleum Geoscience*, 4, 327-338.

ROSER, B. P. & KORSCH, R. J. (1986): Determination of tectonic setting of sandstone-mudstone suites using SiO₂ content and K₂O/Na₂O ratio.- *J. Geol.*, 94, 635-650.

ROSER, B. P. & KORSCH, R. J. (1988): Provenance signatures of sandstone-mudstone suites determined using discriminant function analysis of major-element data.- *Chem. Geol.*, 67, 119-139.

ROYDEN, L. & KEEN, C. E. (1980): Rifting process and thermal evolution of the continental margin of eastern Canada determined from subsidence curves.- *Earth Planet. Sci. Lett.*, 51, 343-361.

RUST, D. J. & SUMMERFIELD, M. A. (1990): Isopach and borehole data as indicators of rifted margin evolution in southwestern Africa.- *Mar. Pet. Geol.*, 7, 277-287.

SANDWELL, D. T. & SMITH, W. H. F. (1997): Marine gravity anomaly from Geosat and ERS 1 satellite altimetry.- *J. Geophys. Res.*, 102, 10039-10054.

SCHMIDT, S., CRAMER, B., GERLING, P. & LITKE, R. (2002): Erdgasbildung und Migration im Bereich des Erdgasfeldes Kudu, Namibia.- *DGMK-Tagungsbericht 2002-1*, S. 171-176.

- SCHMITT, A. K., EMMERMANN, R., TRUMBULL, R. B., BÜHN, B. & HENJES-KUNST, F. (2000): Petrogenesis and $^{40}\text{Ar}/^{39}\text{Ar}$ geochronology of the Brandberg Complex, Namibia: Evidence for a major mantle contribution in metaluminous and peralkaline granites.- *J. Petrol.*, 41, 1207-1239.
- SCHOMMARZ, R. E. (1988): The coal potential of the Toscanini area, Skeleton Coast Park.- Open File Rep., Geol. Surv. Namibia, EG 86, 1-15.
- SCHRECKENBERGER, B. (1997): Magnetische Anomalien über seewärts einfallenden seismischen Reflektorfolgen – eine vergleichende Untersuchung verschiedener Vorkommen im Atlantik.- PhD thesis Univ. Frankfurt, Germany.
- SCLATER, J. G. & CHRISTIE, P. A. F. (1980): Continental stretching: an explanation of the post mid-Cretaceous subsidence of the Central North Sea Basin.- *J. Geophys. Res.*, 85, 3711-3739.
- SIESSER, W. G. (1980): Late Miocene origin of the Benguela upwelling system off northern Namibia.- *Science*, 208, 283-285.
- SKOGSEID, J., PEDERSEN, T., ELDHOLM, O. & LARSEN, B. T. (1992): Tectonism and magmatism during NE Atlantic continental break-up: The Voring margin.- In: STOREY, B. C., ALABASTER, T. & PANKHURST, R. J. (eds.): *Magmatism and the Causes of Continental Break-Up*.- Geol. Soc. London Spec. Pub., 68, 305-230.
- SMITH, R. M. H. (1986): Sedimentation and paleoenvironments of Late Cretaceous crater-lake deposits in Bushmanland, South Africa.- *Sedimentology*, 33, 369-386.
- STACH, E. (1982): The macerals of coal.- In: STACH, E., MACKOWSKY, M.-Th., TEICHMÜLLER, M., TAYLOR, G. H., CHANDRA, D. & TEICHMÜLLER, R. (eds.): *Stach's textbook of coal petrology*.- Berlin (Borntraeger), 87-139.
- STANISTREET, I. G., KUKLA, P. A. & HENRY, G. (1991): Sedimentary basinal response to a Late Precambrian Wilson Cycle: the Damara Orogen and Nama Foreland, Namibia.- *J. Afr. Earth Sci.*, 13, 141-156.
- STANISTREET, I. G. & STOLLHOFEN, H. (1999): Onshore equivalents of the main Kudu gas reservoir in Namibia.- In: CAMERON, N.R., BATE, R.H. & CLURE, V.S. (eds.): *The Oil and Gas Habitats of the South Atlantic*.- Geol. Soc. London Spec. Pub., 153, 345-365.
- STEIN, R., RULLKÖTTER, J. & WELTE, D. H. (1989): Changes in paleoenvironments in the Atlantic Ocean during Cretaceous times: results from black shale studies.- *Geol. Rundsch.*, 78/ 3, 883-901.
- STEWART, J., WATTS, A. B. & BAGGULEY, J. G. (2000): Three-dimensional subsidence analysis and gravity modelling of the continental margin offshore Namibia.- *Geophys. J. Int.*, 141, 724-746.
- STOLLHOFEN, H. (1999): Karoo Synrift-Sedimentation und ihre tektonische Kontrolle am entstehenden Kontinentalrand Namibias.- *Z. dt. geol. Ges.*, 149, 519-632.
- SWART, R. (1992/93): Note: Cretaceous synvolcanic conglomerates on the coastal margin of Namibia related to the break-up of West Gondwana.- *Communs. Geol. Surv. Namibia*, 8, 137-141.
- SWART, R. & CARTWRIGHT, J. (2002): Exploration on Volcanic Margins: Insights from the Namibian Margin.- In: GATLIFF, R., WALKER, I., CARTWRIGHT, J. & MITCHENER, B. (eds.): *Frontier Exploration of Volcanic Continental Margins*, Geol. Soc. London Petroleum Group Meeting, 17th – 18th September 2002, conference abstracts.
- TAGGART, J. E. Jr., LINDSAY, J. R., SCOTT, B. A., VIVIT, D. V., BARTEL, A. J. & STEWART, K. C. (1987): Analysis of geological materials by wavelength-dispersive X-ray fluorescence spectrometry.- In: BAEDEKER, P. H. (ed.): *Methods for Geochemical Analysis*.- USGS Bull., 1170, E1-E19.
- TANKARD, A. J., JACKSON, M. P., ERIKSSON, K. A., HOBDAV, D. K., HUNTER, D. R. & MINTER, W. E. L. (1982): *Crustal Evolution of Southern Africa: 3,8 Billion Years of Earth History*.- Springer (New York), 523pp.

- TEN BRINK, U. & STERN, T. (1992): Rift Flank Uplifts and Hinterland Basins: Comparison of the Transantarctic Mountains With the Great Escarpment of Southern Africa.- *J. Geophys. Res.*, 97, 569-585.
- THOMAS, D. S. G. & SHAW, P. A. (1990): The deposition and development of the Kalahari Group sediments, Central Southern Africa.- *J. Afr. Earth Sci.*, 10, 187-197.
- TISSOT, B. P. & WELTE, D. H. (1984): *Petroleum Formation and Occurrence*.- New York (Springer), 699pp.
- TRUMBULL, R. B., EMMERMANN, R., BÜHN, B., GERSTENBERGER, H., MINGRAM, B., SCHMITT, A. K. & VOLKER, F. (in press): Insights on the genesis of the Cretaceous Damara igneous complexes in Namibia: The Nd- and Sr-isotopic perspective.- *Communs. Geol. Surv. Namibia, Henno Martin Commemorative Issue*.
- TUCKER, G. E. & SLINGERLAND, R. L. (1994): Erosional dynamics, flexural isostasy, and long-lived escarpments: A numerical modelling study.- *J. Geophys. Res.*, 99, 12229-12243.
- TURNER, S., REGELOUS, M., KELLEY, S., HAWKESWORTH, C. & MANTOVANI, M. (1994): Magmatism and continental break-up in the South Atlantic: High precision ^{40}Ar - ^{39}Ar geochronology.- *Earth Planet. Sci. Lett.*, 121, 333-348.
- VAN DER WATEREN, F. M. & DUNAI, T. J. (2001): Late Neogene passive margin denudation history - cosmogenic isotope measurements from the central Namib desert.- *Global and Planetary Change*, 30, 271-307.
- VAN WAGONER, J. C., POSAMENTIER, H. W., MITCHUM, R. M., VAIL, P. R., SARG, J. F., LOUITT, T. S. & HARDENBOL, J. (1988): An overview of the fundamentals of sequence stratigraphy and key definitions.- In: WILGUS, C. K., HASTINGS, B. S., KENDALL, C. G. St. C., POSAMENTIER, H. W., ROSS, C. A. & VAN WAGONER, J. C. (eds.): *Sea-level changes: an integrated approach*, SEPM Spec. Pub., 42, 39-45.
- VISSER, J. N. J. (1995): Post-glacial Permian stratigraphy and geography of southern and central Africa: boundary conditions for climatic modelling.- *Palaeogeog. climat. ecol.*, 118, 213-243.
- WALTER, M., SWART, R. & SUMMONS, R. (1996): Oil and gas shows numerous in Nama Basin, southern Africa.- *Oil and Gas Journal*, 94/ 48, 63-67
- WANKE, A. (2000): *Karoo-Etendeka Unconformities in NW Namibia and their Tectonic Implications*.- PhD Thesis, Univ. Würzburg/ Germany, 164pp.
- WARD, J. D., SEELY, M. K. & LANCASTER, N. (1983): On the antiquity of the Namib.- *S. Afr. J. Sci.*, 79, 175-183.
- WARD, J. D. (1987): The Cenozoic succession in the Kuiseb Valley, central Namib Desert.- *Geol. Surv. S. Afr./ Namibia Memoir*, 9, 1-124.
- WARD, J. D. (1988): Geology of the Tsondab Sandstone Formation.- *J. Sed. Geol.*, 55, 143-162.
- WATTS, A. B., KARNER, G. D. & STECKLER, M. S. (1982): Lithospheric flexure and the evolution of sedimentary basins.- *Phil. Trans. Royal Soc. London*, 305, 249-281.
- WATTS, A. B. (1988): Gravity anomalies, crustal structure and flexure of the lithosphere at the Baltimore Canyon Trough.- *Earth Planet. Sci. Lett.*, 89, 221-238.
- WATTS, A. B. & FAIRHEAD, J. D. (1999): A process-oriented approach to modeling the gravity signature of continental margins, *Leading Edge*, 17, 258-263.
- WEISSEL, J. K. & KARNER, G. D. (1989): Flexural uplift of rift flanks due to mechanical unloading of the lithosphere during extension.- *J. Geophys. Res.*, 94, 13919-13950.

- WELTON, J. E. (1984): SEM Petrology Atlas.- AAPG methods in exploration series, 4, 237pp.
- WERNICKE, B. (1985): Uniform-sense normal simple shear of the continental lithosphere.- *Canad. J. Earth Science*, 22, 108-125.
- WHEELER, H. E. (1964): Baselevel, lithosphere surface, and time-stratigraphy.- *GSA Bull.*, 75, 599-610.
- WHITE, N. & LOVELL, B. (1997): Measuring the pulse of a plume with the sedimentary record.- *Nature*, 387, 888-891.
- WHITE, R. S. & MCKENZIE, D. P. (1989): Magmatism at rift zones: The generation of volcanic margins and flood basalts.- *J. Geophys. Res.*, 94, 7685-7729.
- WICKENS, H. de V. & McLACHLAN, I. R. (1990): The stratigraphy and sedimentology of the reservoir interval of the Kudu 9A-2 and 9A-3 boreholes.- *Communs. Geol. Surv. Namibia*, 6, 9-22.
- WILSON, M. D. & PITTMAN, E. D. (1977): Authigenic clays in sandstones: recognition and influence on reservoir properties and paleoenvironmental analysis.- *J. Sediment. Petrol.*, 47, 3-31.
- ZIMMERMAN, H. B., BOERSMA, A. & McCOY, F. W. (1987): Carbonaceous sediments and palaeoenvironment of the Cretaceous South Atlantic Ocean.- In: BROOKS, J. & FLEET, A. J. (eds.): *Marine Petroleum Source Rocks*.- *Geol. Soc. London Spec. Pub.*, 26, 271-286.

9 Appendix

Appendix 1: Petrographic composition of the Upper Campanian/ Maastrichtian gross sand interval within the postrift succession of well 2012/13-1

Appendix 2-1 to 2-10: Petrographic overview of samples K4, K5, K7, K9, K10, K12, K13, K14, K16, K18

Appendix 3-1 to 3-4: SEM analysis, overview of major components, pore spaces, authigenic cements, special features

Appendix 4-1 to 4-4: SEM analysis, EDX element mapping (Ca, Mg, Si, K, Fe) of samples K4, K9, K12, K18

Appendix 5: List of samples for XRF whole-rock geochemical analysis

Appendix 6: XRF whole-rock geochemical analysis – weight loss by ignition (LOI)

Appendix 7: XRF whole rock geochemical analysis (offshore samples)

Appendix 8: XRF whole rock geochemical analysis (onshore samples)

Appendix 9: XRF whole rock geochemical analysis (offshore samples) plotted versus depth

Appendix 10: STRATA sea level file

Appendix 11: STRATA subsidence file

Appendix 12: STRATA heat flow file

Appendix 13: STRATA sediment flux file (“best fit” model mp4)

Appendix 14: TOC and Rock-Eval pyrolysis data

Appendix 15: Maturity data

Appendix 16: List of figure captions

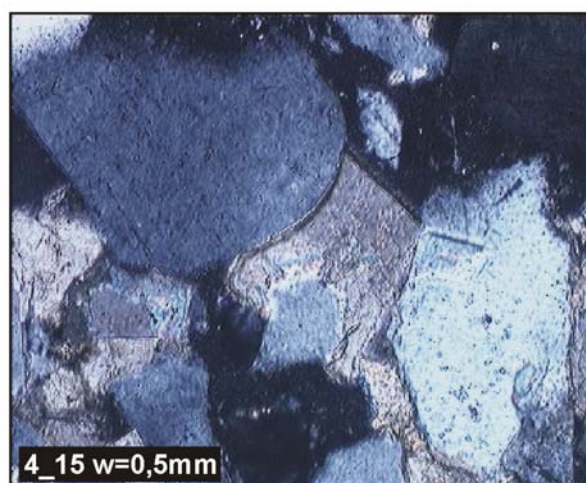
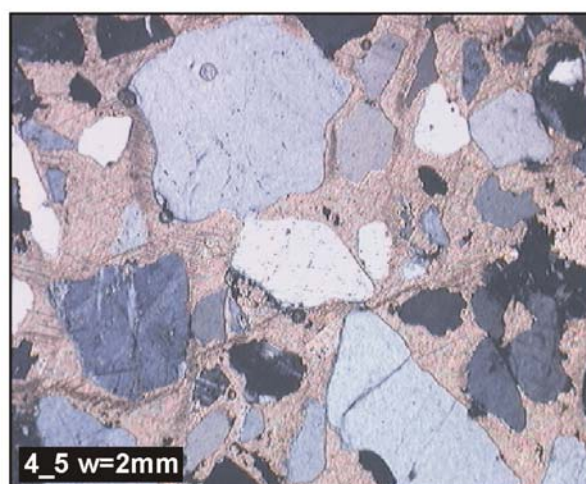
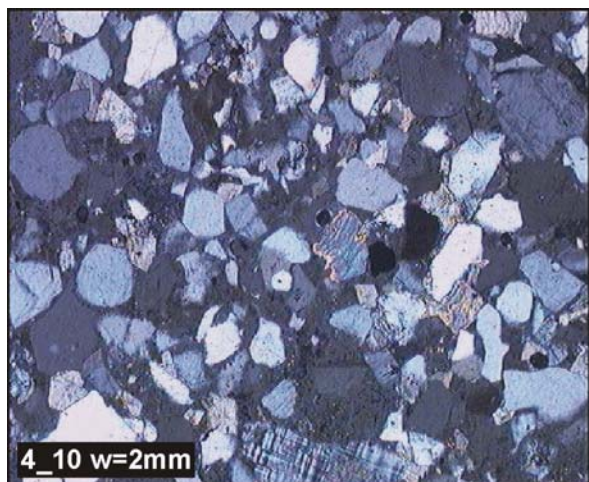
Appendix 17: Selected internet sources

Appendix 18: Curriculum vitae

Appendix 1: petrographic composition of the Upper Campanian/ Maastrichtian gross sand interval within the postrift succession of well 2012/13-1

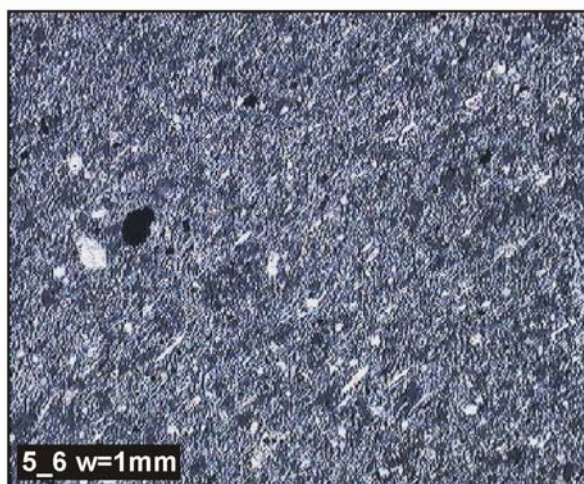
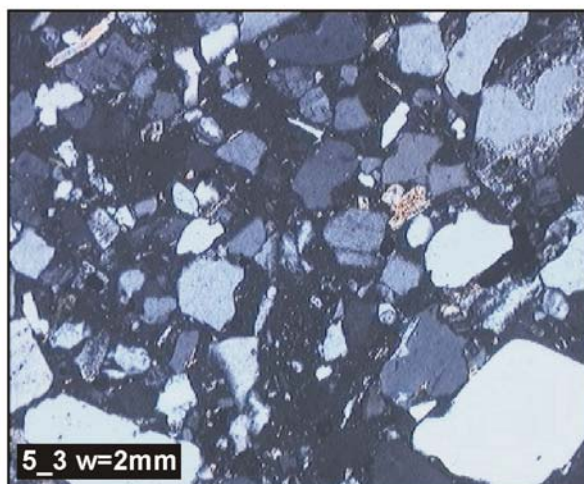
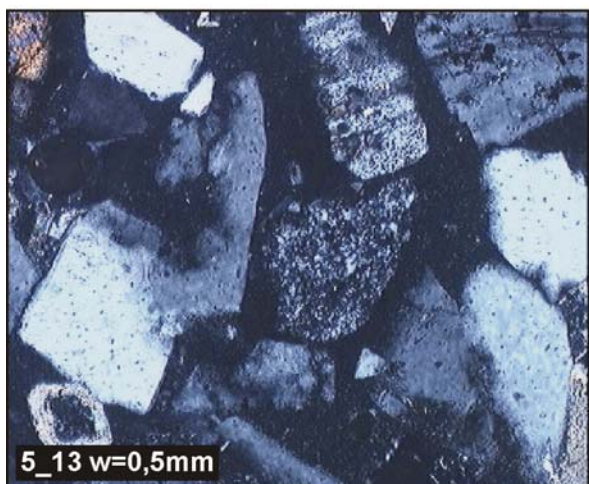
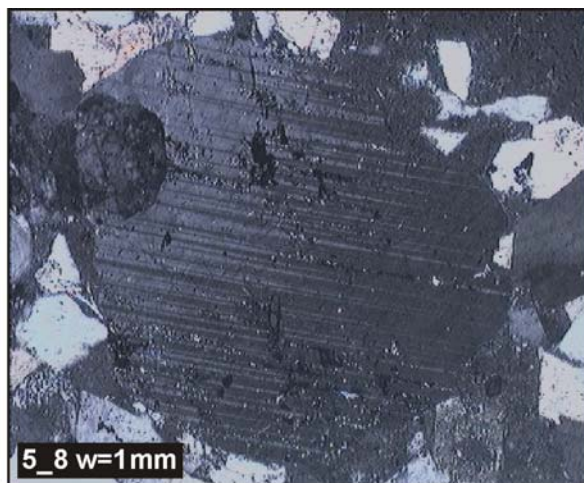
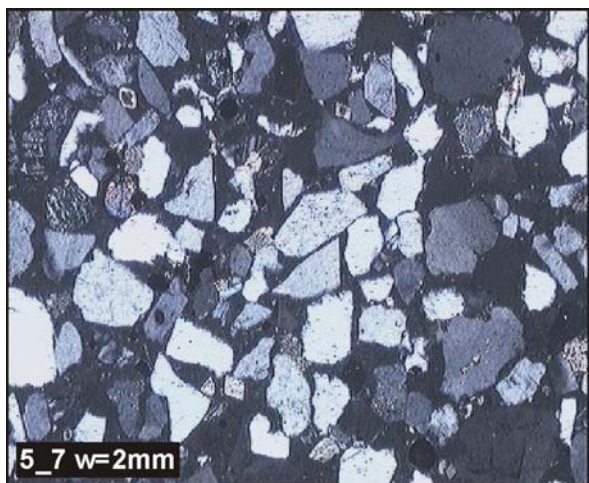
Sample	<i>K4</i>	K5	K7	K9	K10	K12	K13	K14	K16	K18
Depth [m]	2698	2723	2803	2838	2848	2888	2933	2984	2990	2999
Components										
detritic [vol%]										
Qtz mono volc	31,0	21,0	26,0	19,0	31,0	5,0	35,0	33,0	17,0	25,0
Qtz mono plut	14,0	36,0	16,0	21,0	21,0	42,0	11,0	21,0	31,0	32,0
Qtz poly plut	2,0	2,3	-	-	-	-	-	-	-	-
Qtz sut metam	-	-	13,0	2,3	5,0	12,0	0,7	-	-	-
K-Fsp	3,0	-	7,0	2,0	8,0	-	1,0	-	4,0	4,0
Plag	13,0	9,0	5,0	10,0	11,0	2,0	15,0	14,0	11,0	5,0
Lithics	4,0	3,0	4,0	12,0	2,0	4,0	2,0	4,0	5,0	2,0
Musc	-	1,0	0,6	0,3	0,6	-	-	-	-	-
Biot	2,0	0,3	0,3	-	0,6	1,0	2,3	1,3	-	-
Chl	-	1,0	-	-	0,3	-	-	0,3	-	-
Opaque	-	0,3	-	0,3	-	0,6	-	1,3	-	5,0
Heavymin	-	1,0	-	-	-	-	-	-	-	0,3
authigenic [vol%]										
Micro-Qtz	18,0	19,0	26,0	7,0	14,0	15,0	9,0	12,0	-	-
Dolom	13,0	6,0	2,0	26,0	6,0	19,0	25,0	15,0	32,0	27,0

Appendix 2-1: sample K4, petrographic overview



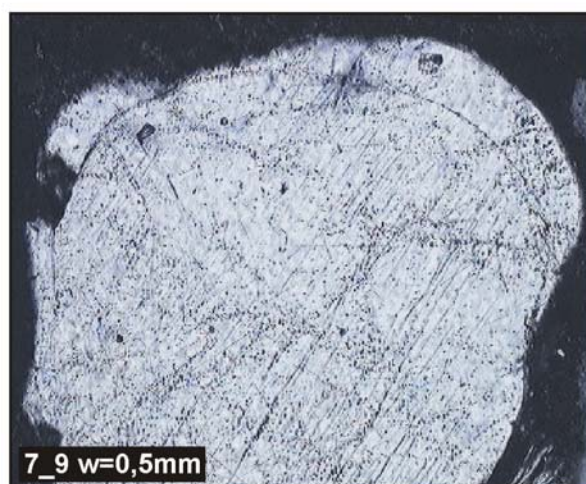
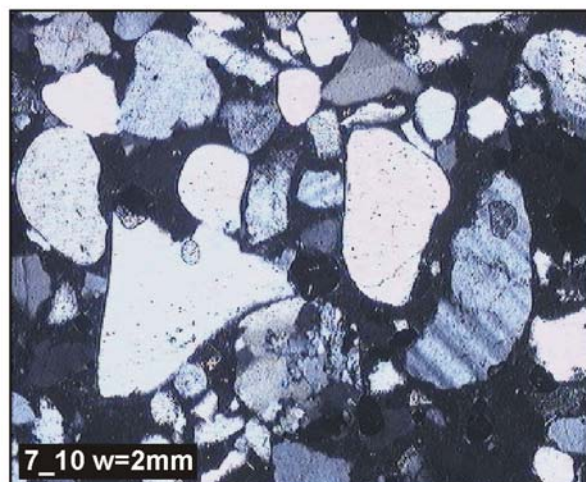
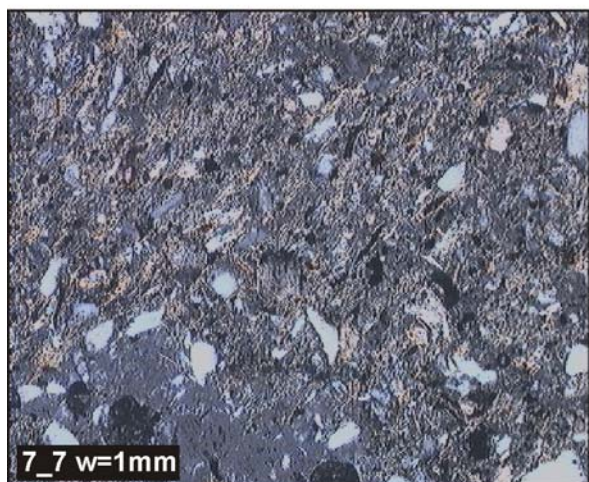
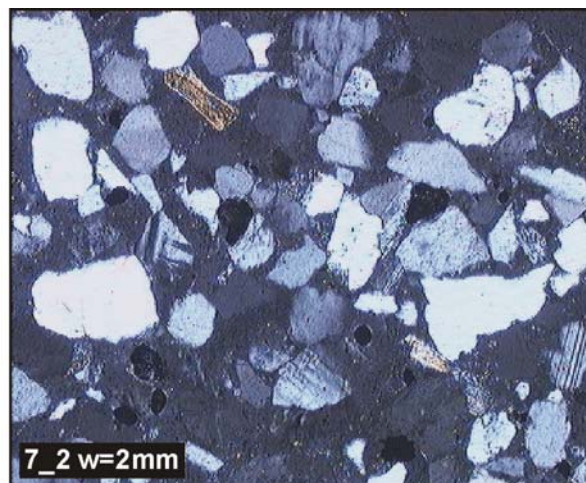
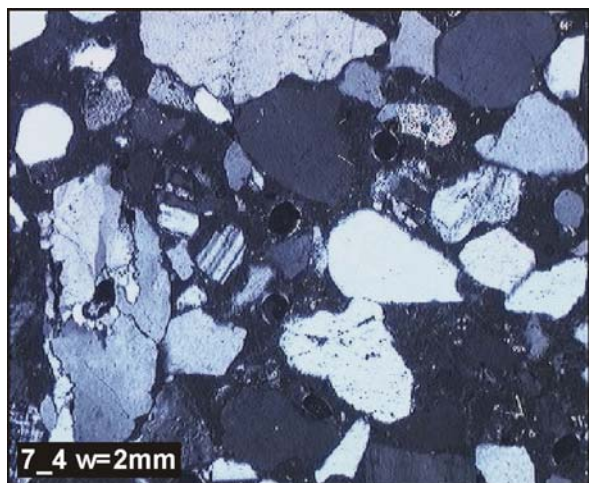
sample depth: 2695-2700m

Appendix 2-2: sample K5, petrographic overview



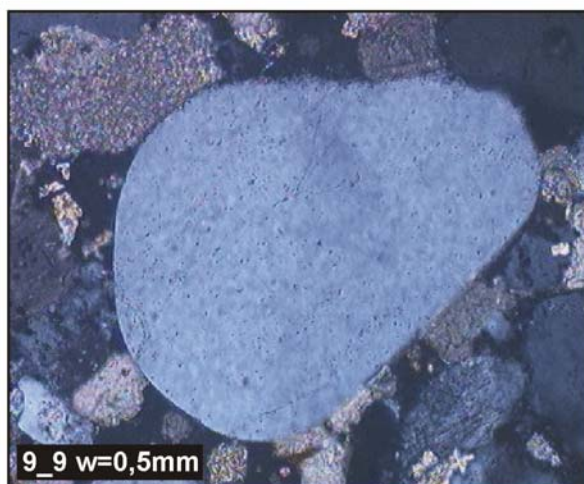
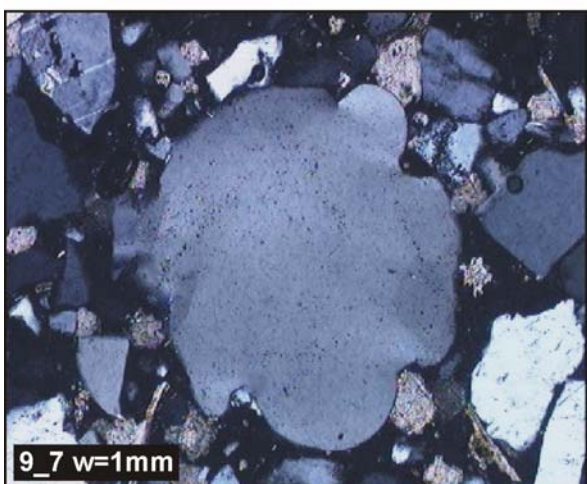
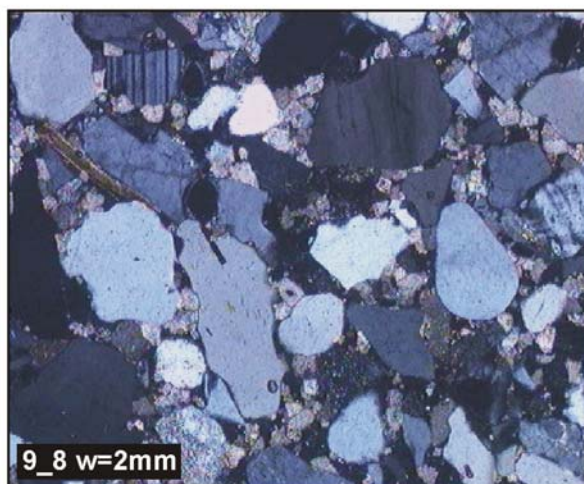
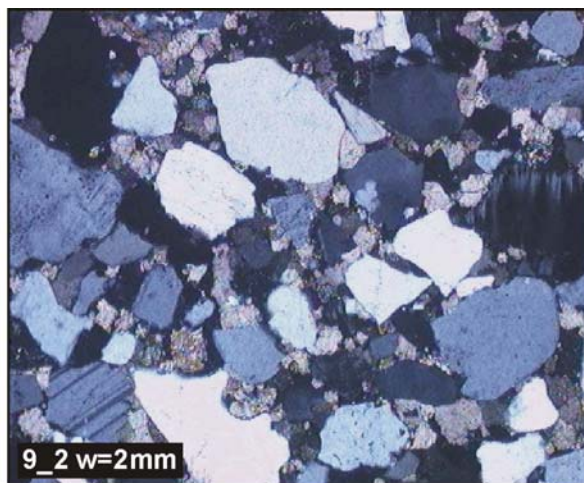
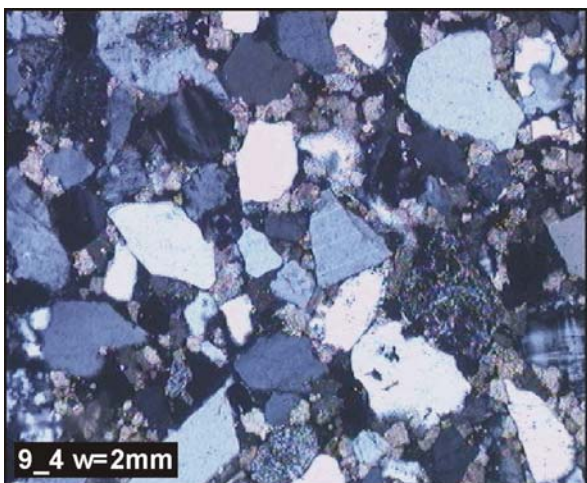
sample depth: 2720-2725m

Appendix 2-3: sample K7, petrographic overview



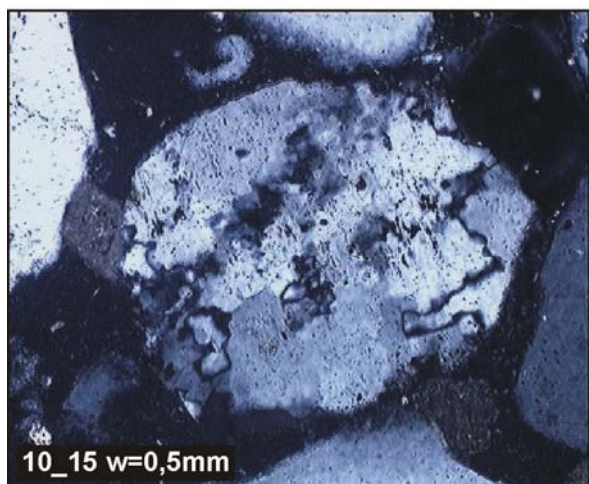
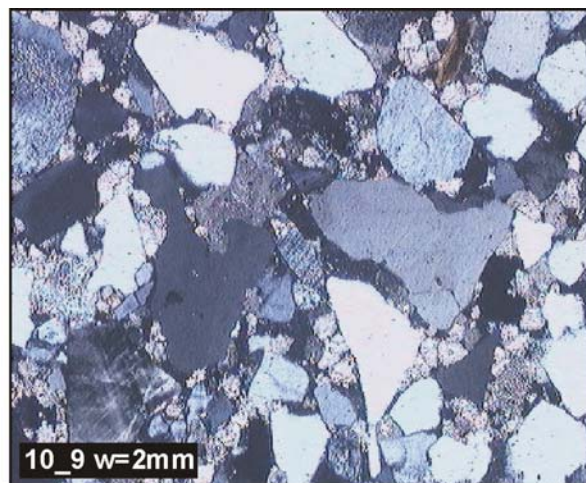
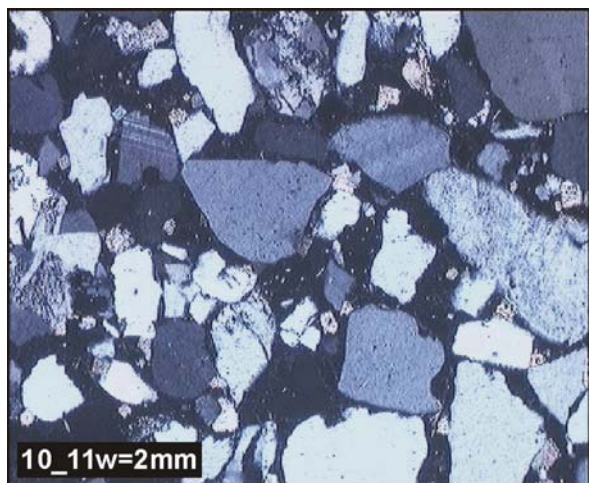
sample depth: 2800-2805m

Appendix 2-4: sample K9, petrographic overview



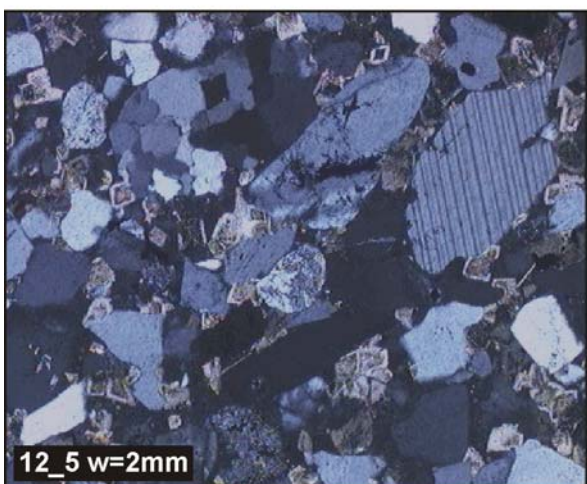
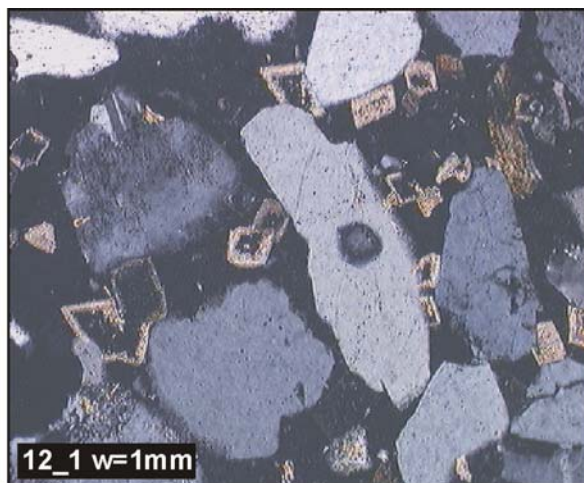
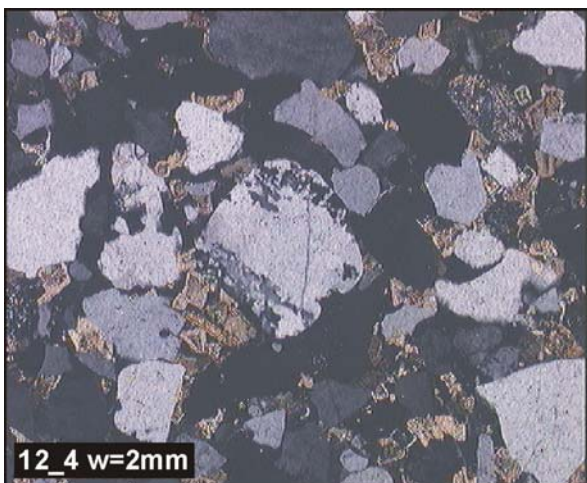
sample depth: 2835-2840m

Appendix 2-5: sample K10, petrographic overview



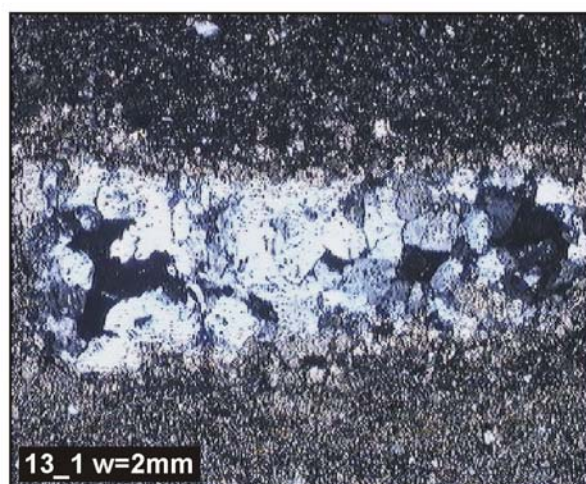
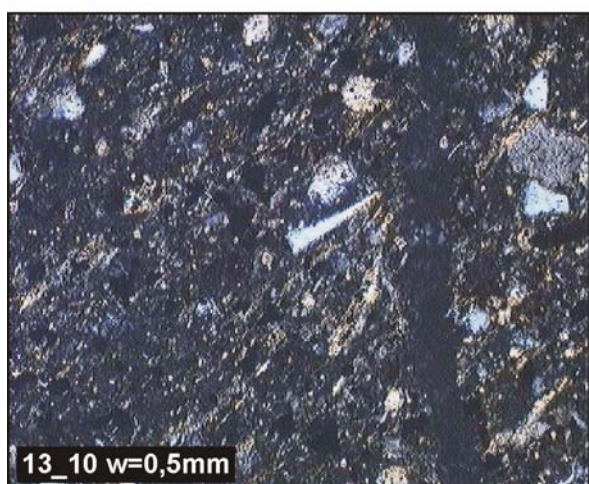
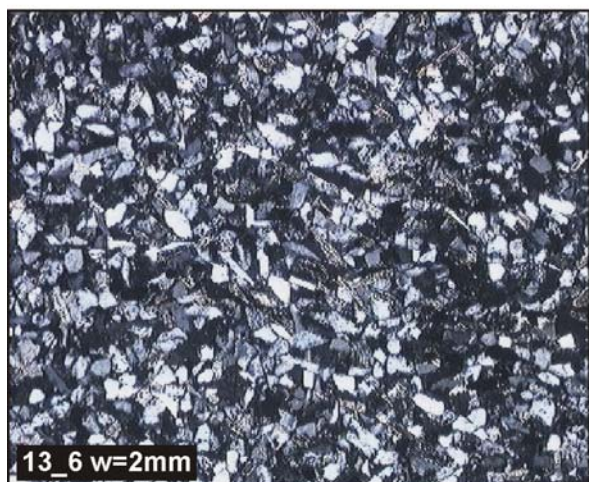
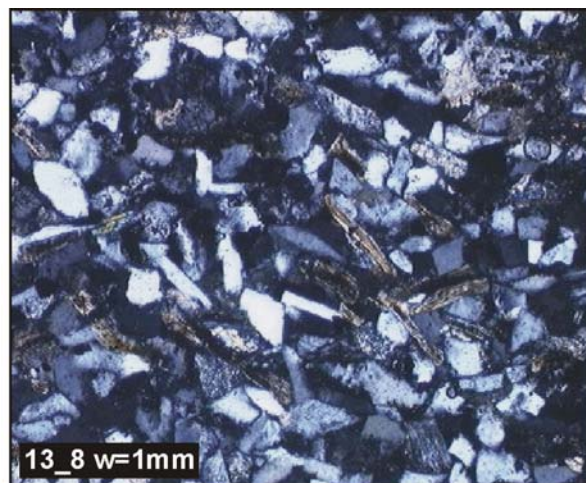
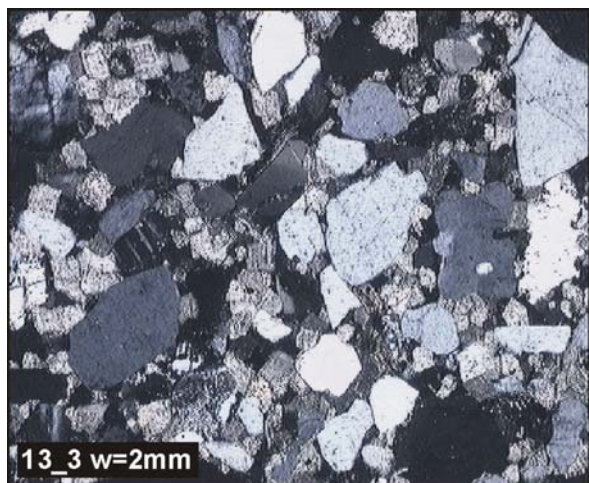
sample depth: 2845-2850m

Appendix 2-6: sample K12, petrographic overview



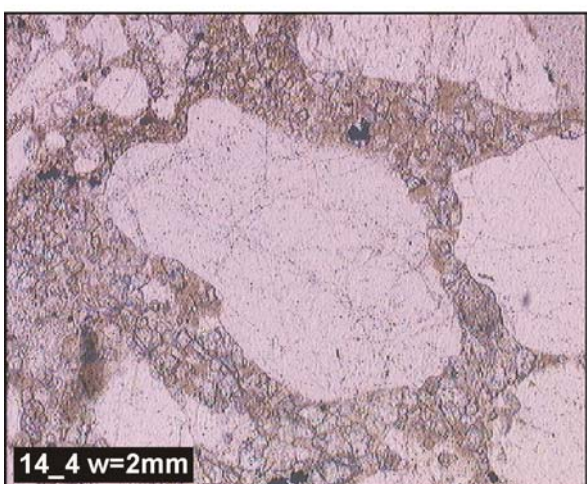
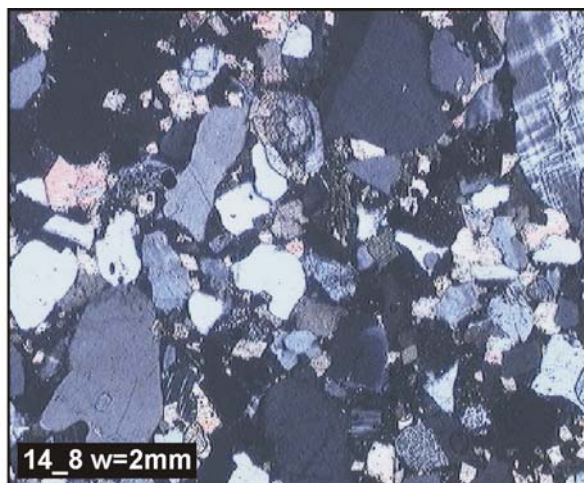
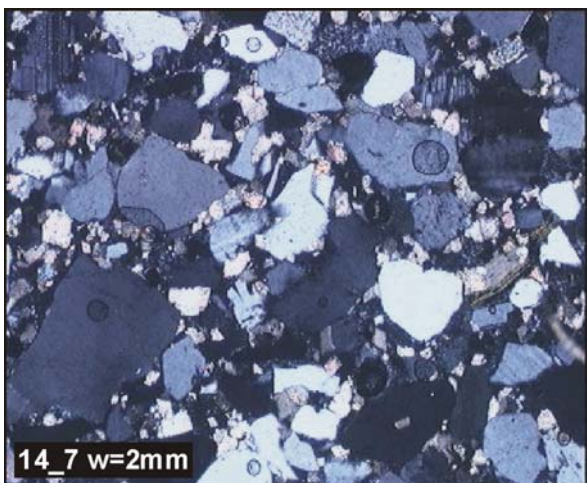
sample depth: 2885-2890m

Appendix 2-7: sample K13, petrographic overview



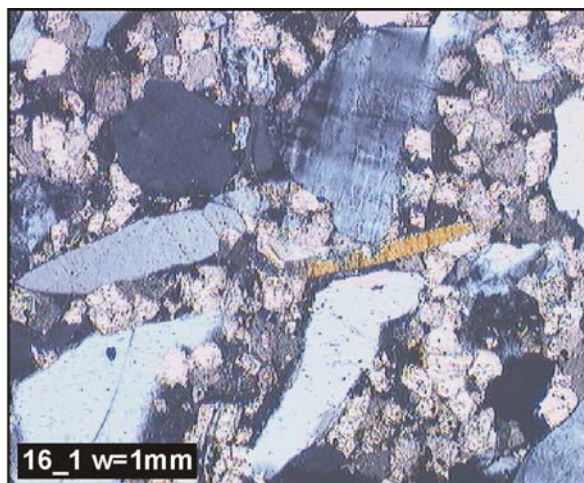
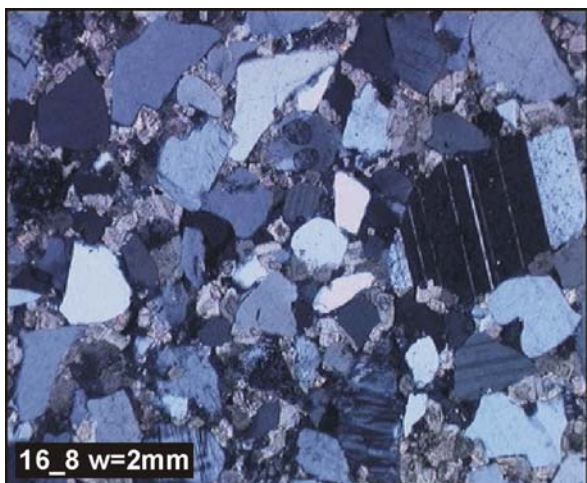
sample depth: 2930-2935m

Appendix 2-8: sample K14, petrographic overview



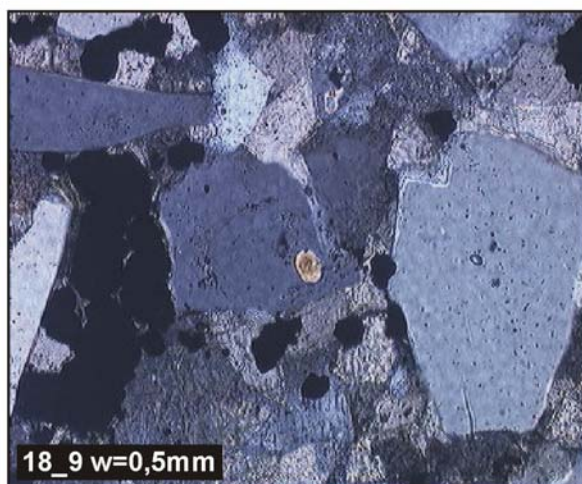
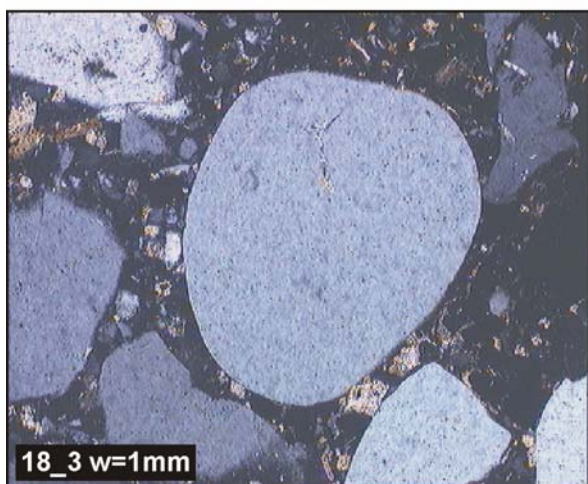
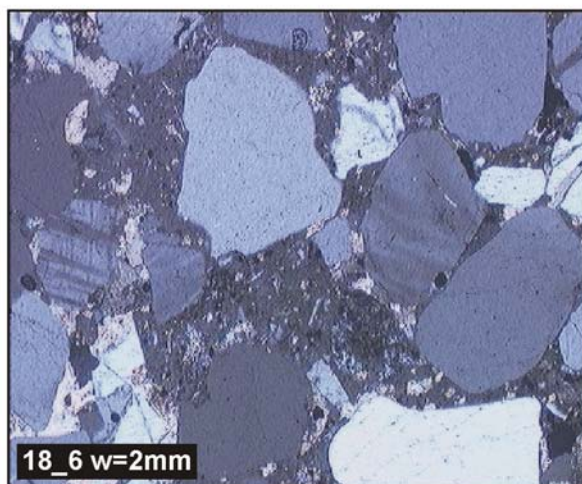
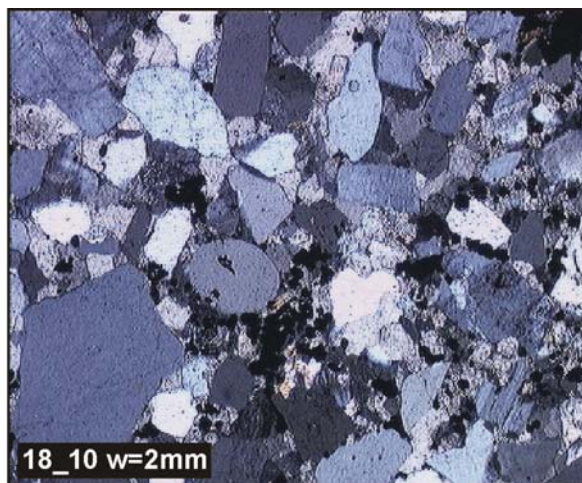
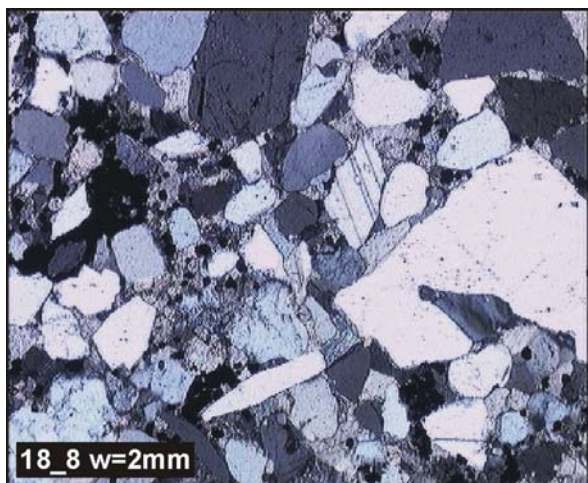
sample depth: 2982-2985m

Appendix 2-9: sample K16, petrographic overview



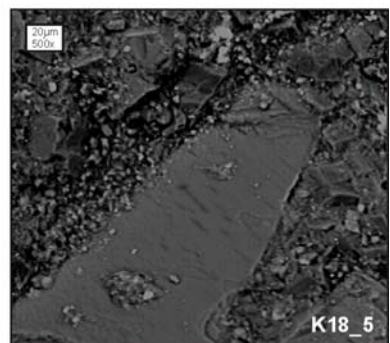
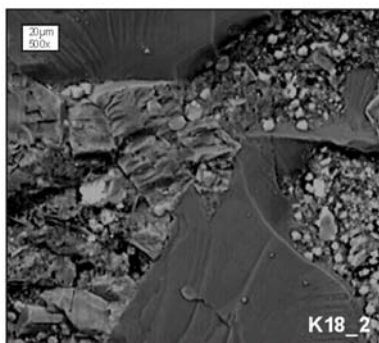
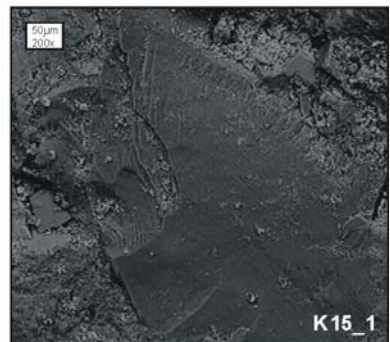
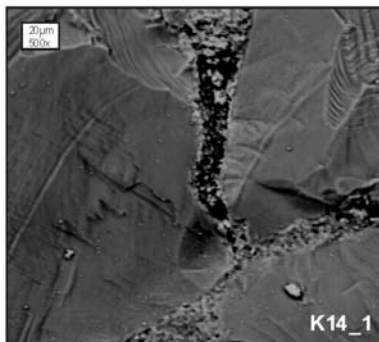
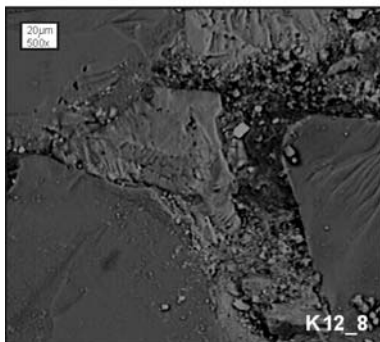
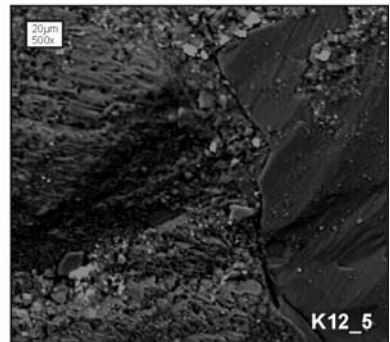
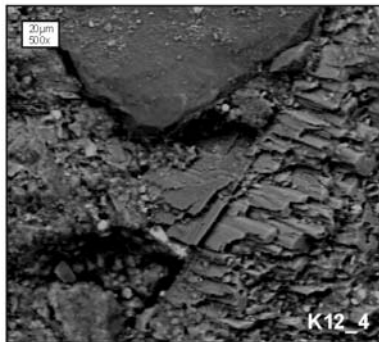
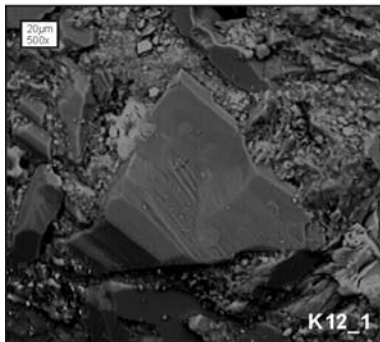
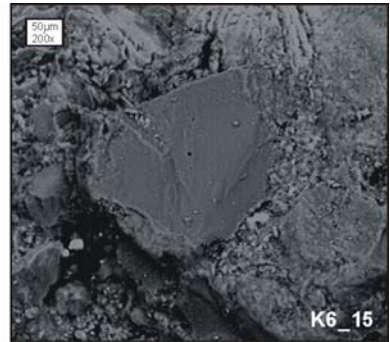
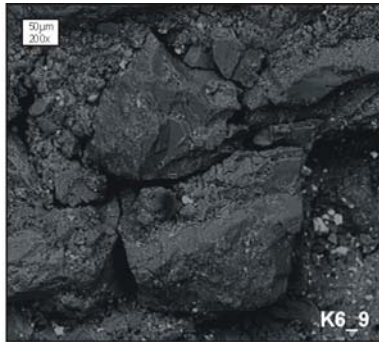
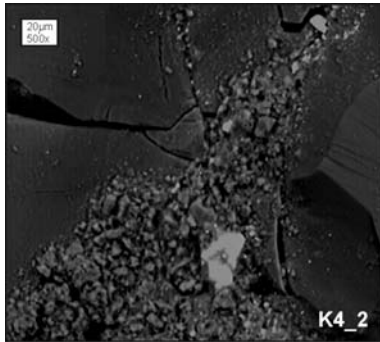
sample depth: 2988-2991m

Appendix 2-10: sample K18, petrographic overview

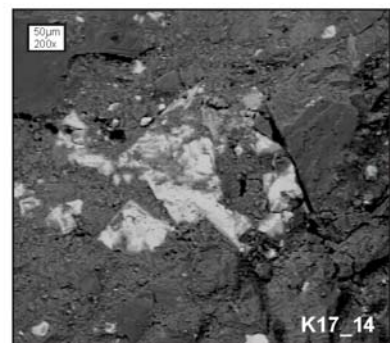
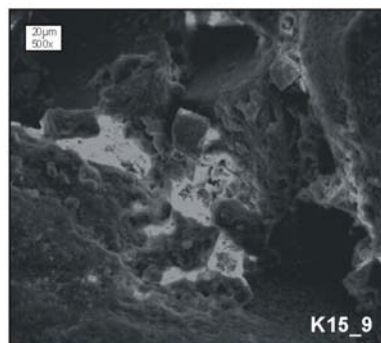
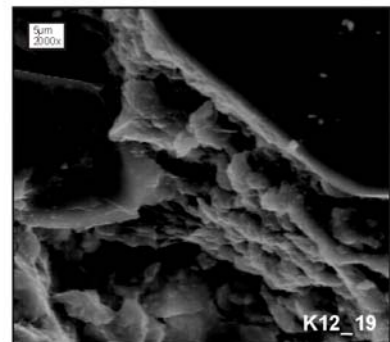
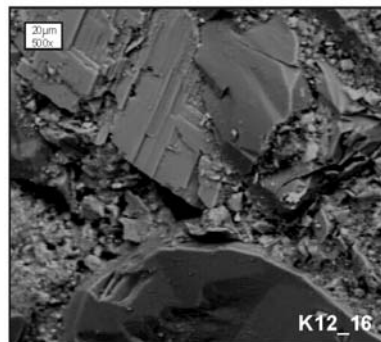
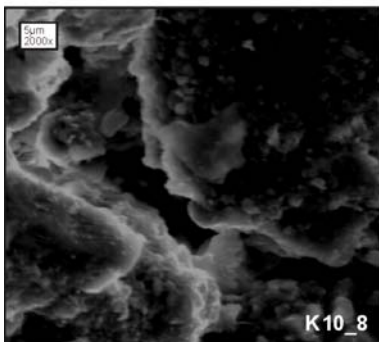
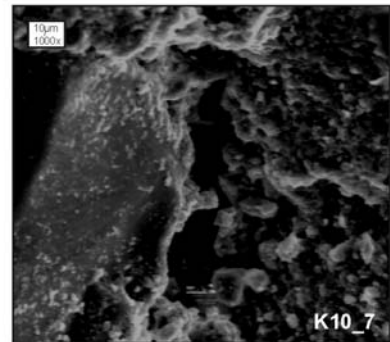
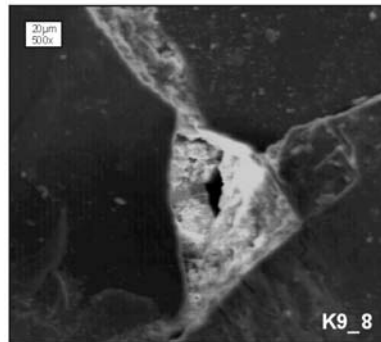
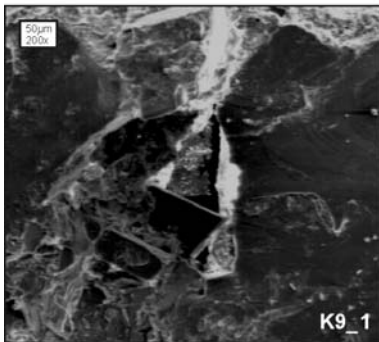
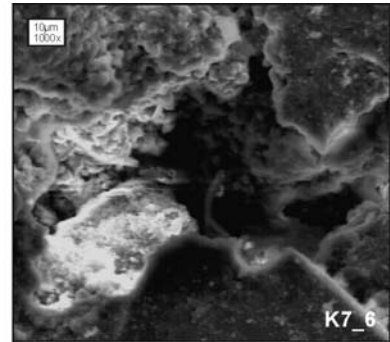
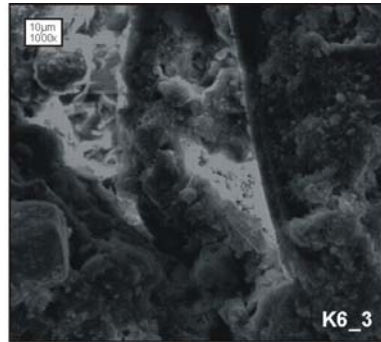
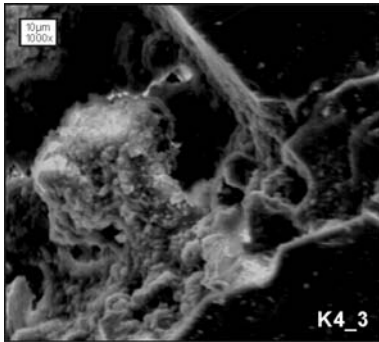


sample depth: 2997-3000m

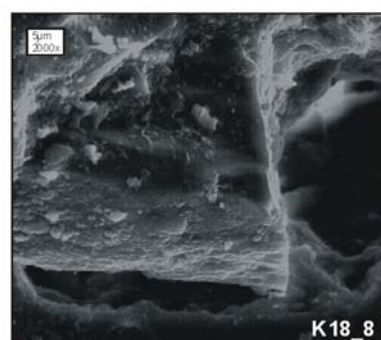
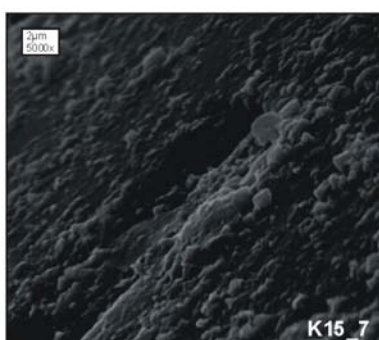
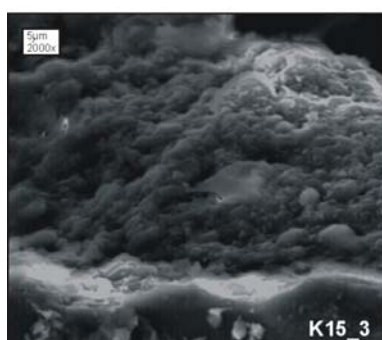
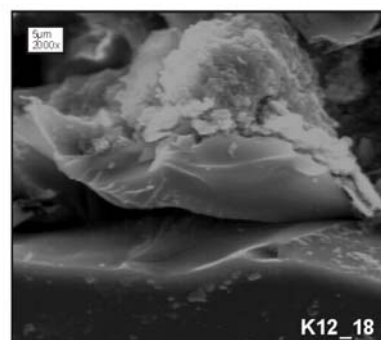
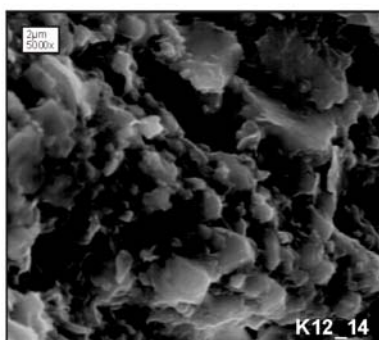
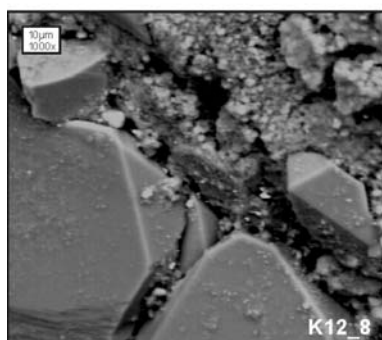
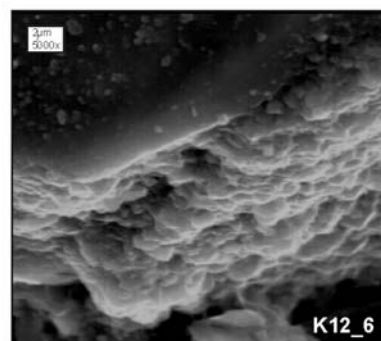
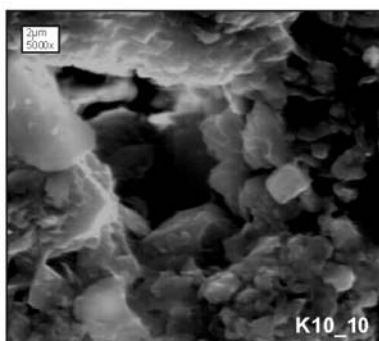
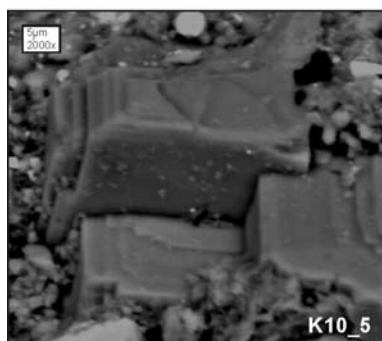
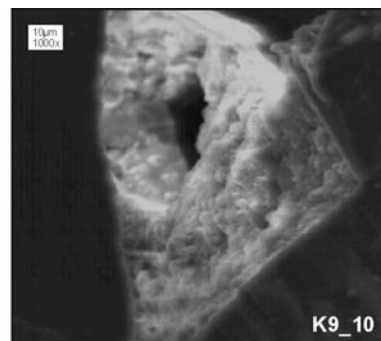
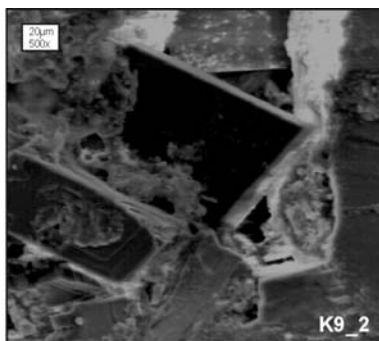
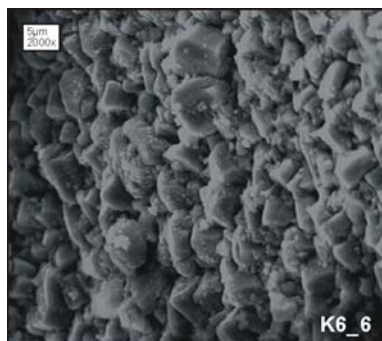
Appendix 3-1: SEM analysis, overview of major components



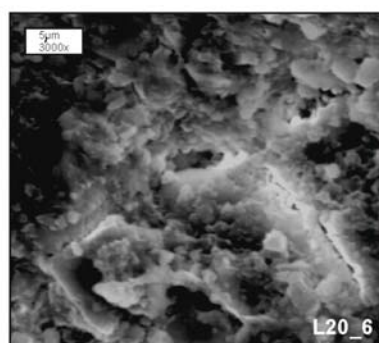
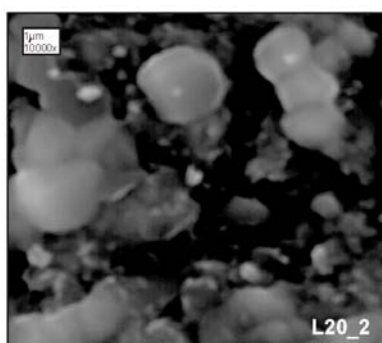
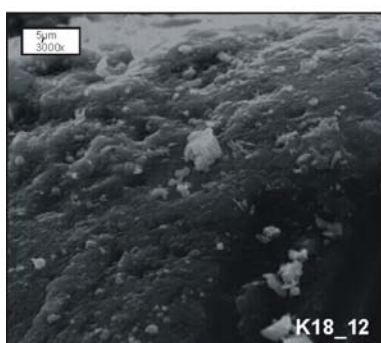
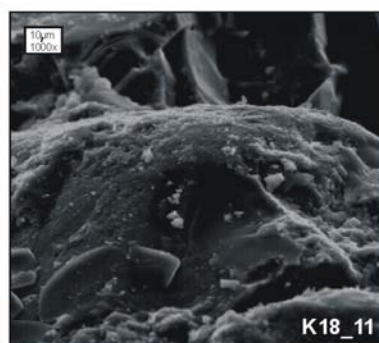
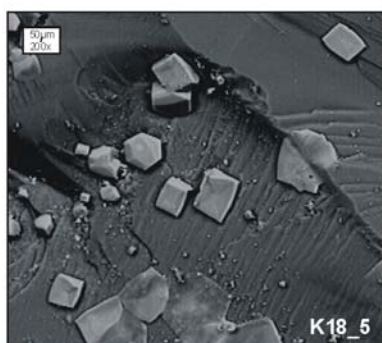
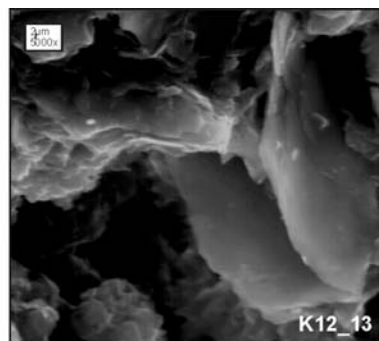
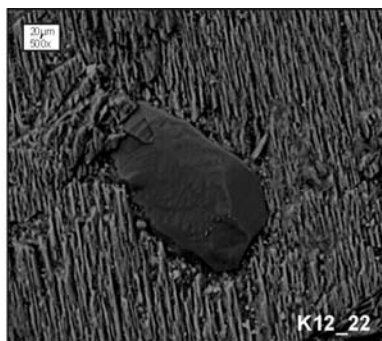
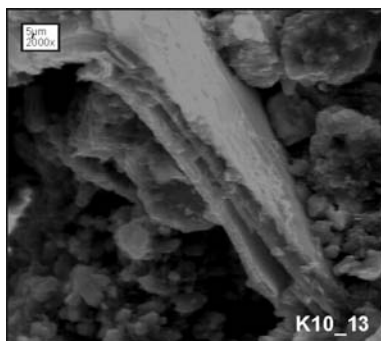
Appendix 3-2: SEM analysis, overview of pore spaces



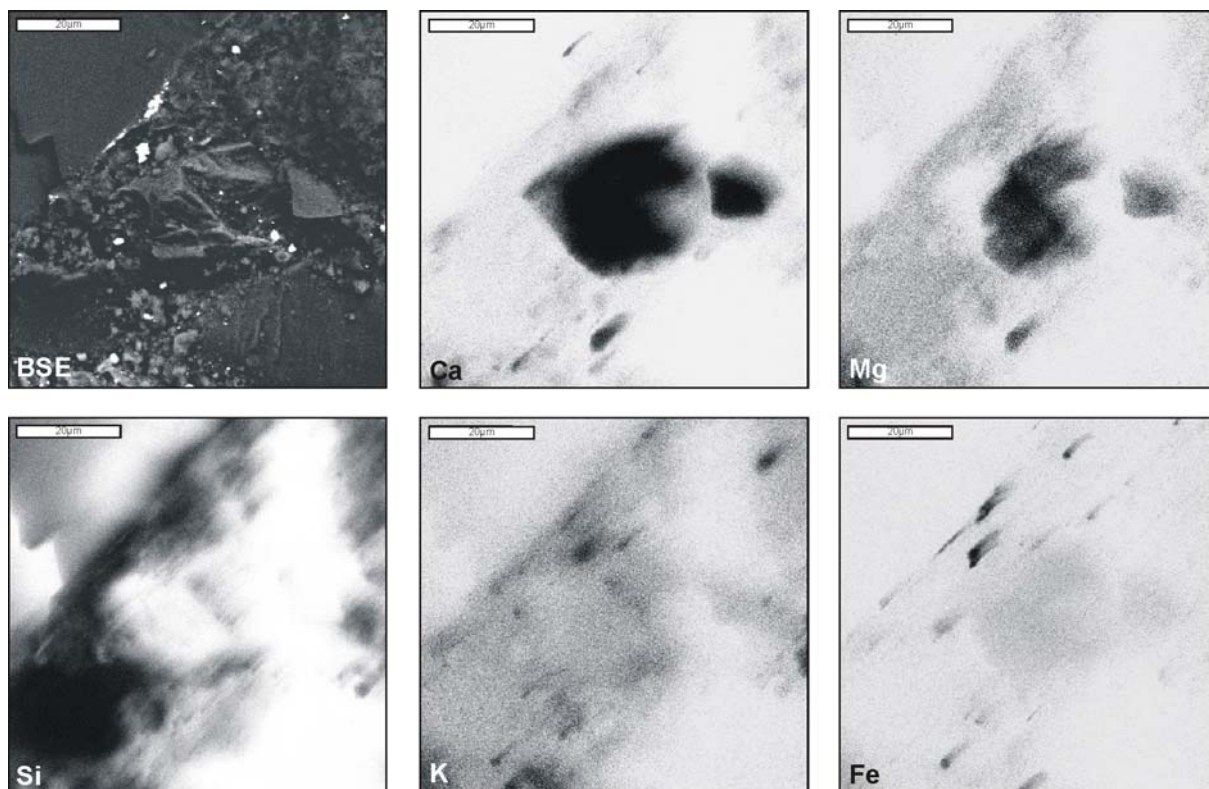
Appendix 3-3: SEM analysis, overview of authigenic cements



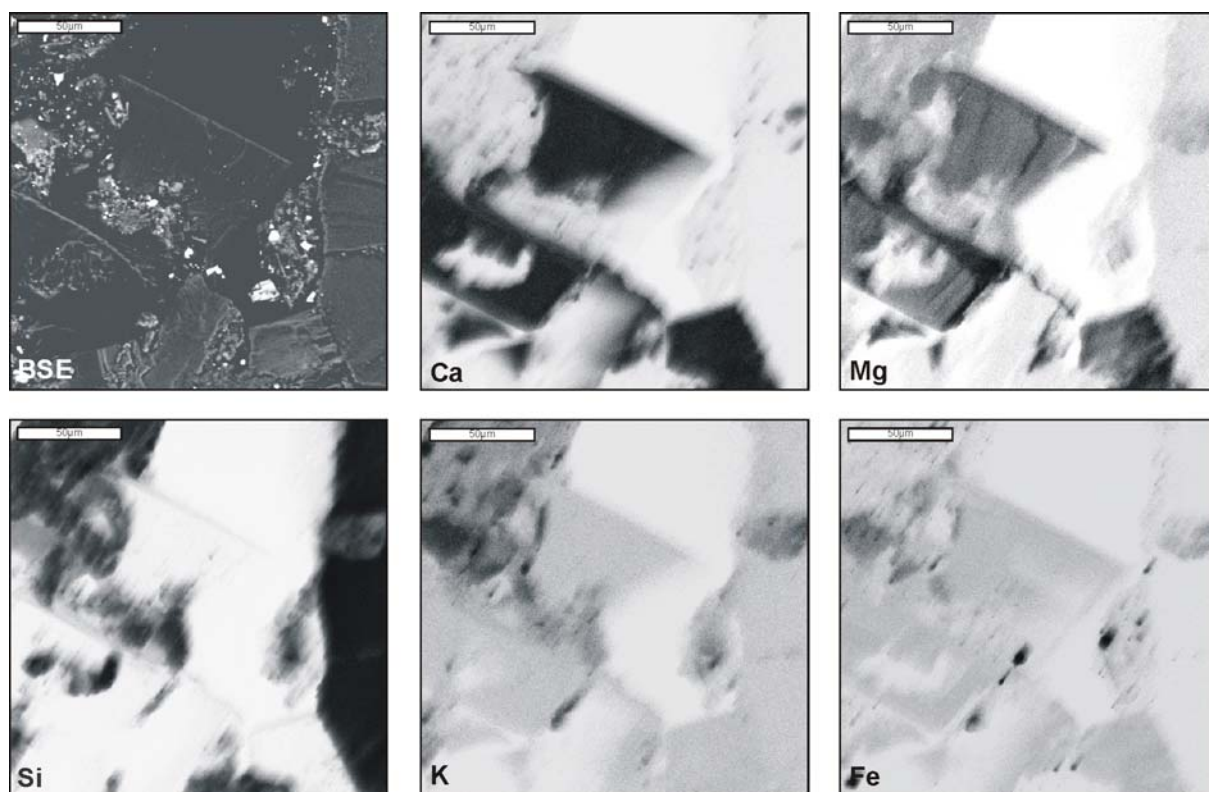
Appendix 3-4: SEM analysis, overview of special features

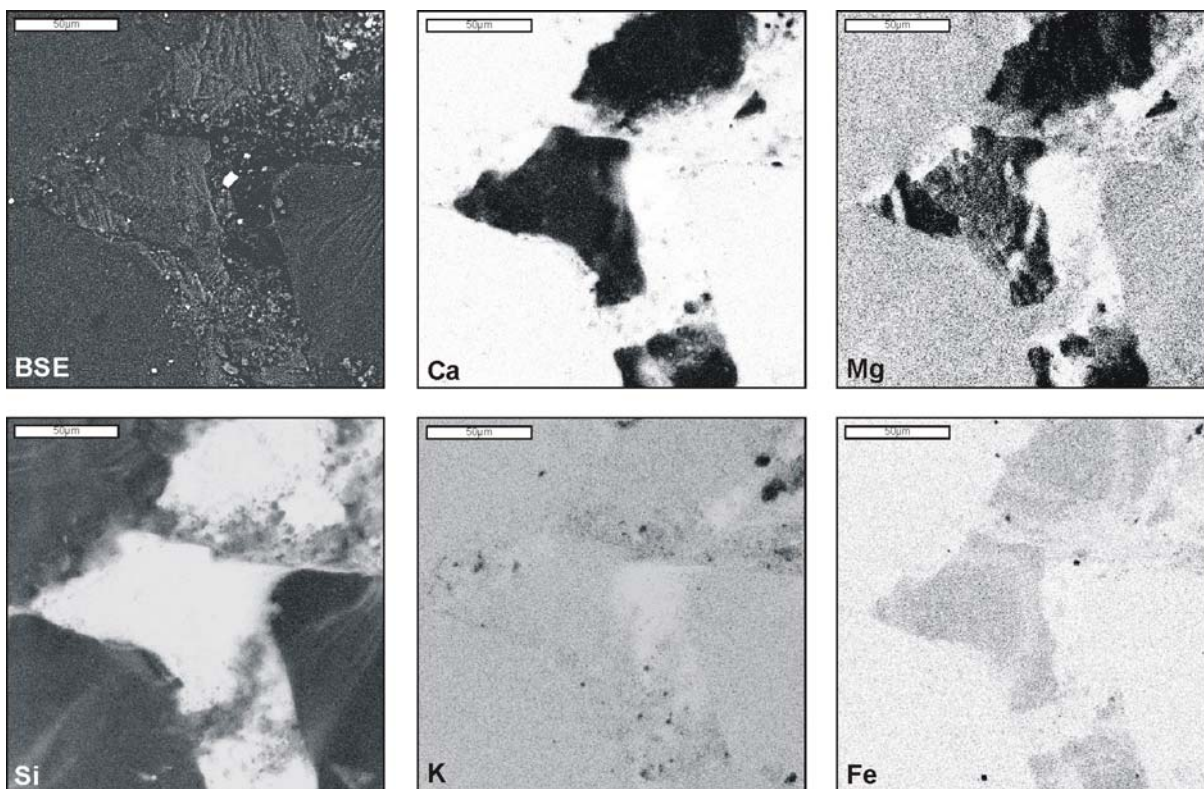
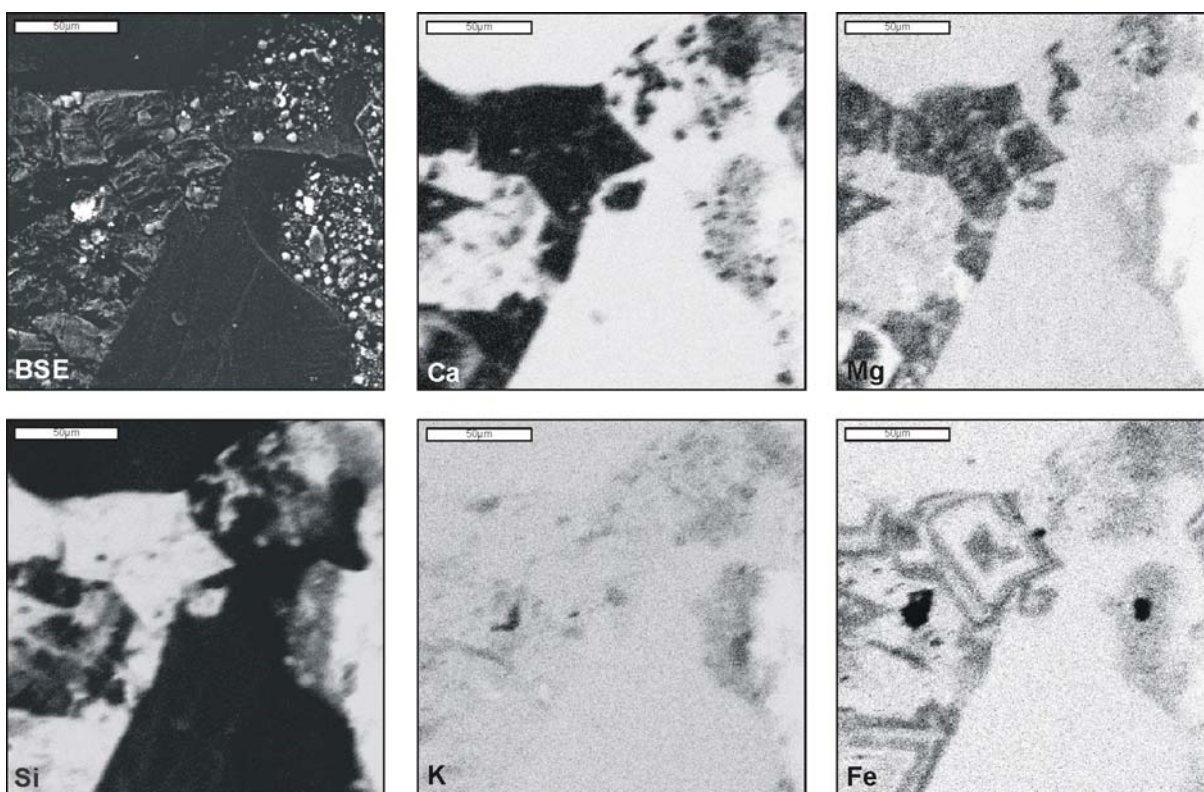


Appendix 4-1: SEM analysis, sample K4, EDX element mapping



Appendix 4-2: SEM analysis, sample K9, EDX element mapping



Appendix 4-3: SEM analysis, sample K12, EDX element mapping**Appendix 4-4: SEM analysis, sample K18, EDX element mapping**

Appendix 5: List of samples for XRF whole-rock geochemical analysis

Offshore samples (well 2012/13-1):

Sample name	Sample depth [m]	Lithology
K1	1430-1440	Claystone, silty
M1	2460-2465	Claystone, silty
L2	2500-2505	Claystone, silty
L4	2540-2545	Claystone, silty
L5	2690-2695	Claystone, silty, partly sandy
L6	2735-2740	Claystone, silty, partly sandy
L7	2860-2865	Claystone, silty, partly sandy
L9	2910-2915	Claystone, silty; partly sandy
L10	2935-2940	Claystone, silty, partly sandy
L12	2970-2975	Claystone, silty, partly sandy
L15	3051-3054	Claystone, silty
L18	3102-3105	Claystone, silty
L20	3141-3144	Claystone, silty
L22	3216-3219	Claystone, silty
L26	3255-3258	Claystone, silty
M9	3384-3387	Claystone, silty
L28	3399-3402	Claystone, silty
M10	3405-3408	Claystone, silty
K20	3711-3712	Claystone, silty

Onshore samples:

Sample name	Lithology	Stratigraphy	Location
26/ 2	Basalt	Etendeka Gp.	20°05,817` S 13°51,797` E
16/ 4	Granite	Torrabay Granite (Cambrian)	20°20,800` S 13°17,327` E
18/ 3	Granite	Mile 110 Granite (Cambrian)	21°14,429` S 13°46,997` E
23/ 2	Metasedim. rock	Damara Seq. (Cambrian)	21°17,155` S 14°02,430` E
12/ 1	Granite	Cape Cross Granite (Cretac.)	21°45,931` S 13°59,047` E
25/ 4	Aeolian sandstone	Twyfelfontein Fm.	20°37,368` S 14°25,137` E
6/ 1	Fluvial sandstone	Albin Ridge Mb.	21°26,737` S 13°54,454` E
14/ 2	Lacustrine siltstone	Gai As Fm.	21°14,906` S 14°03,836` E
16/ 1	Quartz-Latite	Etendeka Gp.	20°22` S 13°26,5` E
18/ 1	Granite	Durissa Bay Granite (Cambrian)	21°15,875` S 13°43,869` E
27/ 4	Fluvial sandstone	Krone Mb.	20°29,128` S 14°01,607` E

Appendix 6: XRF whole-rock geochemical analysis – weight loss by ignition (LOI)

Sample name	Weight after drying* (sample+crucible) [g]	Weight loss on ignition (LOI)** [g]	Weight loss on ignition (LOI)** [%]
L2	10,276	0,084	8,44
L4	9,1961	0,1425	14,12
L5	10,3329	0,0629	6,24
L6	11,0535	0,0798	7,97
L7	10,9121	0,0542	5,46
L9	10,6301	0,0844	8,37
L10	11,1383	0,08	8,02
L12	10,9192	0,1194	11,91
L15	10,074	0,0604	6,09
L18	11,2679	0,0681	6,83
L20	10,8454	0,1471	14,65
L22	9,4013	0,1236	12,23
L26	9,445	0,1489	14,93
L28	10,6485	0,0957	9,60
6/1	10,3963	0,0418	4,15
12/1	10,8334	0,0043	0,43
14/2	11,3385	0,0193	1,93
16/1	11,0975	0,0154	1,55
16/4	10,4471	0,0057	0,57
18/1	10,1721	0,0064	0,64
18/3	11,2958	0,0028	0,28
23/2	10,1394	0,2049	20,30
25/4	11,0052	0,0131	1,31
26/2	11,0147	0,0322	3,20
27/4	10,4201	0,0069	0,69
K1	10,8732	0,2054	20,40
K20	10,0044	0,1026	10,30
M1	11,3446	0,1432	14,36
M9	10,348	0,1437	14,30
M10	10,6737	0,101	10,01

* drying at 105°C, 1h30min

** ignition at 1050°C, 1h30min

Appendix 7: XRF whole rock geochemical analysis (offshore samples)***Oxides [%]:**

Sample	SiO ₂	TiO ₂	Al ₂ O ₃	Fe ₂ O ₃	MnO	CaO	MgO	K ₂ O	Na ₂ O	P ₂ O ₅
	Si2 (%)	Ti (%)	Al1 (%)	Fe2 (%)	Mn (%)	Ca2 (%)	Mg1 (%)	K (%)	Na1 (%)	P1 (%)
K1	46,46	0,67	13,52	6,64	0,04	24,44	3,13	3,11	0,79	0,26
M1	65,81	0,45	7,43	4,12	0,03	16,83	2,06	2,24	0,50	0,10
L2	76,64	0,42	6,99	3,89	0,02	7,30	1,82	1,86	0,41	0,10
L4	62,98	0,56	8,46	5,17	0,05	16,73	2,28	2,52	0,57	0,16
L6	75,18	0,40	7,40	3,98	0,03	4,91	3,14	2,66	0,94	0,15
L7	80,01	0,25	6,56	2,80	0,03	3,42	2,20	2,58	1,03	0,10
L9	76,55	0,40	6,77	3,55	0,03	4,80	3,69	2,26	0,94	0,13
L10	73,09	0,52	8,38	4,21	0,04	4,73	4,16	2,86	1,06	0,15
L12	65,70	0,47	7,77	5,06	0,06	10,48	5,49	2,82	1,01	0,15
L15	75,54	0,59	7,98	4,43	0,03	4,26	2,45	2,22	1,41	0,14
L18	73,95	0,58	7,95	4,66	0,03	6,42	2,03	2,12	1,13	0,13
L20	59,23	0,59	9,04	6,15	0,07	16,83	3,30	2,74	1,04	0,15
L22	59,80	0,69	10,09	6,25	0,07	14,18	3,11	2,83	1,10	0,19
L26	54,31	0,79	11,08	7,46	0,11	18,17	2,97	3,21	0,81	0,19
M9	55,37	0,91	11,42	8,10	0,06	15,99	2,59	3,01	0,96	0,16
L28	62,84	0,94	11,86	8,20	0,04	7,66	2,53	2,98	1,15	0,18
M10	61,78	1,00	12,30	8,22	0,04	8,33	2,52	3,16	1,20	0,21
K20	59,77	0,94	11,85	8,61	0,07	9,91	3,02	3,19	1,22	0,14

Elements I [ppm]:

Sample	Ba	Cr	Cu	Ni	Pb	Rb	Sc	Sr	V	Zn
	Ba2 (ppm)	Cr (ppm)	Cu (ppm)	Ni (ppm)	Pb (ppm)	Rb (ppm)	Sc (ppm)	Sr (ppm)	V (ppm)	Zn2 (ppm)
K1	660	148	69	49	19	111	32	931	107	203
M1	787	106	28	31	20	77	19	389	80	78
L2	551	121	14	25	13	67	13	183	86	69
L4	1606	104	27	34	15	94	19	338	91	110
L6	3074	80	36	32	12	81	8	149	61	98
L7	1304	44	27	16	17	74	5	100	38	41
L9	555	69	18	23	9	65	11	118	60	69
L10	635	78	14	21	15	89	13	87	77	116
L12	1660	70	16	28	18	80	15	145	77	97
L15	1394	106	26	36	12	60	12	135	87	80
L18	3180	84	19	26	12	62	11	218	86	78
L20	3017	84	17	33	13	94	23	366	94	70
L22	8256	106	10	25	10	100	23	485	120	181
L26	5361	97	39	54	18	122	28	477	135	163
M9	7636	91	15	32	14	104	27	528	149	120
L28	6767	103	21	29	14	104	21	358	149	181
M10	2789	105	20	30	13	107	20	285	153	171
K20	8056	102	38	67	57	92	22	443	146	126

Elements II [ppm]:

Sample	Zr Zr3 (ppm)	As As (ppm)	Cd Cd (ppm)	Ce Ce (ppm)	Cl Cl (ppm)	F F1 (ppm)	Ga Ga (ppm)	Ge Ge (ppm)	Hf Hf (ppm)	Hg Hg1 (ppm)
K1	135	10	0	80	64	781	19	9	0	10
M1	63	0	0	66	72	278	13	5	6	5
L2	55	0	0	61	18	158	11	0	0	0
L4	75	0	0	71	28	455	15	5	3	5
L6	86	0	0	61	106	247	11	0	3	0
L7	91	0	0	53	73	122	8	0	5	3
L9	78	0	0	61	69	108	11	4	4	5
L10	109	0	0	66	315	278	13	5	9	6
L12	83	0	0	68	886	454	12	0	6	3
L15	107	0	0	68	486	146	12	0	3	3
L18	96	0	0	67	307	107	12	0	3	3
L20	99	0	0	72	612	466	14	3	0	5
L22	114	0	0	77	469	524	15	0	8	5
L26	125	0	0	82	49	678	18	0	0	0
M9	129	0	0	88	30	488	17	5	0	5
L28	123	0	0	87	38	413	16	5	4	8
M10	129	0	0	89	35	498	19	6	4	6
K20	148	0	3	87	52	400	17	4	6	7

Elements III [ppm]:

Sample	La La (ppm)	Mo Mo1 (ppm)	Nb Nb (ppm)	S S1 (ppm)	Ta Ta (ppm)	Th Th (ppm)	Tl Tl (ppm)	U U (ppm)	Y Y (ppm)	Yb Yb (ppm)
K1	27	6	10	5974	0	12	0	0	35	4
M1	26	3	8	1967	0	13	0	0	17	3
L2	18	3	8	3882	4	13	0	0	14	3
L4	24	3	10	2134	0	12	0	0	24	3
L6	15	6	8	7944	5	14	0	3	15	3
L7	16	4	5	8011	3	14	0	3	14	3
L9	22	4	8	7214	0	14	0	3	14	3
L10	28	3	11	5850	0	13	0	0	23	4
L12	23	3	8	6252	3	15	0	3	19	3
L15	20	4	8	6699	4	14	0	3	13	3
L18	18	3	10	5651	3	15	0	3	12	3
L20	29	5	12	3437	0	16	0	3	21	3
L22	25	5	12	6349	0	11	0	0	24	3
L26	33	4	16	1595	4	11	0	0	33	4
M9	34	5	15	4879	0	12	0	0	28	3
L28	22	4	13	7580	0	14	0	3	24	3
M10	31	4	15	7715	0	13	0	0	30	3
K20	24	3	13	2812	0	10	0	0	27	3

* data recalculated to 100%

Appendix 8: XRF whole rock geochemical analysis (onshore samples)***Oxides [%]:**

Sample	SiO ₂ Si2 (%)	TiO ₂ Ti (%)	Al ₂ O ₃ Al1 (%)	Fe ₂ O ₃ Fe2 (%)	MnO Mn (%)	CaO Ca2 (%)	MgO Mg1 (%)	K ₂ O K (%)	Na ₂ O Na1 (%)	P ₂ O ₅ P1 (%)
16_1	70,48	0,84	12,45	5,68	0,06	1,88	0,67	4,68	2,60	0,27
26_2	53,92	1,87	13,18	14,04	0,19	7,06	3,96	2,23	3,08	0,28
25_4	94,62	0,05	3,16	0,24	0,01	0,48	0,35	0,90	0,04	0,06
27_4	86,06	0,15	7,57	0,51	0,01	0,37	0,12	2,89	2,03	0,02
6_1	79,91	0,16	8,52	1,25	0,03	2,95	1,70	2,84	2,40	0,11
14_2	74,76	0,63	14,31	1,65	0,01	0,28	0,80	7,08	0,20	0,10
23_2	60,80	0,25	2,48	3,16	0,21	30,36	2,34	0,06	0,04	0,15
16_4	75,16	0,09	13,93	1,04	0,05	0,83	0,18	4,79	3,67	0,13
18_3	75,79	0,04	13,12	1,43	0,47	0,94	0,09	4,52	3,45	0,02
12_1	74,12	0,39	13,27	1,89	0,03	0,44	0,15	6,29	3,12	0,07
18_1	65,77	0,67	16,21	4,52	0,07	3,78	1,92	2,89	3,64	0,16

Elements I [ppm]:

Sample	Ba Ba2 (ppm)	Cr Cr (ppm)	Cu Cu (ppm)	Ni Ni (ppm)	Pb Pb (ppm)	Rb Rb (ppm)	Sc Sc (ppm)	Sr Sr (ppm)	V V (ppm)	Zn Zn2 (ppm)
16_1	632	7	37	4	46	151	11	163	75	70
26_2	440	30	141	30	29	45	26	268	376	112
25_4	449	0	5	0	27	20	0	139	7	9
27_4	853	2	6	0	13	45	3	53	17	8
6_1	311	17	21	2	35	78	7	60	18	22
14_2	378	44	18	7	16	139	4	43	69	57
23_2	44	20	36	16	41	0	28	362	45	40
16_4	491	1	6	0	60	148	6	62	7	20
18_3	327	1	6	0	54	185	5	143	7	12
12_1	510	48	15	4	34	308	8	66	29	26
18_1	913	23	12	10	26	106	11	741	78	79

Elements II [ppm]:

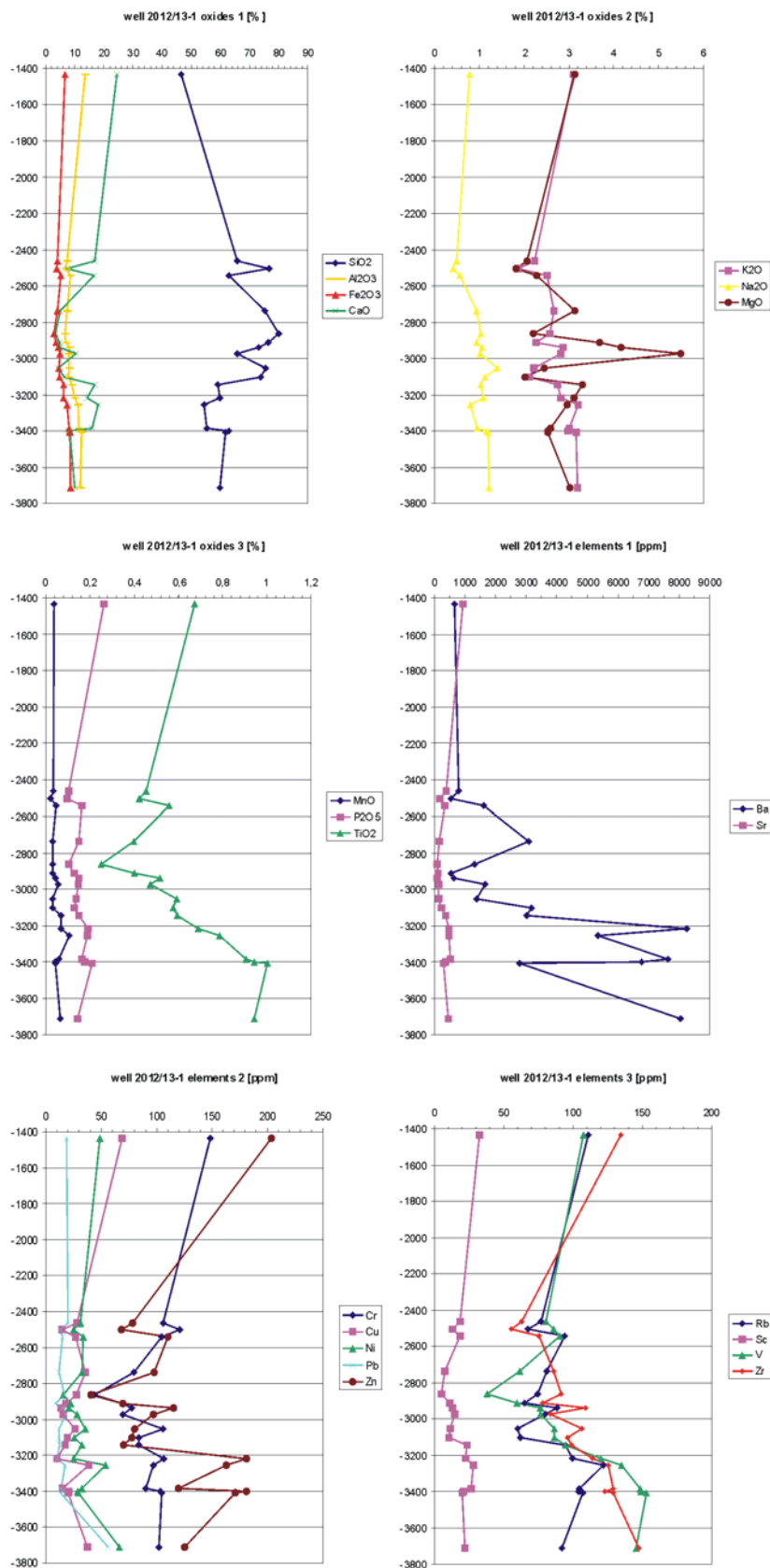
Sample	Zr Zr3 (ppm)	As As (ppm)	Cd Cd (ppm)	Ce Ce (ppm)	Cl Cl (ppm)	F F1 (ppm)	Ga Ga (ppm)	Ge Ge (ppm)	Hf Hf (ppm)	Hg Hg1 (ppm)
16_1	240	0	0	74	557	547	17	0	7	0
26_2	185	0	0	102	91	0	23	0	8	0
25_4	45	0	0	41	22	0	4	0	3	0
27_4	67	0	0	46	236	0	7	0	4	3
6_1	100	0	0	46	326	0	10	0	3	3
14_2	165	0	0	67	0	574	18	0	7	0
23_2	60	0	0	59	45	285	5	5	0	6
16_4	69	0	0	43	240	0	17	0	6	0
18_3	77	0	0	40	186	0	16	0	4	0
12_1	277	0	0	56	250	428	18	0	9	0
18_1	178	0	0	65	137	1180	20	0	4	3

Elements III [ppm]:

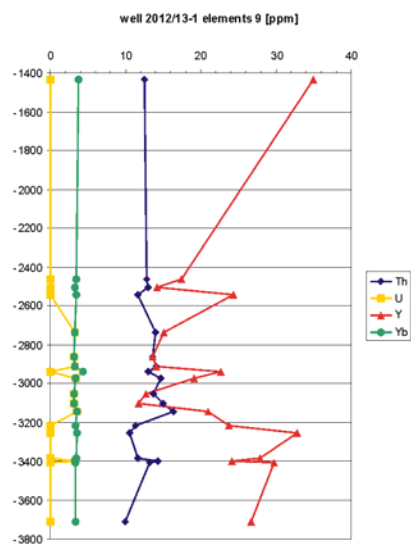
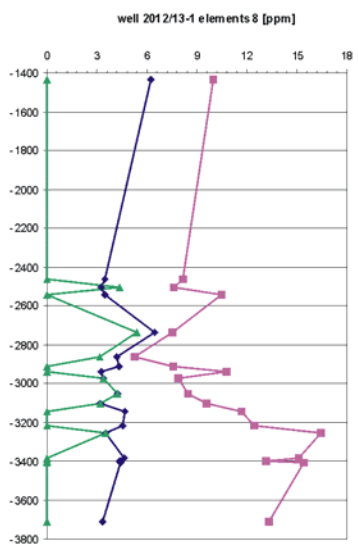
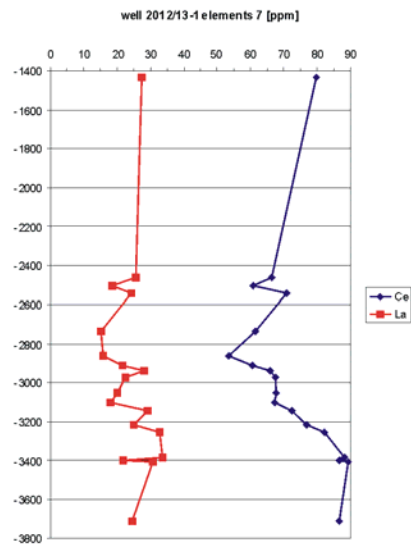
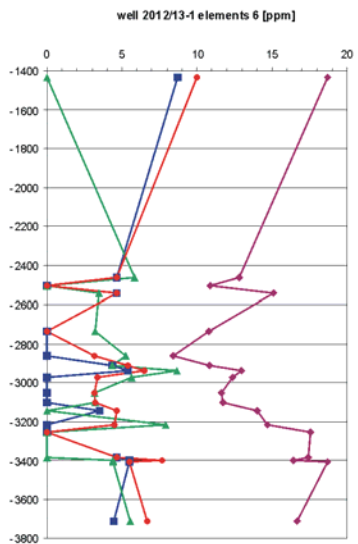
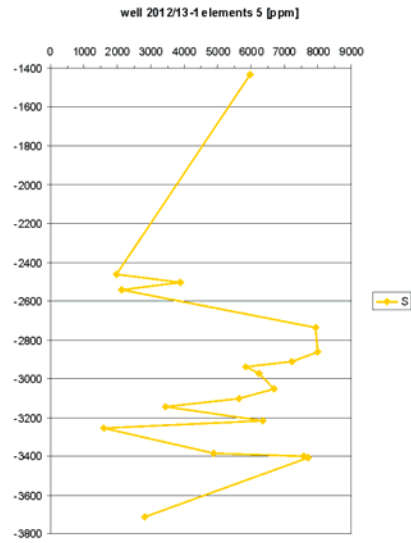
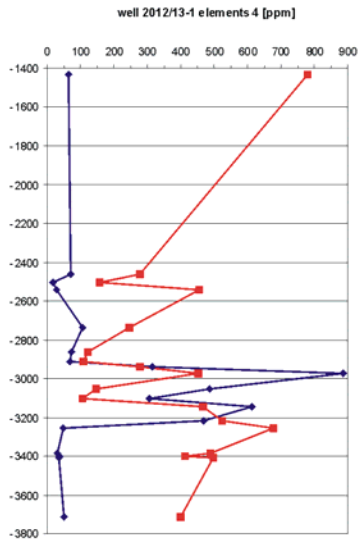
Sample	La La (ppm)	Mo Mo1 (ppm)	Nb Nb (ppm)	S S1 (ppm)	Ta Ta (ppm)	Th Th (ppm)	Tl Tl (ppm)	U U (ppm)	Y Y (ppm)	Yb Yb (ppm)
16_1	44	3	19	909	5	13	0	3	36	3
26_2	24	3	14	0	3	11	0	0	23	0
25_4	9	0	0	0	5	11	0	0	0	3
27_4	12	0	3	1252	3	11	0	0	3	3
6_1	19	0	5	328	5	13	0	0	15	3
14_2	45	0	17	0	4	17	0	5	30	3
23_2	13	4	5	242	0	15	0	0	0	0
16_4	25	0	10	0	5	14	0	4	26	3
18_3	21	0	4	0	4	17	0	5	58	4
12_1	44	4	34	0	8	19	0	6	63	3
18_1	53	0	10	0	0	8	0	0	24	3

data recalculated to 100%

Appendix 9-1: XRF whole rock geochemical analysis (offshore samples) plotted versus depth



Appendix 9-2: XRF whole rock geochemical analysis (offshore samples) plotted versus depth



Appendix 10: STRATA sea level file

Time from simulation start [Ma]	[m]	Time from simulation start [Ma]	[m]	Time from simulation start [Ma]	[m]	Time from simulation start [Ma]	[m]
0,0	128	40,6	136	71,7	56	100,2	3
1,0	115	40,8	169	72,2	80	100,5	18
1,5	100	40,8	196	72,5	110	101,4	36
2,1	82	41,0	218	73,0	146	102,4	50
2,6	64	41,2	226	73,3	172	103,3	61
2,9	44	41,8	228	73,6	187	104,2	70
3,2	22	42,8	225	74,2	186	104,8	86
3,6	-2	43,6	219	75,0	163	105,1	121
3,6	-14	44,0	211	75,1	99	105,2	110
4,3	-21	44,9	195	75,4	76	106,2	130
4,8	-2	45,1	185	75,8	121	107,0	130
5,0	29	45,9	197	76,1	152	107,5	118
5,2	51	46,1	205	76,2	173	107,9	109
6,3	75	46,5	214	76,3	200	108,4	98
7,9	89	47,4	219	76,9	209	108,6	72
9,2	102	47,8	226	77,6	212	109,1	66
10,0	114	48,5	232	78,4	209	110,0	89
11,3	130	49,3	231	78,9	203	110,9	107
11,8	146	49,4	216	79,9	194	111,5	115
12,4	160	49,8	202	80,4	169	112,3	121
13,4	172	49,9	185	80,6	111	113,2	132
14,8	174	50,3	181	80,7	72	113,3	91
16,2	169	50,5	193	81,2	117	114,0	80
16,7	156	50,7	214	81,5	153	114,6	125
17,5	136	51,0	229	81,8	190	115,1	139
17,8	103	52,4	235	82,0	209	115,7	138
18,3	87	53,5	234	83,1	212	116,3	117
19,0	121	54,5	228	83,8	210	116,7	96
19,0	101	54,9	210	84,6	206	117,5	79
19,3	135	55,3	198	85,4	200	117,8	61
20,1	142	55,6	185	86,1	186	118,3	48
21,6	143	55,9	203	86,4	174	119,2	33
22,8	146	56,4	216	86,8	161	119,3	-10
24,4	151	56,8	224	87,1	144	119,4	17
25,8	160	57,8	226	87,8	138	119,4	-41
26,9	166	58,3	219	88,4	148	119,5	-70
28,1	171	59,2	204	88,5	170	119,9	-75
28,9	179	59,3	186	89,0	188	120,5	-44
29,8	189	59,5	190	89,4	184	120,7	-19
30,5	200	60,0	202	89,4	173	121,7	-11
30,9	209	60,3	209	90,0	164	123,3	2
31,8	220	61,2	208	90,2	150	124,2	19
32,4	229	61,5	203	90,4	123	124,5	40
33,3	238	62,0	169	90,7	95	124,6	70
34,1	240	62,0	122	91,0	107	124,8	90
35,4	242	62,2	110	92,1	118	125,6	88
36,1	237	62,6	132	92,9	127	125,9	70
36,2	227	62,9	163	93,7	137	126,1	45
36,3	203	63,4	182	94,4	146	126,2	20
36,4	182	64,0	195	94,5	168	126,4	7
36,9	211	64,6	202	94,8	179	127,7	-11
37,0	227	65,6	202	95,1	191	128,0	-24
37,8	236	67,1	198	96,6	190	128,7	-42
38,0	247	68,9	192	97,3	183	129,1	-45
38,8	252	69,5	180	97,8	176	129,7	-33
39,5	243	70,0	166	98,8	164	129,9	-16
40,0	228	70,2	156	99,5	145	130,0	0
40,1	192	70,7	150	99,8	99		
40,2	134	71,0	143	99,9	72		
40,3	161	71,0	115	99,9	45		
40,5	121	71,4	81	100,0	19		

Appendix 11: STRATA subsidence file

Notation:

well name/ comment
 horizontal position of the well [m]
 age/ depth pairs [a]/ [m]
 end line

Well One:

0e3
 -130e6 0.
 -116e6 0.
 -91e6 0.
 -82e6 0.
 -76e6 0.
 -72e6 0.
 -69e6 0.
 -66e6 0.
 -50e6 0.
 -40e6 0.
 -22e6 0.
 -14e6 0.
 -6.3e6 0.
 0 0

Well Four:

73.5e3
 -130e6 362.
 -116e6 761.
 -91e6 1377.
 -82e6 2108.
 -76e6 2222.
 -72e6 2222.
 -69e6 2592.
 -66e6 2550.
 -50e6 3208.
 -40e6 3435.
 -22e6 3558.
 -14e6 3713.
 -6.3e6 3990.
 0 3846

Well Seven:

211.5e3
 -130e6 335.
 -116e6 703.
 -91e6 1272.
 -82e6 1946.
 -76e6 2051.
 -72e6 2051.
 -69e6 2393.
 -66e6 2354.
 -50e6 2962.
 -40e6 3172.
 -22e6 3285.
 -14e6 3429.
 -6.3e6 3684.
 0 3552

Well Two:

21.5e3
 -130e6 95.
 -116e6 199.
 -91e6 359.
 -82e6 550.
 -76e6 580.
 -72e6 580.
 -69e6 676.
 -66e6 665.
 -50e6 837.
 -40e6 896.
 -22e6 928.
 -14e6 969.
 -6.3e6 1041.
 0 1003

Well Five:

93.7e3
 -130e6 431.
 -116e6 906.
 -91e6 1640.
 -82e6 2509.
 -76e6 2645.
 -72e6 2645.
 -69e6 3086.
 -66e6 3035.
 -50e6 3819.
 -40e6 4089.
 -22e6 4236.
 -14e6 4420.
 -6.3e6 4750.
 0 4579

end: -1

Well Three:

50.4e3
 -130e6 158.
 -116e6 331.
 -91e6 599.
 -82e6 916.
 -76e6 966.
 -72e6 966.
 -69e6 1127.
 -66e6 1108.
 -50e6 1395.
 -40e6 1493.
 -22e6 1547.
 -14e6 1614.
 -6.3e6 1735.
 0 1672

Well Six:

110.3e3
 -130e6 449.
 -116e6 944.
 -91e6 1708.
 -82e6 2614.
 -76e6 2755.
 -72e6 2755.
 -69e6 3214.
 -66e6 3162.
 -50e6 3979.
 -40e6 4260.
 -22e6 4412.
 -14e6 4605.
 -6.3e6 4948.
 0 4770

Appendix 12: STRATA heat flow file

Time from simulation start [Ma]	Heat Flow [mW/ m ²]
0	95
10	88
20	82
30	77
40	72
50	68
60	64
70	60
80	57
90	54
100	52
110	51
120	50
130	49

Appendix 13: STRATA sediment flux file ("best fit" model mp4)

Time from simulation start [a]	Sediment Flux [m ² /a]	Time from simulation start [a]	Sediment Flux [m ² /a]	Time from simulation start [a]	Sediment Flux [m ² /a]	Time from simulation start [a]	Sediment Flux [m ² /a]
0,00E+00	8,799	3,60E+07	5,016	7,10E+07	1,818	1,01E+08	5,811
1,00E+06	8,799	3,70E+07	5,016	7,20E+07	1,818	1,02E+08	5,811
2,00E+06	8,799	3,80E+07	5,016	7,30E+07	1,818	1,03E+08	5,811
3,00E+06	8,799	3,90E+07	5,016	7,40E+07	1,818	1,04E+08	5,811
4,00E+06	8,799	4,00E+07	5,016	7,50E+07	1,818	1,05E+08	5,811
5,00E+06	8,799	4,10E+07	3,761	7,60E+07	3,767	1,06E+08	6,342
6,00E+06	9,369	4,20E+07	3,761	7,70E+07	3,767	1,07E+08	6,342
7,00E+06	9,369	4,30E+07	3,761	7,80E+07	3,767	1,08E+08	6,342
8,00E+06	9,369	4,40E+07	3,761	7,90E+07	3,767	1,09E+08	6,342
9,00E+06	9,369	4,50E+07	3,761	8,00E+07	3,767	1,10E+08	6,342
1,00E+07	9,369	4,60E+07	13,067	8,10E+07	8,472	1,11E+08	5,695
1,10E+07	9,636	4,70E+07	13,067	8,20E+07	8,472	1,12E+08	5,695
1,20E+07	9,636	4,80E+07	13,067	8,30E+07	8,472	1,13E+08	5,695
1,30E+07	9,636	4,90E+07	13,067	8,40E+07	8,472	1,14E+08	5,695
1,40E+07	9,636	5,00E+07	13,067	8,50E+07	8,472	1,15E+08	5,695
1,50E+07	9,636	5,10E+07	17,372	8,60E+07	3,939	1,16E+08	6,312
1,60E+07	9,765	5,20E+07	17,372	8,70E+07	3,939	1,17E+08	6,312
1,70E+07	9,765	5,30E+07	17,372	8,80E+07	3,939	1,18E+08	6,312
1,80E+07	9,765	5,40E+07	17,372	8,90E+07	3,939	1,19E+08	6,312
1,90E+07	9,765	5,50E+07	17,372	9,00E+07	3,939	1,20E+08	6,312
2,00E+07	9,765	5,60E+07	19,474	9,10E+07	1,782	1,21E+08	7,811
2,10E+07	9,061	5,70E+07	19,474	9,20E+07	1,782	1,22E+08	7,811
2,20E+07	9,061	5,80E+07	19,474	9,30E+07	1,782	1,23E+08	7,811
2,30E+07	9,061	5,90E+07	19,474	9,40E+07	1,782	1,24E+08	7,811
2,40E+07	9,061	6,00E+07	19,474	9,50E+07	1,782	1,25E+08	7,811
2,50E+07	9,061	6,10E+07	12,423	9,60E+07	4,286	1,26E+08	6,690
2,60E+07	8,534	6,20E+07	12,423	9,70E+07	4,286	1,27E+08	6,690
2,70E+07	8,534	6,30E+07	12,423	9,80E+07	4,286	1,28E+08	6,690
2,80E+07	8,534	6,40E+07	12,423	9,90E+07	4,286	1,29E+08	6,690
2,90E+07	8,534	6,50E+07	12,423	1,00E+08	4,286	1,30E+08	6,690
3,00E+07	8,534	6,60E+07	8,800				
3,10E+07	7,725	6,70E+07	8,800				
3,20E+07	7,725	6,80E+07	8,800				
3,30E+07	7,725	6,90E+07	8,800				
3,40E+07	7,725	7,00E+07	8,800				
3,50E+07	7,725						

Appendix 14: TOC and Rock-Eval pyrolysis data*

depth [m]	TOC [% of rock]	S1 [ppm]	S2 [ppm]	S3 [ppm]	HI [mg HC/ g TOC]	OI [mg CO ₂ /g TOC]	T max [°C]
3006	0,39	-	-	-	-	-	-
3021	0,87	60	1730	1170	199	134	424
3035	0,78	30	1380	990	177	127	425
3051	0,83	80	1890	780	228	94	424
3066	0,78	70	1540	780	197	100	424
3081	0,75	60	1340	910	179	121	425
3096	0,71	70	1310	860	185	121	425
3111	0,36	-	-	-	-	-	-
3126	0,38	-	-	-	-	-	-
3141	0,39	-	-	-	-	-	-
3156	0,33	-	-	-	-	-	-
3171	0,35	-	-	-	-	-	-
3186	0,3	-	-	-	-	-	-
3201	0,32	-	-	-	-	-	-
3216	0,46	-	-	-	-	-	-
3219	0,58	-	-	-	-	-	-
3231	0,25	-	-	-	-	-	-
3246	0,21	-	-	-	-	-	-
3261	0,54	-	-	-	-	-	-
3276	0,31	-	-	-	-	-	-
3291	0,38	-	-	-	-	-	-
3306	0,34	-	-	-	-	-	-
3271	0,27	-	-	-	-	-	-
3336	0,29	-	-	-	-	-	-
3351	0,35	-	-	-	-	-	-
3348	0,35	-	-	-	-	-	-
3366	0,43	-	-	-	-	-	-
3381	0,53	-	-	-	-	-	-
3396	0,75	50	730	1500	97	200	421
3411	0,82	60	750	1420	91	173	422
3426	0,51	-	-	-	-	-	-
3430	1,13	50	1670	1400	148	124	430
3456	0,71	20	550	1640	77	231	429
3450	3,44	370	14690	1600	427	47	425
3471	2,53	190	8080	1250	319	49	428
3466	0,43	-	-	-	-	-	-
3486	0,38	-	-	-	-	-	-
3489	1,88	90	3140	1160	167	62	433
3501	0,59	-	-	-	-	-	-
3516	0,63	-	-	-	-	-	-
3531	1,2	90	2440	1040	203	87	430
3539	4,6	720	26190	1430	569	31	422
3540	1,61	190	5130	1410	319	88	428
3543	1,71	200	5660	1320	331	77	429
3546	1,63	170	5330	1320	327	81	434
3549	1,76	230	6180	1420	351	81	429
3552	1,83	250	6720	1360	367	74	429

3555	2,34	340	9700	1540	415	66	429
3558	5,45	890	32200	1650	591	30	423
3561	5,23	860	31000	1540	593	29	426
3563	3,65	360	15950	1340	437	37	427
3564	5,86	860	36360	1650	620	28	423
3567	2,82	370	13580	1310	482	46	426
3570	1,03	70	1860	810	181	79	432
3573	1,02	100	2040	1050	200	103	431
3576	1,04	80	1540	1040	148	100	432
3579	1,4	140	2090	1260	149	90	429
3582	0,83	70	940	1100	113	133	432
3591	0,84	70	1040	1130	124	135	430
3606	0,9	60	940	1440	104	160	431
3602	2,65	270	8170	1470	308	55	430
3620	0,81	60	560	1700	69	210	423
3636	1,03	70	1290	1300	125	126	430
3634	2,22	180	6040	960	272	43	427
3642	2,09	150	4110	670	197	32	430
3651	0,81	50	700	1520	86	188	429
3666	0,76	50	620	1470	82	193	426
3681	0,47	-	-	-	-	-	-
3696	0,46	-	-	-	-	-	-
3709	0,49	-	-	-	-	-	-

** Results from organic carbon determination and Rock-Eval pyrolysis for well 2012/13-1.- From: Sasol Petroleum (Namibia) (PTY) LTD: well 2012/13-1, offshore Namibia, exploration well completion report (kindly provided by NAMCOR).*

Appendix 15: Maturity data*

depth	vitrinite reflectance (in situ vitrinite)	vitrinite reflectance (reworked vitrinite)	Spore Colour Index	inertinite	vitrinite	sapropel
[m]	[Ro %]	[Ro %]		[%]	[%]	[%]
1435	0,27	-	2	5	45	50
1515	0,28	-	2,5	5	45	50
1595	0,27	-	2,5	20	40	40
1675	0,28	-	2	50	10	40
1755	0,25	0,42	2	50	10	40
1838	0,33	-	2	50	10	40
1918	0,3	-	2,5	60	20	20
1998	0,37	-	2,5	10	30	60
2078	0,35	-	2,5	30	10	60
2158	-	-	2,75	20	10	70
2318	-	0,43	2,75	80	10	10
2398	0,35	0,51	-	10	85	5
2478	0,31	0,55	3	0	60	40
2558	0,36	0,49	3	50	20	30
2638	0,34	0,53	3	5	0	95
2718	0,37	0,59	2,5	10	5	85
2798	0,36	0,58	3	0	30	70
2878	0,38	0,55	3	5	5	90
2959	0,35	0,56	3,5	10	70	20
3006	0,35	0,54	3,5	15	65	20
3050	0,33	0,7	3,5	0	0	100
3081	0,37	0,53	3,5	5	20	75
3156	0,38	0,59	3,5	30	30	40
3231	0,39	-	4	10	80	10
3291	0,41	-	4	20	65	15
3381	0,42	0,61	4	20	65	15
3456	0,44	0,63	4	0	90	10
3531	0,43	0,63	3,5	5	35	60
3606	0,41	0,61	4,5	20	50	30
3620	0,46	0,67	4,5	10	80	10
3681	0,49	0,79	5,5	70	25	5
3709	0,61	0,9	6,5	70	20	10

* Maturity and kerogen composition data for well 2012/13-1.- From: Sasol Petroleum (Namibia) (PTY) LTD: well 2012/13-1, offshore Namibia, exploration well completion report (kindly provided by NAMCOR).

Appendix 16: List of figure captions

Fig. 1-1. Major structural and geological elements of NW-Namibia relevant for the postrift evolution of the margin. The onshore part of the model traverse covers large areas of the Lower Cretaceous Etendeka volcanic plateau; the offshore part is well documented by the seismic section ECL 89-41 and well 2012/13-1. Major Late Proterozoic basement structures (e.g. Waterberg-Omaruru Lineament) became reactivated as the loci of preferred intrusion of Early Cretaceous igneous complexes as well as of preferred denudation especially during the early passive margin evolution. Map based on <http://www.namcor.com.na/pdfs/GEOMAP.pdf>.

Fig. 1-2. Schematic illustration of the general model concept of a mass and process balance. The main objective of the study is to quantitatively link uplift and erosion onshore with contemporaneous subsidence and sedimentation offshore within a well documented transect across the NW-Namibian passive continental margin. The integrated approach enables quantitative insights into the feedback mechanisms between surface processes and lithospheric processes during passive margin evolution.

Fig. 2-1. Digital elevation model of NW-Namibia generated with *SURFER*. A gently inclined coastal plain (green colours) is separated from the continental interior (brown to yellow colours) by a distinct morphological feature, the Great Escarpment. Data obtained from the USGS global digital elevation model GTOPO30 with a horizontal grid spacing of 30 arc seconds (<http://edcdaac.usgs.gov/gtopo30/gtopo30.html>).

Fig. 2-2. Geological map of a segment of northern Namibia. Modified from the "South West Africa/Namibia geological map 1:1000000" of Miller & Schalk (1980).

Fig. 2-3. Catchment areas of the Hoanib, Uniab, Koigab, Huab, Ugab, and Omaruru ephemeral rivers, respectively. Map based on the "Atlas of Namibia" database provided by the Ministry of Environment and Tourism/ Namibia (<http://www.dea.met.gov.na/data/data.htm>).

Fig. 2-4. Proterozoic cratonic and orogenic zones of southern Africa. Distribution of Phanerozoic rift basins is closely associated with the orogenic belts. Proterozoic zones of crustal weakness exerted fundamental control on the Paleozoic and Mesozoic extensional history of Gondwana. Modified from Daly et al. (1989).

Fig. 2-5. Simplified standard-section of the lithology and stratigraphy in the study area with maximum preserved thicknesses. Compiled from own fieldwork and from Stollhofen (1999), Horsthemke et al. (1990), and Milner et al. (1994).

Fig. 2-6. Lithostratigraphic subdivision and nomenclature of the Etendeka Group in the southern Etendeka province. Modified from Milner et al. (1994).

Fig. 2-7. Airborne magnetic anomaly map of a segment of northern Namibia. Derived from the "Airborne Magnetic Anomaly Map of Namibia 1:1000000" published by the Geological Survey of Namibia; documentation by Eberle et al. (1995, 2002).

Fig. 2-8. Geological map of the Albin Ridge, southern Skeleton Coast/ NW-Namibia (mapped by R. Junker & M. Kukulus, 2000).

Fig. 2-9. Detailed geological map of the Albin Ridge, southern Skeleton Coast/ NW-Namibia (see fig. 2-8 for location).

Fig. 2-10. Schematic lithostratigraphic section of the Karoo and Lower Cretaceous clastic succession of the Albin Ridge (see fig. 2-9 for location).

Fig. 2-11. Selected samples from the clastic sequence of the Albin Ridge. (a) Red cherts of the base of the Prince Albert Formation (Dwyka?) showing characteristic small infaunal trace fossils (Pascichnia); location: 21°26,075`S, 13°53,941`E. (b) Light grey carbonaceous siltstones of the Prince Albert Formation showing ferrous plant or plant-like fossils typical of the Ecca Group; location: 21°26,075`S, 13°53,941`E. (c) Black siltstones of the upper Prince Albert Formation with probably enhanced TOC content; location: 21°25,609`S, 13°53,806`E. (d) Brown conglomerate of the Albin Ridge Member followed by a thin layer of overbank claystones; the latter are topped again by fluvial

coarse clastics with basal erosion; clasts are predominantly metasedimentary sandstones of the Damara sequence and subordinate hydrothermal quartzes; location: 21°28,493' S, 13°55,514' E; diameter of coin = 1,5cm.

Fig. 2-12. SW-NE-oriented cross section through the Albin Ridge and “Messum Ridge” tilted blocks (see fig. 2-8 for location).

Fig. 2-13. Steep sediment-filled fissures at the Albin Ridge Member-Etendeka Group boundary indicate synsedimentary extensional faulting during South Atlantic rifting. It is suggested that the Albin Ridge Member is a rare example of synrift deposition preserved in Namibia; hammer for scale; location: 21°26,737' S, 13°54,454' E.

Fig. 2-14. Sill-dyke-systems and intrusion tectonics at the Albin Ridge Member-Etendeka Group boundary. It is suggested that the dykes did not act as feeder-dykes for the overlying basalts; they show intrusive contacts and are more likely related to the Horingbaai dyke-swarm which is slightly younger than the Etendeka Group basalts (125Ma; Erlank et al., 1984; Renne et al., 1996). Stereographic net diagram indicates spatial orientation of some dykes (black) and sediment-filled fissures (red). Height of section approx. 100m.

Fig. 2-15. Miscoloured satellite image of a section of NW-Namibia comprising the area between the Albin Ridge in the SW and the Brandberg intrusive complex to the NE; created with *ENVI*. Some of the locations referred to in the text are labelled.

Fig. 3-1. Gross architecture of asymmetric conjugated upper-plate and lower-plate margins resulting from continental extension by detachment faulting. The lower plate margin (left) has a complex structure, with tilt-block remnants of the upper plate above bowed-up detachment faults. Multiple detachment has led to two generations of tilt-blocks. The upper-plate margin (right) is relatively unstructured and is uplifted by magmatic underplating to form passive margin mountains (“Great Escarpment”). From Etheridge et al. (1989).

Fig. 3-2. Jurassic pre-drift reconstruction of the South Atlantic Ocean including major transform zones which compensated differential extension during northward prograding oceanic onset in the Early Cretaceous. Modified from Dingle (1992/93).

Fig. 3-3. Reconstruction of the spatial relationship between the Tristan da Cunha hot spot, the South Atlantic spreading axis, and the evolving structure of the Rio Grande Rise (RGR) - Walvis Ridge (WR) volcanic system. The Mercator projections are centred on the island of Tristan da Cunha represented by the open circle (a)-(e); modified from O'Connor & Duncan (1990). (a) 130Ma reconstruction; the light grey circle represents a hypothesised large-diameter hot spot above the upwelling Tristan plume and comprises the surface relicts of the Paraná-Etendeka flood basalt system (black). (b)-(e) Reconstructions for selected spreading anomaly times. Bathymetry of Rio Grande Rise and Walvis Ridge is indicated by thin black lines. Small black circles represent magnetic anomaly picks from Cande et al. (1988). (f) Magmatic and magnetic features of the recent South Atlantic (see fig. 3-4 for details).

Fig. 3-4. Magmatic and magnetic features of the recent South Atlantic (Modified from Bauer et al., 2000). Labelling of magnetic anomalies after Rabinowitz & LaBrecque (1979) and Cande et al. (1988). Rio Grande Rise, Walvis Ridge, Paraná Flood Basalt Province, and Etendeka Flood Basalt Province are indicated by RGR, WR, PFB, and EFB, respectively. Coastal regions that are underlain by seaward dipping reflectors (SDR) are shaded in light grey.

Fig. 3-5. Interpreted p-velocity distribution for the entire crust in the central Walvis Basin area. Solid lines represent first order discontinuities derived from wide-angle reflection data; dashed lines are isovelocity lines interpreted from depth converted line drawings. COB=continent ocean boundary; TNOB=transitional-normal oceanic crust boundary. Modified from Bauer et al. (2000). See figure 1-1 & 4-2 for location of section BGR 95-11.

Fig. 3-6. Seismic section ECL 89-41 through the central Walvis Basin. (a) Seismic section down to 7s (TWT) showing the postrift succession in high resolution and significant, breakup-related seaward dipping reflectors; most of the basement is transparent or obscured by overlying strata; boxes labelled a – f indicate locations for detailed seismic interpretations examined in chapter 3.6.4 and figure 3-15.

(b) Linedrawing of the section and interpretation of the main seismo-stratigraphic elements. See legend and text for discussion. See figure 1-1 & 4-2 for location of the seismic section.

Fig. 3-7. Free-air gravity anomaly map of the Walvis Ridge area offshore NW-Namibia/ SW-Angola. The inset shows a 2D gravity section as indicated by the black line. (a) Thickness of the postrift sedimentary wedge derived from depth-converted seismic sections. (b) 2D gravity profile over the Namibian continental margin showing a pronounced offset of the gravity high landward of the sediment-depocentre (modified from Stewart et al., 2000). A significant coast-parallel gravity high is followed seaward by a less distinct high (grey dashed lines). These are correlated with the COB and TNOB, respectively, by Bauer et al. (2000).

Fig. 3-8. Backstripping and crustal scale gravity modelling for a section through the central Walvis Basin. A high elastic thickness of $T_e = 25\text{km}$ is assumed throughout rifting, backstripping, and modelling. (a) Stretching factor beta obtained from backstripping the sediment megasequences. (b) Rift geometry at the end of rifting. (c) Comparison of modelled gravity anomalies with observed gravity anomaly (see legend for details). Large residual anomalies remain between the modelled sum anomaly and the observed gravity anomaly. (d) Final modelled margin geometry. Modified from Stewart et al. (2000).

Fig. 3-9. 2D section through a 3D backstripped model of the central Walvis Basin. (a) The megasequences 1-4 represent the synrift, early drift, late Cretaceous, and Tertiary/ Quaternary succession, respectively (see legend for corresponding major seismic horizons). Total tectonic (unloaded) subsidence (TTS) is indicated by the black dashed line. (b)-(e) Individual backstrips for the units 1-4. (f) Cumulative backstrip without sediment and water loading. Black arrows indicate lateral variations of subsidence. The main depocentres to shift landwards before migrating oceanward in the Tertiary. This corresponds to the evolution of the shelf edge. Modified from Stewart et al. (2000).

Fig. 3-10. Aptian paleogeographic reconstruction of the South Atlantic. Control on the distribution of evaporites is exerted by the Rio Grande Rise-Walvis Ridge barrier and the Pernambuco Ridge-Cameroon volcanic line, respectively. Modified from Clifford (1986).

Fig. 3-11. Sedimentary regimes, oceanographic climate and current systems in the eastern South Atlantic during Miocene to Holocene times. Modified from Dingle (1992/93).

Fig. 3-12. Major stratigraphic events encountered in well 2012/13-1 related to eustatic sea level changes. Compiled from the Final Well Report of well 2012/13-1 (*Sasol Petroleum Namibia*) and Haq et al. (1987).

Fig. 3-13. Detailed interpretation of marker horizons, seismic sequences, and synsedimentary fault activity of the postrift succession in the central Walvis Basin derived from seismic section ECL 8941. See legend and text for discussion.

Fig. 3-14. Detailed section of the seismic sequence interpretation displaying the onlap history onto the eastern marginal basement high ("hinge zone"). Onlap starts as early as in the Barremian and is accomplished by mid-Turonian times.

Fig. 3-15. Significant seismic features as indicated by the boxes in fig. 3-6a. (a) Late Cretaceous synsedimentary fault activity. (b) Late Albian onlap onto the eastern basement ridge. (c) Downlap and rapid shelf propagation in the Maastrichtian. (d) Significant truncation of older strata during the latest Cretaceous/ Early Paleocene. (e) Toe area of a major Miocene slump sourced from the shelf edge; it cuts deeply into older strata and is immediately onlapped again. (f) Lens-shaped infill of a Neogene depression on the outer slope by high-amplitude parallel reflectors which is possibly due to longshore current activity.

Fig. 3-16. General porosity-/ thickness-depth relationship.

Fig. 3-17. Porosity-depth relationships specified for different lithologies and early cementation. Modified from Bond & Kominz (1984).

Fig. 3-18. Concept of water loading - longterm eustatic sea level changes combined with estimations of paleowater depth - and total subsidence.

Fig. 3-19. Schematic diagram illustrating how a sequence of multiple sediment layers can be backstripped by successive decompaction.

Fig. 3-20. Bandwidth of paleobathymetry estimations based on a high-resolution biostratigraphic study of well 2012/13-1 conducted by *Time Trax Ltd.* on behalf of *NAMCOR*.

Fig. 3-21. Decompacted burial history for a 20-layer 1D model of the postrift succession in the central Walvis Basin. Dashed line represents early drift section inferred from well 1911/15-1 (see Holtar & Forsberg, 2000). Seafloor serves as reference level.

Fig. 3-22. Backstripped tectonic subsidence plot for the central Walvis Basin. Subsidence is corrected for long-term eustatic sea level changes. The error bars account for the correction for minimum and maximum estimations of paleowater depths. Loads on the lithosphere are compensated by local/ Airy isostasy.

Fig. 3-23. Backstripped tectonic subsidence compared with the total basement subsidence of the central Walvis Basin, thus illustrating the effect of sediment loading. Tectonic subsidence is related to cooling curves of normal oceanic lithosphere (see legend and text for details).

Fig. 4-1. Continuous elastic plate model of the SW-African continental margin that is subjected to upward and downward loads. Flexural rigidity increases from oceanic towards the continental lithosphere with a narrow transition zone in the coastal plain area. Modified from Ten Brink & Stern (1992).

Fig. 4-2. Digital bathymetric model of the Walvis Basin generated with *SURFER*. The available offshore database (well and seismic data) is indicated by white boxes; red box outlines the model traverse for which postrift-denudation onshore is quantitatively linked with contemporaneous sedimentation offshore. Compiled from <http://www.namcor.com.na/pdfs/seismap.pdf>.

Fig. 4-3. High-resolution digital elevation model of the onshore part of the model traverse, generated with *SURFER* on the basis of topographic maps 1:250000. Area comprises the catchment areas of the Uniab and Koigab ephemeral rivers and adjacent areas in the coastal plain. The Great Escarpment terminates the model in the NE.

Fig. 4-4. 2D section through the onshore part of the model traverse. The reference levels 1-6 schematically indicate estimations of the topographic elevation of the paleo-landscape at the time of breakup inferred from a variety of stratigraphic and quantitative clues. Green section represents a profile of the Uniab ephemeral river in the coastal plain area. See text for details.

Fig. 4-5. Schematic 3D view of the volumes eroded from the onshore part of the model traverse. Colours are related to different estimations of the elevation of the paleo-landscape at the time of breakup. See text for details.

Fig. 4-6. Map of the estimated postrift denudation of southwestern Africa in [km] from 118-0Ma b.p. derived from apatite fission track analysis. Modified from Brown et al. (2000).

Fig. 4-7. Sedimentation rates, accumulation rates, and denudation rates for the central Walvis Basin and adjacent onshore areas since the time of breakup. Although inferred and modelled from different data sets, a broad correspondence between the curves can be depicted. See legend and text for discussion.

Fig. 4-8. Conceptual model of landscape evolution for the Namibian margin emphasising the degradational morphological evolution of the exterior river catchments (a) at the time of rifting, (b) some time after rifting, (3) when the marginal upwarp is breached by a major river system, and (d) when a stepped landscape due to the exposure of resistant lithology is formed. The location of the initial drainage divide controls the position of the later escarpment rather than rift-related faults. Redrawn from Gilchrist et al. (1994).

Fig. 4-9. Simplified sonic velocity log of the postrift sedimentary succession in the central Walvis Basin. The interval from 1420m to 3712m is inferred from the Final Well Report of well 2012/13-1 kindly provided by *NAMCOR*; the uppermost and lowermost intervals, respectively, are derived from

well 1911/15-1 in the northern Walvis Basin (Holtar & Forsberg, 2000). Seismic horizons are referred to in the text.

Fig. 4-10. Modelled sonic velocity section of the depthconverted seismic line ECL 89-41 as derived from the depthconversion-procedure; generated with *SURFER*. See text for details.

Fig. 4-11. Calculation of the material deposited in the offshore part of the model traverse during passive margin evolution. (a) wedge-shaped 3-layer model (I-III) of the postrift succession in the central Walvis Basin separated by seismic marker horizons; corresponding volumes are given in [km³]; (b) distribution of the accumulated volumes over time (grey boxes) compared with the relative denudation chronology (black line) inferred from AFT data (Gallagher & Brown, 1999, not to scale); (c) porosity-depth-relation after Sclater & Christie (1980) that was applied to reduce computed volumes for depth-dependent porosity in order to obtain effective masses. See text for discussion.

Fig. 4-12. Digital elevation models of the depthconverted seismic marker horizons Q, N, L, and Z within the model traverse which were used as reference surfaces for volume computations with *SURFER*.

Fig. 4-13. (a) Depthconverted 7-layer model of the seismic section ECL 89-41 subdivided by the seismic marker horizons Q, X, N, K, LII, L, Y, and Z; corresponding volumes of accumulated material are inferred from area-calculations of the 7 wedges by incorporating the width of the model traverse; white bar indicates calibration well 2012/13-1. Major structural elements are inferred from Light et al., 1993. (b) Distribution of the accumulated volumes over time and calculation of the average accumulation rates (black curve) in [km³/Ma]. See text for discussion.

Fig. 4-14. Graphic overview of the cumulative petrographic composition [%] of the Upper Campanian/Maastrichtian gross sand interval from c. 2700-3000m within the postrift succession of well 2012/13-1. Abbreviations in legend related to table 4-1.

Fig. 4-15. Provenance analysis of Upper Cretaceous sands of well 2012/13-1. Ternary Qm-F-Lt-plot modified from Dickinson et al. (1983). Sample names, symbols, and related depths are given by the inset in field 3. See appendix 1 for counted and recalculated parameters. The majority of samples reveals a basement or cratonic source (field 1a, 1b); 3 samples indicate recycling of orogens (field 2a).

Fig. 4-16. Provenance analysis of Upper Cretaceous sands of well 2012/13-1 using quartz grain varieties (cumulative percentages). Although the Etendeka volcanic plateau is suggested to be the prominent source area, less than 50% on average are of volcanic origin. Plutonic and metamorphic quartzes of probably basement origin constitute a major contribution.

Fig. 4-17. SEM image (BEI) showing detrital quartz and potassium feldspar, cemented by authigenic quartz. Magnification: 500x. Sample depth: 2885-2890m.

Fig. 4-18. SEM image (SEI) showing a permeable pore neck between relatively weakly cemented detrital quartz grains. Magnification: 2000x. Sample depth: 2845-2850m.

Fig. 4-20. SEM image (SEI) showing the scarred surface of a well-rounded detrital quartz grain. No indicators of aeolian transport can be observed. Magnification: 3000x. Sample depth: 2997-3000m.

Fig. 4-21. Plot of the SiO₂/Al₂O₃-ratio versus depth to approximate the sand-shale-ratio in well 2012/13-1.

Fig. 4-22. Tectonic discrimination diagrams for sandstones. Both diagrams reveal typical quartz-rich passive margin settings for the offshore samples. (a) Plot of K₂O/Na₂O versus SiO₂ after Roser & Korsch (1986); ARC = oceanic island margin, ACM = active continental margin, PM = passive margin. (b) Plot of SiO₂/Al₂O₃ versus K₂O/Na₂O after Maynard et al. (1982).

Fig. 4-23. Plot of TiO₂ versus Ni for the offshore samples. Grey fields (after Floyd et al., 1989) indicate magmatic source rocks of acidic composition.

Fig. 4-24. CaO-Na₂O-K₂O ternary diagram. Average composition of andesite (A), dacite (D), granodiorite (Gr), and granite (G) are inferred from Le Maitre (1976) for comparison with magmatic

rocks of the study area. Sedimentary onshore samples and offshore cutting samples are plotted for completion.

Fig. 4-25. Etendeka volcanic and intrusive rocks plotted on a classification diagram from Le Maitre (1976). The two representative samples of Etendeka basalt (sample 26/2, red square) and Etendeka quartz latite (sample 16/1, green square) analysed in this study fit well into the data set modified from Marsh et al. (2001).

Fig. 4-26. Distribution of the total thickness of erosion and deposition (uncorrected for compaction) for a section across the southern Namibian margin at the latitude of the Orange Basin; inferred from an elastic plate model assuming flexural rigidities of the lithosphere decreasing seaward. See text for discussion. Modified from Ten Brink & Stern (1992).

Fig. 4-27. Schematic concept of a mass balance for a segment across the passive continental margin of NW-Namibia. Volumetric constraints can be inferred from estimations of the amount of postrift erosion, from calculations of the volumes deposited offshore, from provenance studies, and from forward basin modelling, respectively. See text for discussion.

Fig. 5-1. The geometrical relationships of strata to depositional sequence boundaries are critical for the interpretation of seismic sections (from Allen & Allen, 1990).

Fig. 5-2. Depositional sequences are composed of parasequences that represent single episodes of progradation (shallowing upward). The overall stacking pattern of parasequences (progradational, retro-gradational, aggradational) reflects the complex interplay of relative sea level change, sediment supply, and subsidence (from Van Wagoner et al., 1988).

Fig. 5-3. An idealised depositional sequence is the record of one cycle of relative sea level and has a predictable internal structure related to specific segments (A-F) of the sea level curve. The evolution of highstand systems tracts (HST), lowstand fan systems tracts (LFST), lowstand wedge systems tracts (LWST), shelf margin systems tracts (SMST), and marine flooding surfaces (MFS) is illustrated. See text for details (modified from Posamentier et al., 1988).

Fig. 5-4. (a) Chart of global sea level changes applied to the basin model as modified by Junker (2002) from (b) the shortterm eustatic sea level changes (black curve) published by Haq et al. (1987). Longterm changes are indicated by the grey enveloping curve.

Fig. 5-5. (a) Subsidence history of the central Walvis Basin derived from backstripping of well data. Inset (b) shows the geometry of the basin floor obtained from a depthconverted seismic section of the NW-Namibian passive margin. The subsidence file applied to the basin model is given in appendix 11.

Fig. 5-6. Illustration of the heat flow history applied to the basin model. Data are related to Pollack et al. (1993) and Schmidt et al. (2002).

Fig. 5-7. Concept of sediment supply rates applied to the basin model. The grey line represents the supply rate derived from onshore denudation; a hypothetical longshore transport component is indicated by the grey dashed line; a combination of both results in the net sediment flux [m^2/a] to the basin model (black curve).

Fig. 5-8. Composition of model runs 2 and 23 displayed as sand-shale ratio [% Sand]. Run 2 illustrates a clear correlation of sediment supply peaks with coarse-grained facies, especially during early basin evolution. Shallow marine early-drift sedimentation can only be reproduced if the bulk sediment input is concentrated in the early margin evolution (run 23).

Fig. 5-9. Overview of 24 sediment supply rates (black curves) systematically applied to the basin model ("sinusoidal runs") by varying the hypothetical longshore transport component (grey dashed line).

Fig. 5-10. Overview of model results 0-23: colours indicate composition of the basin fill [% Sand].

Fig. 5-11. Overview of model results 0-23: colours indicate paleowater depth [m] at time of deposition.

Fig. 5-12. Upper part: sediment supply rates for the AFT shift runs a-d. Lower part: modelled composition of the basin fill [% Sand]. See text for details.

Fig. 5-13. Upper part: modelled paleowater depths of the AFT shift runs a-d. Lower part: modelled seismic signal [% of impulse amplitude]. See text for details.

Fig. 5-14. Results of manual run 1 (mp1): (a) the particular sediment flux curve, (b) a chronostratigraphic Wheeler-diagramm, (c) the composition of the basin fill [% Sand], (d) a paleowater depth model [m], (e) and a seismic response prediction model [% of impulse amplitude] are illustrated. See text for details.

Fig. 5-15. Results of manual run 2 (mp2): (a) the particular sediment flux curve, (b) a chronostratigraphic Wheeler-diagramm, (c) the composition of the basin fill [% Sand], (d) a paleowater depth model [m], (e) and a seismic response prediction model [% of impulse amplitude] are illustrated. See text for details.

Fig. 5-16. Results of manual run 3 (mp3): (a) the particular sediment flux curve, (b) a chronostratigraphic Wheeler-diagramm, (c) the composition of the basin fill [% Sand], (d) a paleowater depth model [m], (e) and a seismic response prediction model [% of impulse amplitude] are illustrated. See text for details.

Fig. 5-17. Results of the “best fit” model run (mp4): (a) the particular sediment flux curve, (b) a chronostratigraphic Wheeler-diagramm, (c) the composition of the basin fill [% Sand], (d) a paleowater depth model [m], (e) and a seismic response prediction model [% of impulse amplitude] are illustrated. Additionally, interpretations and correlations with calibration data are indicated. See text for detailed discussion.

Fig. 6-1. Location map showing the Namibian continental margin, offshore depocentres, and well sites (after Light et al., 1993).

Fig. 6-2. Simplified lithostratigraphic log of the Toscanini oil-borehole TO 1/72 (drilled by Du Preez, 1972). See fig. 6-1 for location.

Fig. 6-3. Simplified lithostratigraphic columns and chronostratigraphic correlation of wells 1911/15-1 and 2012/13-1. Potential source rocks are indicated in black; potential reservoir intervals are indicated in yellow. See location map and fig. 4-1 for bathymetry information.

Fig. 6-4. Plot of total organic carbon (TOC) content [% of rock] vs. depth for the interval from 3000m to TD of well 2012/13-1.

Fig. 6-5. Composition and distribution of organic matter in well 2012/13-1.

Fig. 6-6. Trend lines for the determination of kerogen types from Rock-Eval pyrolysis data. (a) Plot of Hydrogen index vs. Oxygen index after Tissot & Welte (1984). (b) Plot of Hydrogen index vs. peak temperature (T_{max} , see Holtar & Forsberg, 2000).

Fig. 6-7. Recent upwelling zone offshore NW-Namibia. Upwelling causes high phytoplankton productivity in surface waters. Seabottom sediments are anoxic beneath highly productive waters (modified from Demaison & Moore, 1980).

Fig. 6-8. Plot of S1+S2 vs. depth as a measure of oil generation potential.

Fig. 6-9. Optical indicators for the thermal maturity level of well 2012/13-1. (a) In situ vitrinite (black diamonds) and reworked vitrinite (open squares) reflectance [%Ro] vs. depth. (b) Spore Colour Index vs. depth.

Fig. 6-10. Comparison of modelled Easy%Ro-trends (A) and temperature-trends (B) with calibration data from well 2012/13-1 for different settings of basal heat flow. A low constant basal heat flow of 40mW/m^2 (a) fits the observed vitrinite reflectance data very well. An exponentially decreasing and spatially varying heat flow (b) better fits the measured temperature data.

Fig. 6-11. Illustration of an exponentially decreasing and spatially varying heat flow applied to the maturity model as a function of time (A) and as a contour plot over the modelled section (B).

Fig. 6-12. Maturity modelling for a depthconverted seismic section through the central Walvis Basin with *PetroMod2D*. (a) Modelled temperature section. (b) Modelled vitrinite reflectance section. (c) Maturity stage of the potential source rock interval assuming minimum basal heat flow. (d) Modelled contours of the transformation ratio of generated hydrocarbons.

Fig. 6-13. Maturity model of the central Walvis Basin with *PetroMod2D* comprising synrift- and postrift-related structures. The maturity stage of potential synrift and early drift source rocks is evaluated. (a) Modelled temperature section. (b) Modelled vitrinite reflectance section. (c) Modelled hydrocarbon zonation; box indicates location of figure 6-14. (d) Modelled contours of the transformation ratio of generated hydrocarbons. Synsedimentary faults are incorporated to assess their relevance for hydrocarbon migration. Modified from Beha (2003).

Fig. 6-14. Migration and trapping of hydrocarbons (green) associated with synsedimentary faults and updip pinch-out modelled with *PetroMod2D*. Location is indicated in figure 6-13c. Modified from Beha (2003).

Fig. 6-15. SEM-image of a representative pore space of the potential Upper Campanian/Maastrichtian reservoir rock interval indicating a first generation microcrystalline quartz-cementation and a second generation dolomite cementation (depth: 2838m, exagg.: 500x).

Fig. 6-16. Conceptual illustration of hydrocarbon play types that may have developed in the Walvis Basin during the (a) prerift-phase, (b) synrift-phase, (c) early drift-phase, and (d) late drift-phase of margin evolution. See text for discussion.

Appendix 17: Selected internet sources

National Petroleum Corporation of Namibia (*NAMCOR*): <http://www.namcor.com.na/>

Geological Survey of Namibia: <http://www.gsn.gov.na/>

Ministry of Environment and Tourism/ Namibia:
<http://www.dea.met.gov.na/data/data.htm>

STRATA Homepage: <http://hydro.geosc.psu.edu>

Integrated Exploration Systems (*PetroMod2D*): <http://www.ies.de/>

USGS Global DEM Database: <http://edcdaac.usgs.gov/gtopo30/gtopo30.html>

Tony Watts Homepage: <http://www.earth.ox.ac.uk/~tony/watts/INDEX.HTM>

Garry Karner Quantitative Basin Analysis:
<http://www.ideo.columbia.edu/karner/QBA.word.html>

London Thermochronology Research Group:
<http://www.es.ucl.ac.uk/research/fissiontrack/>

Matthias Raab Homepage: <http://wwwuser.gwdg.de/~mraab/>

The Geological Society of London:
<http://www.geolsoc.org.uk/template.cfm?name=geohome>

English-German online dictionary: <http://dict.leo.org/>

Basic principles of Scanning Electrone Microscope analysis: <http://www.reclot.de/>

“Plano” Scanning Electrone Microscope analysis:
<http://www.plano-em.com/index.html>

Appendix 18. Curriculum vitae

Name	Matthias Kukulus
Anschrift	Neidhartstraße 22, 86159 Augsburg
Geburtsdatum	3. April 1973
Geburtsort	Donauwörth
Staatsangehörigkeit	deutsch
Familienstand	verheiratet
Konfession	evangelisch
Schulbildung	
1983 – 1992	Gymnasium Donauwörth
Zivildienst	
August 1992 – Oktober 1993	Bayerisches Rotes Kreuz/ KV Nordschwaben
Studium	
November 1993 – Dezember 1999	Studium der Geologie/ Paläontologie an der Universität Würzburg; Diplomarbeit zum Thema: „Tektonik und Sedimentation im nordwestlichen Saar-Nahe-Becken/ SW-Deutschland“
Promotion	
seit Januar 2000	zum Thema: “A quantitative approach to the evolution of the central Walvis Basin offshore NW-Namibia: structure, mass balancing, and hydrocarbon potential” an der Universität Würzburg
Praktika	
März/ April 1997	Betriebspraktikum bei der Firma Mobil Oil AG in Celle
August/ September 1998	Betriebspraktikum bei der Firma GEOBohr GmbH in Bermaringen
Mai – Juli 2003	Tutor am Geologischen Institut der Universität Freiburg

Hiermit versichere ich, Matthias Kukulus, dass ich diese Arbeit selbständig verfasst und keine anderen als die angegebenen Quellen und Hilfsmittel benutzt habe.

Ort, Datum

Unterschrift

